

AN ABSTRACT OF THE DISSERTATION OF

Ravi Challa for the degree of Doctor of Philosophy in Civil Engineering presented on December 5, 2014.

Title: Hydrodynamic Contact/Impact Modeling and Application to Ocean Engineering Problems

Abstract approved:

Solomon C. Yim

Abstract:

Fluid-structure interaction (FSI) is a very interesting and challenging multi-disciplinary field involving interaction of a movable or deformable structure with an internal or surrounding fluid flow. FSI has several practical engineering applications such as the determination of the hydrodynamic forces on a structure or the dynamics of motion of bodies on the water-free surface. A requirement for the solution of these class of contact and impact FSI problems need accurate model development and predictive assessment especially when complex structures are involved.

Analysis of FSI problems is often difficult and therefore experimental investigations (or empirical laws) are performed by conducting experiments in a physical wave basin. These experiments though impendent with the real world scenario often are time-consuming and expensive. Importantly, it may not be economically viable to conduct parametric studies using experiments. Alternatively, numerical models when developed with similar capabilities will complement the experiments very well because of the lower costs and the ability to study phenomena that are not completely feasible in a physical laboratory.

This dissertation systematically examines the contact and impact fluid-structure interaction numerical modeling procedure applied to various practical multi-physics ocean engineering problems. The significant component of contact and impact FSI problems addressed in this research is divided into three categories. First, the experimental and numerical investigations for a rigid-body contact and impact (drop tests) is presented, and followed by numerical simulation and analysis of low and high-filled multi-physics sloshing phenomena in the LNG tank including air compressibility effect. Second, the performance of a finite-element method and a smoothed particle hydrodynamic method is evaluated by using a consistent numerical platform for the simulation of contact and impact of a fluid interacting with a flexible body. Finally, numerical simulation and analysis of a complex-body contact and impact (a fully pressurized surface effect ship (SES) bow finger seal motions) is investigated.

©Copyright by Ravi Challa

December 5, 2014

All Rights Reserved

Hydrodynamic Contact/Impact Modeling and Application to Ocean
Engineering Problems

by

Ravi Challa

A DISSERTATION

submitted to

Oregon State University

in partial fulfillment of
the requirements for the

degree of

Doctor of Philosophy

Presented December 5, 2014

Commencement June 2015

Doctor of Philosophy dissertation of Ravi Challa presented on December 5, 2014.

APPROVED:

Major Professor representing Civil Engineering

Head of the School of Civil and Construction Engineering

Dean of the Graduate School

I understand that my dissertation will become part of the permanent collection of Oregon State University libraries. My signature below authorizes release of my dissertation to any reader upon request.

Ravi Challa, Author

ACKNOWLEDGEMENTS

The author wishes to express his sincere and profound sense of gratitude and respect for his research supervisor Prof. Solomon Yim for his guidance and constant support throughout the period of this research. Completion of this dissertation would not have been possible without his mentoring. It is a great privilege working with him and the author is especially thankful for his constant encouragement, untiring support and valuable suggestions at every stage of the research work. I am forever indebted to him for being there for me in the most difficult times of my doctoral studies.

I also wish to thank the members of my committee, Prof. Harry Yeh, Prof. Michael Scott and Prof. William McDougal for their inputs, advice and suggestions during the course of this research. I am also thankful to Prof. Yim and Prof. Harry Yeh for imparting the basic principles in ocean engineering through the challenging course work in finite element methods and water wave mechanics. Imposing course work in this area has proven to be invaluable in my research and will continue to play a major part in my future professional endeavors. Thanks are also due to Prof. William McDougal for giving me the opportunity to work for him on a finite element project which gave me the confidence to tackle practical application oriented problems. I also wish to thank Dr. Ralph Showalter for agreeing to be a part of my graduate committee.

The author expresses gratitude to Prof. Odd Faltinsen of the Department of Marine Hydrodynamics, Norwegian University of Science and Technology, Trondheim, Norway for his valuable comments during the presentation of both the articles (OMAE-10-20658 and OMAE-10-20659) at the 29th International Conference on Ocean, Offshore and Arctic Engineering, Shanghai, China. His critical comments have helped the authors to successfully chronicle the equivalent-radius approximate analytical procedure for the rigid object water entry problem.

I am indebted to Prof. Sundar, Prof. Idichandy and Prof. Vendhan, from the Department of Ocean Engineering, Indian Institute of Technology Madras, India, for introducing me to the astonishing field of ocean engineering in general and computational finite element methods in particular. Their invaluable guidance and perpetual encouragement has been a major contributor in my research career.

This work wouldn't have been possible without the excellent support from the OSU computing system administrators Paul Montagne and Jordan Jones for their help in setting up the high-performance computational platforms on which most of the numerical simulations were performed.

Thanks are also due to my friends who are the fulcrum of my existence: Suraj Darra and Gaurav Bhakar for their love and support: Ali Mohtat, David Newborn and Junhui Lou for keeping the workplace lively with numerous late-night discussions. Special thanks to Ali Mohtat for his inputs and for the quality time spent with him in understanding and deriving several complicated mathematical formulations used in this research. I have learned an unfathomable amount through friendships which

helped me expand my personal growth. Importantly, the experience of working with them taught me to have an open mind, respect people as they are and appreciate the process that goes into becoming a strong individual.

I am also thankful to all those who are close to my heart – family members, relatives and friends who helped me in no small measure to accomplish this target. Particularly, the author wishes to express his sincere gratitude to his father- Sri Rama Murthy Challa, mother- Vasundhara Challa, wife- Sucharita Tata, sister- Lalitha Mallik, brother-in-law- Mallik Pallela and my adorable nephew Abhaya Pallela, for their constant encouragement and the unconditional love and affection that keeps me motivated and willing to go that extra mile. Not to mention their patient wait to see me accomplish my research.

Finally, I am forever indebted to my spiritual guru, Shri Shirdi Samartha Satguru Sainath Maharaj, and the omnipotent and omnipresent, Maa Durga Shakthi, for showing me the path of righteousness and guiding me through the most testing times of my life. Without their blessings, I wouldn't have seen this day.

CONTRIBUTION OF AUTHORS

The author expresses gratitude to Prof. V. G. Idichandy (Retd., Deputy Director and Emeritus faculty of the Department of Ocean Engineering of Indian Institute of Technology Madras) and Prof. C. P. Vendhan (Department of Ocean Engineering, Indian Institute of Technology Madras) for their valuable inputs which played an important role in contributing to the Indian Space Research Organization (ISRO) Water Landing Object research project. Thanks are also due to them for agreeing to be co-authors to two journal papers that emanated from those efforts.

TABLE OF CONTENTS

	<u>Page</u>
1 GENERAL INTRODUCTION	1
1.1 Introduction	1
1.2 Objectives.....	3
1.3 Scientific contributions of the dissertation.....	5
2 RIGID-BODY WATER-SURFACE IMPACT DYNAMICS: EXPERIMENT AND SEMI-ANALYTICAL APPROXIMATION.....	9
2.1 Abstract	9
2.2 Introduction	10
2.3 Experimental investigation of rigid-body impact dynamics using drop tests	13
2.3.1 Drop test I	15
2.3.2 Drop test II	21
2.4 Approximate closed form solutions for maximum impact accelerations.....	27
2.5 An equivalent radius approximate semi-analytical procedure	34
2.6 Discussion and comparison.....	38
2.7 Concluding remarks	40
2.8 Acknowledgements	43
2.9 References	43
3 RIGID-OBJECT WATER-ENTRY IMPACT DYNAMICS: FINITE-ELEMENT/SMOOTHED PARTICLE HYDRODYNAMICS MODELING AND EXPERIMENTAL VALIDATION.....	47
3.1 Abstract	47
3.2 Introduction	48
3.3 Finite element modeling of the experimental WLO drop tests	51
3.4 Finite element simulations	57
3.5 Analytical description of the general contact–impact problem.....	64
3.6 Smoothed particle hydrodynamics (SPH) simulations	67
3.7 Performance studies of ALE and SPH.....	77
3.8 Discussion and comparison.....	81

TABLE OF CONTENTS (Continued)

		<u>Page</u>
	3.9 Concluding remarks	83
	3.10 Acknowledgements	85
	3.11 References	86
4	NUMERICAL MODELING OF FLUID SLOSHING INCLUDING AIR COMPRESSIBILITY EFFECT	91
	4.1 Abstract	91
	4.2 Introduction	92
	4.3 Governing field equations: Arbitrary Lagrangian-Eulerian (ALE) formulation	95
	4.4 Experimental set-up: Pressure field in forced roll motion	96
	4.5 Numerical modeling and simulations	98
	4.6 Systematic study of wave breaking and impact process	103
	4.6.1 Fluid flow in the tank for one full oscillation cycle	104
	4.6.2 Plunge-type wave breaking process	106
	4.7 Quantitative comparison of angle and pressure results	109
	4.8 Estimation of maximum impact pressure	117
	4.9 Pressure impulse analysis	119
	4.10 Multiphase physics with air model and sensitivity of pressure field to air compressibility	121
	4.11 Conclusions	131
	4.12 Acknowledgments	133
	4.13 References	133
5	PREDICTIVE CAPABILITY OF FINITE ELEMENT AND SMOOTHED PARTICLE HYDRODYNAMICS MODELING OF FLUID-STRUCTURE INTERACTION	137
	5.1 Abstract	137
	5.2 Introduction	138
	5.3 Numerical model	140
	5.3.1 Arbitrary Lagrangian-Eulerian formulation and finite element solution procedure	141

TABLE OF CONTENTS (Continued)

	<u>Page</u>
5.3.2 Lagrangian formulation and smoothed particle hydrodynamics solution procedure	144
5.4 Experimental set-up of rapidly-varying flow with flexible elastic gate.....	150
5.5 Numerical simulations.....	152
5.5.1 ALE/FE modeling of FSI: Deformation of an elastic gate	152
5.5.2 Smoothed particle hydrodynamics and finite element modeling.....	156
5.6 ALE/FE and SPH/FE simulation results	159
5.7 Sensitivity and convergence Study	173
5.8 Conclusions	176
5.9 Acknowledgements	178
5.10References	178
6 NUMERICAL SIMULATION OF SURFACE EFFECT SHIP BOW FINGER SEAL FLUID-STRUCTURE INTERACTION	183
6.1 Abstract	183
6.2 Introduction	184
6.3 Free-running SES physical experiment.....	187
6.4 General hydrodynamics of the flow around the SES	191
6.5 Arbitrary Lagrangian-Eulerian formulation and finite-element solution procedure	192
6.6 Finite-Element modeling of air and water domains and SES	193
6.7 Finite-element simulations	197
6.8 FE simulation results of bow finger skirt node deflections.....	209
6.9 Conclusions	217
6.10Acknowledgments	219
6.11References	219
7 GENERAL CONCLUSIONS.....	223
BIBLIOGRAPHY	229
APPENDICES	238
Appendix–A: Inertial properties of the WLO model.....	239
Appendix-B: Surface Effect Ships.....	242

TABLE OF CONTENTS (Continued)

	<u>Page</u>
Appendix–C: Membrane Element Formulation.....	245
Appendix–D: ALE Modeling Guidelines for Fluid-Structure Interaction.....	250

LIST OF FIGURES

<u>Figure</u>	<u>Page</u>
Figure 2.1: Overall configuration of WLO Prototype (All dimensions are in mm)	13
Figure 2.2: Measured data of a 5m drop test: Acceleration time history of a sample test case.....	17
Figure 2.3: Measured data of a 5m drop test: Pressure time history of a sample test case	18
Figure 2.4: Consistency of measured peak acceleration and peak pressure vs. sampling rate (PC based data acquisition).....	19
Figure 2.5: Consistency of measured peak acceleration and peak pressure vs. sampling rate (Oscilloscope Capture).....	19
Figure 2.6: Electromagnet with protruding strut (a) Up-close view of the setup for Drop Test II (b) WLO touchdown with water surface	22
Figure 2.7: Measured electromagnetic release data of a 5m drop test.....	24
Figure 2.8: Maximum impact force vs. square of impact velocity (Drop Tests I & II)....	26
Figure 2.9: Maximum impact pressure vs. square of normalized impact velocity (Drop Tests I & II).....	27
Figure 2.10: Maximum acceleration using von-Karman and Wagner solutions (Drop Test I).....	32
Figure 2.11: Maximum acceleration using von-Karman and Wagner solutions (Drop Test II).....	32
Figure 2.12: Equivalent radius of the WLO model.....	35
Figure 2.13: Equivalent radius (r) of the WLO for different normalized velocities of impact for Drop Test I and Drop Test II using von-Karman and Wagner approaches.....	36
Figure 2.14: Maximum impact accelerations calculated based on the mean equivalent radius (r^*) of the WLO for different normalized velocities of impact for Drop Test I using von-Karman and Wagner approaches	37
Figure 2.15: Maximum impact accelerations calculated based on the mean equivalent radius (r^*) of the WLO for different normalized velocities of impact for Drop Test II using von-Karman and Wagner approaches	37
Figure 3.1: Overall configuration of WLO Prototype (All dimensions are in mm)	53
Figure 3.2: Elevation [L] and top view [R] of the FE-ALE computational mesh (Blue: Water domain /Green: Air Domain/ Red: WLO model)	58

LIST OF FIGURES (Continued)

<u>Figure</u>	<u>Page</u>
Figure 3.3: Animation images at various time steps for vertical impact	59
Figure 3.4: Numerical simulation response of a 5m drop test: Acceleration time history	60
Figure 3.5: Numerical simulation response of a 5m drop test: Pressure time history	60
Figure 3.6: Height of Drop vs. Depth of Immersion for Case-I	61
Figure 3.7. Plan of the SPH Water domain and the WLO (Number of SPH nodes: 712,000)	71
Figure 3.8. SPH Animation images of the particle impingement at various time steps ...	71
Figure 3.9: SPH acceleration time history for a 5m drop height	72
Figure 3.10: Comparison of results for maximum acceleration with ALE and SPH [Weight of WLO = 2.03 kg (Case-I: Mechanical release)] (Vertical Entry/Entry Angle=0 deg)	73
Figure 3.11: Comparison of peak impact acceleration (pitch tests - ALE and SPH methods).....	74
Figure 3.12: Comparison of results for maximum acceleration with ALE and SPH [Weight of WLO = 3.5kg (Case-II: Electromagnetic release)] (Vertical Entry/Entry Angle=0 deg)	75
Figure 3.13: Mesh size variation vs. Maximum impact acceleration	76
Figure 3.14: Number of particles (SPH nodes) vs. Maximum impact acceleration	76
Figure 3.15: Number of CPUs vs. estimated clock time for ALE and SPH test models..	79
Figure 3.16: Clock-time ratios of SPH/ALE vs the number of CPUs	80
Figure 3.17: Speed scaling of the performance of ALE and SPH (N_1/N_p).....	80
Figure 4.1: Two-dimensional rectangular tank with mean water level	97
Figure 4.2: ALE-FE simulation: Computational domain of LNG tank/air/water domains	99
Figure 4.3: ALE-FE simulation results of the impact event for one oscillation cycle....	106
Figure 4.4: ALE-FE simulation results: All frames are equally separated in time $\Delta t / T = 0.021$	108
Figure 4.5: ALE-FE simulation results: Pictures of the wave shape just before the first impact for Cases A–C	109

LIST OF FIGURES (Continued)

<u>Figure</u>	<u>Page</u>
Figure 4.6: Dimensionless pressure and dimensionless angle vs. dimensionless time for case A.....	111
Figure 4.7: Dimensionless pressure and dimensionless angle vs. dimensionless time for case B.....	112
Figure 4.8: Dimensionless pressure and dimensionless angle vs. dimensionless time for case C.....	113
Figure 4.9: Experiment and ALE-FE simulation result comparison	116
Figure 4.10: ALE-FE simulation results: Pictures of the first five impact events for Cases A–C.....	117
Figure 4.11: Experimental and numerical pressure impulse comparison: Dimensionless pressure impulse vs. oscillation cycle.....	120
Figure 4.12: Non-dimensional pressure maxima vs. Bulk modulus (N/m^2) (Results shown are for all the three cases and values are from Table 3).....	124
Figure 4.13: Impact pressure time histories with the air/water interface (80% Fill)	127
Figure 4.14: Impact pressure time history without air domain (80% Fill)	128
Figure 4.15: Non-dimensional pressure maxima for highest pressure peaks for two different fill conditions (comparison between experimental and numerical simulation results).....	128
Figure 4.16: Maximum impact pressure (N/m^2) vs. Bulk modulus (N/m^2) (Results shown are for two high-filled sloshing cases and values are from Table 4.4)	130
Figure 5.1: Scheme of the tank and of the gate: frontal view, lateral and plan	151
Figure 5.2: Initial configuration of the tank and water	153
Figure 5.3: ALE/FE simulation: Computational domain.....	154
Figure 5.4: 3-D configuration of SPH-FEM computational domain (SPH: Water domain; FEM Mesh: Top part – Rigid Wall and Bottom part – Elastic gate)	157
Figure 5.5: Frames and images from ALE/FE simulation (Every 0.04s from $t = 0s$ to $t = 0.4s$).....	160
Figure 5.6: Frames and images from SPH/FE simulation (Every 0.04 s from $t = 0s$ to $t = 0.4s$).....	161

LIST OF FIGURES (Continued)

<u>Figure</u>	<u>Page</u>
Figure 5.7: Horizontal and vertical displacements of the free end of the gate (ALE/FE)	162
Figure 5.8: Horizontal and vertical displacements of the free end of the gate (SPH/FE)	163
Figure 5.9: Water level (m) just behind the gate (ALE/FE)	164
Figure 5.10: Water level (m) 5cm far from it (ALE/FE)	164
Figure 5.11: Water level (m) just behind the gate (SPH/FE).....	165
Figure 5.12: Water level (m) 5cm far from it (SPH/FE).....	165
Figure 5.13: X and Y displacement time histories (of the free end of the elastic gate) for different smoothing lengths (SPH/FE).....	168
Figure 5.14: σ_{xx} distribution at $t = 0.124s$: color scale ranging from $\sigma_{xx} = -49020N / m^2$ (blue) to $\sigma_{xx} = 65000N / m^2$ (red)-ALE/FE.	170
Figure 5.15: σ_{xx} distribution at $t = 0.19s$: color scale ranging from $\sigma_{xx} = -2457N / m^2$ (blue) to $\sigma_{xx} = 7406N / m^2$ (red)-SPH/FE.	171
Figure 5.16: σ_{xy} distribution at $t = 0.124s$: color scale ranging from $\sigma_{xy} = -91960N / m^2$ (blue) to $\sigma_{xy} = 110200N / m^2$ (red)-ALE/FE.....	171
Figure 5.17: σ_{xy} distribution at $t = 0.19s$: color scale ranging from $\sigma_{xy} = -994.5N / m^2$ (blue) to $\sigma_{xy} = 3143N / m^2$ (red)-SPH/FE.....	172
Figure 5.18: σ_{yy} distribution at $t = 0.124s$: color scale ranging from $\sigma_{yy} = -413000N / m^2$ (blue) to $\sigma_{yy} = 400600N / m^2$ (red)-ALE/FE.....	172
Figure 5.19: σ_{yy} distribution at $t = 0.19s$: color scale ranging from $\sigma_{yy} = -547N / m^2$ (blue) to $\sigma_{yy} = 1665N / m^2$ (red)-SPH/FE.....	173
Figure 5.20: Horizontal displacement free end of the gate – ALE mesh size variations ("ds" represents the ALE/FE mesh size = all dimensions are in m).....	175

LIST OF FIGURES (Continued)

<u>Figure</u>	<u>Page</u>
Figure 5.21: Vertical displacements of the free end of the gate – ALE mesh size variations (“ds” represents the ALE/FE mesh size – all dimensions are in m)	175
Figure 6.1: Free-running SES model	188
Figure 6.2: As-installed orientation of bow finger seal high speed cameras mounted on acrylic window.....	189
Figure 6.3: Raw color image of bow finger seal from high speed video.....	190
Figure 6.4: FE-ALE simulation: 3D Computational domain of SES system (Red: water domain Blue: air domain Yellow: SES with rigid bow finger and stern seals).....	194
Figure 6.5: FE-ALE simulation: Isometric view of the 3D computational domain of fully coupled SES domain (SES, water, air and air-pump).....	194
Figure 6.6: Semi-transparent, isometric view of the SES FE model, emphasising the location of the air pump at approximately amidships	199
Figure 6.7: SES FE simulation near equilibrium air cushion pressure. The green domain is water, the semi-transparent red is the SES shell exterior, the purple is the pressurized air cushion, and the semi-transparent tan is ambient air	199
Figure 6.8: Pressurized air cushion in the SES chamber (snapshots of air pumping)	200
Figure 6.9: Pressure time history of three elements (bow, amidships and stern) inside the SES cushion chamber	201
Figure 6.10: SES FEA simulation with a forward speed of 0.7m/s and velocity in the water domain given by the colorbar.....	202
Figure 6.11: Bow section of the SES hull form with a rigid seal (yellow) and water (brown and vectors) at approximately the same forward speed as the SES experiment	202
Figure 6.12: Three dimensional isometric view of the computational domain.	204
Figure 6.13: Example still image from the forward-facing wet deck camera. This image was taken while the SES scale model had zero forward speed and on full air cushion pressure (approximately 408Pa). The blue line highlights the approximate exterior water line, and the red line highlights the approximate interior water line	205
Figure 6.14: (a) SES bow finger seal simplified geometry and boundary conditions shown by small triangles [Left] (b) Membrane element normal pointed outward in direction of water current [Right]. Follower load for cushion pressure acting opposite to surface normal.	206

LIST OF FIGURES (Continued)

<u>Figure</u>	<u>Page</u>
Figure 6.15: Snapshots of the simulation results for fully coupled FSI with a single flexible bow finger and a rigid aft seal geometry	207
Figure 6.16: A snapshot of images depicting the bow seal deflections	208
Figure 6.17: Bottom skirt nodes of the bow finger seal and the middle three nodes and membrane elements of the bow finger seal.....	209
Figure 6.18: X-Displacement time history of bow seal skirt nodes.....	211
Figure 6.19: Y-Displacement time history of bow seal skirt nodes.....	212
Figure 6.20: Z-Displacement time history of bow seal skirt nodes	213
Figure 6.21: Pressure time history for the bottom skirt elements	215
Figure 6.22: Stress time history for the bottom skirt elements	215
Figure 6.23: Computation time for different mesh configurations (Green: 1200 element case for which the numerical results are shown)	216
Figure 6.24: Maximum x, y and z deflections for four different mesh configurations (Green: 1200 element case for which the numerical results are shown)	217

LIST OF TABLES

<u>Table</u>	<u>Page</u>
Table 2.1: Specifications of prototype and model	16
Table 2.2: Results of Drop Test I [Weight of WLO = 2.03kg (Drop Test I: Ordinary Drop Mechanism)] (Vertical Entry/Entry Angle=0 deg).....	20
Table 2.3: Results for Drop Test II [Weight of WLO = 3.5kg (Drop Test II Electromagnetic Release)] (Vertical Entry/Entry Angle=0 deg)	25
Table 2.4: Analytical solution results Von-Karman (1929) and Wagner (1932) approaches.....	31
Table 3.1: Simulation results for maximum impact acceleration [Drop Test-I: Weight of WLO = 2.03kg (Vertical Entry/Entry Angle=0 deg)].....	62
Table 3.2: Summary of the pitch tests (V=9.8m/s) (Weight of WLO = 2.03kg).....	62
Table 3.3: Simulation results for maximum impact acceleration [Drop Test-II: Weight of WLO = 3.5kg (Vertical Entry/Entry Angle=0 deg)].....	64
Table 3.4: Analytical solution results from von Karman and Wagner approaches	66
Table 3.5: Performance study for the ALE and SPH test models.....	79
Table 4.1: Statistics on the dimensionless pressure maxima	118
Table 4.2: Experimental and numerical mean values for the pressure impulse.....	120
Table 4.3: Impact pressure response maxima for varying bulk modulus (cases A-C) ...	124
Table 4.4: Maximum impact pressure response for two high-filled sloshing situations for different bulk modulus values of air	129
Table 5.1. Dimensions of the system and physical characteristics of the elastic gate....	151
Table 5.2. Comparison of computation time for ALE/FE solver	176
Table 6.1. Free-running SES experiment parameters	189
Table 6.2: Comparison between experimental and numerical simulation results for mean equilibrium deflections of the bow finger seal	214

|| Sab Dharti Kaagaz Karu ||

|| Lekhan Ban Raye ||

|| Saath Samundar Ki Mas Karu ||

|| Guru Gun Likha Na Jaye ||

Translation: If the whole earth gets transformed into paper with all the trees made into pens and the water in the seven oceans transformed into writing ink, even then the glories of the Guru cannot be written. Such is his greatness.

– **Sant Kabir (1440 – 1518)**

Dedication

To Lord Ganesha, Shiridi Samartha Satguru Sainath Maharaj, Lord Shiva,

Maa Saraswati and Maa Durga Shakthi

and

To my father and mother, my wife, sister and brother-in-law

HYDRODYNAMIC CONTACT/IMPACT MODELING AND APPLICATION TO OCEAN ENGINEERING PROBLEMS

1 GENERAL INTRODUCTION

1.1 Introduction

The term fluid-structure interaction (FSI) is a generic term that is often used to describe certain physical phenomena. FSI is a very interesting and challenging multi-disciplinary field involving interaction of a movable or deformable structure with an internal or surrounding fluid flow. A flexible solid structure contacting the fluid is subjected to a pressure which causes deformation in the structure. In return, the deformed structure alters the flow field by exerting pressure on the structure. FSI plays a pivotal role in many different types of real-world situations and practical engineering applications involving large structural deformation and material or geometric nonlinearities.

FSI has many practical engineering applications such as the determination of the hydrodynamic forces on a structure or the motion of flexible bodies on the water-free surface which form an intrinsic component of any typical contact and impact FSI system. Analysis of FSI problems is often very difficult and therefore experimental investigations (or empirical laws) are performed by conducting experiments in a physical wave basin. These experiments though close to real world scenario often are time-consuming and expensive. Importantly, it is not economically viable to conduct parametric studies using experiments. Alternatively, numerical models when developed with similar capabilities

will complement the experiments very well because of the lower costs and the ability to study phenomena that are not completely feasible in a physical laboratory.

Performing numerical simulations involving fluid dynamics is computational-intensive and the complexity is magnified by the presence of the flexible structure(s) in the fluid domain. The models are also required to address large-scale domains such as a numerical water channel in order to be suitable to practical problems which demands access to high-performance computing (HPC).

This dissertation is aimed at systematically examining the contact and impact FSI numerical modeling procedure applied to various practical multi-physics ocean engineering problems. The capabilities of the code and limitations of different numerical methods used are presented in the following chapters. This dissertation is also aimed at presenting a consistent computational platform which provides an accurate predictive capability of the numerical code to more detailed and complex models involving flexible structures in a fluid domain.

To this end, numerical simulations were performed to study: (A) rigid body contact and impact (drop tests and fluid sloshing in a LNG tank), (B) flexible body contact and impact (elastic plate deformation), and (C) complex flexible body contact and impact (bow finger seal motions of a surface effect ship). A detailed review of the literature is presented in the following chapters and a list of references is provided in the bibliography section at the end of the dissertation.

1.2 Objectives

The objectives of the present work involving the numerical modeling and simulations of practical multi-physics ocean engineering problems are manifold.

-Rigid body contact and impact

-Study the dynamics of a water landing object (WLO) impacting the water surface by:

- Developing a semi-approximate equivalent-radius analytical procedure based on the von-Karman and Wagner closed form solutions and calibrate with experimental results
- Numerical modeling and simulation of the impact phenomena using a finite element based arbitrary Lagrangian-Eulerian (ALE) formulation and a smoothed particle hydrodynamics (SPH) method and compare the results for maximum impact acceleration and maximum impact pressure with experimental data
- Conducting performance studies of ALE and SPH in the numerical modeling and simulation of the impact scenario

-Investigate the physics of Multi-phase physics of fluid sloshing phenomena by:

- Verification and validation of the finite element based ALE formulation in modeling a multi-physics problem in terms of the dynamics of the flow in a LNG tank
- Estimate and compare the maximum impact pressure on the sloshing tank with experimental test data with careful examination of the physics of the wave breaking and impact process

- Performing a sensitivity study on the effect of air compressibility on the estimation of maximum impact pressure for different fluid-filled sloshing situations

-Flexible body contact and impact

-Study the dynamics of a WLO impacting the water surface by:

- Providing a consistent computational platform for comparison and evaluation of the two numerical methods
- Examining the accuracy and efficiency of each solver independently in capturing the evolution of the water-free surface profiles and the elastic gate deformations
- Ascertaining the predictive capability of ALE and SPH methods in modeling the contact and impact dynamics of a flexible body-fluid interaction

-Complex flexible body contact and impact

-Numerical Modeling and simulation of a surface effect ship bow finger seal motions by:

- Providing a brief insight into the concept of a pressurized air cushion with an experiment conducted on a free-running surface effect ship (SES) at Oregon State University
- Implementing the numerical formulation and procedure to model the interaction between bow finger seals and the water free-surface
- Calculating the maximum bow finger seal deflections of a scale-model of a free-running SES with a fully pressurized air cushion with numerical modeling and simulations

1.3 Scientific contributions of the dissertation

The scientific contributions of this dissertation are documented in the form of two journal papers and three manuscripts (which are in the process of being submitted to journals and conferences). As such, these chapters may be read in sequence or independently. However, in the perspective of a dissertation, these chapters are organized in a logical fashion based on the objectives and the scope mentioned above. Some introductory parts and numerical formulations have common elements in all the numerical based manuscripts so as to provide a common theme and reach a wider audience.

Chapter-1 (Journal Paper) deals with the experimental investigations and analytical estimates involving drop tests with the scaled model of a WLO. The peak accelerations and peak pressures coming on the WLO are presented and an approximate equivalent radius approach is presented.

Chapter-2 (Journal Paper) focuses on a numerical study on the dynamic response of a generic rigid WLO during water impact. The predictive capability of the explicit finite-element ALE and SPH methods are evaluated. The numerical predictions are first validated with experimental data for maximum impact accelerations and then used to supplement experimental drop tests.

Chapter-3 (Manuscript) investigates the contact and impact pressures in the case of different fluid-filled sloshing situations. An arbitrary Lagrangian-Eulerian (ALE) formulation solved by the finite element method is used to simulate the fluid sloshing in a LNG tank. The effect of air compressibility on the estimation of maximum impact pressure for different fluid-filled sloshing conditions is presented.

Chapter-4 (Manuscript) focuses on the predictive capability of two different numerical methods (ALE and SPH) in modeling a flexible structure-fluid interaction which involves the deformation of a plate subjected to time-dependent water pressure. A comparison and the performance of the two numerical methods is presented under a consistent computational platform.

Chapter-5 (Manuscript) examines the bow finger seal motions on a scale-model of a free-running surface effect ship (SES) with a fully pressurized air cushion using numerical modeling and simulations. A systematic approach in modeling the interactions of the various components of the SES such as forward speed, air cushion pressure and the interaction of the bow and stern seals with water free-surface are presented. Numerical simulation results for the maximum bow finger seal deflections are compared with experimental test data.

Chapter-6 manifests conclusions of this research.

The appendices provide a summary of the literature survey which is used in writing the manuscripts. A brief description of the moment of inertia calculations for the generic rigid body used for the drop tests is also shown. A brief introduction to the concept of surface effect ships and under laying physics is presented. This is followed by a detailed description of the finite element membrane formulations used in the SES bow seal analysis is presented. Details of the ALE modeling guidelines for modeling any quintessential FSI problems are presented. These ALE modeling guidelines are of interest to practicing engineers, numerical modelers, analysts and designers who wish to reproduce the test cases and also appreciate the complexity of successfully simulating challenging ocean engineering problems.

The author attempted to provide a balanced presentation of the experimental investigations, numerical methods and modeling techniques by combining both visual and graphical presentations. Therefore, it is hoped that this work will be of interest to not only the esoteric readers but also to those who are interested in applying these numerical methods to challenging practical ocean engineering problems.

RIGID-BODY WATER-SURFACE IMPACT DYNAMICS:
EXPERIMENTAL AND SEMI-ANALYTICAL APPROXIMATION

Ravi Challa, Solomon C. Yim, V.G. Idichandy and C.P. Vendhan

Journal of Offshore Mechanics and Arctic Engineering

ASME

Volume 136, November 2013, Pages 011102-1 - 011102-10

2 RIGID-BODY WATER-SURFACE IMPACT DYNAMICS: EXPERIMENT AND SEMI-ANALYTICAL APPROXIMATION

2.1 Abstract

An experimental study of the dynamics of a generic rigid body during water impact and an equivalent-radius approximate analytical procedure is developed and calibrated in this study. The experimental tests in a wave basin covered a range of drop heights using a 1/6th-scale model of a practical water-landing object prototype for two drop-mechanisms to determine the water impact and contact effects. The first mechanism involved a rope and pulley arrangement while the second mechanism employed an electromagnetic release to drop the rigid body. Hydrodynamic parameters including peak acceleration and touchdown pressure were measured and the maximum impact/contact force was estimated for various entry speeds (corresponding to various drop heights) and weights of the rigid body. Results from the tests show that the impact acceleration and touchdown pressure increases approximately linearly with increasing drop height and the data provides conditions that keep impact accelerations under specified limits for the rigid-body prototype. The experimentally measured maximum accelerations were compared with classical von Karman and Wagner approximate closed-form solutions. In this study, an improved approximate solution procedure using an equivalent radius concept integrating experimental results with the von Karman and Wagner closed-form solutions is proposed and developed in detail. The resulting semi-analytical estimates are calibrated against experimental results and found to provide close matching.

2.2 Introduction

The study of hydrodynamic impact of a moving body on a water free-surface finds variety of applications in the aerospace and ocean engineering fields. The present study is concerned with rigid-body/water-surface impact dynamics of a water-landing object (WLO) in an open ocean using a series of drop tests in a wave basin to assess the maximum force and resulting accelerations. The effect of this impact is prominent in the design phase of the WLO project in determining the maximum design force for material strength determination to ensure structural and equipment integrity and human safety.

Prototype data has been provided by the Indian Space Research Organization (ISRO) to facilitate the making of a physical model of WLO. The prototype used for the Indian space mission is unique in a way that it is conical with a rounded nose (which impacts the water surface first) than compared to the convex shape of the base used for Apollo Command Module (ACM) for the American space missions. This difference precludes meaningful comparison with existing literature available for ACM.

Studies on impact phenomena based on the theoretical and experimental work by von Karman (1929) resulted in equations for the impact of rigid bodies on a fluid assuming that the reaction of water was solely due to its inertia. The accelerations and pressures affecting the rigid body were estimated using an approximate expression for the added mass due to the presence of the water. Baker and Westine (1967) conducted experimental investigations on a 1/4th scaled model of the Apollo Command Module (ACM) to study the structural response to water impact in both the elastic and failure-initiation regimes. Data from the model tests were compared with results of full-scale experiments. Kaplan (1968) examined the specific problem of the ACM impacting water. Their theory and experiments showed

that the peak acceleration was proportional to the square of the impact velocity and the results correlated well with the full-scale ACM impact tests. Miloh (1991) obtained analytical expressions for the small-time slamming coefficient and wetting factor of a rigid spherical shape in a vertical water entry using experimental data from the ACM tests. A semi-Wagner approach was proposed and then used to compute the wetting factor and the Lagrange equations were employed in order to determine the slamming force from the kinetic energy of the fluid. Good agreement between theoretical model and experimental measurements, both for the early-stage impact force and the free-surface rise at the vicinity of the sphere, was observed. Brooks and Anderson (1994) investigated the dynamic response of water-landing space module (WLSM) during impact upon water. A 1/5th-scale model was tested in a three-dimensional (3-D) basin at the Oregon State University Wave Research Laboratory and the results were compared with those obtained using analytical techniques and computer simulations. The 3-D FE model was validated by comparison with previous full-scale test data and theory. Zhao *et al* (1996) studied the slamming loads on two-dimensional sections using two different theoretical models. One of the methods is a fully nonlinear numerical simulation that includes flow separation and the other method is an extension of Wagner's solution which does not include the flow separation. Faltinsen (1997) studied the theoretical methods for water entry of two-dimensional and axisymmetric bodies. A numerical method was developed and compared against asymptotic methods and validated by experiments for cone and sphere shaped rigid bodies. The significance of the effect of local rise up of the water during entry was identified. Faltinsen (1999) studied the relative importance of hydroelasticity for an elastic hull with wedge-shaped cross sections penetrating an initially calm water surface. Wagner's theory

was generalized to include elastic vibrations. The importance of hydroelasticity for the local slamming-induced maximum stresses increases with decreasing deadrise angle β and increasing impact velocity v . Fair agreement between theory and experiments was documented. Scolan and Korobkin (2001) considered the 3-D problem of a blunt-body impact onto the free surface of an ideal incompressible liquid based on Wagner's theory. Scolan and Korobkin (2003) performed hydroelastic slamming analysis of a 3-D cone using Wagner's approach. The results from their work shows significant influence of the elasticity compared with the rigid case. Seddon and Moatamedi (2006) reviewed the work undertaken in the field of water entry between 1929 and 2003, providing a summary of the major theoretical, experimental and numerical accomplishments in the field. The three-dimensional nonlinear theory of water impact was solved by Korobkin (2005) using the modified Logvinovich model, which is slightly more complex than the Wagner's method used in this study.

The physical interpretation of the problem developed by von Karman formed a basis of most of subsequent works. However, there is scanty work done on different shaped WLO impacting water surface. The existing experimental data is confined to a convex shaped rigid body impacting water against the much tested concave shaped rigid body (with large base) impacting water surface (US reentry missions). The objective of the WLO drop tests presented below is to study the dynamic response of a conical shaped WLO during water impact by performing drop test experiments using a scaled model with varying heights, measuring their maximum impact acceleration and touchdown pressure. A semi-analytical estimation procedure for maximum impact acceleration, based on the von-Karman and Wagner closed form solutions and an equivalent-radius approach, is developed and

calibrated with experimental results. The predictive capability of the semi-analytical estimation procedure is calibrated against experimental maximum acceleration results.

2.3 Experimental investigation of rigid-body impact dynamics using drop tests

The experimental investigation carried out in the present study on the rigid body (WLO) consists of drop tests from a range of heights. To simulate the dynamic response of the impact experiment for model testing, a 1/6th Froude scale model of the WLO [made of fiber reinforced polymer (FRP)] was used for the experimental drop tests. The overall configuration of the WLO prototype is shown in Figure 2.1. Specifications of the prototype and model including the scaling factor for each quantity are shown in Table 2.1. The WLO was fabricated as a conical shell with a rounded nose. Note that the conical portion (nose part of the rigid body) impacts the water surface. The origin is located at the deck of the WLO and the position of Z_{cg} is measured from the flat base (Figure 2.1).

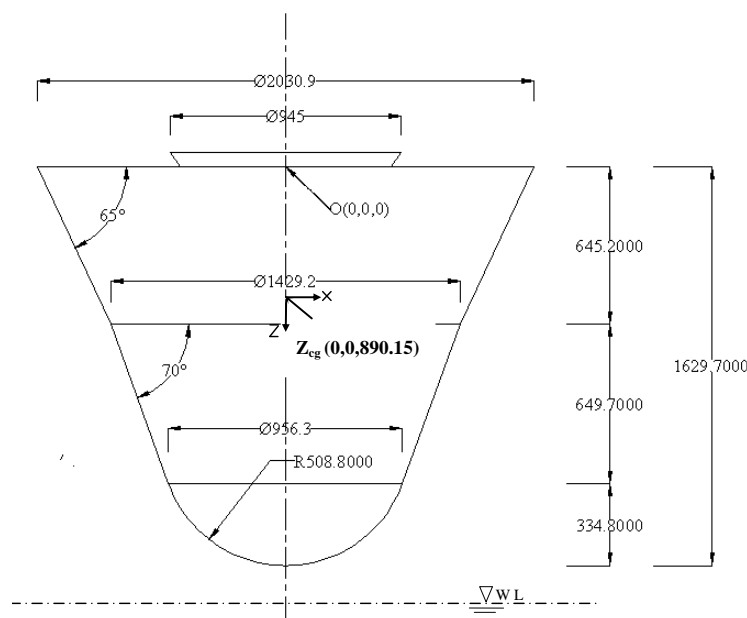


Figure 2.1: Overall configuration of WLO Prototype (All dimensions are in mm)

Two independent sets of drop test are conducted in the experiment. Drop test I involved dropping the rigid body using a rope and pulley arrangement, while Drop Test II employed an electromagnetic release to drop the model. Both sets of experiments provide valuable and complementary experimental data (for different weight distribution ratios) for numerical model calibration.

The horizontal component of velocity was found to have a very little effect on the accelerations in the vertical (Z) direction in both drop tests the experimental investigations have been confined to vertical drop tests only. Hence, no effort was made to measure the horizontal component of velocity or the effects of varying the entry angle. (For information on the effect of horizontal speed of the entering body, see Scolan et al. (2012).)

2.3.1 Drop test I

The first set of drop tests was performed recently in the wave basin (30m x 30m in plan and 3m deep) at the Department of Ocean Engineering at IIT-Madras under calm water conditions. Given the maximum clearance of the laboratory, the achievable maximum velocity of impact was estimated to be about 9.81m/s. This impact velocity was achieved by dropping the model from an overhead crane with a drop height of 5m above the water surface. The drop tests were carried out over a range at 0.5m intervals. An important design parameter is the mass, which is selected as 2.03kg for the test model made of FRP. A skin thickness of 5mm was selected, with extra thickness at the nose (of about 10mm) to withstand the force of impact. The estimated values of the center of gravity and moment of inertia are given in Table 2.1 (Inertial properties of the WLO model are shown in Appendix A). The vertical acceleration of the model was measured on impact by using an accelerometer (HMB B12/2000), placed at the center of gravity (CG) of the model. The B12 series Hottinger-Baldwin accelerometers have a frequency response range of 0-1,000Hz, with an advantage of withstanding impact accelerations up to $\pm 20 g$. A 5-bar strain gauge-type pressure transducer (designed and fabricated specifically for the drop tests) is used to calculate the touchdown pressure during impact (mounted at the nose tip with a measuring area of 15mm ϕ). The motivation behind the use of a diaphragm type strain gauge transducer was the ease of installation, good accuracy, stability, and good shock resistance. The pressure transducer was connected to an MGC amplifier with a full Wheatstones bridge having a sensitivity of 0.1mV/V.

Table 2.1: Specifications of prototype and model

Property	Full-scale prototype specifications	Scale factors $\left(\lambda = \frac{1}{6}\right)$	Values	Model Specifications (1/6 th –Froude scale)
Mass of WLO (Drop Test I)	432kg	λ^3	0.00462	2.03kg
Mass of WLO (Drop Test II)	756kg	λ^3	0.00462	3.5kg
Maximum height of the space capsule	1629.7mm	λ	0.166	271.61mm
Maximum diameter of the space capsule	2030.9mm	λ	0.166	338.48mm
X_{cg}	0	λ	0.166	0
Y_{cg}	0	λ	0.166	0
Z_{cg}	890.15mm	λ	0.166	147.35mm
I_{xx}	169.38kgm ²	λ^5	0.0001286	0.02178kgm ²
I_{yy}	170.76kgm ²	λ^5	0.0001286	0.02195kgm ²
I_{zz}	109.44kgm ²	λ^5	0.0001286	0.01407kgm ²

The accelerometer and the pressure transducer were connected to amplifiers and a PC based data acquisition system was employed to acquire the data. Both the sensors were accurately calibrated and found to be practically perfectly linear with curve-fitted conversion values of less than 0.5% error [For the accelerometer calibration, 1 Volt corresponds to 11.1g and for the pressure sensor, 1 Volt corresponds to 0.166 bar ($0.166 \times 10^5 Pa$)].

Impact Test Results – The WLO was dropped, nose down, from various heights to determine the acceleration of the model during the impact and to measure the impact pressure at the nose. Ten seconds of data, with a sampling rate ranging from 1,000 Hz to 5,000 Hz, were recorded for each drop test to assess the adequacy of sampling rate to capture the peak impact. For the PC based data acquisition, the peak values of acceleration

and pressure upon touchdown are found to be consistent after testing for various sampling frequencies. Sample time series for acceleration and pressure for a 5m drop with a sampling rate of 1 millisecond are shown in Figures 2.2 and 2.3 respectively. Three identical test runs were conducted for each drop height and the averaged values of the maximum impact acceleration and maximum impact pressures are presented and used in subsequent analysis. The absolute value of maximum impact acceleration upon impact is approximately 5.2g and the peak pressure upon impact is 26kPa. The pressure time history depicts that during free fall, the response remains flat ($0 < t < 1.6\text{sec}$) and during touchdown on water surface an impulse is recorded ($1.6 < t < 1.8\text{sec}$). The post impact pressure scenario clearly shows that the model bounces (with its nose up) after impact ($1.8 < t < 2\text{sec}$) and subsequently comes to a static equilibrium with a practically constant submerged pressure ($2 < t < 4\text{sec}$).

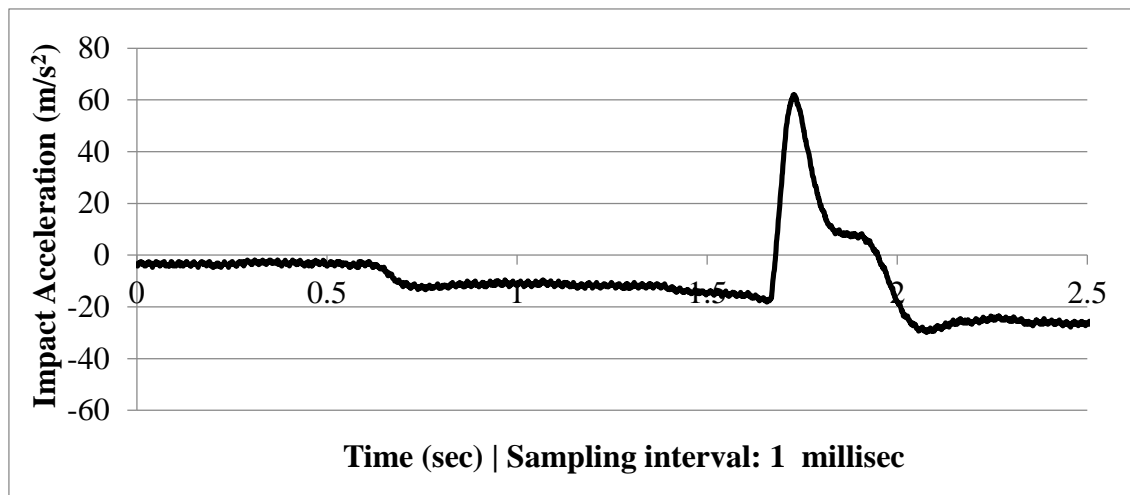


Figure 2.2: Measured data of a 5m drop test: Acceleration time history of a sample test case

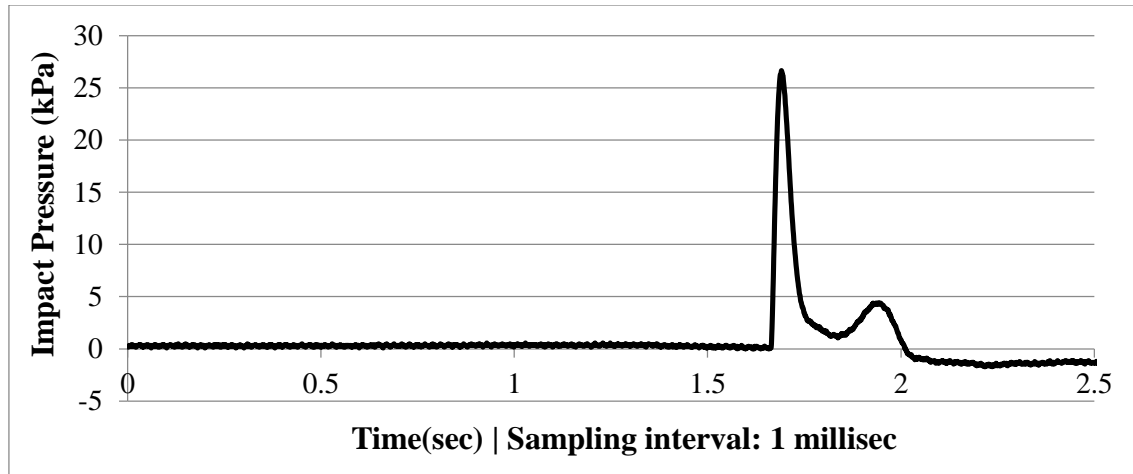


Figure 2.3: Measured data of a 5m drop test: Pressure time history of a sample test case

The details of the pressure distribution during the structural inertia phase are not important as the peak impact pressures are stochastic in nature (Faltinsen 2005). Owing to the highly stochastic nature of the peak pressure estimates on the rigid body, each drop test was repeated thrice and the maximum impact pressure reported in Table 2.2 is the mean value of the three drop test cases. The variation of peak acceleration and impact pressure values derived using different sampling rates (Figure 2.4) demonstrate that the peak values remained consistent (within $\pm 0.8\%$) for a PC based data acquisition for several trials of drop tests. Figure 2.5 depicts the consistency of the peak acceleration and pressure (within $\pm 1.0\%$) for higher sampling frequencies using an oscilloscope capture (0.01ms to 1.0 μ s). The percentage change to show the consistency of the measured acceleration (a) and pressure (p) peaks are calculated by using the formulas ($\frac{a_{mean} - a_{measured}}{a_{measured}} \times 100$) and ($\frac{p_{mean} - p_{measured}}{p_{measured}} \times 100$).

Since the use of oscilloscope for measurement during the drop

tests was impractical, all further tests used only PC based data acquisition to report the peak accelerations and peak pressures upon impact.

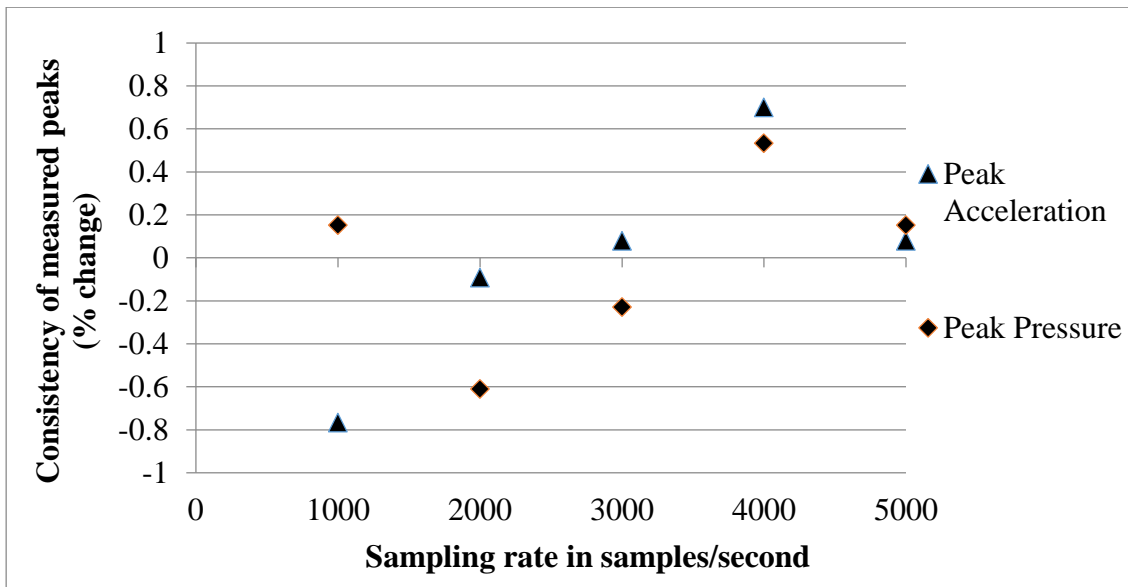


Figure 2.4: Consistency of measured peak acceleration and peak pressure vs. sampling rate (PC based data acquisition)

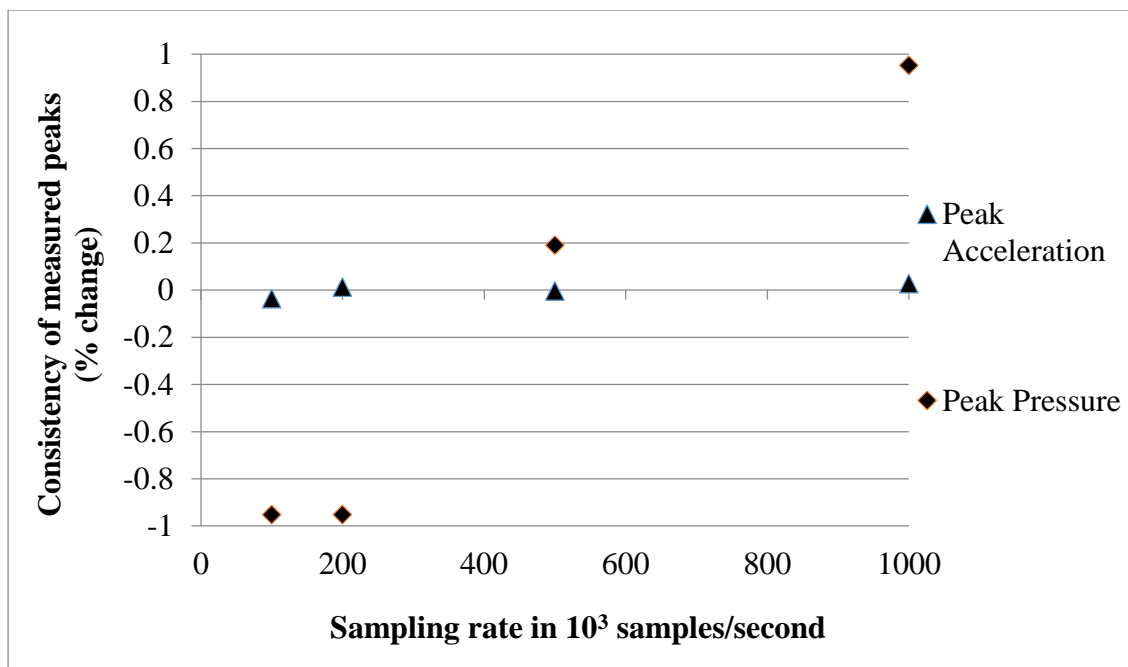


Figure 2.5: Consistency of measured peak acceleration and peak pressure vs. sampling rate (Oscilloscope Capture)

Table 2.2 gives the values of peak pressure, peak acceleration and the estimated force acting on the WLO for drop heights ranging from 1m to 5m with an increment of 0.5m (comprising of average values of three runs for each drop height). The peak value of acceleration for a 5m drop height is 52.17m/s^2 and the peak touchdown pressure is 26KPa. The total force experienced by the model was obtained using the (dry) model mass multiplied by the measured acceleration (105.9N for a 5m drop height). While the theoretical velocity was obtained using the height of drop and a g-value of 9.81m/s^2 (by using the kinematic equation of motion), the experimental velocity was obtained by integrating the measured acceleration time history.

Table 2.2: Results of Drop Test I [Weight of WLO = 2.03kg (Drop Test I: Ordinary Drop Mechanism)] (Vertical Entry/Entry Angle=0 deg)

Drop Height (m)	Acceleration (m/s^2)	Pressure (kPa)	Force (mass x accl.) (N)	Theoretical Velocity (m/s)	Experimental Velocity (m/s)
5.0	52.17	26	105.90	9.81	9.79
4.5	48.32	23	98.08	9.39	9.27
4.0	45.18	22	91.72	8.85	8.61
3.5	38.76	19	78.69	8.28	8.26
3.0	37.78	18	76.70	7.67	7.55
2.5	33.53	16	68.08	7.00	6.87
2.0	30.27	15	61.45	6.26	6.20
1.5	22.86	13	46.42	5.42	5.31
1.0	11.65	12	23.65	4.42	4.39

The experimental velocity obtained by integration of the acceleration time history appears to be accurate and in agreement with the observed data. Both theory and experiments showed that the peak acceleration was proportional to the square of the impact velocity. There is a practically linear fit between the force and the square of velocity for various drop heights (Kaplan 1968) [Figure 2.8]. Comparison of drop heights to theoretical and experimental velocities showed a very good comparison between both the theoretical and experimental velocities ascertaining the accuracy of the maximum impact accelerations measured experimentally.

Observations also reveal that the touchdown pressures increase practically linearly with the increase in the height of the drop. This linear increase can be attributed to the fact that the experimental results for the maximum impact pressure for each drop height (Table 2.2) correctly depict what was observed experimentally. The relative importance of hydroelasticity (for small deadrise angles) for an elastic hull with wedge shaped cross sections (Faltinsen 1997 and 1999) shows that the impact pressure is practically proportional to the square of the velocity which is well supported by the drop test results (Figure 9).

2.3.2 Drop test II

Upon completion of the first set of drop tests presented above, it was decided that a second set of tests with different mass distribution and total weight was warranted. To avoid imprecision in initial condition of the release of the model induced by manual handling (observed during the drop test I) and to achieve better control on the point of release, an electromagnetic release mechanism was designed and implemented. A custom designed

measuring mechanism on board the WLO enabled the automatic transfer of data in real time to a host computer by means of thin wires. The electronic mechanism along with the steel plate (2mm thick) was glued to the top of the model, leading to an increase of weight to 3.5kg. Note that the center of gravity of the WLO for Drop Test II is different from the first experimental test case.

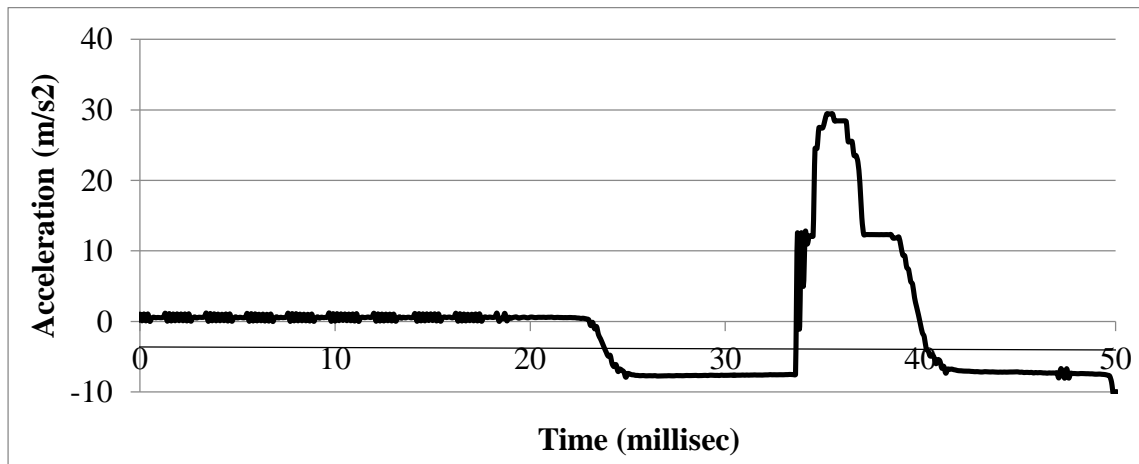
A steel frame (fabricated in the form of a ladder) was installed on the bridge of the wave basin to hold the electromagnet in position over the water surface. A movable strut was fixed to the steel frame in order to drop the model from every 0.5m height. The electromagnet was bolted at one end of the strut which would hold the model in position. A switch mechanism, provided on the outer surface of the cap of WLO, activated the data recording just before actuating the release. An up-close view of the setup for Drop Test II is show in Figure 2.6(a).



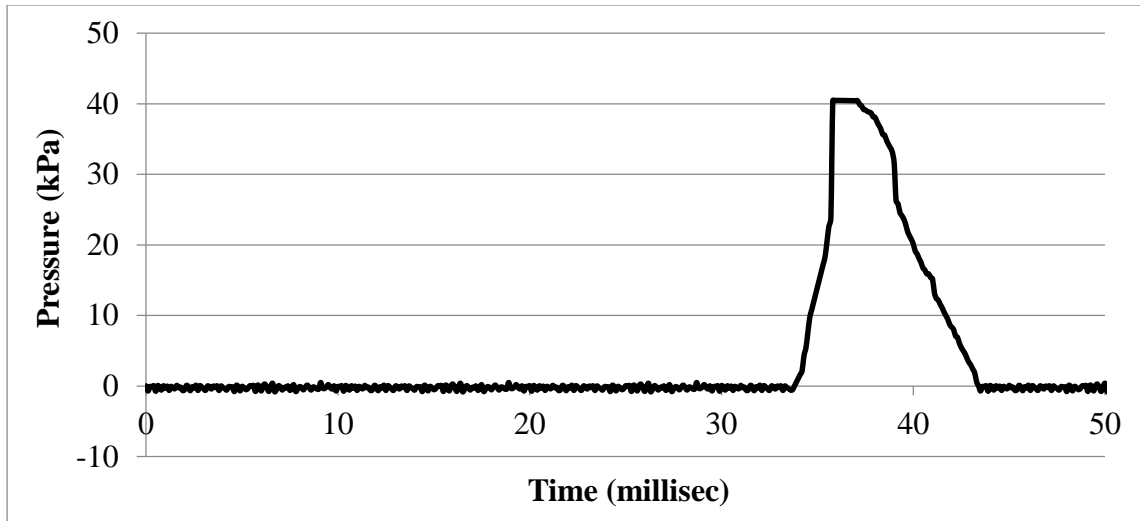
Figure 2.6: Electromagnet with protruding strut (a) Up-close view of the setup for Drop Test II (b) WLO touchdown with water surface

Pressure and acceleration measurements were obtained using built-in amplifiers connected to a computer through a RS485 link. A single axis MEMS-based accelerometer was used to measure the acceleration and a 5-bar strain gauge-type pressure transducer (mounted at

the nose tip) measured the touchdown pressure during impact. The accelerometer and the pressure transducer were connected to amplifiers and a PC based data acquisition system was employed to acquire the data in real time. The WLO was dropped using the electromagnetic release from the frame fixed to the bridge. The WLO touchdown with the water surface is shown in Figure 2.6(b). The model was tested initially for a 0.5m drop and then the height was gradually increased to 5m in steps of 0.5m. The release switch was activated once the model was held to the electromagnet and the acceleration and the pressure data were recorded during the descent. The acceleration and pressure time histories for the single case of a 5m drop, after analysis in the host computer, are shown in Figures 2.7(a) and 2.7(b).



(a) Acceleration time history



(b) Pressure time history

Figure 2.7: Measured electromagnetic release data of a 5m drop test

Table 2.3 gives the values of peak pressure, peak acceleration and the estimated force acting on the WLO for drop heights ranging from 1m to 5m at an increment of 0.5m. Note that the peak value of acceleration for a 5.0m drop height is 36.5m/s^2 and the touchdown pressure is 41KPa. The force experienced by the model was obtained using the model mass and measured acceleration (127.7N for a 5m drop height). While the theoretical velocity was obtained based on drop height and a g-value of 9.81m/s^2 , the experimental velocity in the last column was obtained by integrating the measured acceleration time history. As observed in the first drop test, both the peak acceleration and touchdown pressure increases linearly with the increase in the height of drop. As observed in Drop Test I, the variation of impact force and the square of the impact velocity, for Drop Test II, exhibits a practically linear behavior for various drop heights, confirming the results of Kaplan (1968) [Figure 2.8]. The accuracy of the experimental measurements was ascertained by the very good

comparison between the theoretical and experimental velocities for various drop heights shown in Table 2.3.

Table 2.3: Results for Drop Test II [Weight of WLO = 3.5kg (Drop Test II Electromagnetic Release)] (Vertical Entry/Entry Angle=0 deg)

Drop Height (m)	Acceleration (m/s²)	Pressure (kPa)	Force (mass x acc) (N)	Theoretical Velocity (m/s)	Experimental Velocity (m/s)
5.0	36.50	41	127.72	9.81	9.72
4.5	31.72	38	111.02	9.39	9.30
4.0	27.32	32	95.62	8.85	8.81
3.5	22.82	29	79.87	8.28	8.19
3.0	19.55	25	68.42	7.67	7.54
2.5	15.32	21	53.62	7.00	6.97
2.0	12.12	19	42.35	6.26	6.22
1.5	10.72	18	37.52	5.42	5.35
1.0	9.92	15	20.22	4.42	4.42

Note that the maximum force vs. the square of the impact velocity (Figure 2.8) for Drop Test I shows deviation from a straight line behavior. This may be attributed to the lack of precise control of the initial point of release of the model, and small sample size (only three) to characterize the physical nature of the maximum acceleration and impact pressures.

In order to understand the linear variation of maximum impact pressure for each drop height (for both the drop tests) a figure showing the variation of the maximum impact pressure and the square of the normalized velocity (normalized using the maximum

velocity of impact) are plotted (Figure 2.9). The figure depicts a “practically” linear relationship which is in accordance with the fact that the pressure is directly proportional to the force acting on the rigid body. However, a closer look at the figure with respect to the actual physics of the impact phenomenon shows that there is a deviation from the linear trendline (first three data points) at low entry velocities (when $v \rightarrow 0$). This can be attributed to the fact that the body records a finite impact pressure at low impact velocities resulting in the deviation from the linear trendline shown in Figure 2.9.

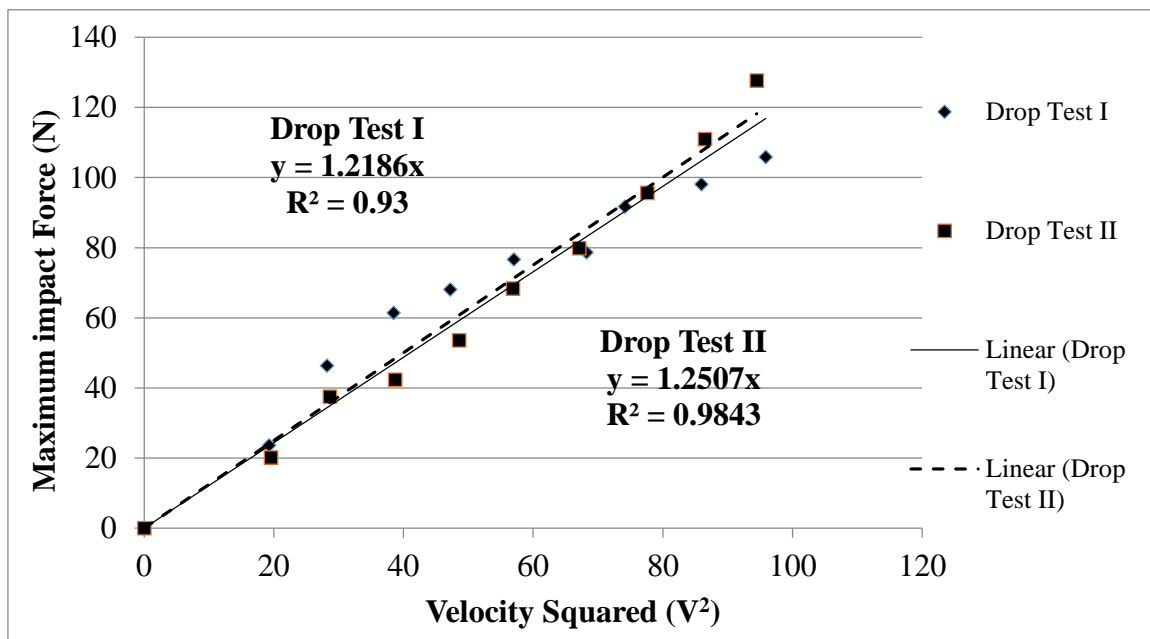


Figure 2.8: Maximum impact force vs. square of impact velocity (Drop Tests I & II)

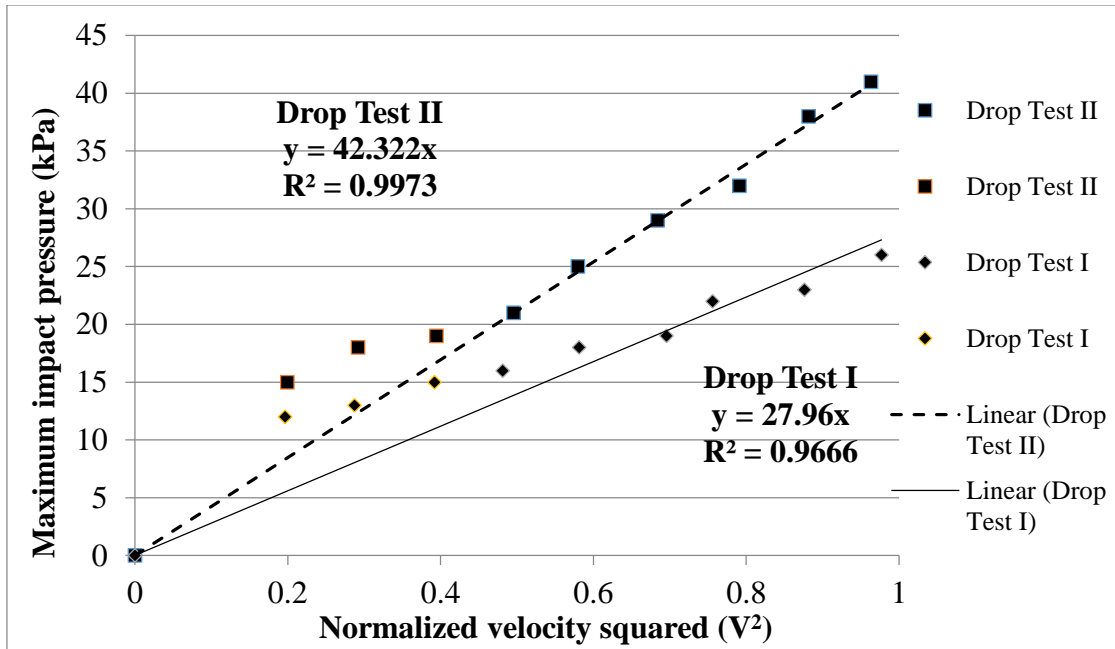


Figure 2.9: Maximum impact pressure vs. square of normalized impact velocity (Drop Tests I & II)

2.4 Approximate closed form solutions for maximum impact accelerations

For a Water Landing Object (WLO) that has a spherical bottom and is assumed rigid, closed form solutions based on the von Karman and Wagner approaches are available for correlating with the results from the experimental analysis (Wang and Lyle 2007). Zhao *et al* (1996) developed a generalized Wagner model, within which only the boundary conditions on the liquid free surface are simplified (linearized BCs). The von Karman approach is based on conservation of momentum and uses an added mass. The penetration depth is determined without considering water splash-up. The Wagner approach uses a more rigorous fluid dynamic formulation and considers the effect of water splash-up on the impact force. The kinematic free surface condition was used to determine the intersection between the free surface and the body in the outer flow domain. Satisfaction of the

kinematic free surface condition implies that the displaced fluid mass by the body is properly accounted for as rise up of the water. This is not true for a von Karman approach that does not account for the local rise up of the water. From the analytical solutions for a spherical bottom body impacting with water using the von Karman method, the magnitude of the virtual mass for a spherical bottom body is (Hirano and Miura, 1970)

$$m_v = \frac{4}{3} \rho h^2 (2R - h)^{\frac{3}{2}} \quad (1)$$

where m_v is the virtual mass, ρ is the mass density of water, h is the penetration depth, and R is the radius of the spherical bottom. The instantaneous velocity, V , of the center of gravity of the rigid body is

$$V = \frac{dh}{dt} = V_0 \left(1 + \frac{m_v g}{W} \right)^{-1} \quad (2)$$

where t is time after impact, V_0 is the initial velocity, g is the gravitational constant, and W is the weight of the rigid body. By substituting Eq. 1 into Eq. 2, and assuming $\frac{h}{R} \ll 1$,

the instantaneous velocity can be rewritten as

$$V = \frac{V_0}{1 + \frac{8\sqrt{2}\rho g R^3}{3W} \left(\frac{h}{R} \right)^{\frac{3}{2}}} \quad (3)$$

The overall acceleration, a , can be written as

$$a = \frac{d^2 h}{dt^2} = - \left[\frac{3 \times 2^{\frac{1}{2}} \left(\frac{3W}{4\pi\rho g R^3} \right)^2 \left(\frac{V_0^2}{gR} \right) \left(\frac{h}{R} \right)^{\frac{1}{2}}}{\pi \left(\left(\frac{3W}{4\pi\rho g R^3} \right) + 2^{\frac{3}{2}} \pi^{-1} \left(\frac{h}{R} \right)^{\frac{3}{2}} \right)^3} \right] g \quad (4)$$

Assuming $\frac{h}{R} \ll 1$, the maximum acceleration can be found as

$$a_{\max-\nu K} = -\frac{256}{243} \left(\frac{4\rho g R^3}{3W} \right)^{\frac{2}{3}} \left(\frac{V_0^2}{R} \right) \quad (5)$$

where νK stands for von-Karman in (5) and the time at which the maximum acceleration is achieved is given at

$$t_{\max-\nu K} = \frac{21}{160} \left(\frac{3W}{4\rho g R^3} \right)^{\frac{2}{3}} \frac{R}{V_0} \quad (6)$$

and the penetration depth at

$$h_{\max-\nu K} = \frac{1}{8} \left(\frac{3W}{4\rho g R^3} \right)^{\frac{2}{3}} R \quad (7)$$

In the von Karman approach, the rise of water due to the splash up is not considered. The effect of splash up was considered by Wagner and found to have significant effect on the impact force. Recently, Miloh (1991) used a semi-Wagner approach to determine the non-dimensional slamming coefficient that is defined as

$$C_s \left(\frac{h}{R} \right) = \frac{2F}{\rho \pi R^2 V_0^2} \quad (8)$$

where F is the impact force. Based on the analytical derivations, Miloh (1991) proposed that

$$C_s \left(\frac{h}{R} \right) = 5.5 \left(\frac{h}{R} \right)^{\frac{1}{2}} - 4.19 \left(\frac{h}{R} \right) - 4.26 \left(\frac{h}{R} \right)^{\frac{3}{2}} \quad (9)$$

is suitable for initial stage slamming. Note the coefficients in equation (9) are determined from a set of experimental data from the ACM tests. Based on these analytical derivations the maximum acceleration can be estimated as

$$a_{\max-W} = \frac{g}{2W} C_s \left(\frac{h_{\max}}{R} \right) \rho \pi R^2 V_0^2 \quad (10)$$

where W stands for Wagner in (10).

Table 4 shows the comparison of the experimental results with analytical solutions. The maximum z -accelerations for a vertical entry for both the drop mechanisms is compared to the closed form solutions based on von Karman and Wagner approaches.

The equivalent radius is a representative or nominal radius of WLO that yields the accelerations comparable to the maximum impact accelerations obtained experimentally with the conical shaped WLO. From the analytical solutions for a spherical bottom body impacting with water surface, for the von-Karman method, equation (5) is used to calculate the equivalent radius by computing $r_{\max-vK}$ corresponding the maximum impact acceleration $a_{\max-vK}$ and is given by

$$r_{\max-vK} = R = -\frac{a_{\max-vK}}{V_0^2} \left(\frac{243}{256} \right) \left(\frac{3W}{4\rho g} \right)^{\frac{2}{3}} \quad (11)$$

and correspondingly for the Wagner method, equation (10) can be used to calculate the equivalent radius by computing the value of $r_{\max-W}$ corresponding the maximum impact acceleration $a_{\max-W}$ and is given by

$$r_{\max-W} = R = \frac{2W a_{\max-W}}{\rho g \pi V_0^2 C_s h_{\max}} \quad (12)$$

Values of the ‘equivalent radius’ of the WLO conical portion is also shown in Table 2.4. A detailed description of the equivalent radius approximate semi-analytical procedure is provided in the subsequent section.

Table 2.4: Analytical solution results Von-Karman (1929) and Wagner (1932) approaches

Water Landing Object (WLO) Drop Test Cases Cone radius: 0.0848m Max. Radius: 0.3385m	Maximum acceleration (Experiments) g: acceleration due to gravity $\left(\frac{m}{s^2}\right)$	Analytical Solutions for maximum accelerations		Equivalent Radius (m) of WLO conical portion	
		von Karman (Eq.5) $a_{\max-vK}$	Wagner (Eq. 10) $a_{\max-W}$	von Karman $r_{\max-vK}$	Wagner $r_{\max-W}$
Drop Test I: Ordinary drop mechanism	5.2g	14.7g	19.8g	0.0300m	0.1075m
Drop Test II: Electromagnetic release mechanism	3.6g	10.4g	25.2g	0.0293m	0.1310m

It is important to note that the maximum radius of the base (for a 1/6th Froude-scale model of a WLO) is 338.5mm and the radius of the conical portion impacting the water surface is 84.8mm. For a WLO model with the dimensions shown in Table 2.1, the accelerations obtained from both von Karman and Wagner approaches for experimental Drop Test I are 14.7g and 19.8g, respectively (see Table 2.4). Similarly, the maximum impact accelerations obtained from both the approaches for Drop Test II are 10.4g and 25.2g, respectively. Figures 2.10 and 2.11 show the normalized values of maximum impact accelerations plotted and normalized impact velocity for both the experimental cases and the corresponding analytical solutions. (Note that all the *abscissae* in the graphs have been

normalized using “ $\sqrt{2gh}$ ”, which is the maximum velocity upon impact for both the drop tests).

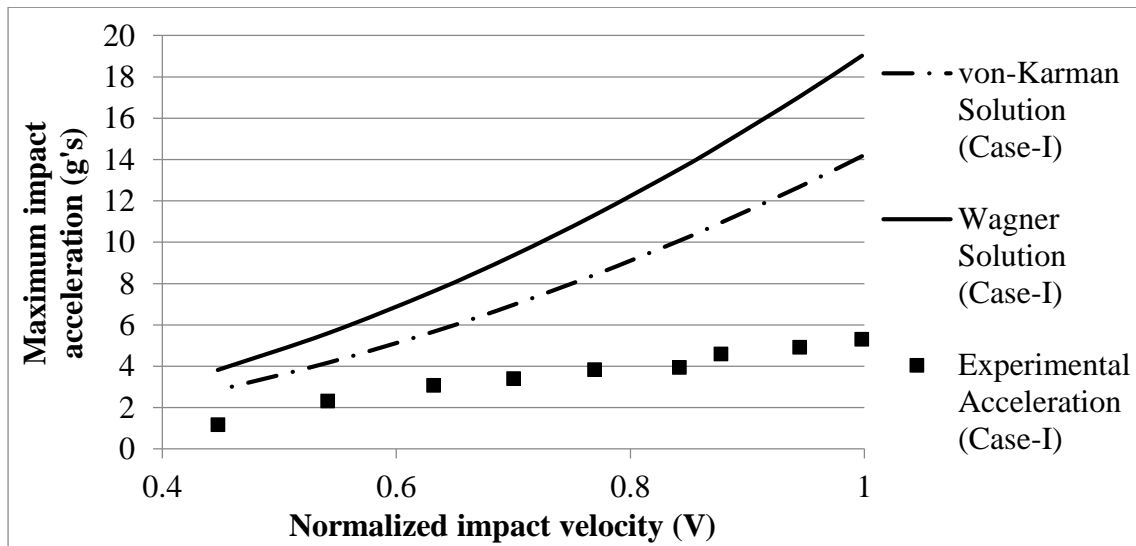


Figure 2.10: Maximum acceleration using von-Karman and Wagner solutions (Drop Test I)

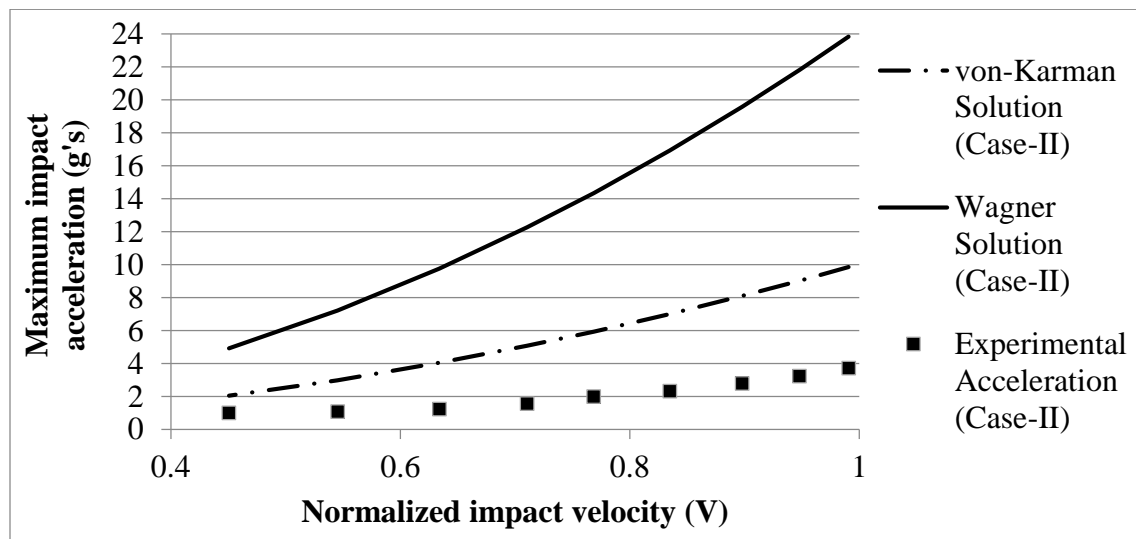


Figure 2.11: Maximum acceleration using von-Karman and Wagner solutions (Drop Test II)

For a conical bottomed rigid body, the analytical results show that there is large difference between the experimental peak impact accelerations and those obtained by von Karman and Wagner analytical estimates. The large difference can be attributed to the conical shape of WLO bottom impacting the water surface compared to the large spherical bottom used in deriving the closed form solutions. It can be deduced from Table 2.4 that for a conical bottomed rigid body (like the WLO), the experimental values of peak impact accelerations (for a 0-degree pitch), do not fit in the bounds on maximum impact accelerations calculated by both von Karman and Wagner approaches.

In addition to the unique shape of the WLO (which is primarily responsible for the large deviation of the experimental impact accelerations from the closed form solutions) the basic assumptions of the formulations for both von Karman and Wagner approaches also play a pivotal role in contributing to the large difference. Also, the continuously varying deadrise angle for WLO convex shaped rigid body impacting water significantly influences the maximum impact acceleration of the experimental results compared to the closed form solutions provided by von Karman and Wagner for constant small deadrise angles. The von Karman approach is based on conservation of momentum (using an added mass) and the penetration depth is determined without considering water splash-up, thus neglecting the highly nonlinear coupled fluid-structure interaction effect. The Wagner approach, on the other hand, attempts to relax the von Karman no-splashing assumption by using a rigorous dynamic formulation and incorporates the effect of the upward splashing of the water and its effects on the motion of the rigid body. With the upward splashing correction, the Wagner approach tends to over predict the maximum impact retardation as it neglects nonlinear effects near the impact zone.

The lack of agreement in the peak acceleration obtained in the present experimental study with the closed form von Karman and Wagner approximate solutions is due to the large initial angle at impact and the relatively rapid changes in contact radius of the inverted cone shape of the WLO as it penetrates the water surface. These deviations from the idealized assumption may be taken into account using the concept of an equivalent radius.

2.5 An equivalent radius approximate semi-analytical procedure

In order to capture the proper modeling of the dynamics of the impact and to ascertain a true fluid behavior, an attempt was made to calculate an equivalent radius of the conical portion of the WLO that would compare well with the experimental maximum impact accelerations [equations (11) and (12)]. Figure 2.12 shows a representative equivalent radius of a conical shaped WLO model using von Karman/Wagner approaches (with values summarized in the right most column of Table 2.4).

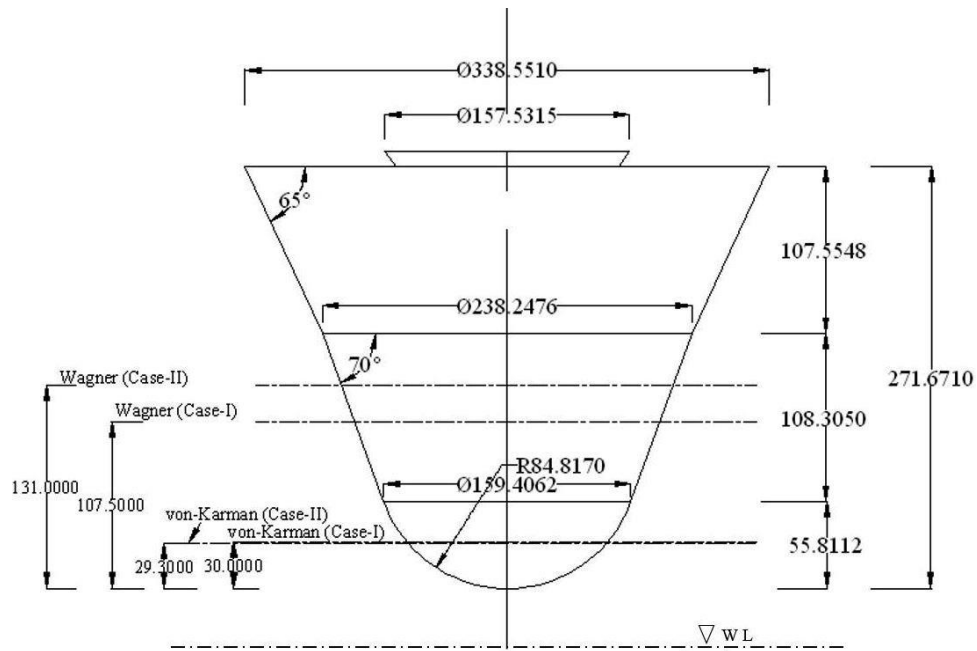


Figure 2.12: Equivalent radius of the WLO model

From the von Karman approach the equivalent radius for Drop Tests I and II are 30mm and 29.3mm, respectively. It can be observed that the von Karman approach tends to estimate a lower value of the radius of the conical portion. As the effect of local rise up of the water is significant during water entry of a rigid 3D rigid body, the von Karman predictions for maximum impact accelerations are not significant in determining the maximum impact accelerations for the water entry of WLO. The Wagner approach on the other hand estimates the equivalent radius for Drop Test I and Drop Test II as 107.5mm and 131mm, respectively. Based on the equivalent radius approach, approximate semi-analytical solutions based on the von Karman and Wagner theories can be used to obtain design maximum accelerations of the WLO model consistent with experimental results. In order to further comprehend the effect of the shape of the rigid body (especially the conical portion of the WLO impacting the water surface first), the values of equivalent radius (r) are plotted against different normalized velocities of impact for both Drop Test I and II

(Figures 2.13). The equivalent radius (r) was initially obtained for each drop velocity for both the experimental cases. The idea is to obtain those values of the radii which would give the same experimental impact accelerations corresponding to the impact velocities. Observe that from Figure 2.13 the values of equivalent radius (r) of the WLO model remain almost constant for different velocities of impact for both cases.

The next step is to compare the accelerations obtained experimentally (Drop Test I and II) to those obtained by using a mean equivalent radius (r^*). The values of r^* were obtained by taking the mean of all the equivalent radii obtained for different impact velocities corresponding to their respective impact accelerations. For each r^* obtained for each case, the impact accelerations were calculated by varying the impact velocity. Figures 2.14 and 2.15 show the comparison for the maximum impact accelerations and those obtained by the mean equivalent radius (r^*) for Drop Test I and II respectively.

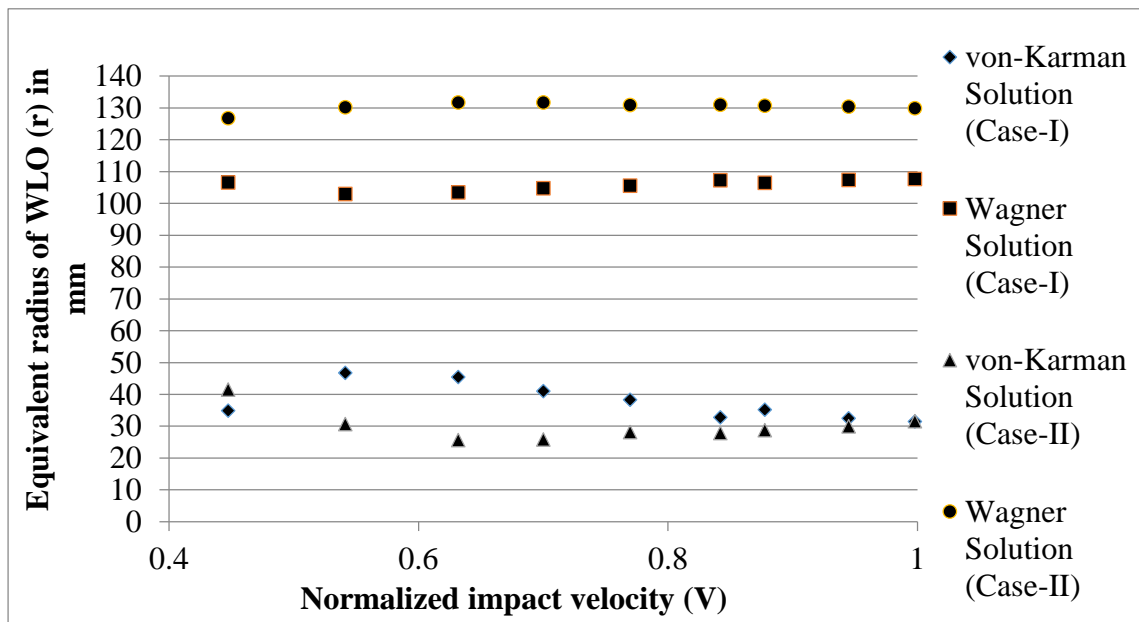


Figure 2.13: Equivalent radius (r) of the WLO for different normalized velocities of impact for Drop Test I and Drop Test II using von-Karman and Wagner approaches

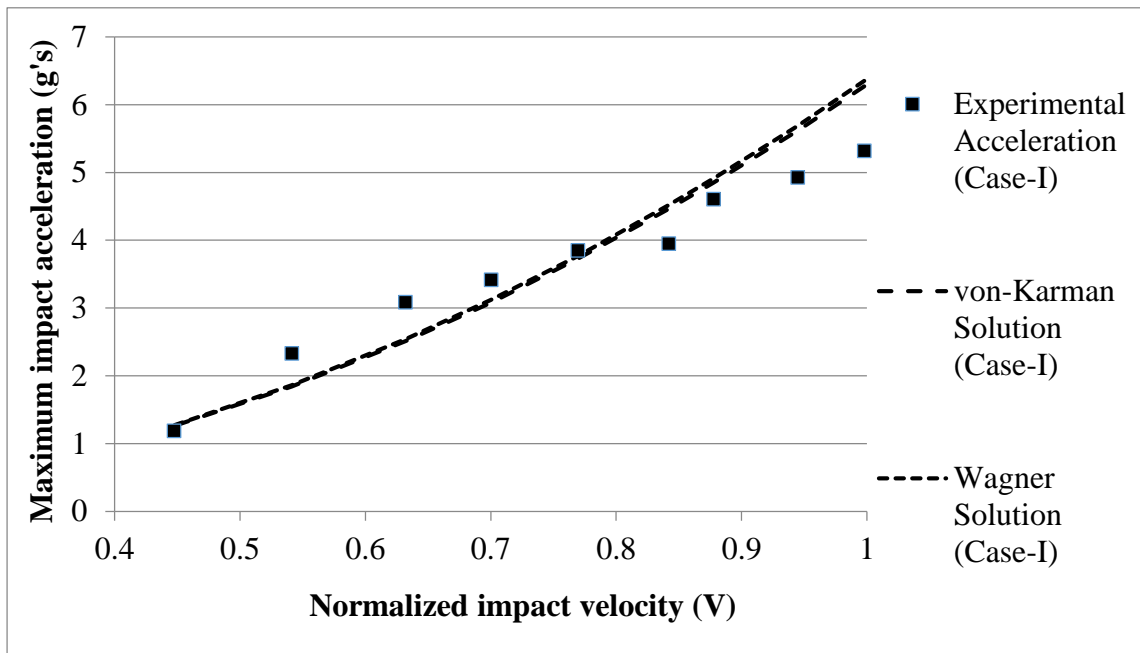


Figure 2.14: Maximum impact accelerations calculated based on the mean equivalent radius (r^*) of the WLO for different normalized velocities of impact for Drop Test I using von-Karman and Wagner approaches

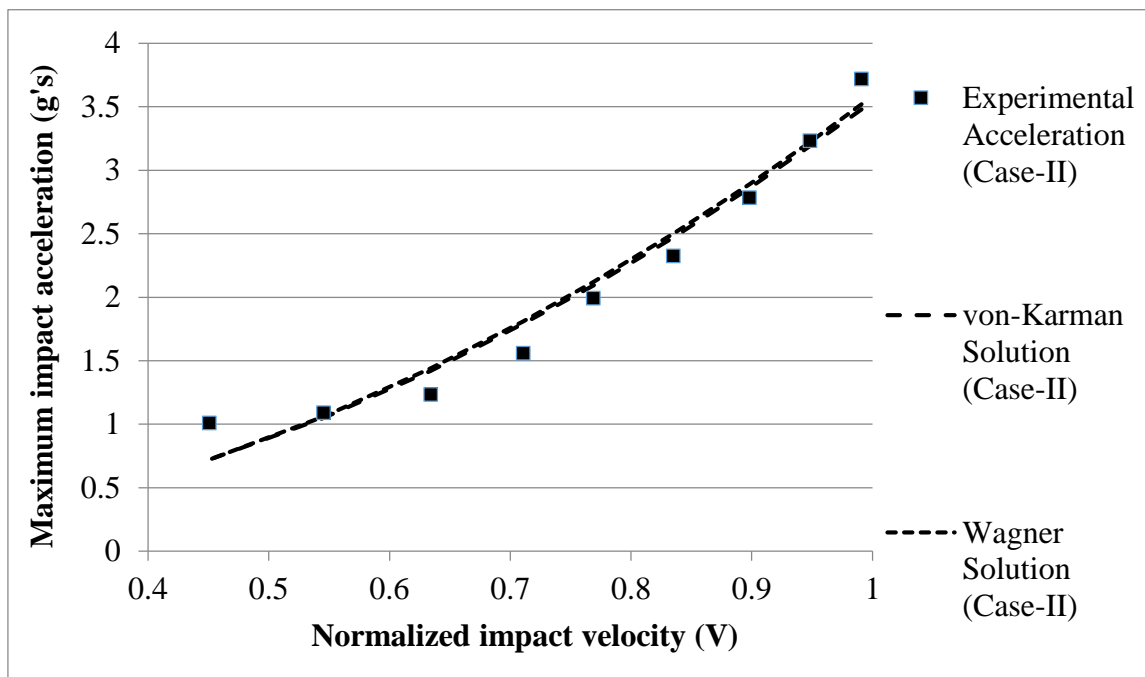


Figure 2.15: Maximum impact accelerations calculated based on the mean equivalent radius (r^*) of the WLO for different normalized velocities of impact for Drop Test II using von-Karman and Wagner approaches

Figures 2.14 and 2.15 show that the maximum impact acceleration obtained by both the semi-analytical models compare well with those obtained experimentally. It is interesting to note that the acceleration values obtained by von Karman and Wagner solutions produce accelerations that are similar ascertaining the importance of the shape of the WLO during water impact. (Note that we call the proposed approximate estimation procedure as “semi-analytical” because experimental data is needed to determine an important parameter, namely, the equivalent radius.)

2.6 Discussion and comparison

An important aspect is the comparison of the shape of space capsule used for the Indian and American space missions. The WLO used for the Indian space mission is conical in shape with a rounded nose than compared to the convex shape of the base used for all the American space missions. This significantly inhibits the comparison with the literature available for ACM or other American space missions. The present work is the first of its kind in testing a scaled-down model of WLO (with a conical shaped base) impacting ocean waters.

An attempt was made to study the impact dynamics of the WLO during and after touchdown with water surface using an underwater camera but they were discarded as the results obtained were not reliable. The hydrodynamic response of the WLO upon water impact which constitutes of measurements such as peak impact acceleration and peak impact pressure can only be used to qualitatively justify the experimental drop tests.

For the WLO weighing 2.03kg (Drop Test I), the acceleration time series for a 10m/s velocity of impact gives a peak acceleration of 52.17m/s^2 ($\sim 5.2\text{g}$) and a touchdown

pressure of 26kPa and for the WLO tests with the electromagnetic release with an increased mass of 3.5kg of the model (Drop Test II), the peak acceleration was found to be 36.5m/s^2 ($\sim 3.6\text{g}$) and the touchdown pressure was computed as 41kPa. In addition, for both independent experimental data sets, the peak force was proportional to the square of the impact velocity, which is in good agreement with Kaplan's theoretical results. Hence, a formal comparison between the two cases cannot qualitatively demonstrate the efficiency of one case over the other. Instead, for an end user, an increased weight of WLO provides a measure of the reduction of the accelerations (3.6g in Drop Test II compared to 5.2g in Drop Test I).

The peak impact force experienced by the model obtained using the model mass and measured acceleration is 105.9N for Drop Test I compared to 127.7N for Drop Test II. Comparison of drop heights to theoretical and experimental velocities depict a very good agreement for both the cases, ascertaining the accuracy of the impact accelerations measured experimentally for successive drop heights.

In order to describe the physics of the slamming problem, the maximum pressure obtained was compared to the pressure calculation when a circular cylinder slams water surface (Faltinsen 1990). The fluid behavior is incompressible at pressure values significantly below the acoustic pressure bound ($\rho c_e V = 14500\text{ kPa}$). The measured values of maximum impact pressure for both the drop test cases were 26 kPa and 41 kPa for Drop Tests I and II, respectively, which are well below the pressure bound confirming the main assumption that the fluid is incompressible (Faltinsen 2005).

The WLO was assumed as rigid for the convenience of comparing experimental results with closed form solutions for maximum accelerations predicted by the classical von

Karman and Wagner. The maximum radius of the base of the model is 338.5mm whereas the radius of the conical portion impacting the water surface is 84.8mm which is primarily responsible for the large difference between experimental and analytical estimates. An improved approximate solution procedure using an “equivalent” radius concept integrating experimental results with the von Karman and Wagner closed-form solutions is proposed and developed in detail.

2.7 Concluding remarks

An important aspect in the assessment of recovery and escape systems of water-impact rigid bodies is the performance of these bodies in ocean water landing. The primary objective of this study is to examine the dynamic response of a conical shaped rigid body with a spherical nose (a water-landing object, WLO) during water impact by conducting experiments using a $1/6^{\text{th}}$ Froude-scale model and two independent drop mechanisms. Drop Test I involved dropping the rigid body using a rope and pulley arrangement, while Drop Test II employed an electromagnetic release to drop the rigid body. The effects of varying the vertical velocity and the rigid body weight are identified and the trend obtained helps the readers to comprehend the conditions that must be avoided during a water impact. The hydrodynamic parameters such as peak acceleration and touchdown pressure were measured and the dynamic response of the rigid body during touchdown was observed. The peak values of acceleration for Drop Test I and II are $5.2 g$ and $3.6 g$, respectively. If a crew member onboard the rigid body (WLO) cannot withstand impact accelerations over $5 g$, these results will give a glimpse of the initial conditions which will keep the peak impact accelerations under specified limits. Note that the maximum impact accelerations

obtained in the experiments will directly predict the prototype values according to Froude scaling (scale factor = 1). Therefore, the maximum impact acceleration for a prototype is expected to be approximately 5 g .

An important aspect is the accuracy and reliability of the experimental results in predicting the impact accelerations and touchdown pressures obtained from both the experimental cases. Results from both the experimental data sets show that the impact acceleration and touchdown pressure increases practically linearly with the increase in the height of the drop.

The reliability of the experimentally measured maximum accelerations was calibrated with classical von Karman and Wagner approximate closed-form solutions. For a conical bottomed rigid body, the analytical results show that there is a large difference between the experimental peak impact accelerations and those obtained by these analytical estimates. The large difference can be partly attributed to the unique shape of the rigid body considered (i.e., the WLO) and partly due to the assumptions of the formulations for both von Karman and Wagner approaches. Owing to the large difference between the experimental accelerations and those provided by von Karman and Wagner approaches, an improved approximate solution procedure using an “equivalent” radius (r) of the rigid body (WLO) was estimated to understand the physics of the impact. It can be observed that the von Karman approach tends to estimate a lower value of the radius of the conical portion whereas the Wagner approach tends to estimate a higher value of the impact radius.

As the effect of local rise up of the water is significant during water entry of a rigid 3D rigid body, the von Karman predictions for maximum impact accelerations are not significant in determining the maximum impact accelerations for the water entry of the

WLO. Based on the equivalent radius approach, the approximate analytical solutions of von Karman and Wagner can be used to obtain design maximum accelerations of the WLO model consistent with experimental results. Further, the mean equivalent radius (r^*) was computed to analytically estimate the maximum impact accelerations (for varying impact velocities). Results show the maximum impact accelerations obtained by both the semi-analytical estimates compared reasonable well with the experimental acceleration values. In order to achieve accelerations comparable to the closed-form solutions, the analytical results show that, for the design of a WLO, the Wagner approach provides a correct estimate of the equivalent radius of the WLO. It is, however, interesting to note that the acceleration values obtained by von Karman and Wagner solutions produce accelerations that are similar ascertaining the importance of the shape of the WLO during water impact. Finally, several areas are worthy of mention at this juncture. Model testing is needed over a wider range of conditions to include improved tests which vary the speed, weight and entry angle and under realistic conditions existing in the oceans. The model used for the drop tests should be specifically designed to avoid structural vibrations. Future work can also include more in-depth analysis of the vehicle impact pressures, fully deformable vehicles and floatation studies. Numerical simulations of the rigid body splashdown can be performed and the possibility of combining the finite element package with a computational fluid dynamics package could more accurately simulate the hydrodynamics during impact.

2.8 Acknowledgements

Financial support from the US Office of Naval Research Grant N0014-11-1-0094 and N00014-13-1-0849, and the Department of Energy Grant DE-FG36-08GO18179-M001 for the first and second author are gratefully acknowledged.

2.9 References

- Baker, E., and Westine, S., 1967. "Model tests for structural response of Apollo Command Module to water impact," *Journal of Spacecraft and Rockets*, **4**(2), pp. 201-208.
- Faltinsen, O. M., 1990. "Sea loads on ships and offshore structures," Cambridge University Press, Cambridge.
- Faltinsen, O. M., 1997, "The effect of hydroelasticity on slamming," *Phil. Trans. R. Soc. Lond. A*, **355**, 575–91.
- Faltinsen, O. M., 1999, "Water entry of a wedge by hydroelastic orthotropic plate theory," *Journal of Ship Research*, **43**(3), 180–193.
- Faltinsen, O.M., 2005. "Hydrodynamics of high-speed marine vehicles," Cambridge University Press.
- Hirano, Y., and Miura, K., 1970. "Water impact accelerations of axially symmetric bodies," *Journal of Spacecraft Rockets*, **7**(6), pp. 762-764.
- Kaplan, A., 1968. "Simplified dynamic analysis of Apollo water impact, including effects of the flexible heat shield," 11176-11176-6004-R0-00, TRW, Redondo Beach, California, USA.
- Karman, T. von, 1929, "The impact on seaplane floats during landing," NACA, Tech. Note

No. 321, Washington, D.C.

Korobkin, A.A., 2005. "Three-dimensional nonlinear theory of water impact," Proceedings of the 18th International Congress of Mechanical Engineering (COBEM). Ouro Preto, Minas Gerais, Brazil.

Korobkin, A. A., and Scolan, Y. M., 2006. "Three-dimensional theory of water impact. Part 2. Linearized Wagner problem," *Journal of Fluid Mechanics*, 549, pp. 343-373.

Miloh, T., 1991. "On the initial-stage slamming of a rigid sphere in a vertical water entry," *Applied Ocean Research*, 13(1), pp. 43-48.

Scolan, Y. M., and Korobkin, A. A., 2001. "Three-dimensional theory of water impact. Part 1. Inverse Wagner problem," *Journal of Fluid Mechanics*, 440, pp. 293-326.

Scolan, Y.M., and Korobkin, A.A. 2012. "Hydrodynamic impact (Wagner) problem and Galin's theorem," Proceedings of the 27th International Workshop on Water Waves and Floating Bodies, Copenhagen, Denmark.

Seddon, C. M., and Moatamedi, M., 2006. "Review of water entry with applications to aerospace structures," *International Journal of Impact Engineering*, 32, pp. 1045-1067.

Von Karman, T., 1929. "The impact of seaplane floats during landing," NACA TN 321, National Advisory Committee for Aeronautics, Washington, USA.

Wagner, H., 1932. "Transformation phenomena associated with impacts and sliding on liquid surfaces," *Math. Mechanics*, 12(4), pp.193-215.

Wang, J. T., and Lyle, K. H., 2007. "Simulating space capsule water landing with explicit finite element method," 48th AIAA/ASME Conference, April, pp. 23-26, Waikiki, HI, USA.

Zhao, R., Faltinsen, O. M., Aarsnes, J. V., 1996, "Water entry of arbitrary two-dimensional

sections with and without flow separation,” Proceedings of 21st Symposium on Naval Hydrodynamics, pp. 408–23, Washington, D.C.: National Academy Press.

Rigid-Object Water-Entry Impact Dynamics: Finite-Element/Smoothed Particle
Hydrodynamics Modeling and Experimental Validation

Ravi Challa, Solomon C. Yim, V.G. Idichandy and C.P. Vendhan

Journal of Offshore Mechanics and Arctic Engineering

ASME

Volume 136, August 2014, Pages 031102-1 - 031102-12

3 RIGID-OBJECT WATER-ENTRY IMPACT DYNAMICS: FINITE-ELEMENT/SMOOTHED PARTICLE HYDRODYNAMICS MODELING AND EXPERIMENTAL VALIDATION

3.1 Abstract

A numerical study on the dynamic response of a generic rigid water-landing object (WLO) during water impact is presented in this paper. The effect of this impact is often prominent in the design phase of the re-entry project to determine the maximum force for material strength determination to ensure structural and equipment integrity, human safety and comfort. The predictive capability of the explicit finite-element arbitrary Lagrangian-Eulerian (ALE) and smoothed particle hydrodynamics (SPH) methods of a state-of-the-art nonlinear dynamic finite-element code for simulation of coupled dynamic fluid structure interaction (FSI) responses of the splashdown event of a WLO were evaluated. The numerical predictions are first validated with experimental data for maximum impact accelerations and then used to supplement experimental drop tests to establish trends over a wide range of conditions including variations in vertical velocity, entry angle and object weight. The numerical results show that the fully coupled FSI models can capture the water-impact response accurately for all ranges of drop tests considered, and the impact acceleration varies practically linearly with increase in drop height. In view of the good comparison between the experimental and numerical simulations, both models can readily be employed for parametric studies and for studying the prototype splashdown under more realistic field conditions in the oceans.

3.2 Introduction

Ocean entry dynamics of a generic WLO is an intrinsic component of many naval applications. Examples include ship slamming, torpedo water entry, and space module water landing impact analysis. The recent emphasis of the Navy on Intelligent, Surveillance and Reconnaissance (ISR), Mine Warfare (MIW), Naval Special Warfare (NSW), and Anti-Submarine Warfare (ASW) further highlights the importance of multi-physics numerical codes capable of modeling the ocean environment and contact/impact phenomena of deployed systems accurately. The present study is concerned with numerical analysis of the ocean water landing of a generic rigid object (WLO) and its comparison with the experimental results. The effect of this impact is often prominent in the design phase of re-entry projects, to determine the maximum force for material strength determination to ensure structural and equipment integrity and human safety.

Prototype data (generic shape and dimensions) has been provided by the Indian Space Research Organization (ISRO) to facilitate the development of a physical WLO model. The shape of the prototype is unique in a way that it is conical with a rounded nose (which impacts the water surface first) than compared to the convex shape of the base used for American space missions. This significantly inhibits the comparison with the literature available for Apollo Command Module (ACM) or other American space missions.

Studies on impact phenomena based on the theoretical and experimental work by von Karman [1] and Wagner [2] resulted in approximate estimates and bounds for the impact accelerations on rigid bodies entering water free surface. Using an expression for the added mass of the water, acceleration of and pressure on the rigid body were determined. Miloh [3] obtained analytical expressions for the small-time slamming coefficient and wetting

factor of a rigid spherical shape in a vertical water entry. A semi-Wagner approach was then used to compute the wetting factor and the Lagrange equations were employed in order to determine the slamming force from the kinetic energy of the fluid. Good agreement between theoretical model and experimental measurements, both for the early-stage impact force and the free-surface rise at the vicinity of the sphere was observed. Brooks and Anderson [4] investigated the dynamic response of water-landing space module (WLSM) during impact upon water. A 1/5th-scale model was tested in a three-dimensional (3-D) basin at the Hinsdale Wave Research Laboratory (HWRL) at Oregon State University and the results were compared with those obtained using analytical techniques and computer simulations. The 3-D FE model was validated by comparison with previous full-scale test data and theory. Zhao and Faltinsen [5] developed a generalized Wagner model, within which only the boundary conditions on the fluid free surface are simplified (linearized BCs). Faltinsen [6] studied the relative importance of hydroelasticity for an elastic hull with wedge-shaped cross sections penetrating an initially calm water surface. Wagner's theory was generalized to include elastic vibrations. The importance of hydroelasticity for the local slamming-induced maximum stresses was found to increase with decreasing deadrise angle β and increasing impact velocity V . Fair agreement between theory and experiments was documented. Scolan and Korobkin [7] considered the 3-D problem of a blunt-body impact onto the free surface of an ideal incompressible liquid based on Wagner's theory. They also found that the bounds on maximum acceleration due to impact of a rigid object water re-entry can be obtained analytically. Souli and Olovsson [8] evaluated the capabilities of FSI and ALE formulation for various fluid dynamics problems and showed that FE code is an efficient tool for analyzing large deformation processes with

its multi-material ALE capabilities. Korobkin and Scolan [9] also performed hydroelastic slamming analysis of a 3-D cone using Wagner's approach. Tutt and Taylor [10] assessed the performance of recovery vehicles in the event of a water landing. They investigated the application of the Eulerian-Lagrangian penalty coupling algorithm and multi-material ALE capabilities for the water impact. Melis and Bui [11] studied the ALE capability to predict splashdown loads on a proposed replacement/upgrade of hydrazine tanks on a thrust vector control system housed within the aft skirt of a Space Shuttle solid rocket booster. Preliminary studies on the booster impacting water showed that useful predictions can be obtained using the ALE methodology to a detailed analysis of a 26-degree section of the skirt with a proposed tank attached. The 3-D nonlinear theory of water impact was solved by Korobkin [12] using a modified Logvinovich model, which is slightly more complex than the Wagner's method used in this study. Seddon and Moatamedi [13] reviewed water entry studies between 1929 and 2003, and provided a summary of major theoretical, experimental and numerical accomplishments in the field. Wang and Lyle [14] simulated space capsule water landing using an arbitrary Lagrangian-Eulerian (ALE) finite-element (FE) solver and a penalty coupling method to predict fluid and structure interaction forces. The capsule was assumed rigid and results were found to correlate well with closed-form solutions. Jackson and Fuchs [15] conducted vertical drop tests on a 5-ft diameter composite fuselage section into water. A detailed FE model was developed to model the impact event using the ALE and smoothed particle hydrodynamics (SPH) approaches in LS-DYNA. Vandamme *et al.* [16] investigated the fluid and floating object interaction using a novel adaptation of the weakly compressible smoothed particle hydrodynamics (WCSPH) method by incorporating a floating object model. Simulations results for water

entry and exit of a buoyant and neutral density cylinder showed good agreement with previous experimental, numerical, and empirical studies in penetration depth, free surface motions, and object movement.

It is apparent that though FE codes were used for many fluid-structure interaction problems in the past, modeling the air and water domains accurately in such problems still poses difficulties. A general-purpose non-linear transient dynamic finite element code for analyzing large deformation rate response of fluids including fluids coupled to structures is used in the present study. Dynamic behavior of the WLO dropped from specific heights (with varying entry speed and weight) to provide data for calibration of prediction results from numerical studies is examined in this article. Experimental and numerical results are correlated with classical solutions using the von Karman and Wagner approaches for maximum impact acceleration.

3.3 Finite element modeling of the experimental WLO drop tests

The present paper is the second of a two-part series to investigate the water entry dynamics of a rigid body, both experimentally and numerically. It constitutes the first part of a project in which two independent sets of experiments were conducted to calculate the maximum impact accelerations and touchdown pressures on a WLO upon impact with water surface [17]. Drop test I involved dropping the object using a rope and pulley arrangement, while Drop Test II employed an electromagnetic release to drop the model [17]. In this article, the numerical study of the dynamic response of a WLO water impact is presented for both drop test cases. Both sets of experiments provide valuable and complementary experimental data (for different weight distribution ratios) for numerical model validation.

Both test cases involved dropping the object over a range of 0.5m intervals where the maximum permissible height of 5m corresponds to an achievable velocity of 9.81m/s.

To simulate the dynamic response of the impact experiment for model testing, a 1/6th Froude scale model of WLO [made of fiber reinforced polymer (FRP)] was used [17]. The overall configuration of the WLO prototype is shown in Figure 3.1. Note that the conical portion (nose part of the rigid-object) impacts the water surface first. The origin of reference is located at the deck of the WLO and the position of Z_{cg} is measured from the flat base (Figure 3.1). The scaled model of the WLO has a maximum base diameter of 338.5mm and a height of 271.6mm. The weight of the WLO is 2.03 Kg. A skin thickness of 5mm was selected, with extra thickness at the nose (of about 10mm) to withstand the force of impact.

A numerical code for nonlinear dynamic analysis of structures in three dimensions (3D), LS-DYNA, is used in the current study (Version: mpp971d R7.0.0 and Revision: 79055). The predictive capability of the nonlinear explicit dynamic finite element code is evaluated. This work utilizes the built-in contact-impact algorithm along with the ALE and SPH features to simulate the fully coupled FSI phenomenon. More details on the version, number of degrees of DOF and the platforms used are presented in the *performance studies of ALE and SPH* section.

For the problem considered, the dynamic response involves the penetration of the object treated essentially as a rigid body through the air/water domain. All the ALE simulation models involve three components (i) WLO, (ii) air domain, and (iii) water domain. Note that all the numerical tests were confined to vertical impact only. For information on the effect of horizontal speed of the entering body, see [18].

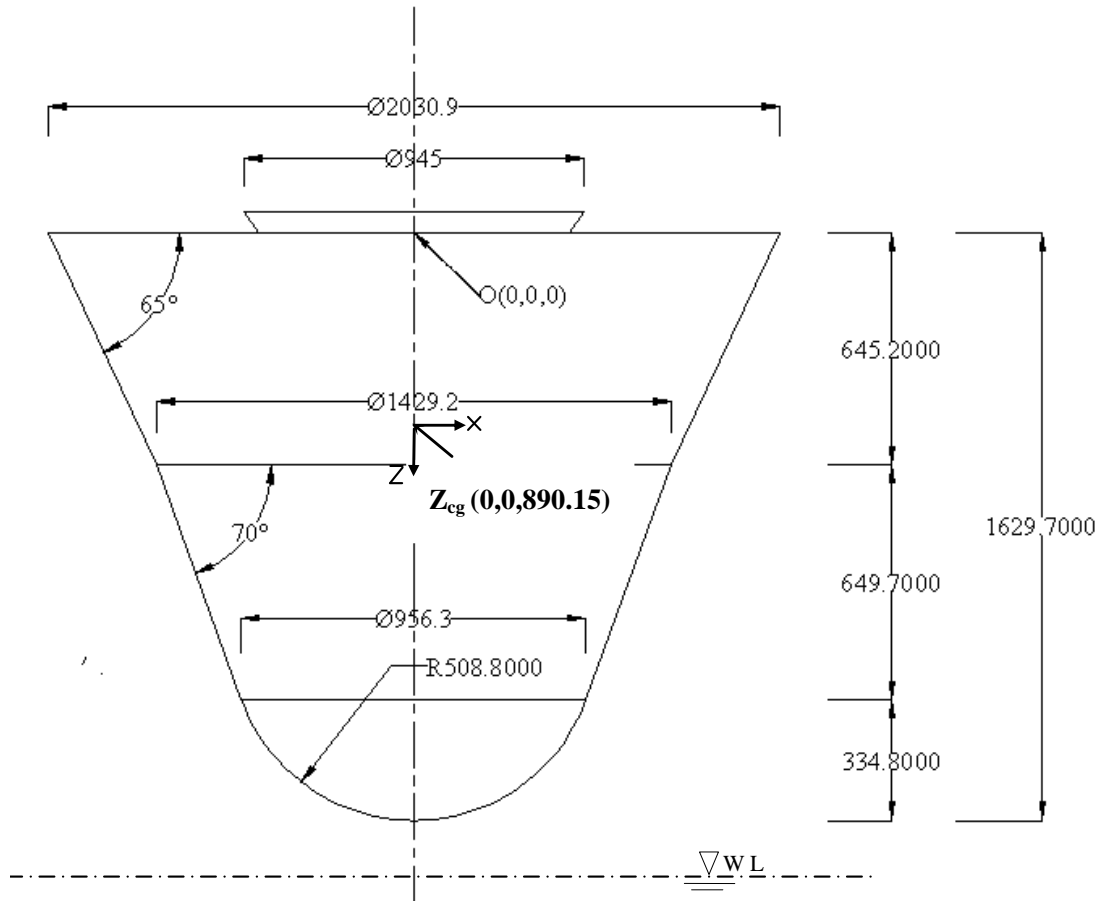


Figure 3.1: Overall configuration of WLO Prototype (All dimensions are in mm)

The air and water domains were modeled using solid brick elements in an axi-symmetric cylindrical domain. An important feature in simulating contact and impact problems is proper modeling of the two-phase flow including the presence of air. A common practice of past studies in modeling the air domain in coupled FSI contact and impact problems is to use either “vacuum” or “void material” to model the air domain. However, this does not capture the physics accurately and leads to unrealistic high impact accelerations. In this paper we include air modeling using material properties and a governing equation of state. The Apollo-like space capsule (used for many previous impact studies) and by Wang and Lyle [14] had a maximum diameter of 198 inches (~5m) and a height of 130 inches

(~3.3m). The weight is estimated to be 16,200 lbs (~7,348 Kg). The FE computational setup for such a model demands large water and air domains requiring a very larger number of nodes and elements to achieve convergence. However, in the present study the maximum diameter of the 1/6th Froude-scale model of the WLO is 338.5mm and a height of 271.6mm with a weight of 2.03 Kg. Hence, a water body of 4m (diameter) x 2m (length) and an air domain of 4m (diameter) x 1.0m (length) are modeled for the impact studies. Null material model which has very little shear strength is used to model the water and air domains with a mass density of 1000 kg/m³ and 1.29 Kg/m³ respectively which needs an equation of state to be defined.

The WLO is made up of fiber reinforced plastic (FRP) and the mass density and Young's modulus values are those of the FRP material used for both experimental test cases and numerical simulations. The WLO is treated as a rigid body with a mass density of 1764.52 kg/m³. (As a side note and for completeness of information, in the numerical computation of the coupled fluid-rigid body interaction, the code uses a penalty function method to determine the location of the common contact surface between the fluid and the rigid body that requires the input of artificial values of Young's modulus and Poisson's ratio of the body to compute the penalty function spring stiffness for intermediate iterations. For the simulations performed in this study, a Young's modulus of 4.895 X 10E9 N/m² and a Poisson ratio of 0.2 appear to be optimal.)

Eight-node brick elements and 4-node Belytschko-Lin-Tsay shell elements [19,20] are used for discretization of the air/water and WLO domains, respectively. A constrained Lagrange interface/contact is used to model the impact event between the object (treated as a rigid body) and the air-water target. In this, the moving surface of 3-D rigid body (a

Lagrangian mesh) is treated as the slave surface, and the target air-water mesh is treated as the master surface.

Importantly, Navier Stokes equations and ALE formulations are solved over the entire computational domain. In the ALE description, an arbitrary referential coordinate is introduced in addition to the Lagrangian and ALE coordinates [21]. The material time derivative of a variable with respect to the reference coordinate can be described as

$$\frac{dg(\bar{X}, t)}{dt} = \frac{\partial g(\bar{x}, t)}{\partial t} + (\bar{v} - \bar{w}) \cdot \overline{\text{grad}} g(\bar{x}, t) \quad (1)$$

Where \bar{X} is the Lagrangian coordinate, \bar{x} the ALE coordinate, \bar{v} is the particle velocity, and \bar{w} the grid velocity of the numerical simulation. The ALE differential form of the conservation equations for mass, momentum, and energy are readily obtained from the corresponding Eulerian forms:

$$\text{Mass: } \frac{\partial \rho}{\partial t} + \rho \text{div}(\bar{v}) + (\bar{v} - \bar{w}) \cdot \overline{\text{grad}}(\rho) = 0 \quad (2)$$

$$\text{Momentum: } \rho \frac{\partial \bar{v}}{\partial t} + \rho(\bar{v} - \bar{w}) \cdot \overline{\text{grad}}(\bar{v}) = \overline{\text{div}}(\overline{\sigma}) + \bar{f} \quad (3)$$

$$\text{Energy: } \rho \frac{\partial e}{\partial t} + \rho(\bar{v} - \bar{w}) \cdot \overline{\text{grad}}(e) = \overline{\sigma} : \overline{\text{grad}}(\bar{v}) + \bar{f} \cdot \bar{v} \quad (4)$$

Where ρ is the mass density, \bar{f} is body force vector, and e is the total energy. $\overline{\sigma}$ denotes the total Cauchy stress given by:

$$\overline{\sigma} = -p\overline{I} + \mu(\overline{\text{grad}}(\bar{v}) + \overline{\text{grad}}(\bar{v})^T) - 2/3\overline{\text{grad}} \cdot \bar{v}\overline{I} \quad (5)$$

Where p is the pressure, \overline{I} is the identity tensor, μ is the dynamic viscosity, and $(\bar{v} - \bar{w})$ is the convective velocity across the grid.

The elements of the air and water domains were given the null hydrodynamic material type that allowed a new equation of state to be specified. An equation of state with a linear

polynomial form is used to define the initial thermodynamic state of the material and pressure [20] is given by:

$$p = C_0 + C_1\zeta + C_2\zeta^2 + C_3\zeta^3 + (C_4 + C_5\zeta + C_6\zeta^2)E \quad (6)$$

where C_{0-6} are user-defined constants, E is initial energy per initial volume, and the volumetric parameter ζ is defined as:

$$\zeta = \frac{1}{V} - 1 \quad (7)$$

where V is relative volume given as:

$$V = \frac{\rho_0}{\rho} \quad (8)$$

with ρ_0 as the reference mass density (which might be different than the current mass density if the material experiences compression or expansion throughout the simulation).

The constant C_1 in Equation 6, when used by itself, is the elastic bulk modulus ($C_1 = \rho c_s^2$),

where ρ is the mass density of the material and c_s is the sound speed in air/water

($c_s = 1480m/s$ for water and $c_s = 343m/s$ for air). Providing this constant only and setting all other constants to zero is sufficient to define the equation of state if the pressure is not significantly influenced by temperature changes.

As another side note, sound speed in water plays a significant role in determining the integration time step and also the total computational time. The time step can be artificially lowered for fluids without affecting the accuracy of the fluid motion computation but can significantly reduce the computational effort by allowing a significantly large time step [22]. A sound speed 100m/s is employed in all subsequent computations in this study. This

provides values of C_1 for air and water domains are $1.0E+05N/m^2$ and $1.0E+07N/m^2$, respectively.

The boundary conditions employed in the numerical model are partially the material surfaces (out-of-plane, in-plane and bending restraint). The material surfaces defined in ALE formulation are: (a) no particles can cross them, and (b) stresses must be continuous across the surfaces.

3.4 Finite element simulations

A number of model development techniques were examined to identify the most efficient and accurate models, some of which are discussed here.

Modeling Air – An air pressurization study was conducted to confirm that the magnitude of the pressure in the air is necessary to not only energize the air around the rigid body but also to get a good velocity contour around the falling object, making it is a significant parameter in modeling these kind of contact and impact problems.

Rigid-body starting location – A review of the starting location of the rigid body was performed. It was clear that the rigid body (with prescribed initial velocity) would need to fall from a height large enough to allow the surrounding air flow to be captured accurately but not so large as to require a very large computational domain (and hence simulation time) that does not improve the predictive accuracy. It was found that starting location of 0.3m above the water surface with a corresponding initial velocity (obtained from analysis) was adequate for all the rigid body impact tests to accurately capture the physics of the

impact. Note that the mesh of the WLO is immersed in the Eulerian meshes of water and air, but the fluid nodes and the structure do not need to be coincident.

Mesh size variation – The mesh size of the ALE air and water domains close to the impact zone were varied from a coarse 100mm grid to a fine mesh of 20mm grid to study the convergence of the peak impact acceleration values. Simulations were performed over a wide range of conditions. The characteristics of entry speed, entry angle, and vehicle weight were varied. The time step was approximately 3.0E-05sec. There were a total of 732,550 nodes and 714,180 in the 3D ALE model. For each simulation, a total of 33,246 data states were created from the simulation. Displacement, velocity and acceleration of the model were recorded (related to the center of mass of WLO). An important result from these simulations is the maximum impact acceleration and maximum impact pressures experienced by the object upon impact for each drop height. Figure 3.2 shows the plan and top view of the computational mesh. In all numerical simulations the accelerations are obtained in reference to the local Z direction, unless indicated otherwise.

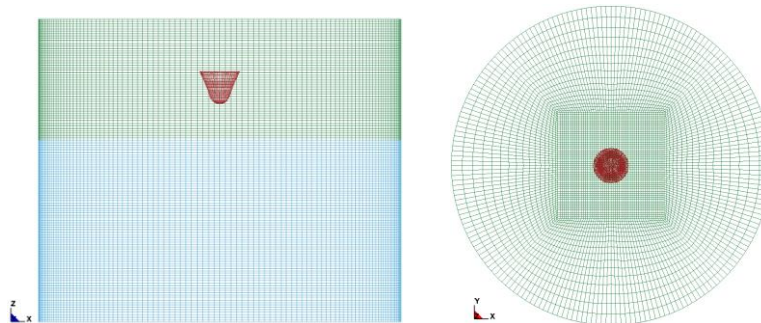


Figure 3.2: Elevation [L] and top view [R] of the FE-ALE computational mesh (Blue: Water domain /Green: Air Domain/ Red: WLO model)

Effects of Vertical Velocity Variation --- The vertical velocities of the WLO considered in this study varied from 9.8m/s to 4.4 m/s (with 9.8 m/s corresponding to Drop Test-I). Figure

3.3 shows the animation images of the impact at various time steps in comparison to the image from the experiment shown exactly during impact.

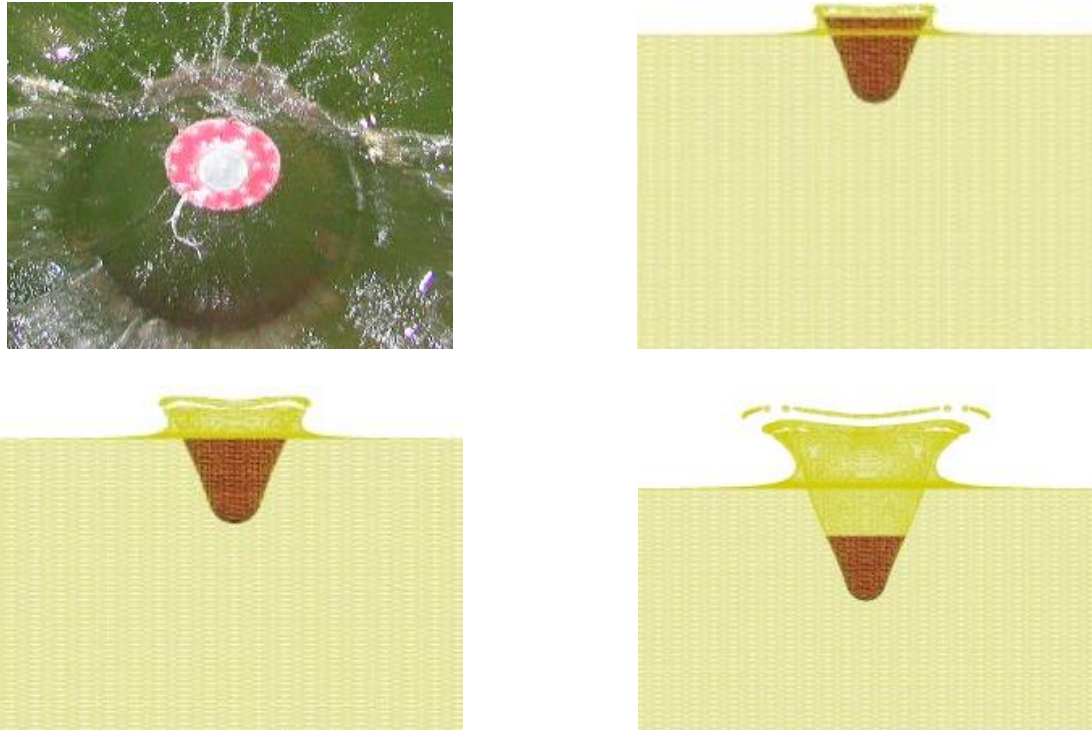


Figure 3.3: Animation images at various time steps for vertical impact

Figures 3.4 and 3.5 show acceleration and pressure time histories for a 5m drop test. It can be observed that the modeling of the two-phase flow with the proper simulation of the dynamics of air provides accurate impact acceleration results that are remarkably close to the WLO experimental impact data, providing a high degree of confidence in the applicability of ALE methodology to this class of intricate contact and impact problems. For a 5m drop height, Figure 4 shows that the peak acceleration upon impact corresponds to 55.10 m/s^2 ($5.5 g$) and Figure 3.5 shows that the peak impact pressure corresponds to 28kPa. Note that the pressure acting on a rigid body is computed using an inbuilt FSI sensor (placed strategically at the nose of the WLO impacting water surface first).

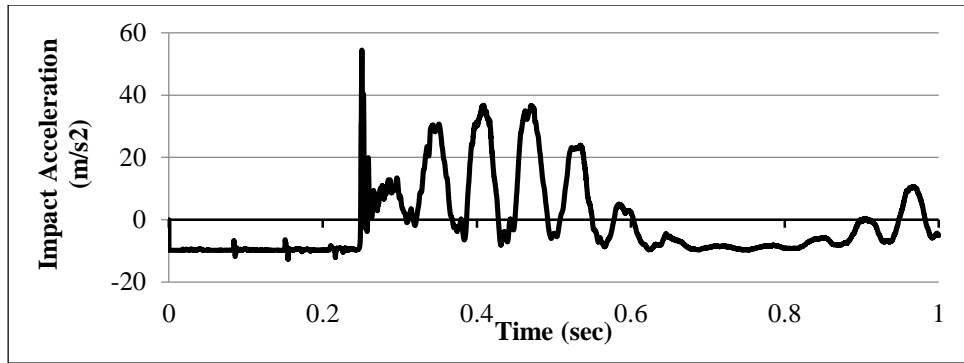


Figure 3.4: Numerical simulation response of a 5m drop test: Acceleration time history

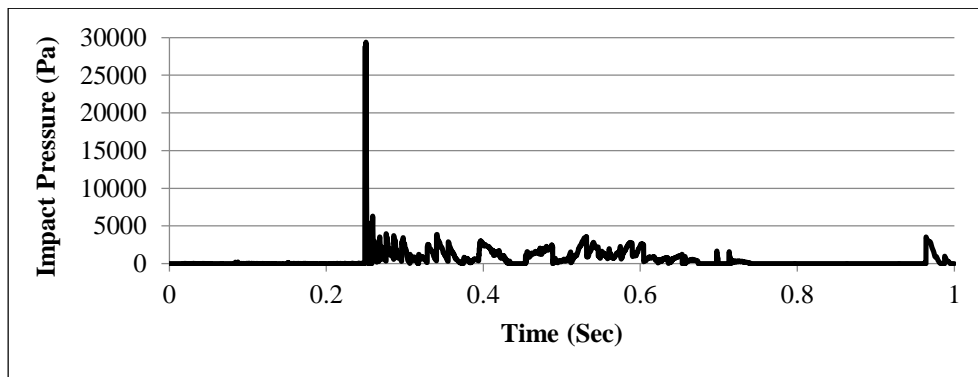


Figure 3.5: Numerical simulation response of a 5m drop test: Pressure time history

The acceleration and pressure time histories (Figures 3.4 and 3.5) also depicts that during free fall, the response remains flat ($0 < t < 0.245 \text{ sec}$), due to the positioning of the rigid body with respect to the water surface and during touchdown on the water surface the acceleration and pressure peaks are recorded ($0.245 < t < 0.254 \text{ sec}$). It is evident from the post impact scenario that the rigid body bounces (with its nose up) after impact ($0.254 < t < 0.55 \text{ sec}$) and subsequently comes to a static equilibrium with a practically constant submerged pressure ($0.55 < t < 1 \text{ sec}$).

Note that, in contrast to the results presented in [4,14-15], the numerical predictions presented in Figures 3.4 and 3.5, which match well with experiment measurements, do not

contain any high frequency oscillatory “noise” and does not require filtering. We attribute this improvement in the predictive capability to the accurate modeling of the behavior of air flow around the rigid body.

An attempt was made to measure the maximum depth of immersion of WLO after impact using the experiments but they were discarded as they were deemed unreliable. A tracer particle approach using a tracer node is used to measure the depth of immersion in the numerical simulations. Figure 3.6 shows a linear relationship between the depth of immersion and the drop height.

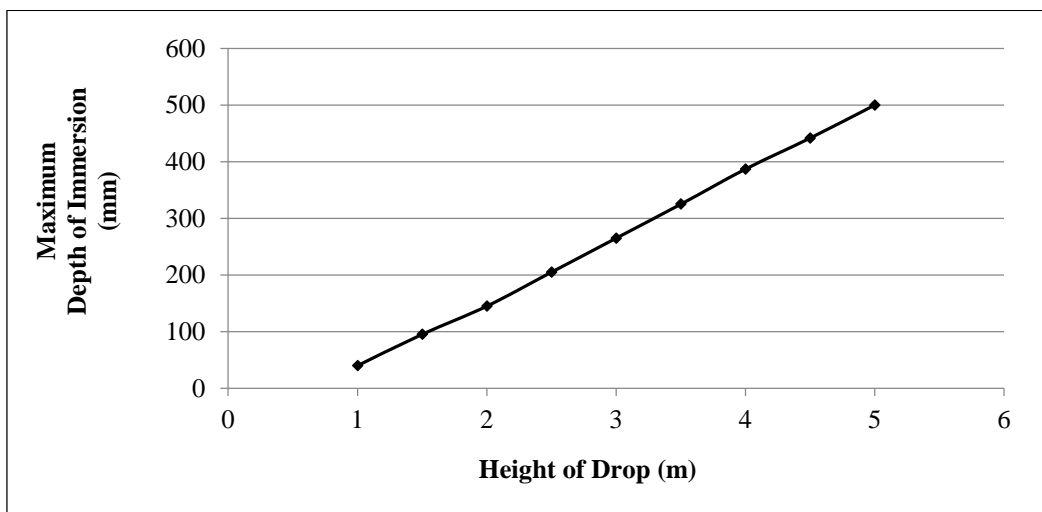


Figure 3.6: Height of Drop vs. Depth of Immersion for Case-I

Table 3.1 shows a comparison of experimental data (Drop Test-I: Mechanical release) with the ALE predictions. Due to the highly stochastic nature of the peak pressure estimates on the rigid body [23], each drop test was repeated thrice and the maximum impact pressure reported in Table 3.1 is the mean value of three drop test cases.

Table 3.1: Simulation results for maximum impact acceleration [Drop Test-I: Weight of WLO = 2.03kg (Vertical Entry/Entry Angle=0 deg)]

Vertical Velocity at Impact (m/s)	Maximum Impact Acceleration (Numerical) (m/s²)	Maximum Impact Acceleration (Experimental) (m/s²)	Maximum Impact Pressure (Numerical) (kPa)	Maximum Impact Pressure (Experimental) (kPa)
9.80	55.10	52.17	28.12	26.10
9.27	52.48	48.32	26.61	23.25
8.61	49.32	45.18	23.42	22.15
8.26	39.80	38.76	22.35	19.25
7.55	38.18	37.78	19.75	18.65
6.87	34.18	33.53	18.11	16.35
6.20	32.10	30.27	16.98	15.20
5.31	24.75	22.86	15.45	13.10
4.39	12.58	11.65	14.20	12.80

Effects of Entry Angle Variation --- The entry angles of the WLO upon impact were varied from 15 to 40 degrees (Table 3.2) to examine its influence on peak acceleration. Simulation results show that the impact acceleration can be reduced by having the WLO enter the water at an angle.

Table 3.2: Summary of the pitch tests (V=9.8m/s) (Weight of WLO = 2.03kg)

Entry Angle (Degrees)	Maximum Impact Acceleration (Numerical) (m/s²)	Maximum Impact Pressure (Numerical) (KPa)
0	55.10	28.12
15	45.75	17.92
30	32.01	11.45
45	15.55	9.50

Note that the experimental studies did not involve pitch tests [17]. When the local dead rise angle (β) between the water surface and the dropping object is not very small at the impact position, the body can be assumed rigid in the hydrodynamic calculations [23]. The relatively high stiffness of the scaled down model is due to the rigid body definition. When β is small, the hydroelastic effects become important [6,23] and the maximum impact accelerations are greatly affected by the hydroelastic interactions at impact [14]. Previous studies on water impact analysis involved objects with small β compared to the present scenario which deals with a unique shape of the WLO with a large β during impact with water surface. This is one of the reasons for the excellent comparisons between the experimental and numerical test data.

Effects of Weight Variation -- The effects of variations in the weight of the WLO on maximum impact acceleration and pressure was examined by varying the object weight from 2.5 kg to 5 kg (3.5kg corresponds to Drop Test-II involving an electromagnetic drop mechanism). Trends obtained from acceleration and pressure time histories for a 3.5 kg model were similar to those obtained for Drop Test-I [17]. The acceleration time history for a weight of 3.5kg of WLO yields a peak impact acceleration value of 38.20 m/s^2 (3.8 g) and a touchdown pressure of 43.5KPa. Table 3.3 shows a comparison of experimental results from the electromagnetic release mechanism with the ALE formulation. The peak accelerations obtained from the FE simulations and the experimental data for Drop Test-II are 38.20 m/s^2 and 36.50 m/s^2 , respectively, showing good predictive capability of the numerical model.

Table 3.3: Simulation results for maximum impact acceleration [Drop Test-II: Weight of WLO = 3.5kg (Vertical Entry/Entry Angle=0 deg)]

Vertical Velocity at Impact (m/s)	Maximum Impact Acceleration (Numerical) (m/s²)	Maximum Impact Acceleration (Experimental) (m/s²)	Maximum Impact Pressure (Numerical) (kPa)	Maximum Impact Pressure (Experimental) (kPa)
9.72	38.20	36.50	43.50	41.15
9.30	32.85	31.72	42.35	38.20
8.81	28.20	27.32	35.70	32.75
8.19	24.80	22.82	31.65	29.35
7.54	22.35	19.55	26.22	25.15
6.97	18.50	15.32	23.17	21.25
6.22	15.10	12.12	20.85	19.10
5.35	11.75	10.72	19.85	18.45
4.42	10.90	9.92	17.33	15.75

3.5 Analytical description of the general contact–impact problem

For a rigid object with a spherical bottom, closed-form solutions based on the von Karman and Wagner approaches are available to correlate with results from the explicit finite element analyses [14]. The von Karman approach is based on conservation of momentum and uses an added mass [1]. The penetration depth is determined without considering water splash-up. The Wagner approach uses a more rigorous fluid dynamic formulation and includes the effect of water splash-up on the impact force [2]. From the analytical solutions for a spherical bottom body impacting with water using the von Karman method [24], the magnitude of the virtual mass for a spherical bottom body is given by:

$$m_v = \frac{4}{3} \rho h^2 (2R - h)^2 \quad (9)$$

where m_v is the virtual mass, ρ is the mass density of water, h is the water depth, and R is the radius of the spherical bottom.

Assuming $\frac{h}{R} \ll 1$, the maximum acceleration can be found as

$$a_{\max-\nu K} = -\frac{256}{243} \left(\frac{4\rho g R^3}{3W} \right)^{\frac{2}{3}} \left(\frac{V_0^2}{R} \right) \quad (10)$$

where νK stands for von-Karman in (10)

A semi-Wagner approach to determine the non-dimensional slamming coefficient [3] is based on these analytical derivations the maximum acceleration can be estimated as

$$a_{\max-w} = \frac{g}{2W} C_s \left(\frac{h_{\max}}{R} \right) \rho \pi R^2 V_0^2 \quad (11)$$

where w stands for Wagner in (11).

The equivalent radius is a representative or nominal radius of WLO that yields the accelerations comparable to the maximum impact accelerations obtained experimentally with the conical shaped WLO [17]. From the analytical solutions for a spherical bottom body impacting with water surface, for the von-Karman method, equation (10) is used to calculate the equivalent radius by computing $r_{\max-\nu K}$ corresponding the maximum impact acceleration $a_{\max-\nu K}$ and is given by

$$r_{\max-\nu K} = R = -\frac{a_{\max-\nu K}}{V_0^2} \left(\frac{243}{256} \right) \left(\frac{3W}{4\rho g} \right)^{\frac{2}{3}} \quad (12)$$

and correspondingly for the Wagner method, equation (11) can be used to calculate the equivalent radius by computing the value of $r_{\max-W}$ corresponding the maximum impact acceleration $a_{\max-W}$ and is given by

$$r_{\max-W} = R = \frac{2Wa_{\max-W}}{\rho g \pi V_0^2 C_s h_{\max}} \quad (13)$$

Values of the “equivalent radius” of the WLO conical portion is also shown in Table 3.4. A detailed description of the equivalent radius approximate semi-analytical procedure is provided in [17]. Table 3.4 also shows a comparison of the FE simulation results (Drop Test-I and Drop Test-II) with analytical solutions using von Karman and Wagner approaches and experimental test data.

Table 3.4: Analytical solution results from von Karman and Wagner approaches

Water Landing Object (WLO) Experimental Cases	Maximum acceleration g: acceleration due to gravity ($\frac{m}{s^2}$)		Analytical Solutions for maximum accelerations		Equivalent Radius of WLO conical portion (m)	
	Experimental (Drop Tests)	Numerical (FE tests)	von Karman (Eq.5) a_{\max}	Wagner (Eq. 10) a_{\max}^*	von Karman r_{\max}	Wagner r_{\max}^*
Cone radius: 0.0848m Max. Radius: 0.3385m						
Drop Test-I: Mechanical mechanism	5.2g	5.5g	14.7g	19.8g	0.0300 m	0.1075 m
Drop Test-II: Electromagnetic release mechanism	3.6g	3.8g	10.4g	25.2g	0.0293 m	0.1310 m

It is important to note that the maximum radius of the base (for a 1/6th Froude-scale model of WLO) is 338.5mm and the radius of the conical portion impacting the water surface is 84.8mm. For a conical bottomed rigid object, the FE results show that there is large

difference between the numerical peak impact accelerations and those obtained by von Karman and Wagner analytical estimates. This large difference can be attributed to the conical shape of WLO bottom impacting the water surface compared to the large spherical bottom used in deriving the closed-form solutions. In addition to the unique shape of the WLO the basic assumptions of the formulations for both the von Karman and Wagner approaches also play a pivotal role in contributing to the large difference. The von Karman approach is based on the momentum theorem (using an added virtual mass) and the penetration depth is determined without considering the splash-up of the water level, thus neglecting the highly nonlinear coupled fluid-structure interaction effect. The Wagner approach, on the other hand, attempts to relax the von Karman no-splashing assumption by using a rigorous dynamic formulation and incorporates the effect of the upward splashing of the water and its effects on the object. With the upward splashing correction, the Wagner approach tends to over predict the maximum impact retardation as it neglects the water compressibility (i.e. a more yielding fluid) near the impact zone. The lack of agreement in the maximum impact accelerations obtained in the present numerical study with the closed form von Karman and Wagner approximate solutions is due to the large initial angle at impact and the relatively rapid changes in contact radius of the inverted cone shape of the WLO as it penetrates the water surface. These deviations from the idealized assumption may be taken into account using the concept of an equivalent radius [17].

3.6 Smoothed particle hydrodynamics (SPH) simulations

Smoothed particle hydrodynamics (SPH) is an N-body integration scheme initially developed by Gingold and Monaghan [25] and Lucy [26] to avoid the limitations of mesh

tangling encountered in extreme deformation problems with the FE method. The main difference between classical methods and SPH is the absence of grid. Hence, the particles constitute the computational framework on which the governing equations are resolved. The main advantage arises directly from its Lagrangian nature, since such an approach can tackle difficulties related with lack of symmetry, large voids that may develop in the field, and a free water surface much more efficiently than Eulerian methods. The conservation laws of continuum fluid dynamics, in the form of partial differential equations, are transformed into particle form by integral equations through the use of an interpolation function that gives kernel estimation of the field variables at a point [20]. Null material model with an equation of state is used to model the water domain. The speed of sound at the reference density was set to 100m/s as the acoustic speed is not important for the present problem. It is worthy to note that this sound speed is much lower than that of water, but much faster than the water wave propagation in the model.

SPH Formulation --- The particle approximation function is given by:

$$\Pi^h f(x) = \int f(y)W(x-y, h)dy \quad (14)$$

where W is the kernel function. The Kernel function W is defined using the function θ by the relation:

$$W(x, h) = \frac{1}{h(x)^d} \theta(x) \quad (15)$$

where d is the number of space dimensions and h is the so-called smoothing length which varied in time and space. $W(x, h)$ is a centrally peaked function. The most common smoothing kernel used by the SPH is the cubic B-spline which is defined by choosing θ as:

$$\theta(u) = Cx \begin{cases} 1 - \frac{3}{2}u^2 + \frac{3}{4}u^3 & \text{for } |u| \leq 1 \\ \frac{1}{4}(2-u)^3 & \text{for } 1 \leq |u| \leq 2 \\ 0 & \text{for } 2 < |u| \end{cases} \quad (16)$$

where C is a constant of normalization that depends on the spatial dimensions.

The particle approximation of a function is now defined by:

$$\Pi^h f(x_i) = \sum_{j=1}^N w_j f(x_j) W(x_i - x_j, h) \quad (17)$$

where $w_j = \frac{m_j}{\rho_j}$ is the “weight” of the particle. The weight of a particle varies

proportionally to the divergence of the flow.

Discrete form of conservation equation --- The conservation equations are written in their discrete form and the momentum conservation equation is:

$$\frac{dv^\alpha}{dt}(x_i(t)) = \frac{1}{\rho_i} \frac{\partial(\sigma^{\alpha\beta})}{\partial x_i}(x_i(t)) \quad (18)$$

where α, β are the space indices.

Energy conservation equation is given by:

$$\frac{dE}{dt} = -\frac{P}{\rho} \nabla \cdot \mathbf{v} \quad (19)$$

Artificial Viscosity---The artificial viscosity is introduced when a shock is present.

Shocks introduce discontinuities in functions. The role of artificial viscosity is to smooth the shock over several particles. To take into account the artificial viscosity, an artificial viscous pressure term Π_{ij} is added such that:

$$P_{i \rightarrow i+} \Pi_{ij} \quad (20)$$

where $\Pi_{ij} = \frac{1}{\rho_{ij}} (-\alpha \mu_{ij} \bar{c}_{ij} + \beta \mu_{ij}^2)$. The notation $X_{ij} = \frac{1}{2}(X_i + X_j)$ is used for median

between X_i and X_j , c is the adiabatic sound speed, and

$$\mu_{ij} = \begin{cases} \bar{h}_{ij} \frac{v_{ij} r_{ij}}{r_{ij}^2 + \eta^2} & \text{for } v_{ij} r_{ij} < 0 \\ 0 & \text{otherwise} \end{cases} \quad (21)$$

Here, $v_{ij} = (v_i - v_j)$, and $\eta^2 = 0.01 \bar{h}_{ij}^2$ which prevents the denominator from vanishing.

Time Integration--- A simple and classical first-order scheme for integration is used. The time step is determined by the expression:

$$\delta t = C_{CFL} \text{Min} \left(\frac{h_i}{c_i + v_i} \right) \quad (22)$$

where the factor C_{CFL} is a numerical constant.

Description of the SPH model --- Water was simulated by using SPH particles. There is no need for the modeling of the air domain in SPH. A water body of 4m (diameter)x 2m (height) was modeled as a cylindrical mesh, was chosen for the impact studies (number of SPH particles/nodes=1,23,570). The edges of the water were defined as fixed-SPH nodes allowing the water block to be relatively small in size. Figure 3.7 shows the plan of the SPH particle setup. The same material properties that were used in the ALE simulations were retained for the rigid object and the water domain for the SPH simulations.



Figure 3.7. Plan of the SPH Water domain and the WLO (Number of SPH nodes: 712,000)

Effects of Vertical Velocity Variation ---The vertical velocities ranged from 9.8m/s to 4.4 m/s, of which 9.8m/s corresponds to Drop Test-I. SPH animation images of particle impingement (by the rigid body) are shown in Figure 3.8. Acceleration time history for a 5m drop test (Figure 3.9) shows that the maximum impact acceleration is approximately 49m/s^2 .

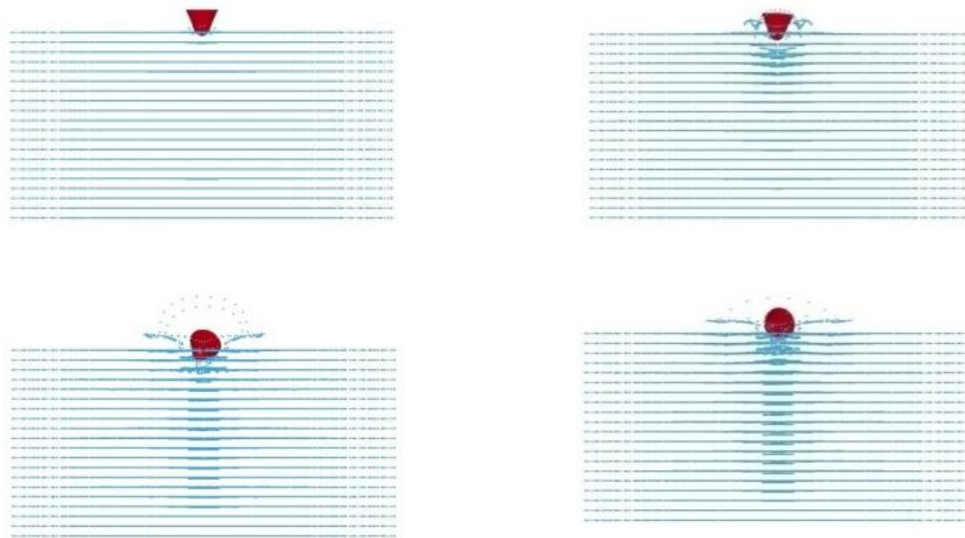


Figure 3.8. SPH Animation images of the particle impingement at various time steps

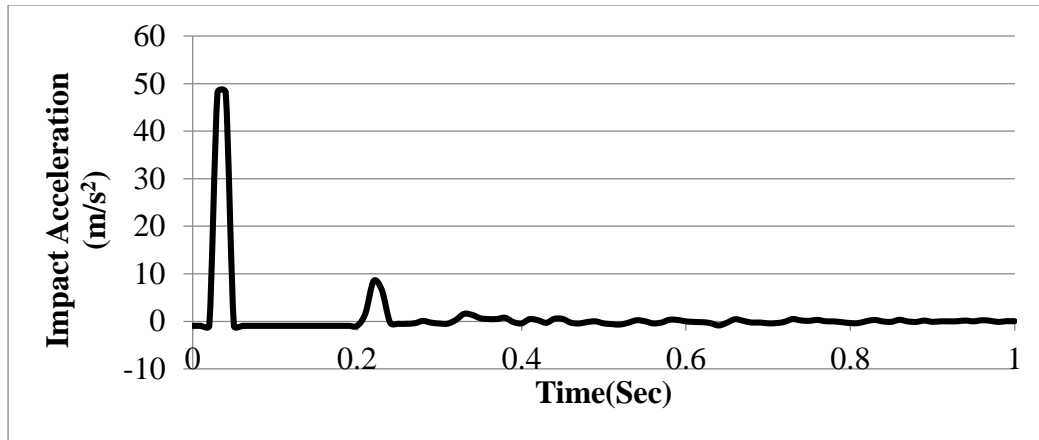


Figure 3.9: SPH acceleration time history for a 5m drop height

Note that the acceleration time history was filtered at 1000Hz using Butterworth filter (same frequency that was used to sample the experimental results) to remove the high frequency content that is part of modeling water using a compressible fluid solver. Figure 3.10 shows a good comparison between the experimental and the ALE and SPH results for maximum impact acceleration. The graph indicates that the trend of impact accelerations increases with an increase in the entry speed. Figure 3.10 also shows the plot of accelerations obtained analytically vs. drop height for the WLO model (using the original radius of the WLO). It is important to note the values of maximum impact accelerations are almost identical for both von Karman and Wagner solutions.

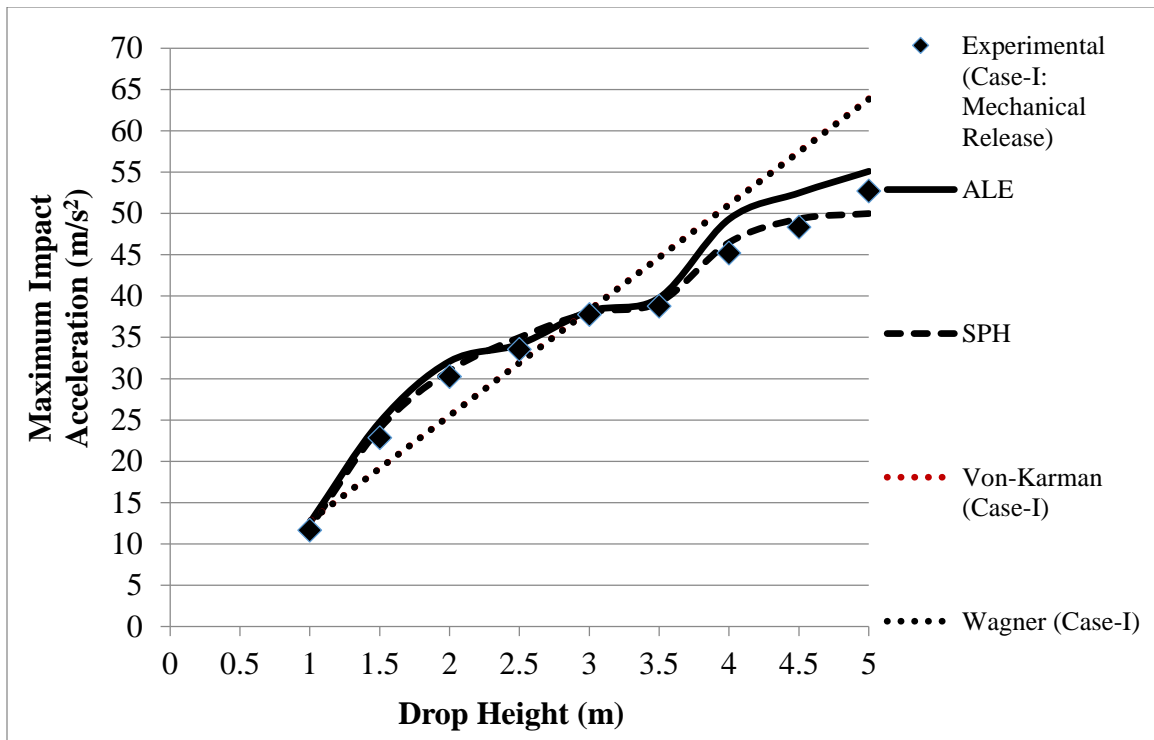


Figure 3.10: Comparison of results for maximum acceleration with ALE and SPH [Weight of WLO = 2.03 kg (Case-I: Mechanical release)] (Vertical Entry/Entry Angle=0 deg)

Effects of Entry Angle Variation (Pitch Tests) --- To determine the effect of varying the entry angle of the WLO upon impact; the entry angle was varied from 15 to 30 degrees. Comparative results with ALE from these tests are shown in Figure 3.11. As expected, the impact acceleration can be reduced by having the WLO enter the water surface at an angle. It is also important to note that the SPH results match reasonably well with the ALE results for the inclined impact tests. Though experimental investigation was not carried out for pitch tests to calibrate the numerical predictions, it is nevertheless interesting to observe the closeness of prediction results obtained by the two numerical models. This also demonstrates the usefulness of numerical simulations once the models have been calibrated by other experimental data.

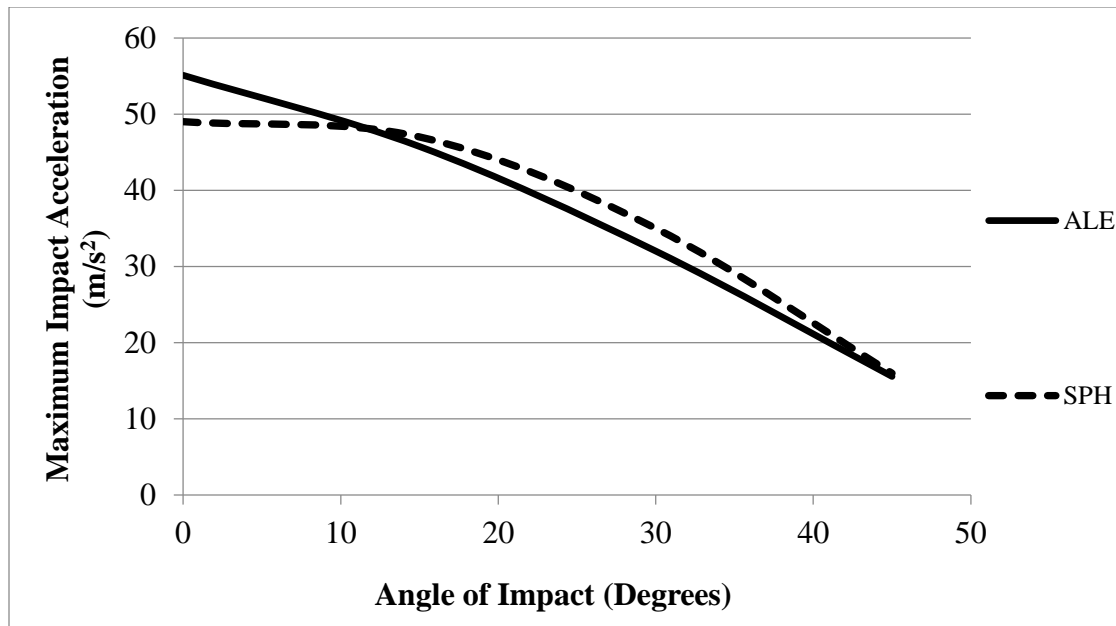


Figure 3.11: Comparison of peak impact acceleration (pitch tests - ALE and SPH methods)

Effects of Weight Variation --- Effect of varying the rigid body weight on impact accelerations was studied by varying WLO weight from 2.5 kg to 5 kg. A test for 3.5 kg corresponds to Drop Test-II involving an electromagnetic drop mechanism. The general trend shows a small advantage gained in reduced g -force for a large increase in weight. Figure 3.12 shows the comparison of experimental results from the electromagnetic release mechanism with the ALE and SPH formulation. Observe that the peak acceleration decreases linearly with the successive decrease in the height of drop and the peak acceleration is reduced due to the increase in the weight of WLO. Importantly, there is good comparison of the experimental results with both the numerical simulations.

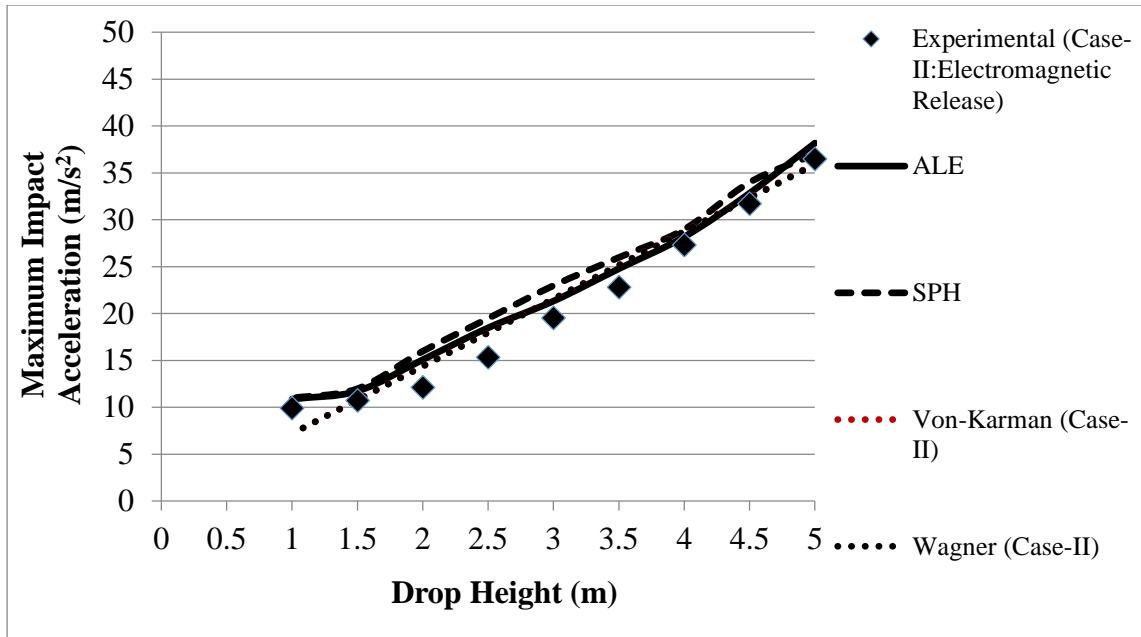


Figure 3.12: Comparison of results for maximum acceleration with ALE and SPH [Weight of WLO = 3.5kg (Case-II: Electromagnetic release)] (Vertical Entry/Entry Angle=0 deg)

The plot of accelerations obtained analytically vs. drop height for the WLO model (using the original radius of the WLO) is also shown in Figure 3.12. The plot also depicts that the values of maximum impact accelerations (obtained analytically) are almost similar for both von Karman and Wagner solutions.

Mesh refinement studies --- To investigate convergence of the numerical solution, a mesh refinement study of the numerical models with a rigid body at a zero-degree pitch angle using different mesh sizes for the impact interaction region, are analyzed (Figure 3.13). Mesh sizes coarser than 100mm near the impact zone not only fail to provide sufficient coupling between the rigid body and the air/water domains but also fails to model the water splash-up very accurately. Figure 3.13 shows that with a very fine mesh sizes the maximum acceleration values converge, hence, providing confidence in the methodology adopted to

simulate the complex event. The values of maximum impact acceleration with variation in the number of SPH particles are shown in Figure 3.14. Both figures show that with a finer mesh size the solution for maximum impact acceleration seems to converge but the mesh should be not be too fine to increase the computational time unnecessarily.

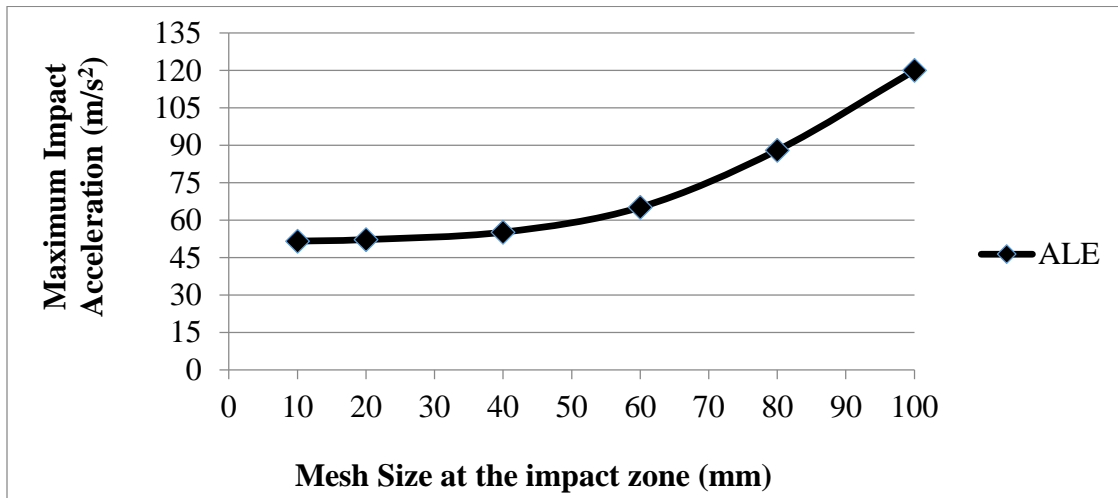


Figure 3.13: Mesh size variation vs. Maximum impact acceleration

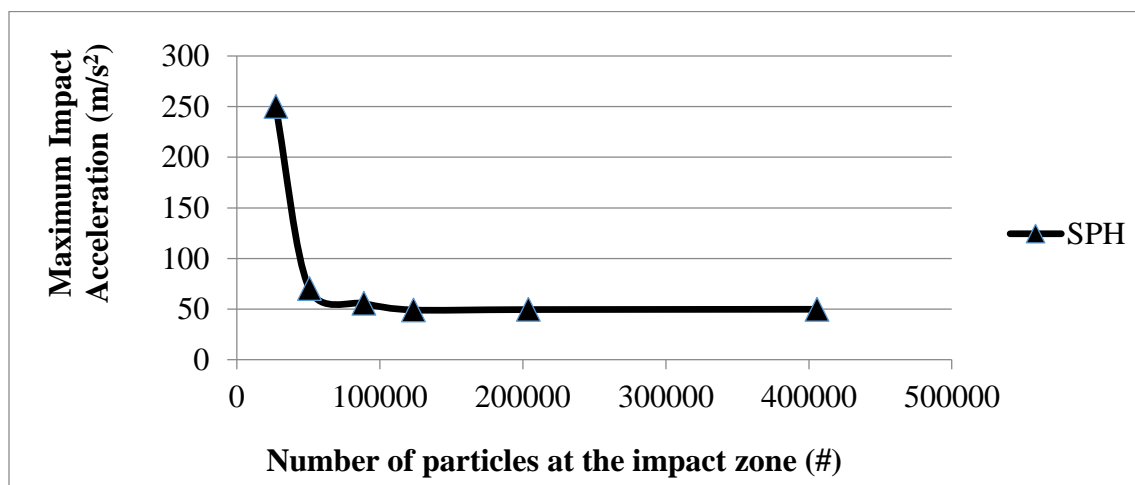


Figure 3.14: Number of particles (SPH nodes) vs. Maximum impact acceleration

3.7 Performance studies of ALE and SPH

Solving practical engineering analysis problems often requires use of large-scale numerical models (which can have several thousands or millions of nodes and elements) and access to the high-performance computing (HPC) platforms to achieve reasonable accuracy. Advanced numerical codes like ALE and SPH need such HPC platforms combined with a definitive model size to solve real time 3-D FSI problems. Model size plays a pivotal role in not only capturing the physics of the problem but also determines the computational effort needed to reach the full termination time.

In the present case, the code used is an MPP version, i.e., it works on multiple processors. This capability enables us to take full advantage of High Performance Computing (HPC) platforms to model larger domains using fine discretization. A Dell Precision WorkStation 690 with eight nodes (two processor socket quad core), Intel Xeon 3 GHz, 64GB RAM and loaded with 64 bit Redhat Linux Enterprise 5 is dedicated as a testbed. This is an example of a shared memory type of computing systems. The platform used is Linux RHEL 5.4 with OS Level of MPICH 1.2.6 Xeon64. Compiler is Intel Fortran 10.1 with a Double Precision (I8R8).

In addition to the model size, the run times also plays a significant role in determining the choice of the numerical code. This inherently provides the end users and scientists to proceed with a balanced approach in making a choice in terms of the available hardware, optimum model size and the accuracy in obtaining satisfactory test results.

The performance of ALE and SPH model tests were studied for the typical case of a vertical impact of the WLO. The ALE test case had 732,552 nodes and 714,180 elements whereas the SPH case had 1,23,570 particles/nodes. The model was run on the OSU HPC platform

on various nodes and the estimated clock time was recorded for each run. Table 6 shows the execution time taken to execute the jobs on a single cluster by varying the number of CPUs. It also reports the speedup scale factors [which is the ratio of clock time using a single processor divided by the clock time using multiple processors ($=N_1/N_p$)]. The ratio of execution time for both ALE and SPH are also shown in the performance Table 3.5.

Figure 3.15 graphically illustrate the performance using even number of processors (for two difference numerical methods). Figure 3.16 graphically demonstrates the ratios of the execution times for both ALE and SPH using number of CPUs. All these figures indicate that as the number of CPUs increases there is a significant reduction in the estimated clock time. The performance studies also reveal that the number of nodes used in the ALE tests is approximately seven times the number of nodes used in the SPH tests, but the ALE formulation is slightly faster than the SPH method. This is due to a very fine ALE mesh size for both the air and water domain. As evident from these figures, the user is now equipped with interesting design choices with the number of processors to achieve an optimal clock time for a given model.

Ideally it is desirable to have linear speedup with respect to the number of processors used to run the model. However, Figure 3.17 shows the (speedup) scaling performance of ALE and SPH with increasing number of nodes. Note that scaling performance is far below linear and that they both show a similar trend. Hence, there is little gain in using more than 10 processors for either of the numerical models.

Table 3.5: Performance study for the ALE and SPH test models

ALE test model: Number of time steps = 33,246 SPH test model: Number of time steps = 75,098					
Number of processors (ncpu)	ALE execution time (seconds)	ALE-Speedup (N_1/N_p)	SPH execution time (seconds)	SPH-Speedup (N_1/N_p)	SPH/ALE clock-time ratios
1	73440	1	229132	1	3.12
2	51718	1.42	160325	1.45	3.10
4	48315	1.52	146394	1.65	3.03
6	43200	1.70	133056	1.76	3.08
8	31930	2.30	101218	2.20	3.17
10	30347	2.42	97413	2.25	3.21

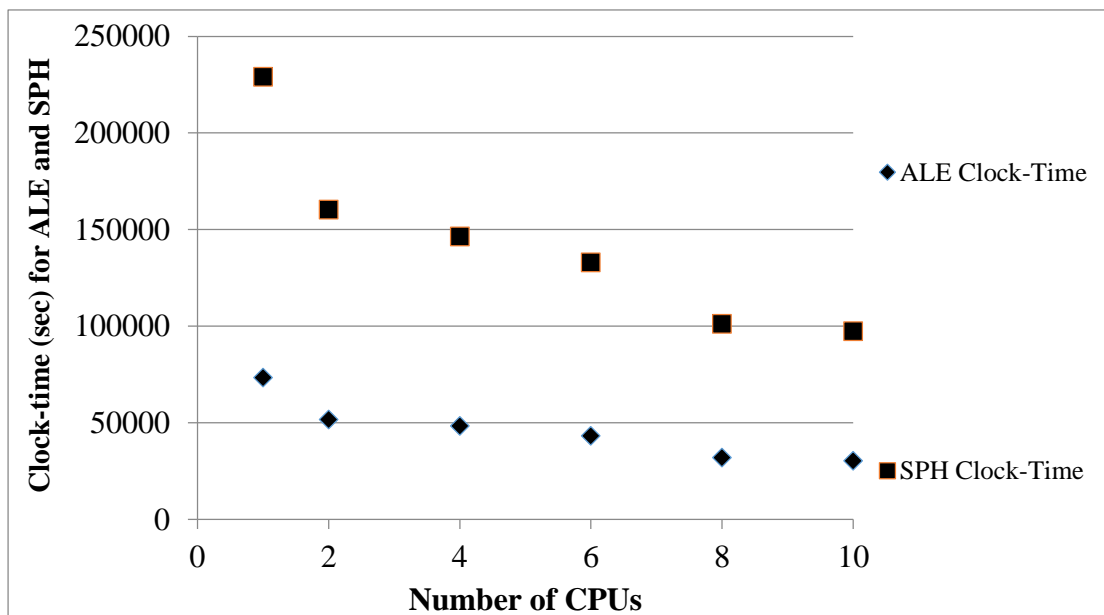


Figure 3.15: Number of CPUs vs. estimated clock time for ALE and SPH test models

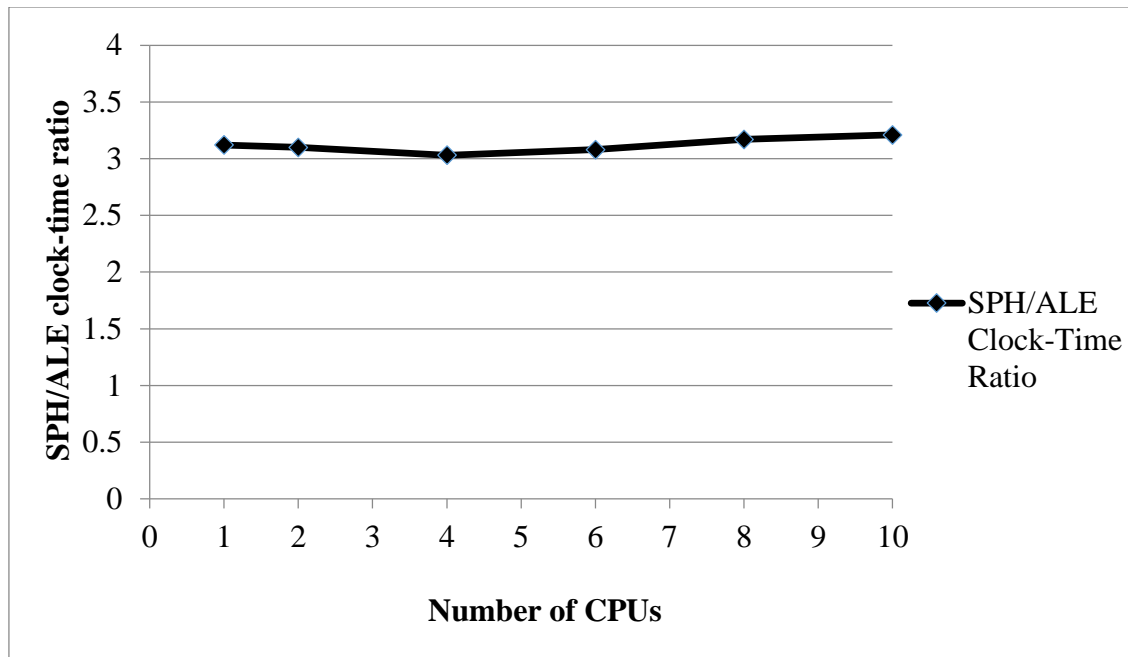


Figure 3.16: Clock-time ratios of SPH/ALE vs the number of CPUs

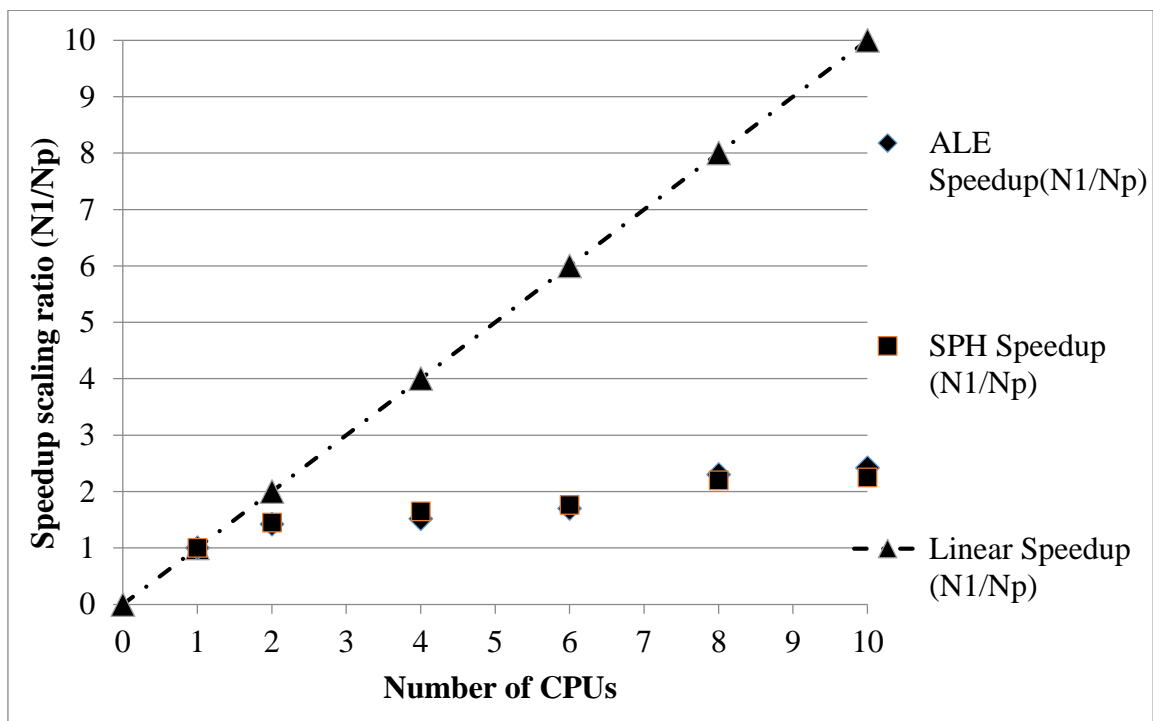


Figure 3.17: Speed scaling of the performance of ALE and SPH (N_1/N_p)

3.8 Discussion and comparison

The study of hydrodynamic impact between a body in motion and a water free-surface finds variety of applications in the aerospace and ocean engineering fields. The analytical approaches put forth by von Karman, Wagner and others provide us with the beginnings for a complete solution of the impact phenomena through use of numerical techniques such as finite elements. The effects of varying the vertical velocity, entry angle and the WLO weight were identified and the numerical results obtained from these tests help us understand and establish conditions that must be avoided during the water impact. For instance, if a crew member onboard the WLO cannot withstand impact accelerations over $5g$, these results will give a glimpse of the initial conditions which will keep the peak impact accelerations under the specified limits.

The application of multi-material Eulerian formulation and a penalty based Lagrangian-Eulerian coupling algorithm combined with a proper working model for both air and water is shown to capture the water landing well. The current work, simulating the complex impact event, using ALE and SPH techniques, demonstrates some of the problems encountered when modeling air and water. The robust contact-impact algorithm of the current FE code simulated the behavior of water for a very short duration of time and the initial period was sufficiently long to establish the trends occurring under a wide range of conditions.

Fluid properties of air and water are defined by the bulk modulus that gives relation between the change of volume and pressure. Reducing the speed of sound in water in the input to the order of about 10 times the celerity of wave, causes a significant reduction in

the bulk modulus, thereby resulting in faster execution time as the time step becomes bigger. Because the focus of the wave impact behavior is gravity dominated and not sound propagation sensitive. This technique provides a faster solution without sacrificing accuracy.

The acceleration values obtained from the simulation results compared well with experimental values. Mesh refinement studies for both the numerical methods showed that maximum impact accelerations converge for a very fine mesh size and are adequate for a good comparative analysis. Importantly, there is a good comparison between the experimental and the ALE and SPH results for maximum impact accelerations for all the three cases of varying the vertical velocity, entry angle and the weight of the object.

The application of multi material ALE technique and a penalty based coupling algorithm (used for large deformation of water at the free surface upon impact) currently can be properly analyzed only at the cost of high computational time. Use of the SPH method is notably less complicated in generating the model due to the absence of mesh and the ease with which it can successfully model the large deformation problems involving the water domain. The main advantage of using SPH is that it can capture the post impact dynamics (buoyancy effect) more graphically. However, the computational effort required of the SPH method is significantly higher than that of ALE (for multi-phase SPH domains) [16,22 and 27].

An attempt was made to measure the pressure distribution and the structural deformation coming onto the WLO by treating it as a flexible body, to compare both ALE and SPH codes, but it was discarded due to the high computational time and expense. However, the maximum impact pressure that the WLO is subjected to upon touchdown with the water

surface is calculated using an FSI sensor (at the bottom of the WLO) using both the numerical methods.

The WLO was assumed as rigid for convenience of comparison of the numerical results with closed form solutions for maximum accelerations predicted by the classical von Karman and Wagner. In order to emphasize the importance of the analytical estimates, the accelerations obtained analytically were plotted against the drop height for the WLO model (using the original radius of the WLO). In order to achieve accelerations comparable to the closed-form solutions, the analytical results show that, for the design of a WLO, the Wagner approach provides a reasonably correct estimate of the equivalent radius of the WLO.

3.9 Concluding remarks

A preliminary study of simulating the water landing of a conceptual Water Landing Object with an explicit numerical code is presented. The non-linear transient dynamic code with its finite-element ALE and SPH capability for analyzing large deformation structural and fluid dynamic applications is used to model the scaled down experiments. The present work is the first of its kind in testing a scaled-down model of WLO impacting ocean waters for the Indian Space Mission. An important aspect in evaluating the predictive capability of the FE-ALE and SPH is the accuracy and reliability of the numerical simulation results in determining the impact accelerations.

A constrained Lagrange interface/contact is shown to successfully capture impact phenomenon between the object and the water target. The effects of varying the vertical velocity, entry angle and the WLO weight are identified and the numerical predictions are

first validated with experimental data for maximum impact accelerations. The maximum acceleration upon impact is about 5.5g for a 0-degree pitch angle (vertical velocity tests) and 4.5g for a 15-degree pitch test (pitch tests). Analyses were performed for the rigid object entering the water with different weights. The weight of 3.5kg corresponds to the experimental Case-II involving an electromagnetic drop mechanism. The general trend shows advantage gained in reduced g-force for a large increase in weight (3.8g for Case-II compared to 5.5g for Case-I). This indicates that the analyses performed can produce satisfactory results to use in design studies.

An important feature in simulating contact and impact problems is proper modeling of the two-phase flow with the actual modeling of the air with associated density and state equation. Previous studies in simulations of impact events in the absence of air domain resulted in very high impact accelerations with a very high frequency content, which requires filtering when compared to experimental results. In addition to the modeling of the actual air domain, another important aspect that is usually ignored in simulating such complex FSI impact event is the positioning of the rigid body with respect to the water surface. A comprehensive study using both the “realizations” facilitates the capturing of the physics of the impact event accurately and provides data sets that are comparable to experimental test cases.

Tasks performed in this study also include the comparison of the numerical solutions with analytical solutions for the rigid object and understanding the filtering techniques needed to predict the correct maximum impact accelerations. These predictions suggest that the fully coupled FSI models can capture the water-impact response accurately for all range of

drop tests and there is a good comparison between the simulations and the experimental results.

Several observations can be made. Model testing is needed over a wider range of conditions to include improved tests that vary the speed, weight and entry angle and under realistic conditions existing in the oceans. Modeling of the rigid body impact problem used for correlation with the experimental results, demonstrates some of the challenging problems encountered when modeling the air and water domains.

The possibility of combining the finite element package with a computational fluid dynamics package could more accurately simulate the hydrodynamics during impact. Further levels of complexity can be introduced to the model as well as scrutinizing the results further. Future work may include more in-depth analysis of the WLO water impact pressure distribution, fully deformable vehicles and floatation studies. The development of a more accurate numerical solution to capture the nonlinear nature of the FSI problem should be pursued by employing robust modeling of the basic physics of water impact. Finally, full-scale prototype testing is needed over a wider range of conditions to include cases with varying speed, weight and entry angle under realistic conditions existing in the oceans.

3.10 Acknowledgements

Financial support from the US Office of Naval Research Grants N0014-11-1-0094 and N00014-13-1-0849, and the Department of Energy Grant DE-FG36-08GO18179-M001 for the first and second authors are gratefully acknowledged.

3.11 References

- [1] Von Karman, T., 1929. "The impact of seaplane floats during landing," NACA TN 321, National Advisory Committee for Aeronautics, Washington, USA.
- [2] Wagner, H., 1932. "Trans. Phenomena associated with impacts and sliding on liquid surfaces," *Journal of Mathematics and Mechanics*, **12**(4), pp. 193-215.
- [3] Miloh, T., 1991. "On the initial-stage slamming of a rigid sphere in a vertical water entry," *Applied Ocean Research*, **13**(1), pp. 43-48.
- [4] Brooks, J. R., and Anderson, L. A., 1994. "Dynamics of a space module impacting water," *Journal of Spacecraft and Rockets*, **31**(3), 509-515.
- [5] Zhao, R., Faltinsen, O. M., Aarsnes, J. V., 1996, "Water entry of arbitrary two-dimensional sections with and without flow separation," *Proceedings of the 21st Symposium on Naval Hydrodynamics*, pp. 408–23, Washington, D.C.: National Academy Press.
- [6] Faltinsen, O. M., 1999, "Water entry of a wedge by hydroelastic orthotropic plate theory," *Journal of Ship Research*, **43**(3), 180–193. DOI 0022-4502/99/4303-0180\$00.53/0
- [7] Scolan, Y. M., and Korobkin, A. A., 2001. "Three-dimensional theory of water impact. Part 1. Inverse Wagner problem," *Journal of Fluid Mechanics*, 440, pp. 293-326.
- [8] Souli, M., Olovsson, L., and Do, I. 2002. "ALE and Fluid-Structure Interaction Capabilities in LS-DYNA," 7th International LS-DYNA Users Conference.
- [9] Korobkin, A. A., and Scolan, Y. M., 2006. "Three-dimensional theory of water impact. Part 2. Linearized Wagner problem," *Journal of Fluid Mechanics*, 549, pp. 343-373.

- [10] Tutt, B. A., and Taylor, A. P., 2004. "The use of LS-DYNA to simulate the water landing characteristics of space vehicles," 8th International LS-DYNA Users Conference, May 2-4, Dearborn, Michigan, USA.
- [11] Melis, E. M., and Bui, K., 2002. "Characterization of water impact splashdown event of space shuttle solid rocket booster using LS-DYNA," 7th International LS-DYNA Users Conference, May 19-21, Dearborn, Michigan, USA.
- [12] Korobkin, A.A., 2005, "Three-Dimensional Nonlinear Theory of Water Impact," *Proc. 18th International Congress of Mechanical Engineering (COBEM)*. Ouro Preto, Minas Gerais, Brazil.
- [13] Seddon, C. M., and Moatamedi, M., 2006. "Review of water entry with applications to aerospace structures," *International Journal of Impact Engineering*, 32, pp. 1045-1067.
- [14] Wang, J. T., and Lyle, K. H., 2007. "Simulating space capsule water landing with explicit finite element method," 48th AIAA/ASME Conference, April, pp. 23-26, Waikiki, HI, USA.
- [15] Jackson, K. E., and Fuchs, Y. T., 2008 "Comparison of ALE and SPH simulations of vertical drop tests of a composite fuselage section into water," *Proceedings of the 10th International LS-DYNA Users Conference*, Dearborn, MI, June 8-10.
- [16] Vandamme, J., Zou, Q., and Reeve, D. E. 2011. "Modeling floating object entry and exit using Smoothed Particle Hydrodynamics," *Journal of Waterway, Port, Coastal, and Ocean Engineering*, **137**(5), 213-224.
- [17] Challa, R., Yim, S. C., Idichandy, V. G., and Vendhan, C. P., 2014. "Rigid-Body Water-Surface Impact Dynamics: Experiment and Semi-Analytical Approximation,"

- Journal of Offshore Mechanics and Arctic Engineering, 136, pp. 011102, 1-10.
- [18] Scolan, Y.M., and Korobkin, A.A. 2012. "Hydrodynamic impact (Wagner) problem and Galin's theorem," Proceedings of the 27th International Workshop on Water Waves and Floating Bodies, Copenhagen, Denmark.
- [19] Belytschko, T., Flanagan, D. F., and Kennedy, J. M., 1982. "Finite element method with user-controlled meshes for fluid-structure interactions," Journal of Computer Methods in Applied Mechanics and Engineering, 33, pp. 689–723.
- [20] Hallquist, J. O., 1998. "LS-DYNA Theoretical Manual," Livermore Software Technology Corporation.
- [21] Souli, M., and Benson, D.J. 2010. "Arbitrary Lagrangian-Eulerian and fluid-structure interaction – Numerical Simulation." Wiley publications, USA.
- [22] Dalrymple, R.A., and Rogers, B. D., 2006. "Numerical modeling of water waves with the SPH method," Coastal Engineering Journal, **53**(2-3), pp. 141-147.
- [23] Faltinsen, O.M., 2005. "Hydrodynamics of high-speed marine vehicles," Cambridge University Press.
- [24] Hirano, Y., and Miura, K., 1970. "Water impact accelerations of axially symmetric bodies," Journal of Spacecraft and Rockets, **7**(6), pp. 762-764.
- [25] Gingold, R.A., and Monaghan, J.J., 1977. "Smoothed particle hydrodynamics: Theory and application to nonspherical stars," Monthly Notices of the Royal Astronomical Society, 181, pp. 375–389.
- [26] Lucy, L., 1977. "A numerical approach to testing of the fusion process," The Astronomical Journal, 88, pp. 1013-1024.
- [27] Herault, A., Vicari, A., Negro, C., and Dalrymple, R. A., 2009. "Modeling water

waves in the surf zone with GPU-SPHysics,” 4th International SPHERIC Workshop.

Numerical Modeling of Fluid Sloshing Including Air Compressibility Effect

Ravi Challa and Solomon C. Yim, F.ASCE

To be submitted

4 NUMERICAL MODELING OF FLUID SLOSHING INCLUDING AIR COMPRESSIBILITY EFFECT

4.1 Abstract

The contact and impact pressure in the case of fluid sloshing is investigated numerically for a forced rolling motion. A finite element (FE) based arbitrary Lagrangian-Eulerian (ALE) formulation is used to analyze the sloshing phenomena. Numerical simulation results are validated by comparing the pressure field data obtained from experiments. The predictive capability of the ALE-FE formulation in modeling a multi-physics problem in terms of the dynamics of the flow is validated for two different fluid fill conditions. Numerical simulation results for maximum impact pressure show good comparison with both experimental test cases. Given the complex nature of the gas/fluid phenomenon, the ambient air is often ignored in many numerical simulations in the literature. In this study, it is found that, for the low-filled condition, the effect of the presence of air has practically negligible influence on the pressure field (thus validating the “neglecting air” assumption). For the high-filled condition, numerical results also match well with experimental data, but only for those cases when the effect of air is included. In fact, a detailed sensitivity analysis for this high-filled condition shows that the pressure field is highly sensitive to the compressibility of air. Numerical simulations neglecting the presence of air consistently under-predict the maximum impact pressures by several orders of magnitude.

Keywords: Fluid, air, sloshing phenomena, pressure field, compressibility, ALE-FE

4.2 Introduction

Situations involving liquid impact on solid surfaces represent a class of mechanics that has broad practical applications. As the demand for natural gas grows, there is an increasing interest in floating production, storage, and off-loading systems for offshore oil and gas developments as transport tankers filled with liquefied natural gas (LNG). With the growth in ship size and the treacherous weather conditions in which these tanks have to maneuver there is a need for operating with less restricted filling levels than under current standard practice (Faltinsen et al. 2000). Consequently, one of the main concerns in the design of LNG tanks is the accurate prediction of impact loads caused by violent sloshing for the design of these tanks to ensure structural integrity. Experimental investigations have been conducted to study the sloshing loads due to the impact wave on walls (Berg 1987; Pastoor et al. 2005). However, available literature describing these test cases is scarce due to commercial proprietary restrictions. Difficulties in scaling of the experimental impact pressures has been extensively reported (Bass 1985; Berg 1987). The complex relation between impact pressures due to the collision of a breaking wave with a wall and its sensitivity to the shape of the wave surface profile was first studied by Bagnold (1939). Apparently for identical waves the pressure records show great variability (Peregrine 1983 and 2003). For breaking waves of various types, the highest impact pressures occur when the air bubble trapped between the wall and the wave face is the smallest (Hattori et al. 1994). For a low-filled condition, experimental and numerical showed that the liquid turbulence, viscosity, compressibility, and the liquid–gas density ratio are not significant parameters for the dimensionless impact pressure, while the wall flexibility, the gas cushioning, and the ullage pressure under a critical level are parameters significantly

affecting the impact phenomenon (Bass et al. 1985; Pastoor et al. 2005; Lee et al. 2007). Flow in a sloshing tank interacting with an elastic body was investigated by experimental and SPH numerical simulation results (Souto-Iglesias et al. 2008). The fluid used in their experiment was a vegetable oil with a viscosity fifty times that of water. Sinusoidal oscillation was prescribed to the tank. The amplitude and period of the motion along with the local displacements at the tip of the elastic body were examined and compared to the numerical simulations. Delorme et al. (2009) investigated experimentally and numerically the impact pressure in (non-pressurized) shallow water sloshing for forced rolling motions. Experimental results were compared with numerical ones obtained using a smoothed particle hydrodynamics (SPH) method. They developed new methods of calculating the pressures on the walls with the SPH method.

Most practical applications of liquid impact on solid surfaces occur in the presence of a vapor or gas (Yung et al. 2010). This multiphase physics is complex, and the ambient vapor is shown to have a major influence on the maximum impact pressure. Yung et al. (2010) found that the ambient vapor is a critical component in analyzing this class of challenging multi-phase problems and their experimental data illustrates that ambient vapor/liquid properties and their interaction during an impact event can alter maximum pressures by as much as two orders of magnitude. They proposed a dimensionless “interaction index” based on an analysis of the experimental results. The postulated index is a function of the ambient vapor and liquid properties that accounts for their effects on the resulting pressure time history. The experimental results show that the interaction index performs remarkably well in physical tests over a broad range of vapor properties.

Aquelet et al. (2003) developed a finite element based ALE formulation to solve a fuel sloshing problem. They explained the analysis capabilities of the ALE by presenting a detailed formulation procedure and validated their numerical results against theoretical using potential flow for calculating the sloshing frequencies. Lee et al. (2007) developed a numerical solver based on the finite volume method with a volume of fluid (VOF) free-surface tracking technique. Experimental and 2-D ALE numerical study on a low-filled sloshing problem was conducted by Lee et al. (2010). They studied the sloshing problem as a multi-physics problem with both the air and water phases. They carried out numerical simulation for a partially filled 2-D tanks subjected to a harmonic sway motions with various water depths and frequencies and compared them to experimental data.

In this study an ALE-FE numerical method was used to simulate the multi-phase sloshing problem in a section of one of the tanks of an LNG vessel in operation, for which results from a series of experimental test cases are available. The experimental tests corresponding to a low-filling level condition for which traveling and breaking waves were found at the resonance condition (Delorme et al. 2009). A description of the numerical model and the ALE governing equations are presented first. It is followed by a brief description of the experimental sloshing setup. Importantly, details of the numerical simulations in terms of an ALE-FE methodology are shown with emphasis on modeling techniques. Subsequently, a qualitative and quantitative comparison of the physics of fluid sloshing between experimental test data and numerical results is presented. The main objective of this work is to estimate and compare the maximum impact pressure on the sloshing tank with experimental test data with careful examination of the physics of the wave breaking and impact process. Finally, a sensitivity study on the effect of air compressibility on the

estimation of maximum impact pressure for different fluid-filled sloshing conditions is presented.

4.3 Governing field equations: Arbitrary Lagrangian-Eulerian (ALE) formulation

This work utilizes an ALE formulation to model the air and water domains (Eulerian) whereas the rigid LNG tank (Lagrangian) is modeled using the standard finite element formulation. Coupling between the Eulerian set and the Lagrangian domain is performed using a contact-impact algorithm. The compressible Navier-Stokes equations in ALE form are solved over the entire computational domain. In the ALE description, an arbitrary referential coordinate is introduced in addition to the Lagrangian and ALE coordinates (Aquelet et al. (2003), Donea et al. (2004); Souli and Benson (2010)). The material time derivative of a variable with respect to the reference coordinate can be described as

$$\frac{dg(\bar{X}, t)}{dt} = \frac{\partial g(\bar{x}, t)}{\partial t} + (\bar{v} - \bar{w}) \cdot \overline{grad}g(\bar{x}, t) \quad (1)$$

where \bar{X} is the Lagrangian coordinate, \bar{x} the ALE coordinate, \bar{v} is the particle velocity, and \bar{w} the grid velocity of the numerical simulation. The ALE differential form of the conservation equations for mass, momentum, and energy are readily obtained from the corresponding Eulerian forms:

$$\text{Mass: } \rho \frac{\partial \rho}{\partial t} + \rho \text{div}(\bar{v}) + (\bar{v} - \bar{w}) \cdot \overline{grad}(\rho) = 0 \quad (2)$$

$$\text{Momentum: } \rho \frac{\partial \bar{v}}{\partial t} + \rho (\bar{v} - \bar{w}) \cdot \overline{grad}(\bar{v}) = \overline{div}(\overline{\sigma}) + \bar{f} \quad (3)$$

$$\text{Energy: } \rho \frac{\partial e}{\partial t} + \rho (\bar{v} - \bar{w}) \cdot \overline{grad}(e) = \overline{\sigma} : \overline{grad}(\bar{v}) + \bar{f} \cdot \bar{v} \quad (4)$$

where ρ is the mass density, \vec{f} is body force vector (per unit volume), and e is the total energy. $\overline{\overline{\sigma}}$ denotes the total Cauchy stress given by:

$$\overline{\overline{\sigma}} = -p\overline{\overline{I}} + \mu(\overline{\overline{grad(\vec{v})}} + \overline{\overline{grad(\vec{v})}}^T) - 2/3\overline{\overline{grad \cdot \vec{v}}}\overline{\overline{I}} \quad (5)$$

where p is the pressure, $\overline{\overline{I}}$ is the identity tensor, μ is the dynamic viscosity, and $(\vec{v} - \vec{w})$ is the convective velocity across the grid.

4.4 Experimental set-up: Pressure field in forced roll motion

The case studied here is a longitudinal section of a tank of one of the LNG membrane tankers built in the Puerto Real Shipyard of Navantia, at a scale of 1:50. Model dimensions are 90x58x5cm and the water depth is $d = 9.3\text{cm}$ ($d/B \approx 0.1$, where B is the width of the tank) (Delorme 2009). The tank is excited with a sinusoidal rotational motion with amplitude $\theta_{\max} = 4^\circ$ about the mid-point of the tank bottom and with different excitation frequencies. The initial free surface is horizontal. When the motion starts, the rotational amplitude was ramped up linearly such that the tank acquires a sinusoidal motion after one cycle of oscillation. The oscillation angle is registered with an encoder placed on the rotation axis. A flush mount pressure sensor is placed on the tank wall at the initial height of the free surface, on the left side on the tank wall. The sensor sampling frequency is set to 2,400Hz with a low pass filter cut-off frequency of 400Hz (Delorme 2009).

For of a simplest case of two-dimensional sloshing in a planar rectangular tank with finite depth, multidimensional modal analysis of nonlinear sloshing is given by Faltinsen et al. (2000) and importantly, exact analytical solutions to compute the natural modes and frequencies of sloshing and are given in Faltinsen and Timokha (2009). Fluid in the tank

is treated as incompressible which means that the velocity potential ϕ exists for the fluid. As we are looking for time-periodic solutions with circular frequency σ_i and time period T_i , the spectral boundary problem can be analyzed by solving the Laplace equation with a variable separable method with appropriate kinematic and dynamic boundary conditions. As a consequence, the Eigen frequencies and corresponding eigen modes are nontrivial solutions for these class of problems. Figure 4.1 shows the two-dimensional rectangular tank with the mean water level.

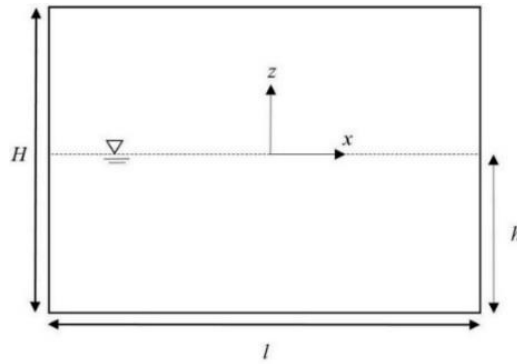


Figure 4.1: Two-dimensional rectangular tank with mean water level

The natural sloshing frequencies and periods are given as:

$$\left. \begin{aligned} \sigma_i &= \sqrt{g \frac{\pi i}{l} \tanh\left(\frac{\pi i}{l} h\right)}; \\ T_i &= \frac{2\pi}{\sqrt{g \pi i \tanh(\pi i h / l) / l}}, \quad i = 1, 2, \dots \end{aligned} \right\} \quad (6)$$

where l and h are the length and quiescent water depth as shown in Figure 4.1. For the rectangular tank dimensions mentioned above, eqn. (6) gives the corresponding fundamental sloshing period as $T_{i=1} = 1.92s$ (defined as T_0 in Delorme et al. 2009). Three different excitation periods (T) have been studied, one being the first sloshing period (T_0),

one case with a smaller period, and a third one with a larger period. The following notation has been used in the paper.

- Case A: $T/T_0 = 1.1$
- Case B: $T/T_0 = 1.0$
- Case C: $T/T_0 = 0.9$

Note that case B is for a resonance condition. These cases are representative of the different impact scenarios that can be found for this filling level, as will be discussed later.

4.5 Numerical modeling and simulations

The fully coupled FSI problem is discretized using the ALE-FE technique where both the air and water domains are modeled using solid brick elements (ALE formulation for the fluid domain and FE for the structure). The only solid part in the computational domain is the LNG tank and is modeled as rigid finite elements. A numerical solver for nonlinear dynamic analysis of structures in three dimensions (3D), LS-DYNA¹ (Hallquist 2006), is used in the current study. Figure 4.2 shows the initial configuration for the ALE-FE simulation. Sloshing of water in the tank is studied as a two-dimensional phenomenon, consistent to the physical experiment. Numerical results are compared with experimentally measured pressure response to sinusoidal excitation.

¹ Version: mpp971d R7.0.0 and Revision: 79055

An important feature in simulating contact and impact problems is proper modeling of the air-water interaction (Challa et al. 2014). In order to capture the physics accurately and reduce the often unrealistic high impact pressures, in this study actual air modeling is incorporated with a governing equation of state. Lee et al. (2010) though study sloshing a multi-physics problem do not show comparative results without air.

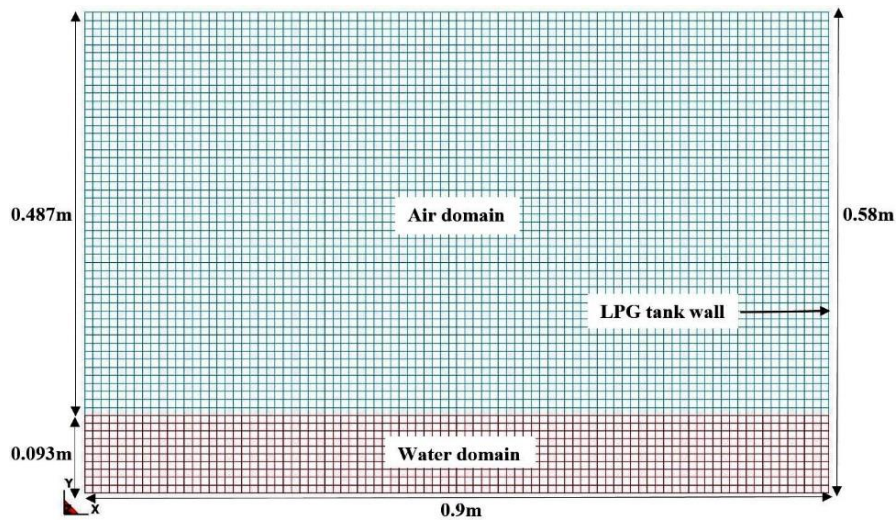


Figure 4.2: ALE-FE simulation: Computational domain of LNG tank/air/water domains

For the FSI problem considered, the structural response involves the impact of fluid(s) on a rigid body (LNG tank) due to the rolling motion of the tank (but not the motion of the tank itself). The contact interaction event now involves more than just the normal surface face of the inner tank walls. The influence of the sliding contact along the inner tank wall surfaces, as the fluid slides along the walls affects the impact pressures coming on the tank significantly. As a proper coupling of the contact interaction between the fluid domains and the tank is essential, the importance of the selection of simulation parameters also becomes important. The FSI model involves three components: water domain, air domain and the LNG tank. Figure 2 shows that the air domain is created on top of the water domain

to capture the air behavior and the air-water interface (characterized by the water free surface). The air-water mesh is modeled as a rectangular mesh (mesh size of 10mm grid, see Figure 4.2). There are 33,306 nodes, 27,000 solid elements with two solid parts of which there are 1500 rigid shell elements and 27000 deformable elements (air and water ALE three-dimensional solid elements).

A fluid material with an equation of state is used to model the water and air domains with a mass density of 1000 kg/m^3 and 1.29 Kg/m^3 , respectively. The LNG tank elements are given a rigid body definition with a mass density of 7850 kg/m^3 , Young's modulus of $2.0E+11 \text{ N/m}^2$ and Poisson's ratio of 0.3. In the numerical computation of the coupled fluid-rigid body interaction, the code uses a penalty function method to determine the location of the common contact surface between the fluid and the rigid body that requires the input of artificial values of Young's modulus and Poisson's ratio of the rigid body to compute the penalty function spring stiffness for intermediate iterations (Challa et al. 2014).

The air-water domains are discretized using 8-noded solid brick elements and the LNG tank walls are discretized using 4-noded Belytschko-Lin-Tsay shell element formulation (Belytschko 1982; Hallquist 2006). This shell element formulation is used as it is computationally very efficient (Hallquist 2006). The Belytschko-Lin-Tsay shell element is based on a combined co-rotational and velocity-strain formulation. The efficiency of the element is obtained from the mathematical simplifications that result from these two kinematical assumptions. The co-rotational portion of the formulation avoids the complexities of non-linear mechanics by embedding a coordinate system in the element.

The choice of velocity-strain rate of deformation in the formulation facilitates the constitutive evaluation, since the conjugate stress is the more familiar Cauchy stress.

A penalty type coupling of interface/contact is used to model the impact event between the LNG tank and the air-water domains. This type of interface/contact is mainly used when there is a need for the Arbitrary Lagrangian and Eulerian (ALE) transformations for the impact scenario. Coupling is between a Lagrangian mesh (slave) of shells to the material points of an Eulerian mesh (master surface). In this, the moving surface of three-dimensional tank walls (Lagrangian mesh) is treated as the slave surface, and the target air-water solid mesh is treated as the master surface. Note that the penalty method is used in explicit finite element programs that consists of placing normal interface springs between all penetrating nodes and contact surface.

A slip boundary condition is imposed to the fluid flow on the rigid tank to allow the fluid to move freely along and be able to detach from the side walls and the bottom. The boundary conditions employed in the numerical model are partially the material surfaces (out-of-plane, in-plane and bending restraint). The material surfaces defined in the ALE formulation are: (a) no particles can cross them, and (b) stresses must be continuous across the surfaces.

The elements of the both the air and the water domains are given the null hydrodynamic material type that allowed a new equation of state to be specified. An equation of state with a linear polynomial form is used to define the initial thermodynamic state of the material and pressure is given by (Hallquist 2006):

$$p = C_0 + C_1\zeta + C_2\zeta^2 + C_3\zeta^3 + (C_4 + C_5\zeta + C_6\zeta^2)E \quad (7)$$

where C_{0-6} are user-defined constants, E is initial energy per initial volume, and the volumetric parameter ζ is defined as:

$$\zeta = \frac{1}{V} - 1 \quad (8)$$

where V is the relative volume given as:

$$V = \frac{\rho_0}{\rho} \quad (9)$$

with ρ_0 as the reference mass density (which might be different than the current mass density if the material experiences compression or expansion throughout the simulation).

The constant C_1 in Equation 6, when used by itself, is the elastic bulk modulus

($C_1 = \rho c_s^2$), where ρ is the mass density of the material and c_s is the sound speed in

air/water ($c_s = 1,484m/s$ for water and $c_s = 343m/s$ for air)². However, in the

computations, providing the $c_s = 148.4m/s$ constant only and setting all other constants to

zero is sufficient to define the equation of state for water as the pressure is not significantly

influenced by temperature changes for the cases considered in this study. Hence the values

of C_1 for air and water domains are $1E+05N/m^2$ and $1E+07N/m^2$, respectively. The

time step in the numerical simulation is governed by the Courant-Friedrichs-Lewy (CFL)

number which is a necessary condition for stability while solving the partial differential

² Sound speed in water plays a significant role in determining the integration time step and also the total computational time. Time step can be artificially increased for fluids without affecting the accuracy of the fluid motion computation but can significantly reduce the computational effort by allowing a significantly large time step (Lee et al. 2007). Minimum sound speed applied should be about ten times greater than the maximum expected flow speeds (Dalrymple and Rogers 2006). Sound speeds of 1,484m/s (i.e., the exact value), 148.4m/s and 14.84m/s, are used to test the computational efficiency and the predictive accuracy. Observation revealed that the numerical model diverges when the selected sound speed is 14.84m/s (100 times less than real sound speed). On the other hand, the numerical model predictions are accurate when the selected sound speed is 148.4m/s (ten times less than real sound speed). The associated computational effort using 148.4m/s sound speed is one fifth of that using the real sound speed (1,484m/s), and the maximum difference in the predictions is about 2%. Therefore, the sound speed 148.4m/s is employed in all subsequent computations in this study.

equations. For the ALE-FE simulations, as the mesh does not distort and the material advects in time, the time step size is computed by the program and for this particular problem it is $1.25E-05s$ which is constant throughout the simulation.

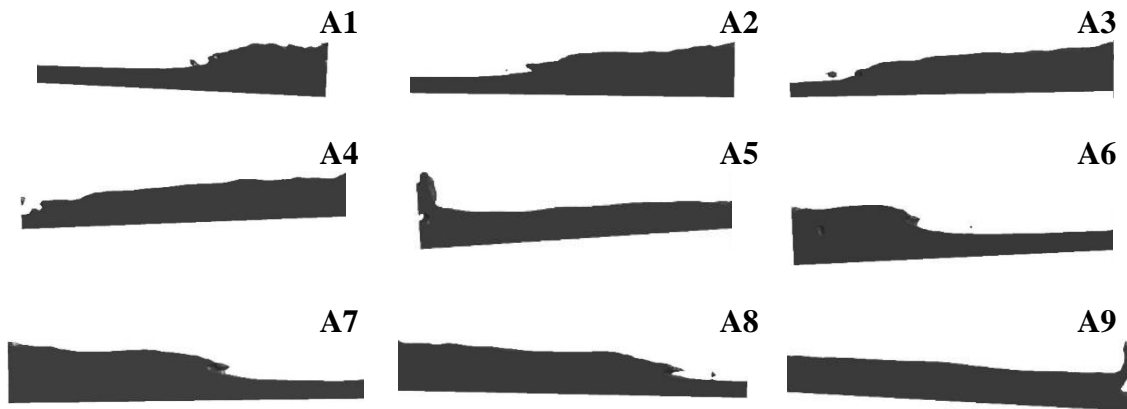
4.6 Systematic study of wave breaking and impact process

A systematic numerical study is conducted to analyze the physics of fluid sloshing process in the tank for three different excitation periods (around model resonance). First case corresponds to a larger period (above the resonance frequency: case A), second case corresponds to the first sloshing period (resonance condition: case B) and the third one correlates to the one with a smaller period (below the resonance frequency: case C). Particularly, the physics of sloshing process in the tank is analyzed for all the cases by studying the motion of the fluid in the tank for one full oscillation cycle and then by taking a closer look at the wave breaking and impact process on the tank walls itself. Results for fluid sloshing in the tank for one full oscillation cycle (Figure 4.3) and the plunge type breaking process (Figure 4.4) shown below demonstrate that the fluid motion in the tank is practically periodic. Corresponding experimental results for the first sloshing period (resonance case B) in the form of snapshots are shown in Delorme et al. (2009) (Figures 2, 3 and 4 respectively, not presented here due to copy right restriction). Though experimental results in Delorme et al. (2009) are confined to the resonance case B alone, in this paper, we show the numerical simulation results for all the cases.

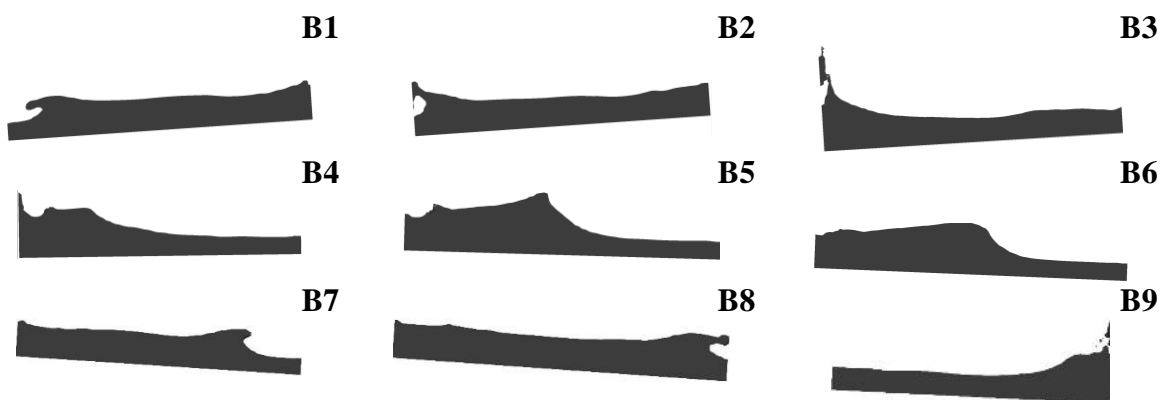
4.6.1 Fluid flow in the tank for one full oscillation cycle

Figure 4.3 shows the frames from the numerical simulations of the impact event (for one full oscillation cycle of the tank) for all the cases. Experimental results show that the complexity of the wave impact phenomena is due to the air-water mixture entrapping air bubbles around the impact zone [see Delorme et al. (2009) Fig. 3]. Comparative numerical simulation results shows that the entire sloshing process along with the fluid-free surface and the breaking process is well reproduced. Results for case A (Figure 4.3(a): Frames A1-A9)) shows that the wave breaks much earlier and farther away from the tank wall due to the slower motion of the tank. Of particular interest are the results for the resonance case B (Figure 4.3(b): Frames B1-B9). At the beginning of the oscillation cycle, frame B1 show that a wave front reaches the left end of the tank at which point a secondary wave starts to form and propagate at the right wall. The wave front at the left begins to impact the tank wall (B2). Frame B3 shows that when the tank reaches its maximum oscillation angle to the left, the wave front violently impacts the left end of the tank with high velocity, and the fluid slides up the tank wall. Subsequently, the tank starts oscillating to the right and the fluid falls down under the action of gravity and the collapsed wave starts its journey to the middle of the tank (shown in frame B4). This results in the formation of a steep wave crest (B5). The wave crest observed in frames B4 and B5 reach the right end of the tank, ready to break and create another impact event, this time on the right end of the tank wall (shown in frame B6-B9). Results for case C (Figure 4.3(c): frames C1-C9) shows that the impact event is very violent because of the faster motion of the tank. The fluid mixes with the entrapped air and the main wave breaks just before reaching the wall which then

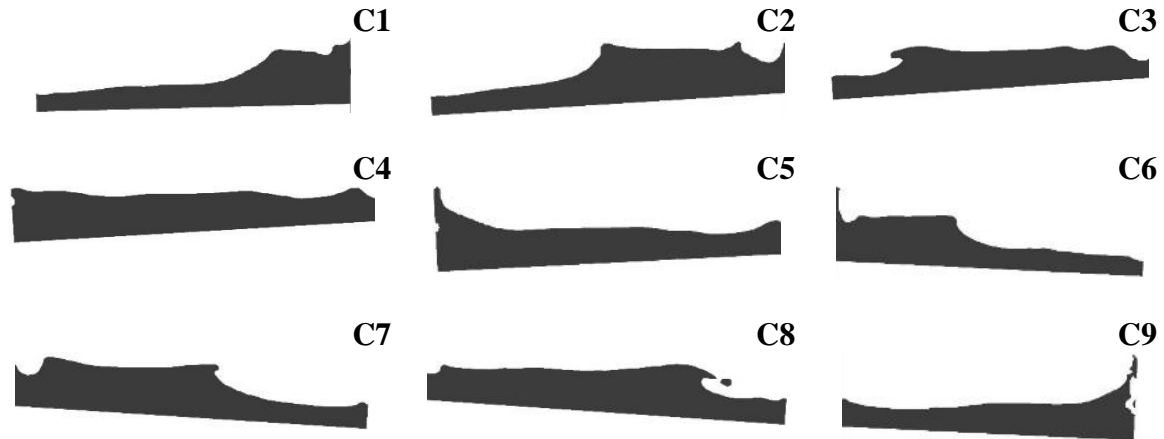
convalesces on the wave face and the consequently formed wave impacts on the tank wall directly after the tank has already started its motion in the opposite direction. For all the cases, this entire process of wave travelling from one end to the other based on the oscillation cycle of the tank is quite repetitive resulting in a periodic wave breaking and impact process.



(a) Case A: Frames A1-A9 correspond to $t/T = 5.37, 5.46, 5.51, 5.61, 5.70, 5.84, 5.97, 6.04, 6.14$



(b) Case B: Frames B1-B9 correspond to $t/T = 8.78, 8.82, 8.91, 9.03, 9.09, 9.14, 9.18, 9.24, 9.37$



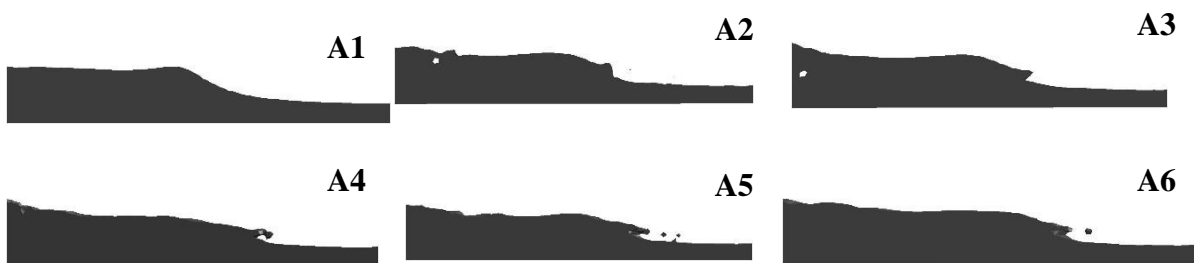
(c) Case C: Frames C1-C9 correspond to $t/T = 7.56, 7.67, 7.78, 7.84, 8.01, 8.17, 8.22, 8.28, 8.37$

Figure 4.3: ALE-FE simulation results of the impact event for one oscillation cycle.

4.6.2 Plunge-type wave breaking process

The general trend of the sloshing process in the tank for all the cases shows that the flow in the tank is composed of a main wave, traveling from one side of the tank to the other, breaking during its propagation and impacting the tank wall. The simulation results show that the free surface motion is well reproduced and the water motion in the tank is qualitatively periodic, including the breaking process. Numerical simulation results highlight the fact that it is predominantly the air-water mixture (with the entrapped air) that impacts the tank walls first for each oscillation cycle (Hattori (1994)). Numerical simulation results for cases A (Figure 4.4(a)) and C (Figure 4.4(c)) also capture the physics accurately, results for the resonance case B (Figure 4.4(b)) are interesting as the plunge-type wave breaking process occurs close to the wall and therefore discussed in detail. Numerical simulation for case A (frames A1-A6) shows that the sloshing is periodic with a plunge-type breaking occurring farther away from the tank walls than compared to case

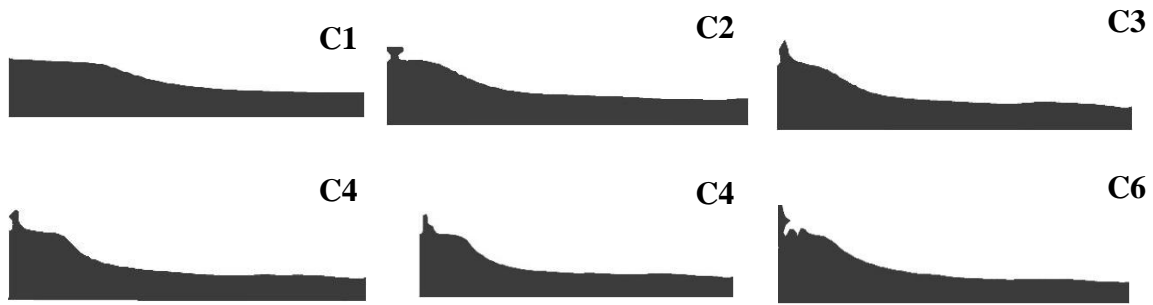
B (frames B1-B6) where the breaking and impact occurs close to the walls. Appropriately, for the resonant case B, Figure 4.4(b) shows the numerical simulation results of the wave breaking process which occurs on the interior of the free surface away from the wall boundaries. In this particular resonance case, the breaking event is a plunging breaker (entrapping air). Two water jets are formed successively: a first jet appears in the first quarter of the tank (B1), it enters into the wave face (B2) and an initial phase of a jet appears (B3). The jet grows in amplitude (B4 and B5) and then plunges and impacts the unperturbed water free surface (B6). Interestingly, in case C (frames C1-C6) as mentioned above, the wave front impacts the tank walls directly without breaking.



(a) Case A: Plunge-type breaking process



(b) Case B: Plunge-type breaking process



(c): Case C: Wave impacting the tank

Figure 4.4: ALE-FE simulation results: All frames are equally separated in time $\Delta t / T = 0.021$.

Figure 4.5 shows the numerical results of wave shape just before the first impact on the left tank wall. Experimental snapshots of the wave shape just before the first impact for all the cases is shown in Fig.3 in Delorme et al. (2009). As mentioned above, the wave breaking and impact process is different for all the three cases owing to the different speeds of the tank motion. Particularly in case A ($T / T_0 = 1.1$) the wave breaks much earlier and farther away from the tank walls with lesser energy due to the slower motion of the tank. For the resonance case B ($T / T_0 = 1.0$) the breaking event is a plunge-type breaker entrapping air and the wave front (with an air-water mixture) impacts the tank close to wall. Motion of the tank is faster in case C ($T / T_0 = 0.9$), the impact event is very violent, and it is marked by a main wave that breaks just before reaching the tank wall leading to high impact pressures.

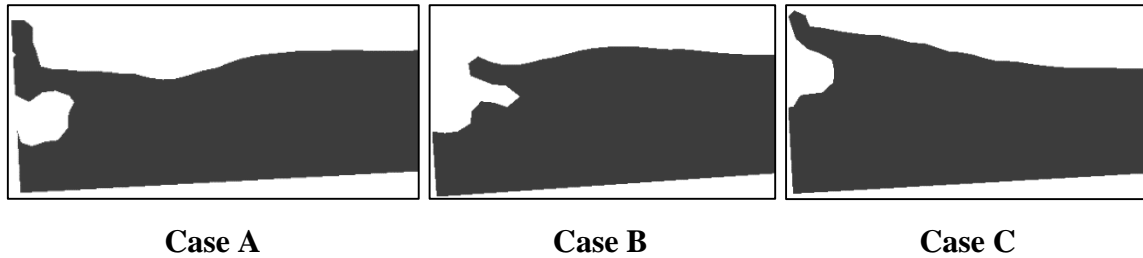


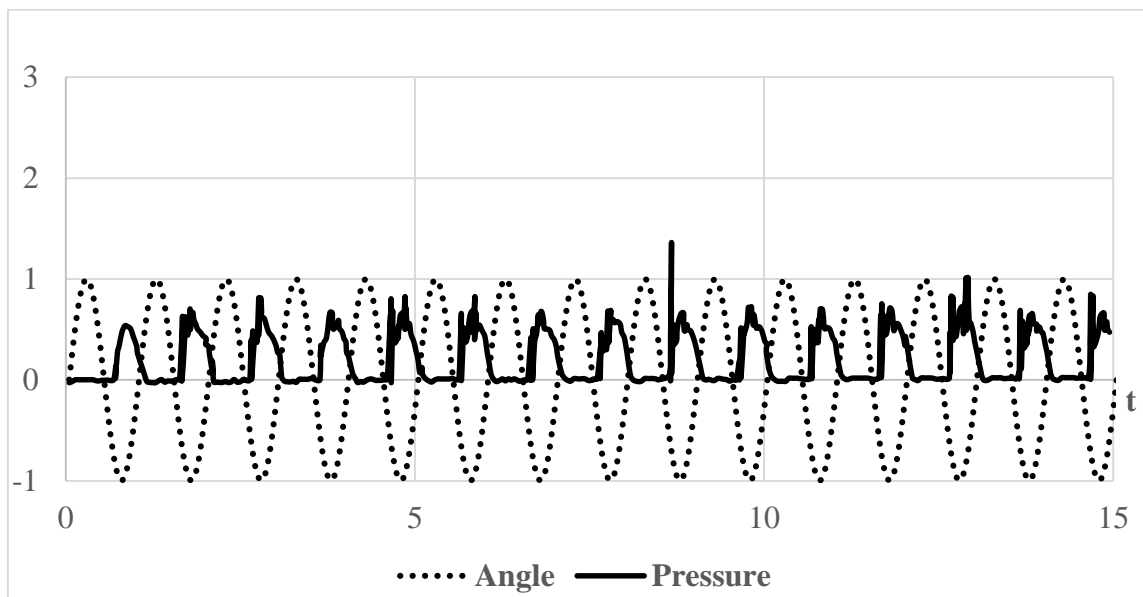
Figure 4.5: ALE-FE simulation results: Pictures of the wave shape just before the first impact for Cases A–C

Figures 4.3, 4.4 and 4.5 show that qualitatively there is good agreement between the experimental and numerical simulation results even when the sloshing phenomena involves, overturning waves and subsequent impact on the tank walls. The impact zone for all the cases is near the pressure sensor which is located on the left end of the tank wall. Quantitative numerical simulation results in terms of the maximum impact pressure obtained from the pressure sensors are shown in the following sections.

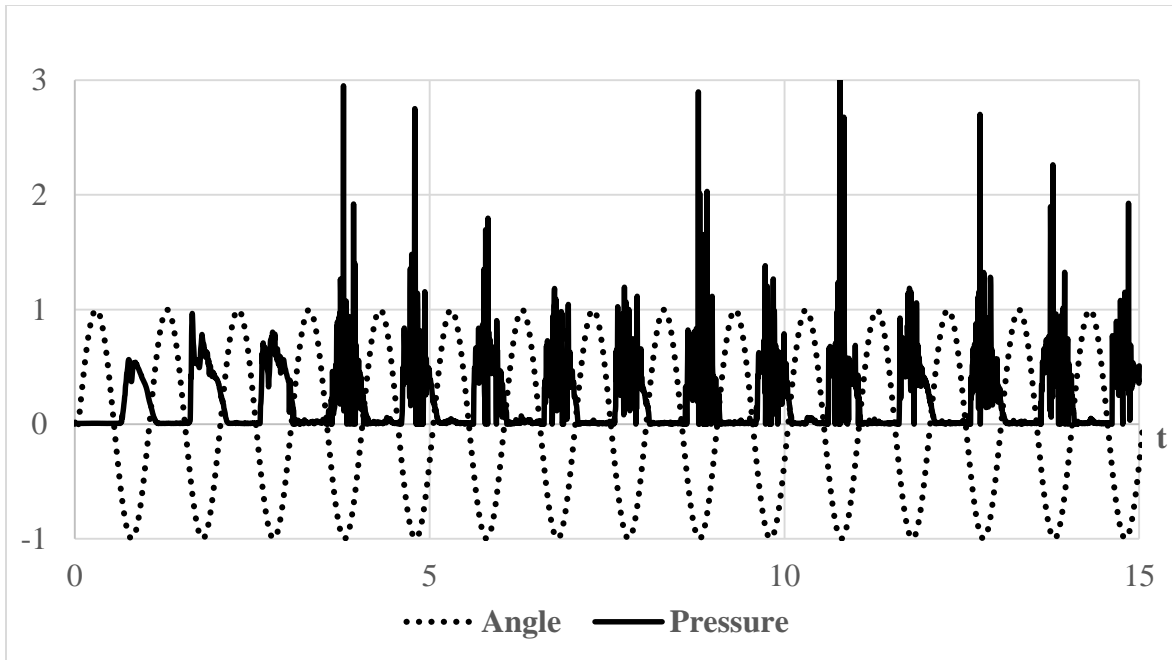
4.7 Quantitative comparison of angle and pressure results

Figures 4.6(a), 4.7(a) and 4.8(a) show the experimental angle and pressure time series (Delorme *et al.*, 2009). Time has been normalized and made dimensionless with respect to the excitation period, and by the same token, pressure with the hydrostatic pressure (P_0) at the reference depth (d), and angle with the maximum angle of excitation (θ_{\max}). Due to the highly stochastic nature of the pressure in these class of impact problems (Bagnold 1939), the first peak at each cycle results from the impact of the wave and presents a random behavior since the duration of the impact is very short and the impact pressure is extremely sensitive to the shape of the wave just before impact (Bass *et al.*, 1985; Berg 1987;

Peregrine 2003). The ALE-FE simulation results for all the three cases A-C are shown in Figures 4.6(b), 4.7(b) and 4.8(b). The pressure time history is qualitatively repetitive at each cycle. Comparison with experimental time series (Figs. 2, 3 and 4 of Delorme et al. (2009) show that the maximum impact pressure calculated from the numerical simulations (during impact at each cycle) compare well those measured experimentally. This can be attributed to the proper modeling of the air domain and the resulting two-phase flow.

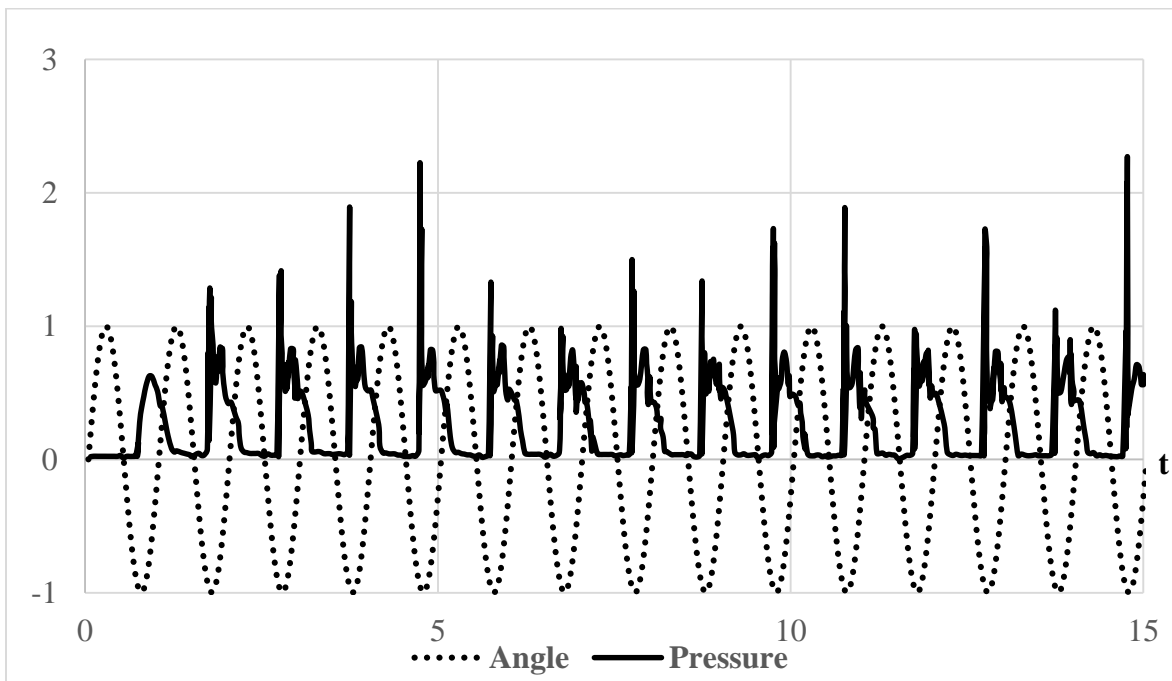


(a) Experiment (Delorme et al. (2009))

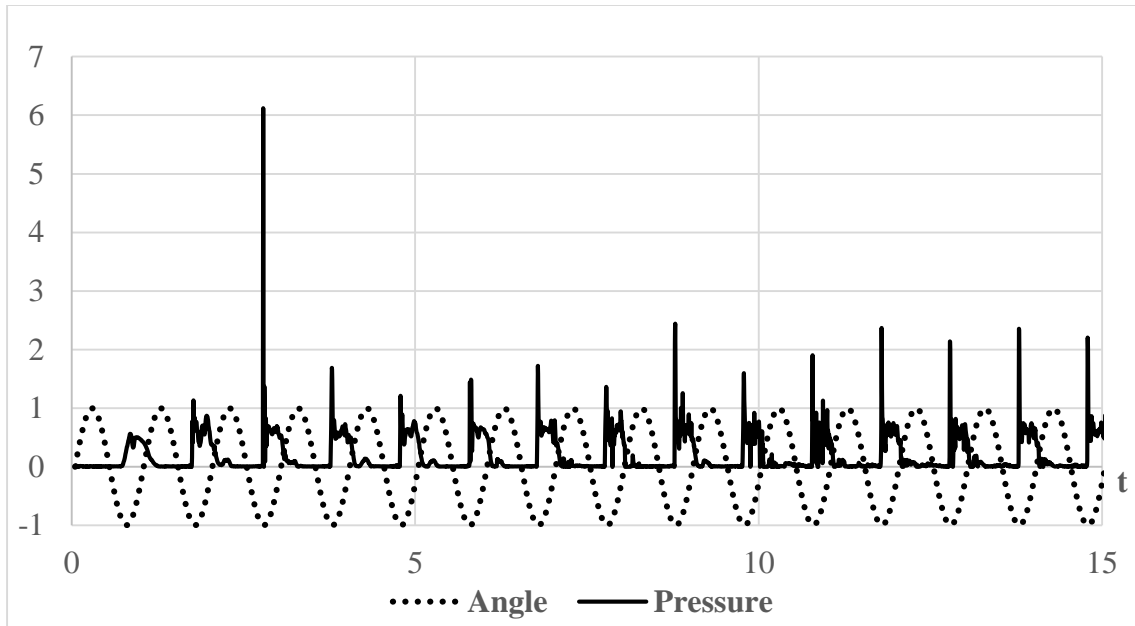


(b) ALE-FE simulation results

Figure 4.6: Dimensionless pressure and dimensionless angle vs. dimensionless time for case A

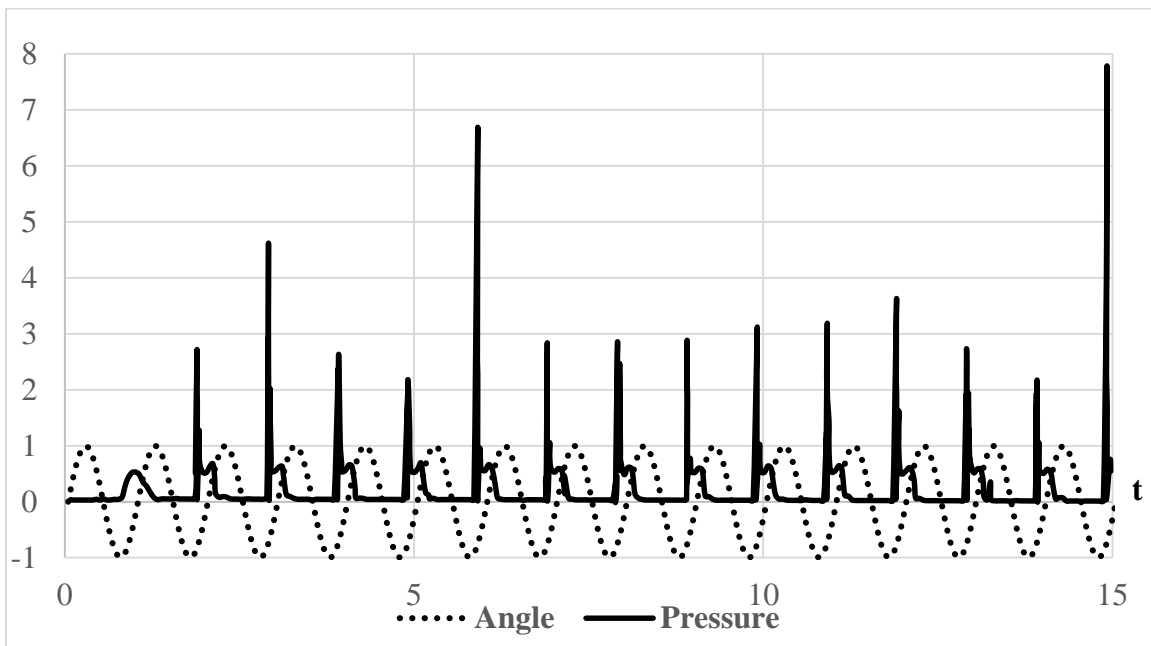


(a) Experiment (Delorme et al. (2009))

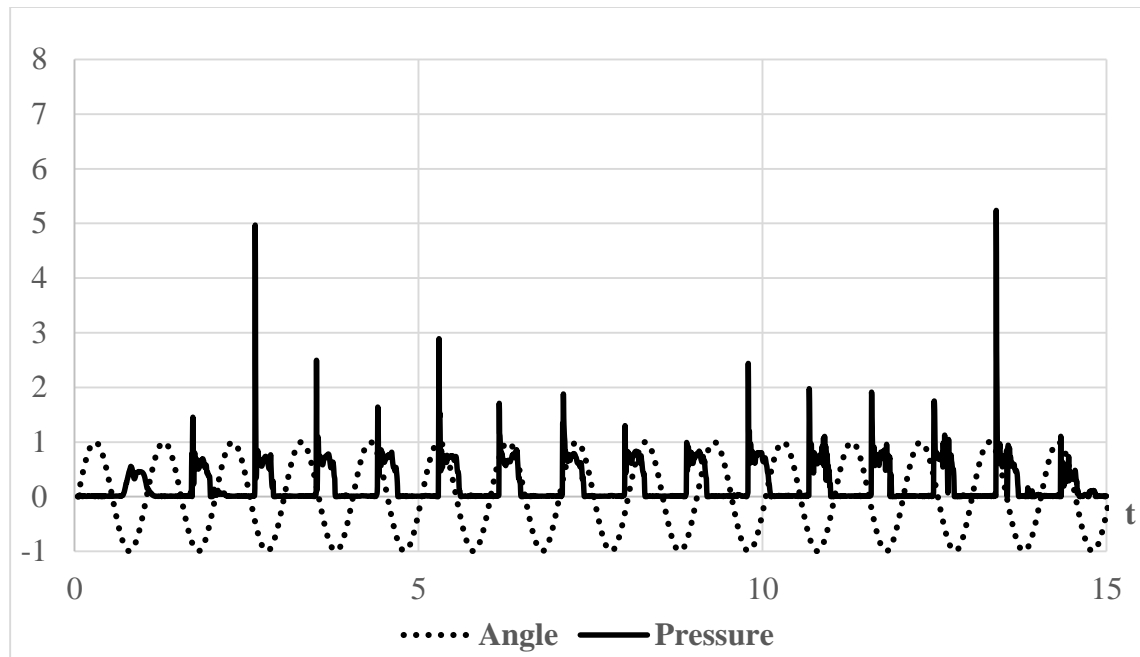


(b) ALE-FE simulation results

Figure 4.7: Dimensionless pressure and dimensionless angle vs. dimensionless time for case B



(a) Experiment (Delorme et al. 2009)



(b) ALE-FE simulation results

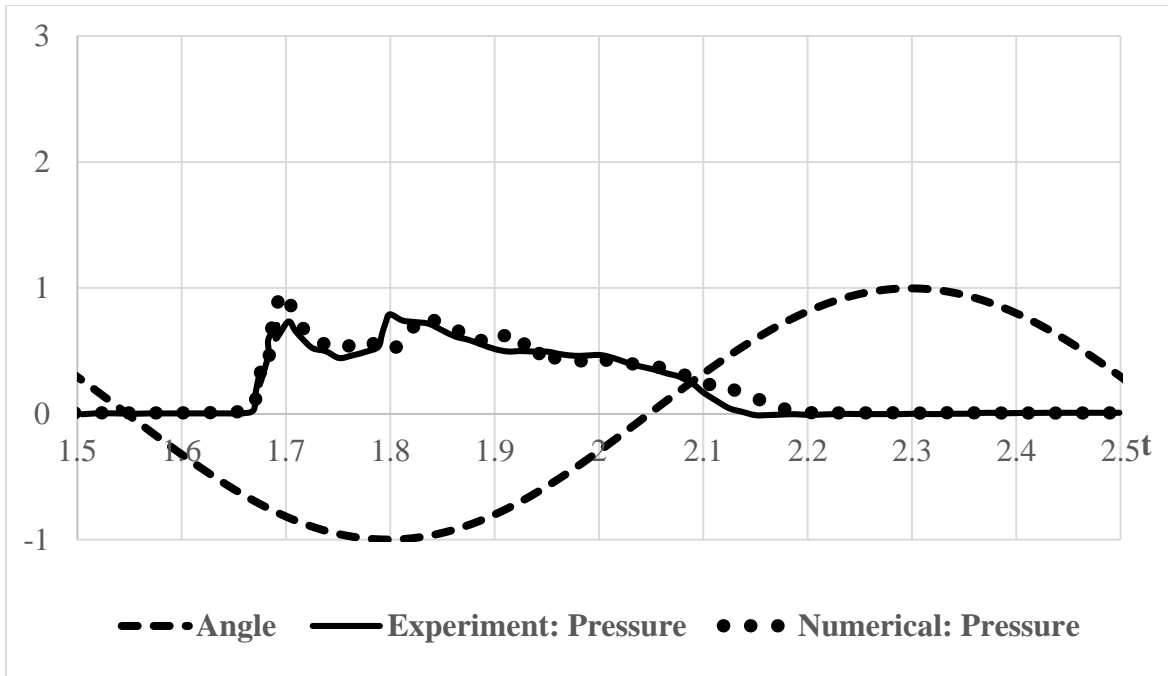
Figure 4.8: Dimensionless pressure and dimensionless angle vs. dimensionless time for case C

Quantitative comparison of the experimental time series (Figures 4.6(a), 4.7(a) and 4.8(a)) with ALE-FE numerical simulation results over the first impact event are shown in Figures 4.9(a), 4.9(b) and 4.9(c). These comparative results show that the global shape of the pressure curve is well reproduced for all the test cases. Note that the pressure sensors are located on the left wall of the tank (at the impact zone), in flush with the air-water interface. It is interesting to note that, in case A (Figure 4.9(a)), the impact occurs when the tank has not reached its maximum angle. As the impact zone in this case is located below pressure sensor position, the first peak recorded is because of the wave front (which is a plunging type wave breaking process with an air-water mixture, see Figure 4.4(a): frames A4-A6) hitting the pressure sensor. Then the fluid goes up along the tank wall and the pressure curve passes through a local minimum. As soon as the remaining part of the wave arrives

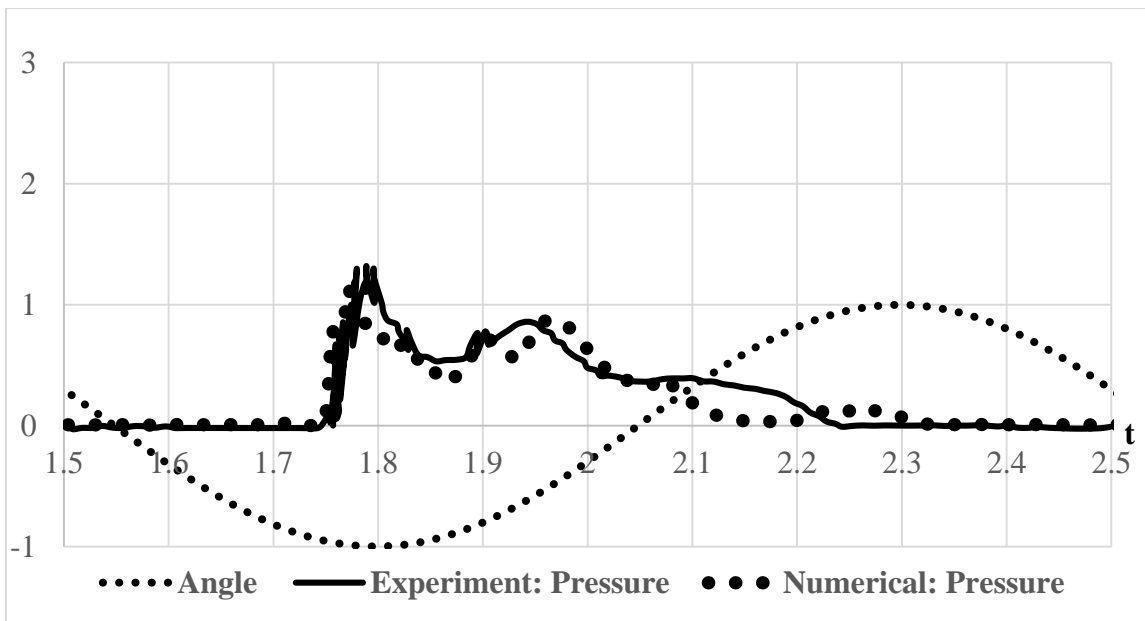
and impacts the pressure sensor during which time the tank is moving in the opposite direction, a second local maximum pressure is recorded. Subsequently, as the tank is already moving in the opposite direction, the fluid is pushed out of the tank walls and the pressure recorded is zero.

For the resonance case B (Figure 4.9(b)), the impact occurs precisely at the instant when the tank reaches its maximum rotation angle and a similar pressure curve (as seen in Figure 4.9(a)) with multiple pressure peaks are recorded. Higher values for the pressures are recorded as the impact zone is at the location of the pressure sensor. Also note that for case B, the front of the wave reaches the tank wall later in the oscillation cycle. A secondary wave propagating in the tank (Figure 4.3(b): frames B1-B4) traveling with a phase lag with respect to the main one resulting in a third peak.

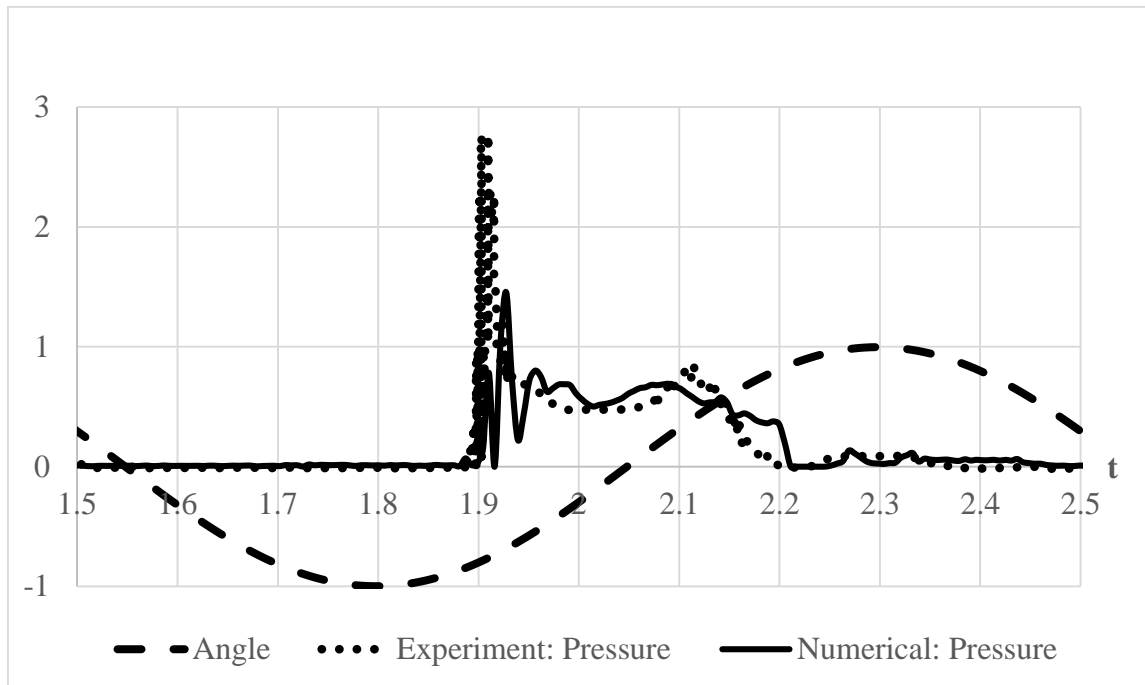
However, for case C (Figure 4.9(c)), the impact occurs well after the tank has reached its maximum angle of rotation and when it starts moving in the direction opposite to the wave's motion. The maximum pressure recorded in this particular case are much higher than those compared to cases A and B. This is because, during the point of impact, the plunge-type breaking wave is not fully developed and fluid and air do not mix (see Figure 4.4(c): frames C4-C6). The impacting wave rebounds on the upwardly moving water and impacts the pressure sensor recording a very high pressure peak.



(a) Case A: Zoom of Figs. 6(a) and 6(b) over the first impact event



(b) Case B: Zoom of Figs. 7(a) and 7(b) over the first impact event



(c) Case C: Zoom of Figs. 8(a) and 8(b) over the first impact event

Figure 4.9: Experiment and ALE-FE simulation result comparison

Figure 4.10 shows the images from the numerical results for the first five impact events for all the three cases A-C. It can be observed that the plunging wave breaking process is very well captured by the numerical simulations (including the air-fluid mixture near the impact zone). Please refer to Fig. 7 of Delorme et al. (2009) for the experimental snapshots of the first five impact events.

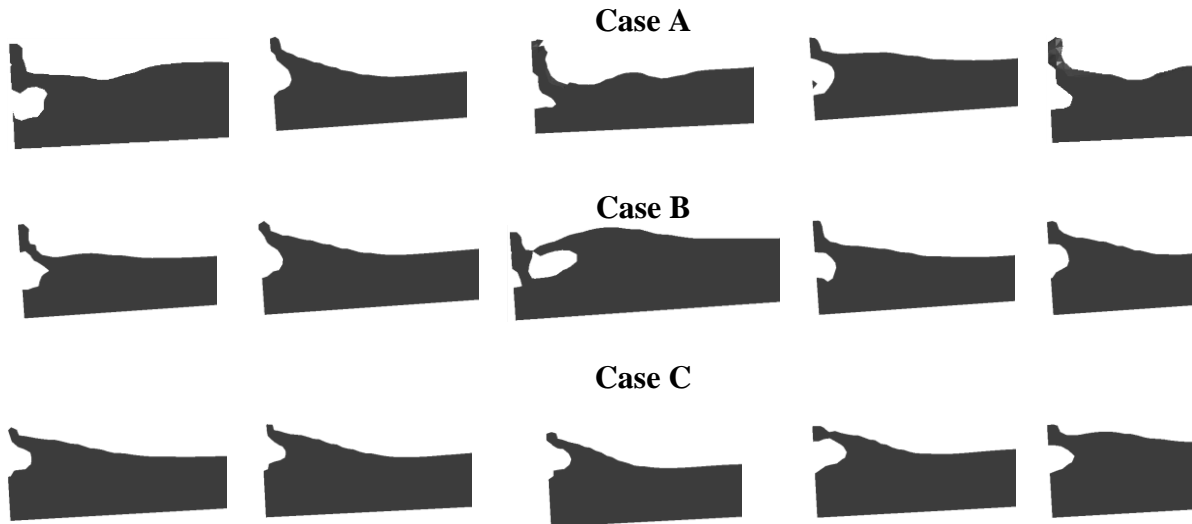


Figure 4.10: ALE-FE simulation results: Pictures of the first five impact events for Cases A–C

4.8 Estimation of maximum impact pressure

Sloshing is a highly complex nonlinear phenomenon and the impact pressure can be considered as a random process owing to its strong dependence on not only the details of the wave's shape just before impact but also the mixing of the air and the water (Bass et al. 2005; Peregrine 2003). In order to evaluate this dependency, the pressure maximum at each oscillation cycle is obtained for three different runs for all cases, each run containing more than thirty oscillation cycles. Table 4.1 shows the comparison between the experimental and ALE-FE simulation results for the average of the dimensionless pressure maxima for each case. Table 4.1 shows that the numerical simulation results tend to overestimate the pressure maxima. Maximum impact pressure for case A is 1323Pa, for case B it is 1880Pa and for case C it is 2053Pa. Table 4.1 also highlights the fact that, as the amount of the air trapped decreases gradually from case A to C, the maximum impact pressure increases

linearly (Hattori 1994). Therefore, the maximum pressure coming on to the tank walls in this particular low-filled sloshing problem is for case C and it is 2053Pa.

Table 4.1: Statistics on the dimensionless pressure maxima

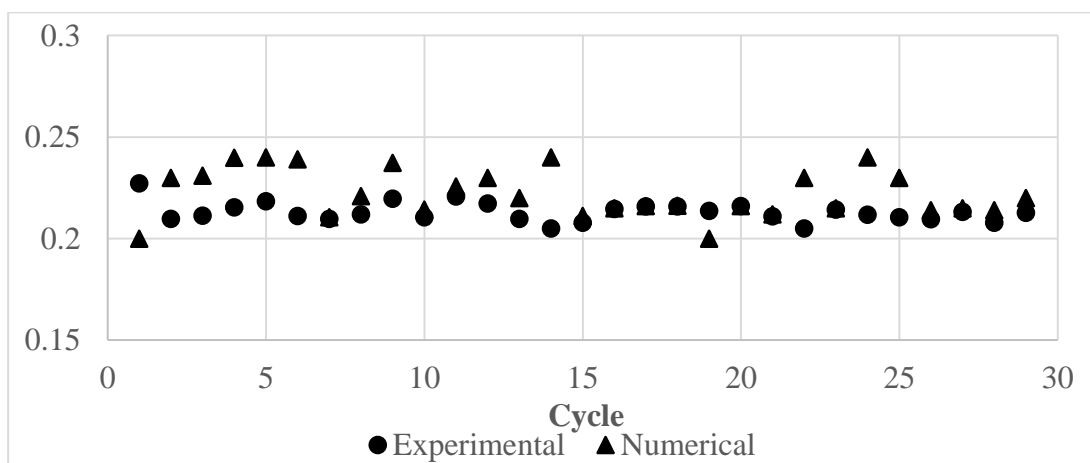
Case	A	B	C
Dimensionless pressure maxima: Experiments (Delorme et al. 2009)	0.859	1.71	3.23
Dimensionless pressure maxima: Numerical	1.84	2.02	2.25

Experimental results given in Delorme et al. (2009) emphasize the fact that in both case A and case B, the air–water mixture is not the same for each cycle, but smaller variations in the pressure curve are registered, due to the presence of air bubbles, which tend to smooth out the impact. Numerical simulations on the other hand cannot capture this phenomena hence resulting in higher pressure maximums for these cases. However, where the breaking event is not fully developed during the impact and the air entrapped is minimum the global wave shape at each sloshing cycle is well reproducible. It is important to note that the first impact event for each oscillation shows less variability than the impact from one cycle to the next. Though the numerically obtained dimensionless pressure maxima (Table 4.1) are slightly higher than those obtained by experimental data, the general agreement of the pressure field is quite good.

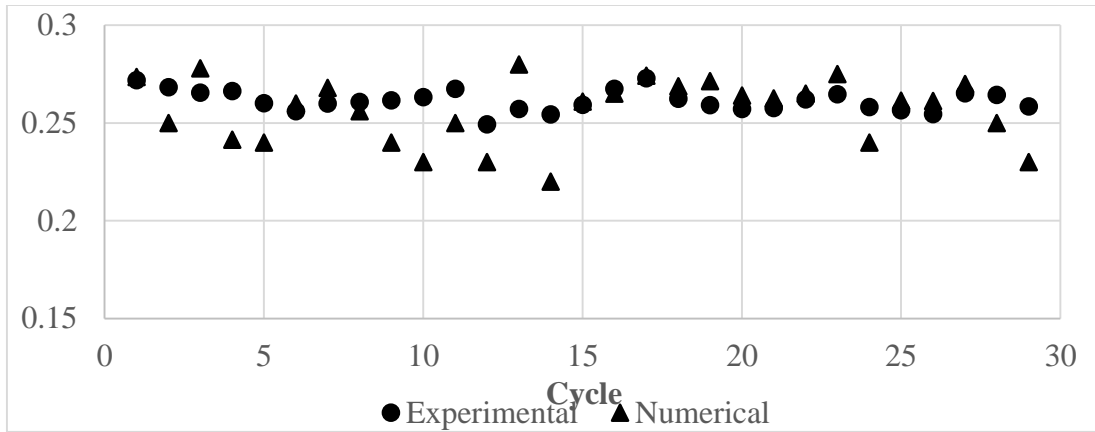
4.9 Pressure impulse analysis

In order to understand the discrepancy between experimental and numerical values of the maximum impact pressure on the tank wall over the impact duration, the pressure impulse has been calculated for the ALE-FE simulation results and averaged in order to provide the mean value of the pressure impulse over the oscillation cycles. The pressure impulse is the integral of the pressure over the duration of the impact. This characteristic is useful when analyzing the impact of a wave since it is more consistent than the value of the maximum pressure (Peregrine 2003). Figures 4.11(a), 4.11(b) and 4.11(c) shows the comparison between the experimental and ALE-FE dimensionless pressure impulse versus the oscillation cycles for cases A, B and C respectively.

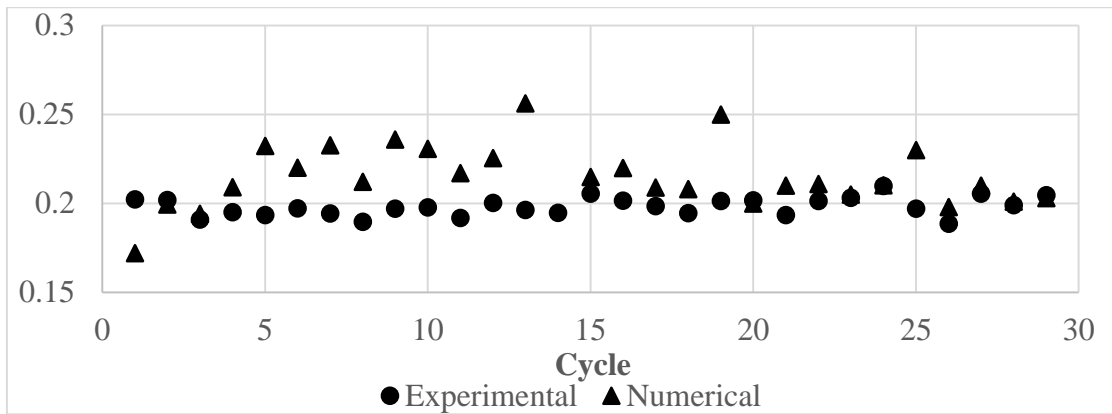
Table 4.2 shows the comparative mean values for the pressure impulse between the experimental and simulation results. Results show that pressure impulse estimated by the numerical simulations compare well with those obtained by experimental data. This can be attributed to the multi-phase flow characteristics of the sloshing phenomenon.



(a) Case A



(b) Case B



(c) Case C

Figure 4.11: Experimental and numerical pressure impulse comparison: Dimensionless pressure impulse vs. oscillation cycle

Table 4.2: Experimental and numerical mean values for the pressure impulse

Case	A	B	C
Pressure impulse: Experiments (Delorme et al. 2009)	0.21	0.26	0.22
Pressure impulse: Numerical	0.224	0.254	0.2116

4.10 Multiphase physics with air model and sensitivity of pressure field to air compressibility

Brief description of the effect of compressibility on the equation of the fluid flow (assuming an adiabatic process), the governing equations for fluid motion are usually based on the conservation of mass and conservation of linear momentum. Assuming the body forces to be conservative, the governing equations can be written as,

$$\frac{D\rho}{Dt} + \rho \nabla \cdot \vec{u} = 0 \quad (10)$$

$$\rho \frac{D\vec{u}}{Dt} = \nabla \cdot \tau_{ij} + \rho \nabla E \quad (11)$$

Respectively, where ρ is the fluid density, t is the time, τ_{ij} is the stress tensor, E is the body-force scalar potential (e.g. $E = -gy$), the operator $\frac{D}{Dt}$ is the material derivative

$$\left(\frac{D}{Dt} = \frac{\partial}{\partial t} + \vec{u} \cdot \nabla \right),$$

and ∇ is the del operator. For Newtonian fluids, the stress tensor τ_{ij} is linearly proportional to the gradient of velocity vector, and we find

$$\tau_{ij} = -p\delta_{ij} + S_{ij}; \quad S_{ij} = 2\mu \left(e_{ij} - \frac{1}{3} \left(\nabla \cdot \vec{u} \right) \delta_{ij} \right); \quad \text{and} \quad e_{ij} = \frac{1}{2} \left(\nabla u + \left(\nabla u \right) \right),$$

where p is the pressure, defined as the isotropic part of the stress tensor, i.e.

$$p = \frac{1}{3} \text{Trace}[\tau_{ii}], \quad \mu \text{ is the dynamic viscosity of the fluid (the proportionality constant}$$

between the stress tensor and the velocity gradient, and it is a function of temperature), S_{ij}

is the deviatoric stress tensor, e_{ij} is the rate-of-strain tensor, and the superscript, and T denotes the transpose. The consequence is that pressure p is only a function of the density ρ of the fluid; that is, mathematically, $p = p(\rho)$. The equation of state expressing the relationship between pressure and density (Faltinsen 2009) can be rewritten by the continuity equation. Eq. (4) can also be expressed as

$$\frac{\partial p}{\partial t} + u_i \frac{\partial p}{\partial x_i} = -\rho c^2 \frac{\partial u_i}{\partial x_i} \quad \text{where } c = \sqrt{\frac{\partial p}{\partial \rho}} \quad (12)$$

In order to avoid nonlinearities, the quantity $c^2 = \frac{\partial p}{\partial \rho}$ in eqn. (14) is considered at $\rho = \rho_0$.

Alternatively, the governing equation relating the speed of sound and the density of fluid and its bulk modulus can also be expressed as

$$c_s = \sqrt{\frac{E_v}{\rho}} \quad (13)$$

$$E_v = \rho c_s^2$$

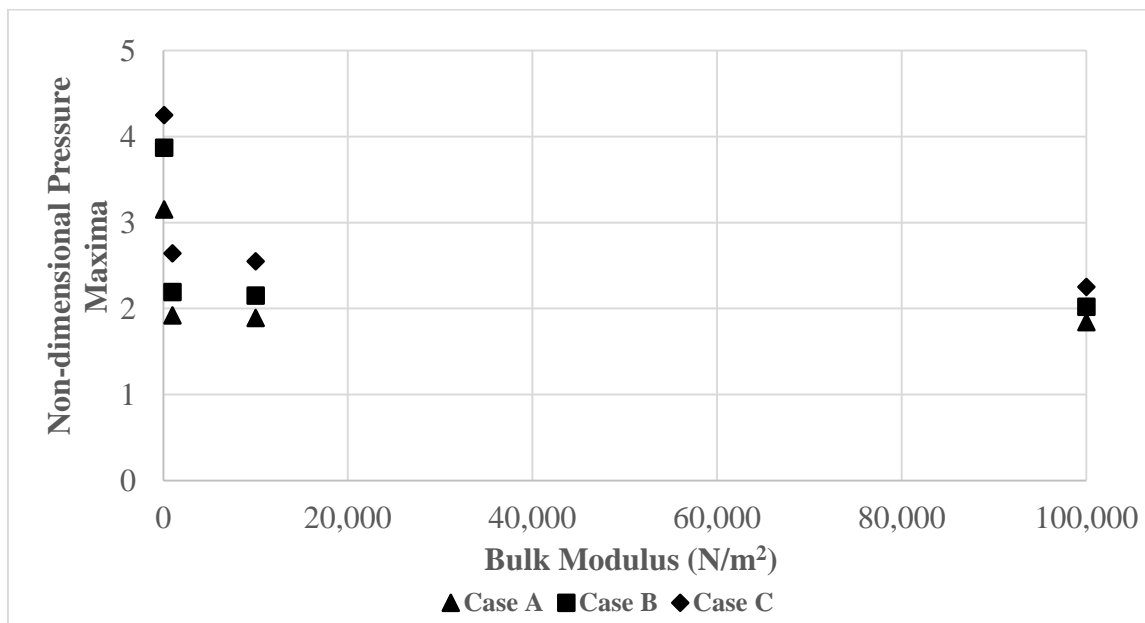
where E_v is the bulk modulus for elasticity. Note that the bulk modulus in eqn. (13) is the same as the one that was used in the numerical simulations ($C_1 = \rho c_s^2$).

Numerical test cases were also conducted for the low-filled fluid sloshing without the air domain and the results of the impact pressure time history are similar to those obtained with the air and hence not shown here. Experimental and numerical studies conducted in the past confirm this finding that for a low-filled condition, liquid turbulence and compressibility are not significant parameters for estimating the dimensionless pressure maxima (Pastoor et al. 2005). However, a mixture of gas and liquid can significantly influence the speed of sound (Lee et al. 2007; Souto-Iglesias et al. 2008). In order to understand the compressibility effects of modeling the air in the case of a low-filled water

sloshing problem where the flow is predominantly multi-physics in nature, the bulk modulus of the air (C_1) was reduced in steps of $1/10^{\text{th}}$ of the original value to examine the variation of the maximum impact pressure. Table 4.3 shows the results of maximum impact pressure for varying bulk modulus for all the three cases. Results from the table show that for a low-filled tank sloshing, the variation in the non-dimensional pressure maxima remains almost consistent for most of the cases (with a slight deviation for the case where the bulk modulus value is $1/1000^{\text{th}}$ of the original value). This also underscores the importance of air modeling in smoothing the pressure response during its impact on the wall. The large difference between the non-dimensional pressure maxima for the original bulk modulus compared to the smallest case can be attributed to the incompressible nature of the fluid and theoretically for such a scenario the impact pressures are significantly higher (Table 4.3). In order to illustrate the results shown in Table 4.3 better, the effect of varying the bulk modulus of the air on the maximum impact pressure is shown in Figure 4.12. The figure shows that the pressure field in rolling motion is broadly insensitive to the bulk modulus of the air in the case of low-filled sloshing scenario.

Table 4.3: Impact pressure response maxima for varying bulk modulus (cases A-C)

Numerical Test Cases	Air Bulk Modulus (Pa)	Non-dimensional Pressure Maxima
Case A	1.00E+05	1.84
	1.00E+04	1.89
	1.00E+03	1.92
Case B	1.00E+05	2.02
	1.00E+04	2.15
	1.00E+03	2.19
Case C	1.00E+05	2.25
	1.00E+04	2.55
	1.00E+03	2.64

**Figure 4.12: Non-dimensional pressure maxima vs. Bulk modulus (N/m²) (Results shown are for all the three cases and values are from Table 3)**

In order to further understand the role of modeling the air in this multi-physics problem in general and the effect of varying the bulk modulus of air, simulations were carried out for a high filled sloshing situation for which experimental results are available (Yung et al.

2010). The main goal of their work was to carry out a series of experiments to study the effect of ullage conditions on liquid sloshing and to investigate the phenomena of wave run-up impact on the container roof and breaking wave impact on the container walls. The tests were divided into two main categories: (i) water with various gases (air, nitrogen, helium and sulfur hexafluoride) at room temperature and (ii) water and steam. However, water interaction with air alone is of interest in this particular numerical study.

The test section (container) is a rectangular carbon steel pressure vessel with inner dimensions of length x height x depth = 1250 x 400 x 100 mm. The test tank was subjected to a simple harmonic motion along the horizontal direction near the first resonant mode of the free surface. Two different fill levels were tested, one with a fill level of 323mm (80% of depth, or the free surface of 77mm from the tank roof) and the other with a fill level of 358mm (90% of depth, or the free surface of 42mm from the tank roof), both with the same oscillation amplitude of 50mm at 0.57Hz ($T = 1.754s$). Note that the fundamental sloshing periods (resonance condition from equation (6)) for the 80% and 90% fill cases are $T_0 = 1.54s$ and $T_0 = 1.49s$, respectively. As the tests were conducted in harmonic oscillations higher than resonance (80% fill: $T/T_0 = 1.14$ and 90% fill: $T/T_0 = 1.17$), each oscillation produced a sloshing event and the maximum impact pressures on the top of the wall were recorded. Nine sensors (with a sensing diameter of 5mm) were arranged in an array (placed 1cm apart) centered on the roof panel at the wall junction were to calculate the dynamic pressure. Each experimental test case lasted 600 seconds with all the nine channels sampling at a very high rate of 100 kHz.

The same numerical formulation approach that was used to model the low-filling sloshing case is used to simulate both the high-filling sloshing situations. The computational domain

and the sensor locations are per the design provided by Yung et al. 2010. The experimental results were sampled at a very high sampling frequency (100 kHz) making it impossible to compare the pressure time histories with those obtained by numerical simulations. Maximum allowable sampling frequency in the numerical simulations was 10kHz. In addition, the simulations were carried out for only 15 seconds, taking the computational time into account (estimated clock time for a 10mm grid was 378 hours). However, a 10kHz sampling frequency along with the actual air model was sufficient to capture the maximum impact pressure (if not the entire pressure time history). Though precise matching of the numerical simulation results with experimental data is not the objective of this study (as the proprietary experimental data is not available in the literature), significance of modeling the air is. Sensitivity of the impact pressure to air compressibility is another aspect that is highlighted in this study. Specifically, the 80% and 90% fill sloshing cases are used to study the effect of air modeling on the impact pressures and to further study the sensitivity of the pressure response to the variation of bulk modulus of air. Simulations were conducted for three different resonance frequencies and the results shown below are for the one which the highest sloshing frequency as the impact pressures coming on to the tank are found to be highest in this particular case.

Figure 4.13 shows the impact pressure time history with the air/water interface for the 80% fill case. Results show that for a high-filled condition where the wave run-up impacts the container roof leads to large pressures accompanied by oscillations. Figure 4.14 shows the impact pressure time history in the absence of the air domain. Note that, for brevity, simulation results for the 80% fill sloshing case are only presented as the results of 90% fill case look similar to those shown in Figures 4.13 and 4.14. However, the results obtained

from the 90% fill case are presented in Table 4.4, which shows the comparison of the maximum impact pressure response for different bulk modulus of air for both the cases. Figure 4.15 shows the comparative results between the experimental and numerical simulations for the non-dimensional pressure maxima for the highest pressure peaks for the two different fill conditions. Note that the maximum impact pressure values presented in Figure 4.15 are non-dimensionalized by the atmospheric pressure (P_{air}).

The difference between the experimental and numerical results for the 80% and 90% fill cases are -12% and 12.5%, respectively. In the absence of the air the comparative difference between the numerical test cases with and without air for 80% and 90% fill cases are approximately 47% and 122.1%, respectively, which confirms the importance of modeling of air in high-filled sloshing cases.

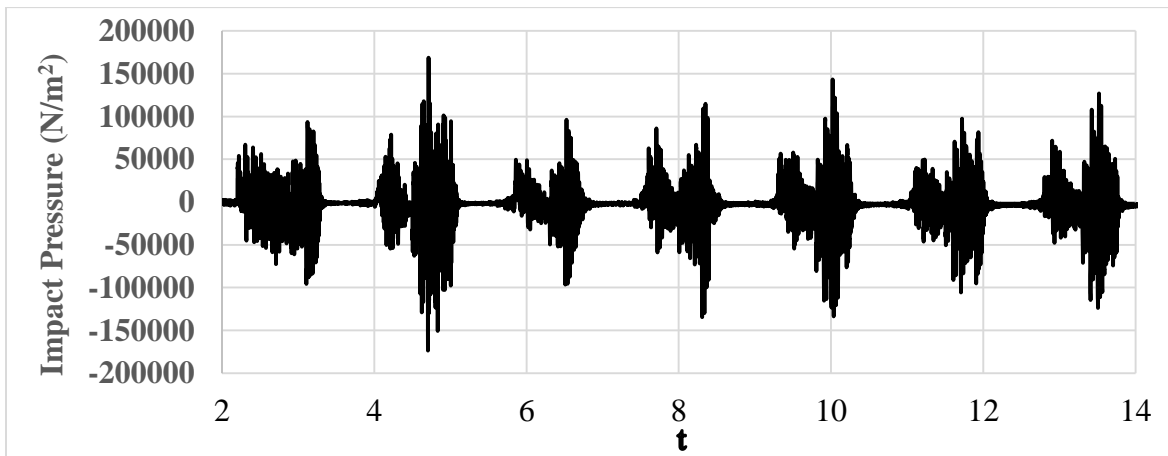


Figure 4.13: Impact pressure time histories with the air/water interface (80% Fill)

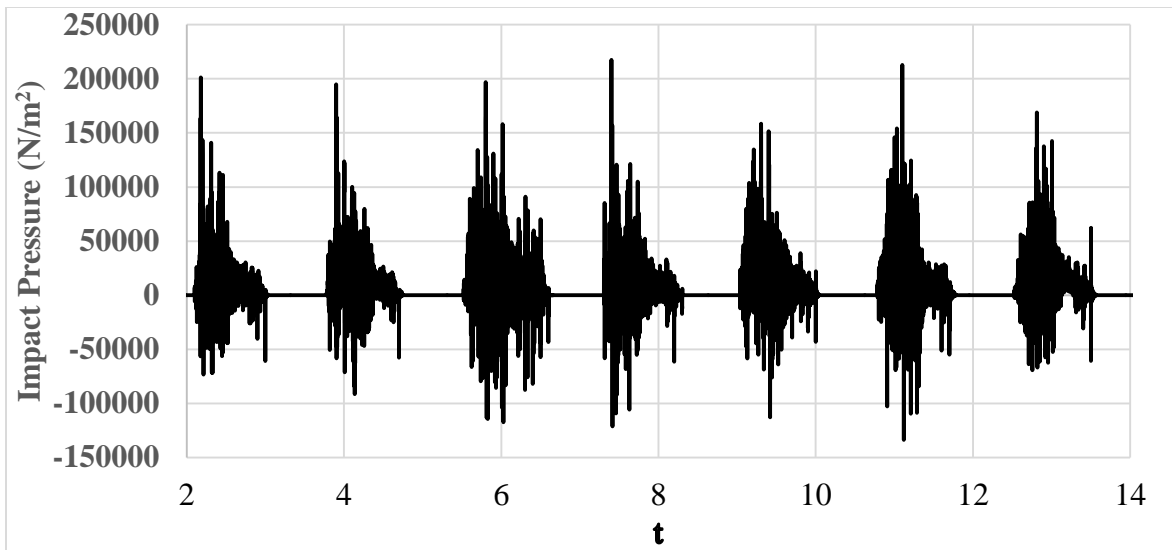


Figure 4.14: Impact pressure time history without air domain (80% Fill)

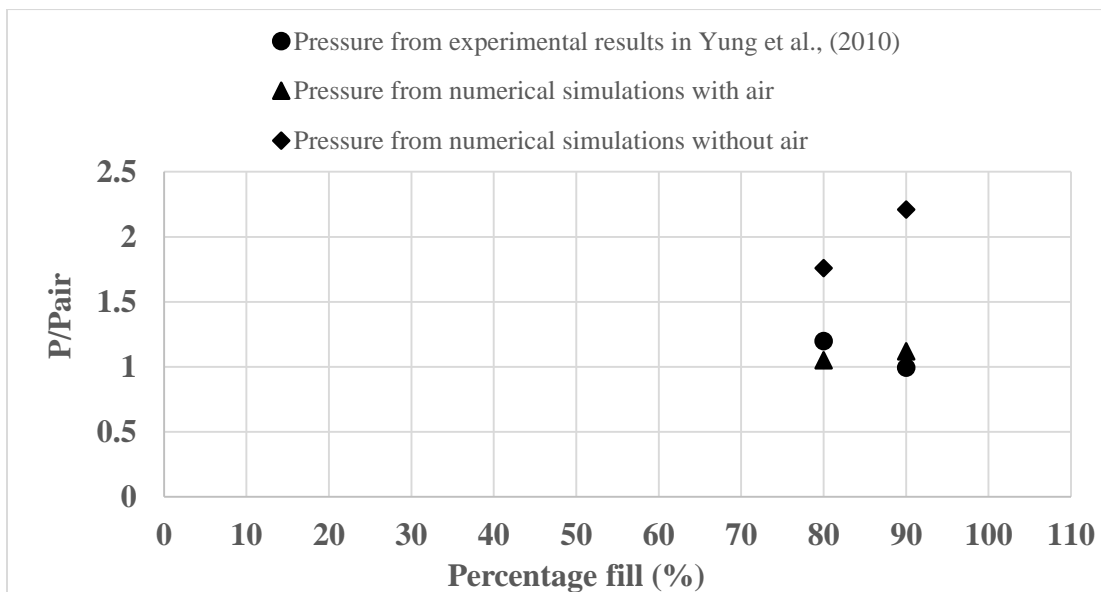


Figure 4.15: Non-dimensional pressure maxima for highest pressure peaks for two different fill conditions (comparison between experimental and numerical simulation results)

Results from the Figure 4.15 show that the numerical simulation results for both the 80% and 90% fill cases compare well with the experimental test results from Yung et al. (2010).

Table 4.4 shows the maximum impact pressure for both the 80% and 90% fill cases for

varying bulk modulus of air. The comparative results of maximum impact pressure in the absence of air is also shown in Table 4.4. In order to visualize the data shown in Table 4.4, the results are shown in Figure 4.16. Note that the results shown depict the average of the ten largest pressure peaks. The results from Table 4.4 reveal that the maximum impact pressure for the case without air is larger than the one with air for the fill cases by close to a fraction of two, accentuating the fact that modeling the actual air is significant in these class of high-filled sloshing problems. Both Table 4.4 and Figure 4.16 depict that the maximum pressure response is also sensitive to the bulk modulus of the air. Slight variation in the bulk modulus analogous to different ullage pressures for the gas/water mixture can lead to significantly high impact pressures on the sloshing vessel.

Table 4.4: Maximum impact pressure response for two high-filled sloshing situations for different bulk modulus values of air

Numerical Test Cases Case I: 80% Fill Case II: 90% Fill		Air Bulk Modulus (Pa)	Maximum Impact Pressure (kPa)
Case-I 80% Fill	I(a)	1.00E+05	106.665
	I(b)	1.00E+04	118.101
	I(c)	1.00E+03	151.745
Case-I 80% Fill No-Air	I(d)	-	178.333
Case-II 90% Fill	II(a)	1.00E+05	113.485
	II(b)	1.00E+04	156.220
	II(c)	1.00E+03	186.216
Case-II 90% Fill No-Air	II(d)	-	223.928

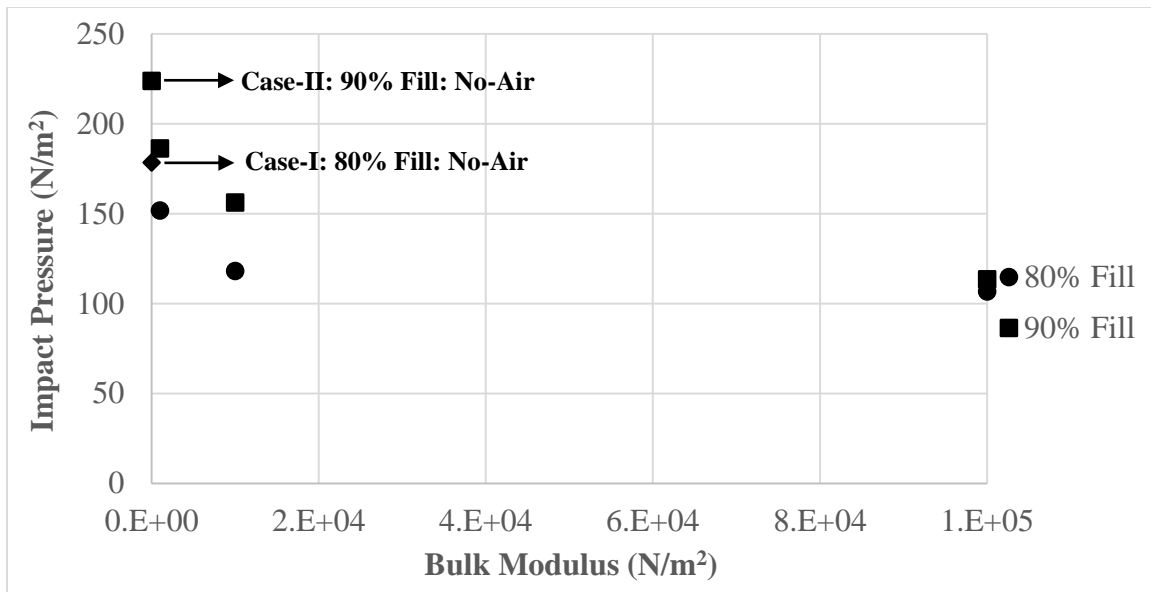


Figure 4.16: Maximum impact pressure (N/m²) vs. Bulk modulus (N/m²) (Results shown are for two high-filled sloshing cases and values are from Table 4.4)

Computational time --- Simulating the multi-phase phenomena such as the shallow and high-filled fluid sloshing requires large-scale numerical models with hundreds of thousands of nodes and elements and the computational run time becomes important to model these class of problems using optimum number of computer nodes. To model such large domain problems, all the three test cases were run on a Dell Precision Workstation 690 with twelve nodes. The platform used is Linux RHEL 5.4 with OS Level of MPICH 1.2.6 Xean64. Compiler is Fortran 10.1 with a Double Precision (I8R8). The total elapsed time for the numerical simulation for a 35sec termination time for Case A is approximately 32 hours. For Case B (for a termination time of 30sec) the total elapsed simulation time was approximately 31 hours. And for Case C the total elapsed time for the numerical simulation for a 30 seconds is roughly 30 hours. At the initial time, the fluid is assumed to be in hydrostatic conditions, while the impact pressures on the tank equal to zero.

4.11 Conclusions

A systematic numerical simulation study was conducted to analyze the physics of fluid sloshing process in a tank subjected to a forced rolling motion. Three different excitation periods are examined first for a low filled condition: below resonance, at resonance, and above resonance. The accuracy of the numerical simulations is validated against qualitative and experimental data.

Numerical simulation results show that the fluid sloshing in the tank is practically periodic with wave breaking in the interior of the fluid domain or impacting the tank walls. The wave breaking and impact process is investigated further by analyzing the sloshing scenario for a typical oscillation cycle and for the plunge type breaking process in the tank. Numerical simulation results are shown to accurately capture not only the global sloshing scenario in terms of the fluid free surface but also the overall dynamics of the wave breaking and impact process. Though the available qualitative experimental results are limited to the resonance case alone, this study provides the results for all the three excitation periods.

Quantitative numerical simulation predictions, with a specific focus on estimating the maximum impact pressure, are compared to experimental data. Results show that the maximum pressure occurs at an excitation frequency that is higher than the first sloshing frequency (case C) where the amount of air entrapped is significantly less. Maximum impact pressure results for all the cases show that the numerical simulations appear to slightly over predict the impact pressures. This can be attributed to the complex random nature of the air-water-bubble mixture at the impact zone (which tends to smooth of the impact pressures). Thus perfect matching of pressure time histories and individual peaks

should not be expected of the simulations. However, the impact behavior of the pressure response is well reproduced.

Due to the highly nonlinear and complex behavior of the maximum impact pressure during the time of impact with the tank walls, the numerical simulation results presented in terms of pressure impulse (not just the pressure maxima) showed greater consistency as the variation of the pressure impulse with the oscillation cycles is minimal.

The sensitivity of the pressure field to the multiphase physics with an air model is carried out in the form of a detailed parametric study for two fluid-fill situations. For the low-filled fluid situation the maximum impact pressure on the tank walls is extracted for different values of bulk modulus of air. Numerical results show that the air compressibility has negligible effect on the non-dimensional pressure maxima for all the three excitation periods. Though the complex air-water mixture at the impact zone can locally effect the pressure, the global values of the maximum impact pressure do not vary significantly thus validating the assumption the effect of air on sloshing impact pressures is negligible.

However, for a high-filled fluid situation the significance of air modeling is investigated, by comparing the numerical simulation results with experimental test data in the presence of air for two different high-fill conditions. Numerical simulations results for maximum impact pressure (only in the presence of air) match well with the experimental data for both the fill conditions. A detailed sensitivity analysis for this high-filled condition shows that the pressure field is highly sensitive to the compressibility of air. Numerical simulations neglecting the presence of air consistently under-predict the maximum impact pressures by several orders of magnitude.

Note that the fluid and gas in this study are restricted to water-air interaction only.

However, the methodology and computational tool presented can be applied to other fluids and gases sloshing interaction. Validation for non-water-air combinations will be needed to determine the effect of gas compressibility on the estimation of maximum impact pressures.

4.12 Acknowledgments

Financial supported from the US Office of Naval Research Grant N00014-13-1-0849 and the Department of Energy Grant DE-FG36-08GO18179-M001 is gratefully acknowledged.

4.13 References

- Aquelet, N., Souli, M., Gabrys, J., and Olovson, L. (2003). "A new ALE formulation for sloshing analysis." *Structural Engineering and Mechanics*, 16(4), 423-440.
- Bass, R., Bowles, E., Trudell, R., Navickas, J., Peck, J., Endo, N., and Pots, B. (1985). "Modeling criteria for scaled LNG sloshing experiments." *Transactions of the ASME*, 107, 272-280.
- Bagnold, R. (1939). "Interim report on wave-pressure research." *Journal of ICE*, 12, 202-226.
- Belytschko, T., Flanagan, D.F., and Kennedy, J.M. (1982). "Finite element method with user controlled meshes for fluid-structure interactions." *Computer Methods in Applied Mechanics and Engineering*, 33, 689-723.
- Berg, A. (1987). "Scaling laws and statistical distributions of impact pressures in liquid sloshing." Technical Report No. 87-2008, Det Norske Veritas (DNV).

- Challa, R., Yim, S. C., Idichandy, V. G., and Vendhan, C. P. (2014). "Rigid-Object Water-Entry Impact Dynamics: Finite-Element/Smoothed Particle Hydrodynamics Modeling and Experimental Validation." *Journal of Offshore Mechanics and Arctic Engineering*, 136(3): 031102-031102-12, doi: 10.1115/1/4027454.
- Dalrymple, R.A., and Rogers, B.D. (2006). "Numerical Modeling of Water Waves with the SPH Method." *Coastal Engineering*, 53(2-3), 141-147.
- Delorme, L., Colagrossi, A., Souto-Iglesias, A., Zamora-Rodriguez, R., and Botia-Vera, E. (2009). "A set of canonical problems in sloshing, Part I: Pressure field in forced roll-comparison between experimental results and SPH." *Ocean Engineering*, 36, 168-178.
- Donea, J., Huerta, A., Ponthot, J.P., and Rodríguez-Ferran, A. (2004). "Arbitrary Lagrangian-Eulerian methods." *Encyclopedia of Computational Mechanics*. John Wiley & Sons, Ltd.
- Faltinsen, O. M., and Timokha, A. N. (2009). "Sloshing" Cambridge University Press, NY.
- Faltinsen, O.M., Rognebakke, O.F., Lukovsky, I.A., and Timokha, A.N. (2000). "Multidimensional modal analysis of nonlinear sloshing in a rectangular tank with finite water depth." *Journal of Fluid Mechanics*, 407, 201-234.
- Hallquist, J. O. (2006). "LS-DYNA Theoretical Manual" Livermore Software Technology Corporation, California, USA.
- Hattori, M., Arami, A., and Yui, T. (1994). "Wave impact pressure on vertical walls under breaking waves of various types." *Coastal Engineering*, 22, 79-114.
- Lee, D., Kim, M., Kwon, S., and Lee, Y. (2007). "A parametric sensitivity study on LNG tank sloshing loads by numerical simulations." *Ocean Engineering*, 34, 3-9.

- Lee, S. G, Baek, Y., Lee, I. H., Yang, K. K., and Kim, Y. (2010). “Numerical simulation of 2D sloshing by using ALE2D technique of LS-DYNA and CCUP methods.” Proceedings of the Twentieth International Offshore and Polar Engineering Conference, Beijing, China, June 20-25, 192-199.
- Pastoor, W., Klungseth-Ostfold, T., Byklum, E., Valsgard, S. (2005). “Sloshing load and response in LNG carriers for new designs, new operations and new trades.” Technical report, Det Norske Veritas (DNV) Technical Paper.
- Peregrine, D. (2003). “Water-wave impact on walls.” Annual Review of Fluid Mechanics, 35, 23-43.
- Souli, M., and Benson, D.J. (2010). “Arbitrary Lagrangian-Eulerian and fluid-structure interaction – Numerical Simulation.” Wiley Publication, USA.
- Souto-Iglesias, A., Idelsohn, S., Marti, J., Zamora-Rodriguez, R., and Onate, E. (2008). “Modeling of free surface flows with elastic bodies interactions,” 27th Symposium on Naval Hydrodynamics, Korea.
- Yung, T.W., Sandstrom, R.E., He, H., and Minta, M.K. (2010). “On the physics of vapor/liquid interaction during impact on solids,” Journal of Ship Research, 54, 174-183.

Predictive Capability of Finite Element and Smoothed Particle Hydrodynamics Modeling
of Fluid-Structure Interaction

Ravi Challa and Solomon C. Yim, F.ASCE

To be submitted

5 PREDICTIVE CAPABILITY OF FINITE ELEMENT AND SMOOTHED PARTICLE HYDRODYNAMICS MODELING OF FLUID-STRUCTURE INTERACTION

5.1 Abstract

The predictive capability of an arbitrary Lagrangian-Eulerian (ALE) formulation based finite-element (FE) method and a smoothed particle hydrodynamics (SPH) method in modeling the fluid dynamics and contact and impact dynamics of a fully coupled fluid-flexible structure interaction (FSI) problem is presented in this paper. While the rapidly varying fluid flow is modeled using both FE based ALE and SPH formulations, the elastic deformation of an elastic gate (structure) is modeled using a standard Lagrangian finite element method. The fluid flow is governed by the Navier-Stokes equation and the structure is modeled as elastic. The predictive capability of the ALE-FE/FE and SPH/FE numerical methods is validated by comparing the simulation results with experimental data of an elastic gate subjected to rapidly varying fluid flow. This study provides a comparison and an evaluation of the performance of the two methods applied to predicting the response of a multi-physics FSI problem under a consistent computational platform. Numerical simulation results show that the ALE-FE/FE continuum approach not only captures the dynamic behavior accurately, but also predicts the water-free surface profiles and the elastic gate deformations accurately. On the other hand, the coupled purely Lagrangian approach of the SPH/FE under identical computational platform is found to be less accurate and efficient in predicting the dynamics of the elastic gate motion and the water-surface profiles.

Keywords: Arbitrary Lagrangian-Eulerian formulation, Lagrangian formulation, fluid-structure interaction, smoothed particle hydrodynamics, finite element, flexible structure

5.2 Introduction

Determining the hydrodynamic forces on a structure is an intrinsic component of any typical fluid-structure interaction (FSI) problem. Analytical solutions of such problems are often difficult to obtain and therefore experimental investigations are necessary. These FSI experiments often are often time-consuming and detailed parametric studies are expensive to conduct. Alternatively, well-validated numerical methods can complement or supplant the physical experiments because of the lower costs, faster turn around and capability to perform parametric studies.

Fluids are often described by an Eulerian formulation whereas the structural motions are usually described by a Lagrangian formulation. Coupling of the two media can be modeled using an Arbitrary-Lagrangian-Eulerian (ALE) formulation for the fluid domain. The ability of the ALE formulation to successfully model large deformation multi-physical interaction problems including metal forming, underwater explosions are well documented (Donea et al. 2004; Le Tallec et al. 2009). Coupling the dynamics of the fluid flow domain and the solid boundaries is a necessity whenever the motions of both the media are comparable (Rugonyi et al. 2001; Bathe et al. 2004; La Tallec et al. 2009). These classes of FSI problems can be solved by employing either a simultaneous (or direct) solution or a partitioned (or iterative) solution (Rugonyi et al. 2001). The direct solution technique is particularly convenient when the interaction between the structure and the fluid is strong

and the displacements of the structure are significant. Developments in the simulation of viscous incompressible and compressible fluid flows with structural interactions are discussed in great detail in Bathe et al. (2004).

Modeling of both the fluid and structure motions by using a pure Lagrangian formulation, such as the SPH method, is often used as an alternative to the FE method for the numerical simulation of coupled FSI problems. The SPH method can be especially effective when studying problems characterized by large displacements of the fluid-structure interface and by a rapidly moving fluid free-surface. SPH was first developed in astrophysics by Lucy (1997) and by Gingold and Monaghan (1977). As a fully Lagrangian meshless method, SPH has been successfully applied to various free-surface problems such as dam-break flow (Colagrossi et al. 2003), modeling of free-surface flows with elastic bodies interactions (Souto-Iglesias et al. 2008), breaking waves on a beach (Monaghan 1994; Monaghan et al. 1999), wedge drop (Oger et al. 2006), flow in a sloshing tank (Delorme et al. 2009) and for complicated geometries such as high speed ship flow (Yang and McCue 2012). A Lagrangian motion for the numerical simulation of FSI problems in which both the fluid and solid phases were described by a pure SPH method was investigated in detail in Randles et al. (1996), who extended the use of the SPH into problems involving free-surface flows interacting with a deformable structure. A complex FSI problem involving simulation of a two-dimensional (2-D) free-stream flow interacting with a deformable, pressurized surface, such as an ACV/SES bow seal was studied using the FEM-SPH coupling approach (Yang et al. 2012). In their study the fluid domain was based on SPH and the structural domain employs a large-deformation standard Lagrangian finite element method (FEM). They also provided validation of two benchmark FSI problems. The first

test case was flow in a sloshing tank interacting with an elastic body (Souto-Iglesias et al. 2008) and the second one was the dam-break flow through an elastic gate (Antoci et al. 2007).

In this study, the predictive capability of an arbitrary Lagrangian-Eulerian (ALE) formulation solved by the FE method and a smoothed particle hydrodynamics (SPH) formulation and solution method is used in the numerical simulation of a benchmark FSI problem. In particular, the accuracy and reliability of the numerical simulation results obtained by these numerical methods are validated against experiments presented in Antoci et al. (2007), where an elastic gate deforms under the effect of a rapidly varying fluid flow. The objectives of this work are to provide a consistent computational platform for comparison and evaluation of the two numerical methods and examine the accuracy and efficiency of each solver independently in capturing the evolution of the water free-surface profiles and the elastic gate deformations. First, the formulations of both numerical methods are presented. Then the FE solutions of the ALE formulation are contrasted with those of the SPH formulation in terms of the deformation of the structure and the evolution of the fluid free-surface.

5.3 Numerical model

The elastic deformation of an elastic gate under the effect of a rapidly varying fluid flow is modeled using two solution procedures. An FE based ALE formulation and a SPH Lagrangian formulation are used to simulate the fluid domains (air and water). The governing conservative field equations for the fluid dynamics part of the FSI was studied

by both the ALE differential form and a discrete particle form of Navier-Stokes equations. As the validation models involve large deformation with no mesh distortion or entanglement, the structural domain (in this case the elastic gate) is modeled from a pure Lagrangian finite element (FE) perspective. A brief description of the ALE and SPH formulations are presented below before the experimental and numerical setup are discussed followed by the results from both numerical simulations.

5.3.1 Arbitrary Lagrangian-Eulerian formulation and finite element solution procedure

The Navier Stokes equations and the ALE formulations are solved over the entire computational domain (Donea et al. 2004; Souli and Benson et al. 2010). In the ALE description, an arbitrary referential coordinate is introduced in addition to the Lagrangian and ALE coordinates. The material time derivative of a variable, $g(\vec{x}, t)$, with respect to the reference coordinate can be described as

$$\frac{dg(\vec{X}, t)}{dt} = \frac{\partial g(\vec{x}, t)}{\partial t} + (\vec{v} - \vec{w}) \cdot \overline{\text{grad}} g(\vec{x}, t) \quad (1)$$

where \vec{X} is the Lagrangian coordinate, \vec{x} is the ALE coordinate, \vec{v} is the particle velocity, and \vec{w} is the grid velocity of the numerical simulation. The ALE differential form of the conservation equations for mass, momentum, and energy are readily obtained from their corresponding Eulerian forms:

Mass:

$$\frac{\partial \rho}{\partial t} + \rho \text{div}(\vec{v}) + (\vec{v} - \vec{w}) \cdot \text{grad}(\rho) = 0 \quad (2)$$

Momentum:

$$\begin{aligned} \rho \frac{\partial \vec{v}}{\partial t} + \rho(\vec{v} - \vec{w}) \cdot \overline{\text{grad}}(\vec{v}) &= \overline{\text{div}}(\overline{\sigma}) + \vec{f} \\ \rho \frac{d\vec{v}}{dt} &= \overline{\text{div}}(\overline{\sigma}) + \vec{f} \end{aligned} \quad (3)$$

Energy:

$$\begin{aligned} \rho \frac{\partial e}{\partial t} + \rho(\vec{v} - \vec{w}) \cdot \overline{\text{grad}}(e) &= \overline{\sigma} : \overline{\text{grad}}(\vec{v}) + \vec{f} \cdot \vec{v} \\ \rho \frac{de}{dt} &= \overline{\sigma} : \overline{\text{grad}}(\vec{v}) + \vec{f} \cdot \vec{v} \end{aligned} \quad (4)$$

where ρ is the mass density, \vec{f} is the body force vector (per unit volume), and e is the total energy. $\overline{\sigma}$ denotes the total Cauchy stress given by:

$$\overline{\sigma} = -p\overline{\mathbf{I}} + \mu(\overline{\text{grad}}(\vec{v}) + \overline{\text{grad}}(\vec{v})^T) - 2/3 \overline{\text{grad}} \cdot \vec{v} \overline{\mathbf{I}} \quad (5)$$

where p is the pressure, $\overline{\mathbf{I}}$ is the identity tensor, μ is the dynamic viscosity, and $(\vec{v} - \vec{w})$ is the convective velocity across the grid.

A major difficulty in time integration of the ALE Navier-Stokes equations is due to the nonlinear term in the general ALE Navier-Stokes equations (2)-(4), with the relative velocity $(\vec{v} - \vec{w})$, for some ALE formulations, the mesh velocity can be solved by remeshing and using a smoothing process. In the Eulerian formulation, the mesh velocity $\vec{w} = 0$, this assumption eliminates and simplifies the remeshing and smoothing process, but does not satisfy the Navier-Stokes equations (2)-(4). There are basically two approaches to implement the Navier-Stokes equations. The first approach is to solve the fully coupled equations (2)-(4). The second approach, which is widely used in hydrocodes, is to use an operator splitting method (Bathe et al. 2004; Souli and Benson 2010). Operator splitting is a convenient means to break up complicated problems into a series of simpler problems.

In this approach, first a Lagrangian phase is performed, using an explicit finite element procedure, in which the mesh moves with the fluid particle. This phase is usually referred to as a linear Stokes problem wherein the velocity, pressure and internal energy are computed due to the action of external and internal forces. The equilibrium equations for the Lagrangian phase are

$$\rho \frac{d\vec{v}}{dt} = \overline{\text{div}}(\overline{\overline{\sigma}}) + \overline{f} \quad (6)$$

$$\rho \frac{de}{dt} = \overline{\overline{\sigma}} : \overline{\text{grad}}(\vec{v}) + \overline{f} \cdot \vec{v} \quad (7)$$

Note that in the Lagrangian formulation, the mass conservation is guaranteed, because the mass moves with and stays inside the mesh at each time step. Since in using the Lagrangian meshes to compute the density, mass conservation is described in an integrated form rather than as a partial differential equations. In the second phase, also called the advection and transport phase, the transportation of mass, momentum and energy across the element boundaries are computed. This can be thought of as remapping the displaced mesh at the Lagrangian phase back to its initial position. The transport equations for the advection phase are

$$\frac{\partial \phi}{\partial t} + \vec{u} \cdot \overline{\text{grad}}(\phi) = 0 \quad (8)$$

$$\phi(\vec{x}, 0) = \phi_0(\vec{x}) \quad (9)$$

where $\vec{u} = (\vec{v} - \vec{w})$ is the convective velocity. Equations (8)-(9) are solved for the conservative variables: mass, momentum and energy along with the initial condition $\phi_0(\vec{x})$ taken at the current time step, which is the solution obtained from the Lagrangian calculation (equations (6)-(7)). The hyperbolic equation system (8)-(9) is solved for mass,

momentum and energy by using a finite volume method using either a first-order upwind method or a second-order Van Leer advection algorithm (Leer 1977). In a nutshell, to solve a fluid problem for one time step, during the first phase, a finite element formulation with an explicit time integration method is used to solve equations (6)-(7) for mass, momentum and energy conservation. The density, momentum and energy from the first phase are used as initial conditions for the transport equation in the second phase. A second-order time integration explicit method is used for the transport equation.

5.3.2 Lagrangian formulation and smoothed particle hydrodynamics solution procedure

Smoothed particle hydrodynamics (SPH) is an N-body integration scheme initially developed by Lucy (1997), and Gingold and Monaghan (1997) to avoid the limitations of mesh tangling encountered in extremely large deformation problems with the FE method. The main difference between traditional methods (such as finite element, finite volume and finite difference) and SPH is the absence of a grid. Hence, the particles constitute the computational framework on which the governing equations are resolved. The main advantage of SPH arises directly from its Lagrangian nature, since such an approach can tackle difficulties related with lack of symmetry, large voids that may develop in the field, and tracks a free water surface much more efficiently than Eulerian methods (Liu et al. 2003; Lacomme 2009). The Lagrangian conservation laws of continuum fluid dynamics, in the form of partial differential equations, are transformed into particle form by integral equations through the use of an interpolation function that gives a kernel estimation of the field variables at a point (Monaghan 1992). A fluid material model with an equation of

state is used to model the water domain. The speed of sound at the reference density was set to a lower than actual value of 100m/s as the acoustic speed is not important for the present problem (Dalrymple 2006). It is worthy to note that this sound speed is much lower than that of water, but much faster than the water wave propagation in the model.

SPH Formulation – Formulation of SPH is divided into two key steps. First step is the integral representation or the so-called kernel approximation of field functions. The second step is the particle approximations.

The integral representation of a function $f(x)$ is given by:

$$f(x) = \int_{\Omega} f(y) \delta(x-y) dy \quad (10)$$

where f is a function of the three-dimensional position vector x , and $\delta(x-y)$ is the Dirac delta function given by

$$\delta(x-y) = \begin{cases} 1 & x = y \\ 0 & x \neq y \end{cases} \quad (11)$$

In equation (10), Ω is the volume integral that contains x .

The particle approximation function is given by:

$$\Pi^h f(x) = \int_{\Omega} f(y) W(x-y, h) dy \quad (12)$$

where W is the kernel function, which is defined using the function θ by the relation:

$$W(x, h) = \frac{1}{h(x)^d} \theta(x) \quad (13)$$

where d is the number of space dimensions and h is the so-called smoothing length which varied in time and space; $W(x, h)$ is a centrally peaked function; and the most

common smoothing kernel used by the SPH is the cubic B-spline which is defined by choosing θ as:

$$\theta(u) = Cx \begin{cases} 1 - \frac{3}{2}u^2 + \frac{3}{4}u^3 & \text{for } |u| \leq 1 \\ \frac{1}{4}(2-u)^3 & \text{for } 1 \leq |u| \leq 2 \\ 0 & \text{for } 2 < |u| \end{cases} \quad (14)$$

where C is a constant of normalization that depends on the spatial dimensions.

In the SPH method when the entire system is represented by a finite number of particles that carry individual mass and occupy individual space. The continuous SPH integral for $f(x)$ when written in discretized *particle approximation* is now defined as:

$$\Pi^h f(x_i) = \sum_{j=1}^N w_j f(x_j) W(x_i - x_j, h) \quad (15)$$

where $w_j = \frac{m_j}{\rho_j}$ is the “weight” of the particle. The weight of a particle varies

proportionally to the divergence of the flow. Note that the mass is distributed around the center of mass of each particle based on the density distribution defined by the kernel function (Monaghan 2005).

Discrete form of conservative equations – The solution of the equation is of the form

$$L_v(\phi) + \text{div}F(x, t, \phi) = S \quad (16)$$

Where $\phi \in R^d$ is the unknown, F^β with $\beta \in \{1 \dots d\}$ represents the conservation law and L_v

is the transport operator defined by:

$$L_v : \phi \rightarrow L_v(\phi) = \frac{\partial \phi}{\partial t} + \sum_{i=1}^d \frac{\partial (u_i \phi)}{\partial x_i} \quad (17)$$

Weak formulation approximation – The strong formulation approximation is not conservative, therefore they are not used in numerical solutions. However, the weak formulations shown below are conservative and all the conservative equations encountered in SPH are usually solved using the weak form (Monaghan 1994). In the weak formulation, the adjoint of the L_v operator is used:

$$L_v^* : \phi \rightarrow L_v^*(\phi) = \frac{\partial \phi}{\partial t} + \sum_{i=1}^d u \frac{\partial \phi}{\partial x} \quad (18)$$

The discrete form of this operator corresponds to the discrete formulation of the adjoint of

$$D_{h,s} : D_{h,s}^* \phi(x_i) = \sum_{j=1}^N w_j (\phi(x_i) A_{ij} - \phi(x_j) A_{ji}) \quad (19)$$

A discrete adjoint operator for the partial derivative is also necessary, and is taken to be the α^{th} component of the operator

$$D_\alpha^* \phi(x_i) = \sum_{j=1}^N w_j \phi(x_j) A^\alpha(x_i, x_j) - w_j \phi(x_i) A^\alpha(x_j, x_i) \quad (20)$$

Applications to conservation equation – The Lagrangian conservation equations are written in their discrete form and the momentum conservation equation are given below.

Particle approximation of density is given by

$$\frac{D\rho_i}{Dt} = -\rho_i \sum_{j=1}^N \frac{m_j}{\rho_j} u_{ij} \cdot \frac{\partial W_{ij}}{\partial x_i} \quad (21)$$

Particle approximation of momentum: If we choose the smoothing function to be symmetric, this can lead to the following equation

$$\frac{Du_i}{Dt} = \sum_{j=1}^N m_j \left(\frac{\sigma_i}{\rho_i^2} + \frac{\sigma_j}{\rho_j^2} \right) \frac{\partial W_{ij}}{\partial x_i}$$

$$\frac{Du_i}{Dt} = -\sum_{j=1}^N m_j \left(\frac{p_i}{\rho_i^2} + \frac{p_j}{\rho_j^2} \right) \frac{\partial W_{ij}}{\partial x_i} + \sum_{j=1}^N m_j \left(\frac{\mu_i \varepsilon_i}{\rho_i^2} + \frac{\mu_j \varepsilon_j}{\rho_j^2} \right) \frac{\partial W_{ij}}{\partial x_i} \quad (22)$$

This is what is called as the “symmetric formulation”.

Another possible choice is to define the momentum equation by:

$$\frac{Du_i}{Dt} = \sum_{j=1}^N m_j \frac{\sigma_i + \sigma_j}{\rho_i \rho_j} \frac{\partial W_{ij}}{\partial x_i}$$

$$\frac{Du_i}{Dt} = -\sum_{j=1}^N m_j \frac{p_i + p_j}{\rho_i \rho_j} \frac{\partial W_{ij}}{\partial x_i} + \sum_{j=1}^N m_j \frac{\mu_i \varepsilon_i + \mu_j \varepsilon_j}{\rho_i \rho_j} \frac{\partial W_{ij}}{\partial x_i} \quad (23)$$

This is the “fluid formulation” used in the present analysis which gives better results than other SPH formulations when fluid particles are present or when material with very different stiffness are used.

Particle approximation of energy is given by

$$\frac{De_i}{Dt} = \frac{1}{2} \sum_{j=1}^N m_j \frac{p_i + p_j}{\rho_i \rho_j} \frac{\partial W_{ij}}{\partial x_i} + \frac{\mu_i}{2\rho_i} \varepsilon_i \varepsilon_j \quad (24)$$

In equations (21)-(24), u is the particle velocity, e is the energy, p is the pressure, σ is the total stress tensor, μ is the dynamic viscosity and ε is the shear strain rate.

Note that in a pure Lagrangian formulation such as the SPH, as the flux over the mesh width is zero, there is no need to solve a conservation of mass equation as the mass moves with the mesh and the conservation of mass is guaranteed.

Artificial Viscosity – An artificial viscosity is introduced when a shock is present. Shocks introduce discontinuities in functions. The role of the artificial viscosity is to smooth the shock over several particles. To take into account the artificial viscosity, an artificial viscous pressure term Π_{ij} (Monaghan and Gingold 1983) is added such that:

$$P_i \rightarrow P_{i+} \mathbf{\Pi} \mathbf{\Pi}_{ij} \quad (25)$$

where $\Pi_{ij} = \frac{1}{\rho_{ij}} (-\alpha \mu_{ij} \bar{c}_{ij} + \beta \mu_{ij}^2)$. The notation $\bar{X}_{ij} = \frac{1}{2}(X_i + X_j)$ is used for median between X_i and X_j , c is the adiabatic sound speed, and

$$\mu_{ij} = \begin{cases} -h_{ij} \frac{v_{ij} r_{ij}}{r_{ij}^2 + \eta^2} & \text{for } v_{ij} r_{ij} < 0 \\ 0 & \text{otherwise} \end{cases} \quad (26)$$

Here, $v_{ij} = (v_i - v_j)$, and $\eta^2 = 0.01 \bar{h}_{ij}^2$ which prevents the denominator from vanishing.

In this SPH formulation, the default values for the artificial viscosity ($\alpha = 1.5$ and $\beta = 0.06$) were originally designed for Lagrangian solid elements only and they are not appropriate when SPH particles are used in the simulation. The SPH recommended values are $\alpha = 1.5$ and $\beta = 1.0$ (Schwer 2009).

Time Integration--- A simple, classical first-order scheme for integration is used with the time step determined by the following expression:

$$\Delta t = C_{CFL} \text{Min} \left(\frac{h_i}{c_i + v_i} \right) \quad (27)$$

where the factor C_{CFL} is a numerical constant enforcing the Courant-Friedrichs-Lewy (CFL) stability condition (Monaghan 1994).

In many numerical simulations involving a Lagrangian formulation, an SPH description (and solution) of the fluid motion is coupled to a finite element formulation for the solid dynamics. Before presenting the numerical simulation test results from the proposed FE-based ALE fluid and FE-based Lagrangian structure (ALE-FE/FE) and SPH-based fluid and FE-based Lagrangian structure (SPH/FE) methodologies, a brief description of the

experimental setup is shown below. This will be followed by a detailed description of the computation domain used for the numerical setup. Subsequently, these two methods are validated by comparing the results obtained with available experimental test data.

5.4 Experimental set-up of rapidly-varying flow with flexible elastic gate

The pressure exerted by a fluid flow on the confining solid gate boundary in the form of a flexible elastic gate is studied. The predictive capability of the ALE-FE fluid/Lagrangian FE structure technique is validated by comparing the numerical simulation results with data measured during suitable laboratory experiments (illustrated in Antoci et al. 2007). In the experiments, an elastic gate, clamped at one end and free at the other one, interacts with a mass of water initially confined in a free-surface tank behind the gate. The conception behind choosing this particular experimental set-up is because it involves the interaction between a flexible elastic structure and a fluid flow accompanied by large displacements of the structure and the fluid free surface flow. A section of a plexiglass flume has been confined by two vertical walls, thus creating a tank, as represented in Figure 5.1. The walls constitute an upper rigid part and in a lower flexible plate made of elastic. The elastic gate is free at its lower end, thus representing an elastic gate completing the enclosure of the tank. The geometric dimensions of the experimental system and the physical characteristics of the elastic gate are reported in [Table 5.1](#).

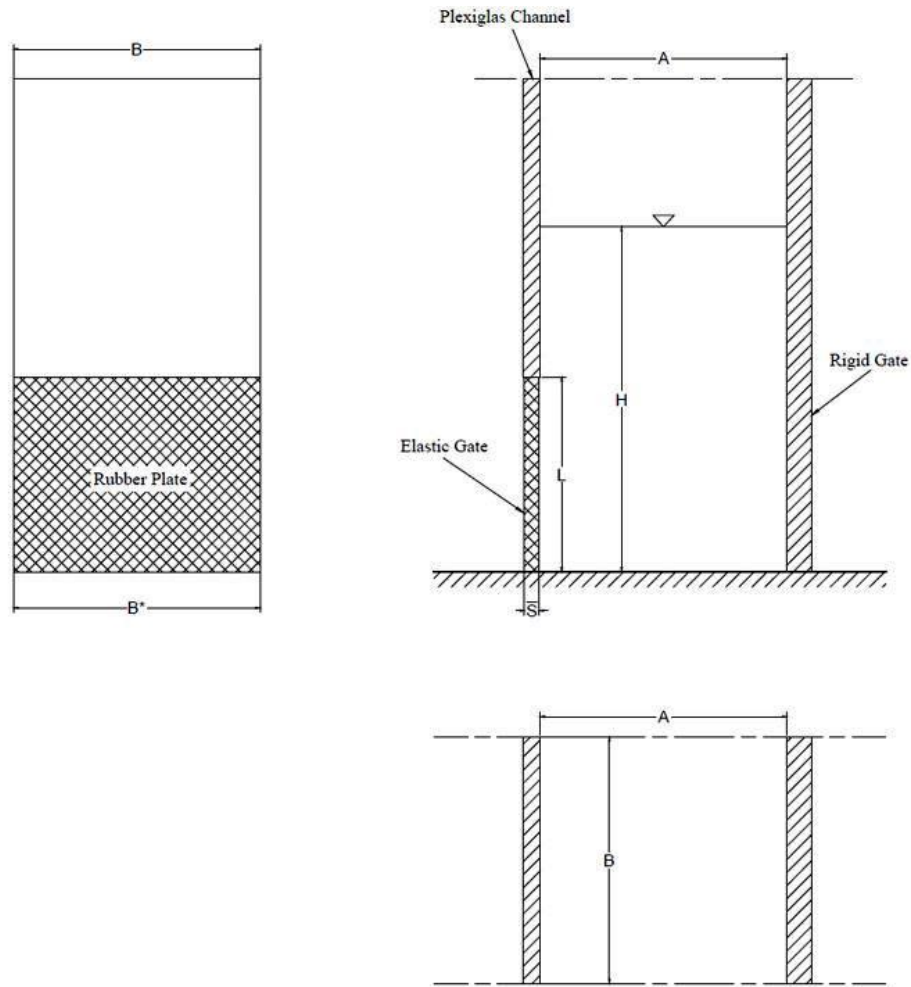


Figure 5.1: Scheme of the tank and of the gate: frontal view, lateral and plan

Table 5.1. Dimensions of the system and physical characteristics of the elastic gate

<i>Dimensions</i>	
A (m)	0.1
H (m)	0.14
B (m)	0.1
B* (m)	0.098
L (m)	0.079
S (m)	0.005
<i>Elastic elastic gate</i>	
ρ (kg / m^3)	1100
E (MPa)	$\cong 10$

The elastic gate (clamped only along its upper edge) is free to deform when subjected to the pressure of the fluid behind it. The elastic gate is held fixed by an external rigid support during the process of filling the tank with water up to the desired level. When the water in the tank is in hydrostatic conditions, the rigid support is suddenly removed, thus allowing the gate to deform while water flows under it. The experiments were recorded by a digital video camera, at a frequency of 25 frames per second. The displacements of the free end of the gate and the water levels in the tank were measured by digital image processing (Antoci et al. 2007).

5.5 Numerical simulations

5.5.1 ALE/FE modeling of FSI: Deformation of an elastic gate

A numerical code for nonlinear dynamic analysis of structures in three dimensions (3-D), LS-DYNA, is used in the current study (Version: mpp971d R7.0.0 and Revision: 79055). An ALE/FE technique is used to model the fully coupled FSI problem where both the air/water domains and the solid parts (gate and rigid wall) are modeled using solid brick elements. The compressible fluid solver is analyzed as weakly incompressible to retain the explicit solution of the continuity equation. A lower value of the compressibility modulus was adopted. Figure 5.2 shows the initial configuration for the 3D ALE-FE/FE simulation.

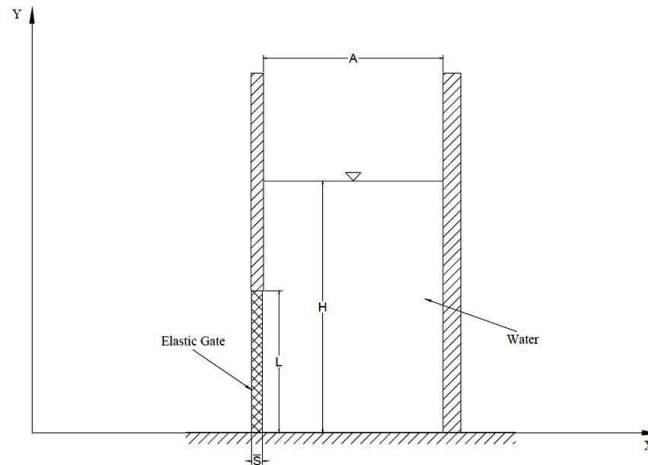


Figure 5.2: Initial configuration of the tank and water

The ALE-FE/FE analysis of the experiments including the water transient flow and the gate deformation is studied as a three-dimensional phenomenon. It should be noted that, in the experiments, no bending of the elastic gate was observed along the direction normal to the lateral walls (Antoci et al. 2007). An important feature in simulating contact problems is proper modeling of the two-phase flow including the presence of air. In this study we include air modeling using its material properties with a proper governing equation of state. Note that air is modeled in the ALE-FE/FE formulation but not the SPH/FE method.

Both the air and water domains are modeled with solid elements which needs a prescribed equation of state. The elastic gate is treated as an elastic material and the upper rigid wall is given a rigid body definition. The dimensions and the properties of the elastic gate (mass density and Young's modulus) are shown in Table 5.1. The elastic gate is discretized by solid elements having density of $1,100 \text{ kg} / \text{m}^3$. The results of the simulation with $E = 1.2e7 \text{ N} / \text{m}^2$, better reproduces the experimental phenomenon. The Poisson ratio is set to 0.4. This value, although lower than the theoretical one for an incompressible elastic

material, allows us to use larger time steps while maintaining the CFL condition without sacrificing accuracy. Figure 5.3 shows the 3D ALE-FE/FE computational domain.

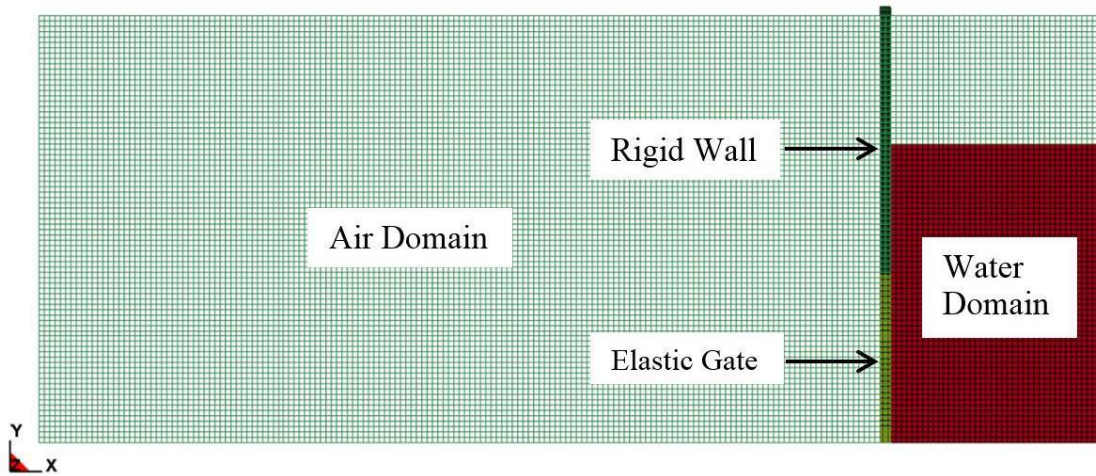


Figure 5.3: ALE/FE simulation: Computational domain

Eight-node brick elements and constant stress solid elements (Belytschko et al. 1982) are used for discretization of the Lagrangian (rigid wall and elastic gate) and Eulerian (air and water domains) components of the 3-D computational domain.

The interaction force between the air-water domains and the elastic gate are computed through a penalty based coupling procedure (La Tallec 2000; Hallquist 2006). In this two-way coupling, the moving surface of 3-D elastic body and the rigid wall (a Lagrangian mesh) is treated as the slave surface, and the air-water domain (an Eulerian mesh) is treated as the master surface. The interaction forces are calculated based on the number of coupling points between the Lagrangian surface and the ALE elements and the penetration distance between them. The elements of the air and water domains are given the null hydrodynamic material type that allowed a new equation of state to be specified (Hallquist 2006). An equation of state with a linear polynomial form is used to define the initial thermodynamic state of the material and pressure is given by:

$$p = C_0 + C_1\zeta + C_2\zeta^2 + C_3\zeta^3 + (C_4 + C_5\zeta + C_6\zeta^2)E \quad (28)$$

where C_{0-6} are user-defined constants, E is initial energy per initial volume, and the volumetric parameter ζ is defined as:

$$\zeta = \frac{1}{V} - 1 \quad (29)$$

where V is relative volume given as:

$$V = \frac{\rho_0}{\rho} \quad (30)$$

with ρ_0 as the reference mass density (which might be different than the current mass density if the material experiences compression or expansion throughout the simulation).

The constant C_1 in Equation 6, when used by itself, is the elastic bulk modulus ($C_1 = \rho \times c_s^2$), where ρ is the mass density of the material and c_s is the sound speed in air/water ($c_s = 1,480m/s$ for water and $c_s = 343m/s$ for air). Providing this constant only and setting all other constants to zero is sufficient to define the equation of state if the pressure is not significantly influenced by temperature changes. Speed of sound in water plays a significant role in determining the total computational time. Monaghan et al. (1994) and Dalrymple and Rogers (2006) suggested that the minimum sound speed should be about one tenth of the maximum expected flow speeds. The values of C_1 for air and water domains are $1.0e5N/m^2$ and $1.0e7N/m^2$, respectively.

A slip boundary condition is imposed to the fluid flow on the rigid walls. The boundary conditions employed in the numerical model are partially the material surfaces (out-of-plane, in-plane and bending restraint). The material surfaces defined in ALE formulation

are: (a) no particles can cross them, and (b) stresses must be continuous across the surfaces. Clamp conditions (on the gate) are imposed by a layer of fixed nodes on the top of the gate. The computational domain is made up of four solid parts which constitutes 670,104 nodes, 641,600 solid elements of which there are 1,000 rigid elements and 640,600 deformable solid elements (air and water ALE solid elements).

5.5.2 Smoothed particle hydrodynamics and finite element modeling

Description of the SPH/FE model – Figure 5.4 illustrates the three dimensional numerical configuration of the SPH/FE computational domain which shows the SPH water domain and the clamped edge of a flexible gate along with the rigid wall (FE mesh). Fluid is simulated by using SPH particles. The scheme of the tank and of the elastic gate (Figure 5.1) and the dimensions of the system and physical characteristics of the elastic gate are similar to those that are used in the ALE model (Table 5.1). Consistent with most SPH models in the literature, the air domain is not modeled in the SPH/FE approach. The edges of the water were defined as fixed-SPH nodes (analogous to SPH ghost particles) allowing the water block to act as a tank. Same material properties that were used in the ALE simulations were retained for the rigid wall, elastic gate and the water domain. Material and element properties of the individual components of the SPH/FE computational domain are shown below.

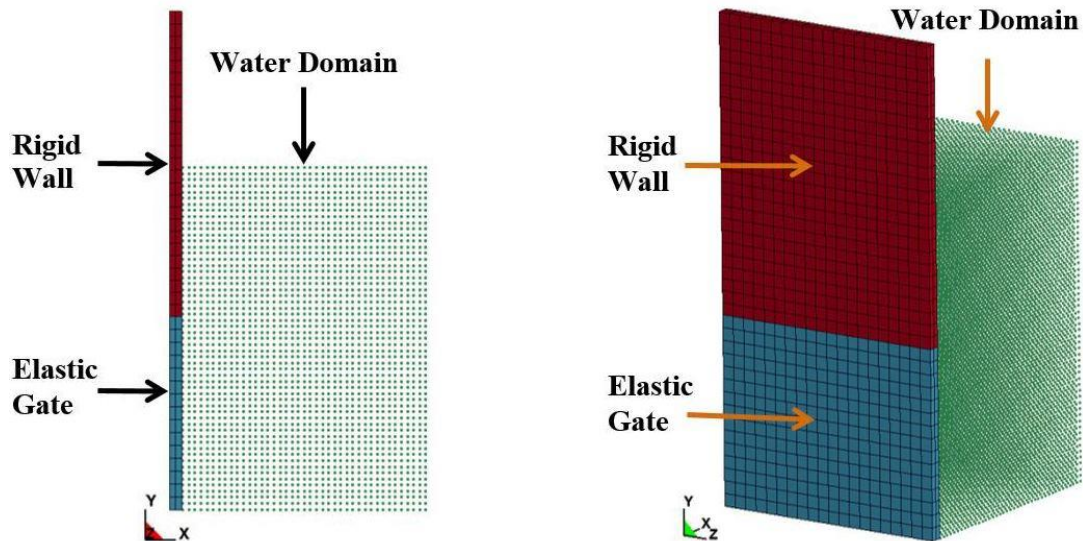


Figure 5.4: 3-D configuration of SPH-FEM computational domain (SPH: Water domain; FEM Mesh: Top part – Rigid Wall and Bottom part – Elastic gate)

The same material properties that were used in the ALE-FE/FE formulation are used for the SPH test cases. However, the fluid domain has been discretized with SPH elements. The number of SPH particles/nodes used is 95,817 (with the distance between the particles as 0.2mm) and the number of shell elements used for both the wall and the gate combined are 1,600. As there is no mesh connectivity, the interaction between the SPH fluid and structural elements is defined by using a one-way tied or penalty type interface/contact. Note that a free-surface tracking technique is not needed. In this type of penalty coupling, the moving surface of three-dimensional SPH water domain is treated as the slave surface, and the target FE mesh (rigid wall and elastic gate) are treated as the master surface. There are different ways of introducing the boundary conditions for the SPH formulations. Boundary particles can be placed on the walls directly which in turn exert a repulsive force on the fluid particles adjacent to it as in Monaghan and Kos (1999). The use of this boundary force introduces initial instability (Souto-Iglesias et al. 2006). In

order to obtain a smooth flow near the boundaries, slip boundary conditions are imposed to the fluid flow on the rigid walls: these conditions are imposed through the technique of ghost particles (Colagrossi and Landrini 2003) on the right tank wall and on the bottom and by layers of fixed ghost particles in the upper rigid part of the left tank wall. Rigid wall by itself is restrained in translation and rotation (fixed globally in the x , y and z directions) and the top nodes of the elastic gate are fixed in translation and rotation (clamped condition). An equation of state with a linear polynomial form (eqn. 23) is used to define the initial thermodynamic state of the material for the water domain. The sound speed is usually set to ten times the maximum expected velocity in the fluid (Monaghan 1994). This will allow the sound speed in the numerical simulations to be sufficiently low for time step optimization.

The only force acting on the SPH particles is gravity ($g = 9.81m/s^2$). This load should be pre-applied gradually over a finite time and the elastic gate is then released at $t = 0$ which means that the pressure in the fluid domain is equal to static pressure at $t = 0$.

The termination time for the simulations was set to 0.4 seconds. At the initial time, the fluid is assumed to be in hydrostatic conditions, while in the gate, stresses and deformations are equal to their corresponding static equilibrium values. The time step in both the numerical methods was governed by the CFL number (eqn. 22) which is a necessary condition for stability while solving the partial differential equations. For both methods the smallest timestep is governed by the solid elastic elements ($6.77E-06$) which remained consistently constant throughout the simulation.

5.6 ALE/FE and SPH/FE simulation results

Quantities of interest for the validation case are the displacements of the free end of the gate (x and y displacements) and the water levels in the tank (just behind the wall and 5cm away from it). Frames from the numerical simulations (images) of ALE and SPH at every 0.04s are shown in Figures 5.5 and 5.6, respectively. Numerical simulation results show that the dynamics of the phenomenon, in terms of deformation of the gate and of evolution of the fluid free-surface, in the most generic sense, is well reproduced by both the ALE-FE/FE and the SPH/FE numerical solution procedures. It can be observed that the predicted shape of the elastic gate is similar to the observed one in experimental investigation where the deformation is maximum near the clamp (with null second derivative of the horizontal displacements), whereas, close to the free end, the gate seems to move almost as a rigid body. However, the amount of deformation and the evolution of the fluid free surface vary for both the numerical solution procedures and are discussed in the following sections. In the SPH/FE pure Lagrangian method, boundary conditions are imposed in the form of ghost particles. The resultant displacement oscillation of the free end of the elastic gate is a result of these virtual boundaries. Significant pressure oscillations (a numerical artifact) originating from the wall and bottom boundaries propagate throughout the fluid domain resulting in large displacements. The performance of ALE/FE and SPHFE solution procedures in terms of the computational efficiency is also studied. Computational clock-time for the ALE simulation for a 0.4s termination time (12 CPUs) is approximately 19 hours. On the other hand, the execution time for the SPH Lagrangian method on the same number of CPUs is slightly more than 75 hours (i.e. about four times longer than the ALE/FE simulation).

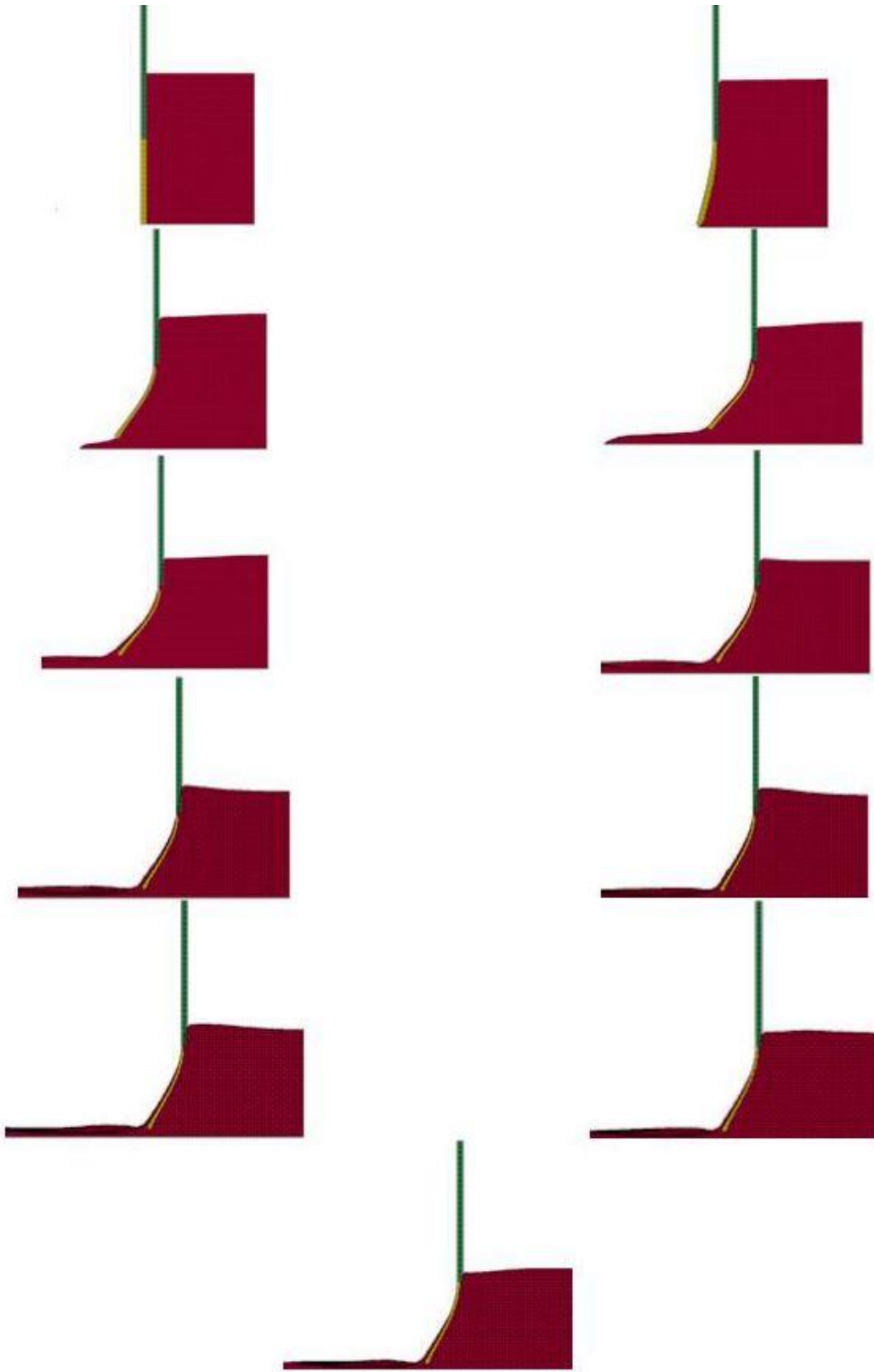


Figure 5.5: Frames and images from ALE/FE simulation (Every 0.04s from $t = 0s$ to $t = 0.4s$)

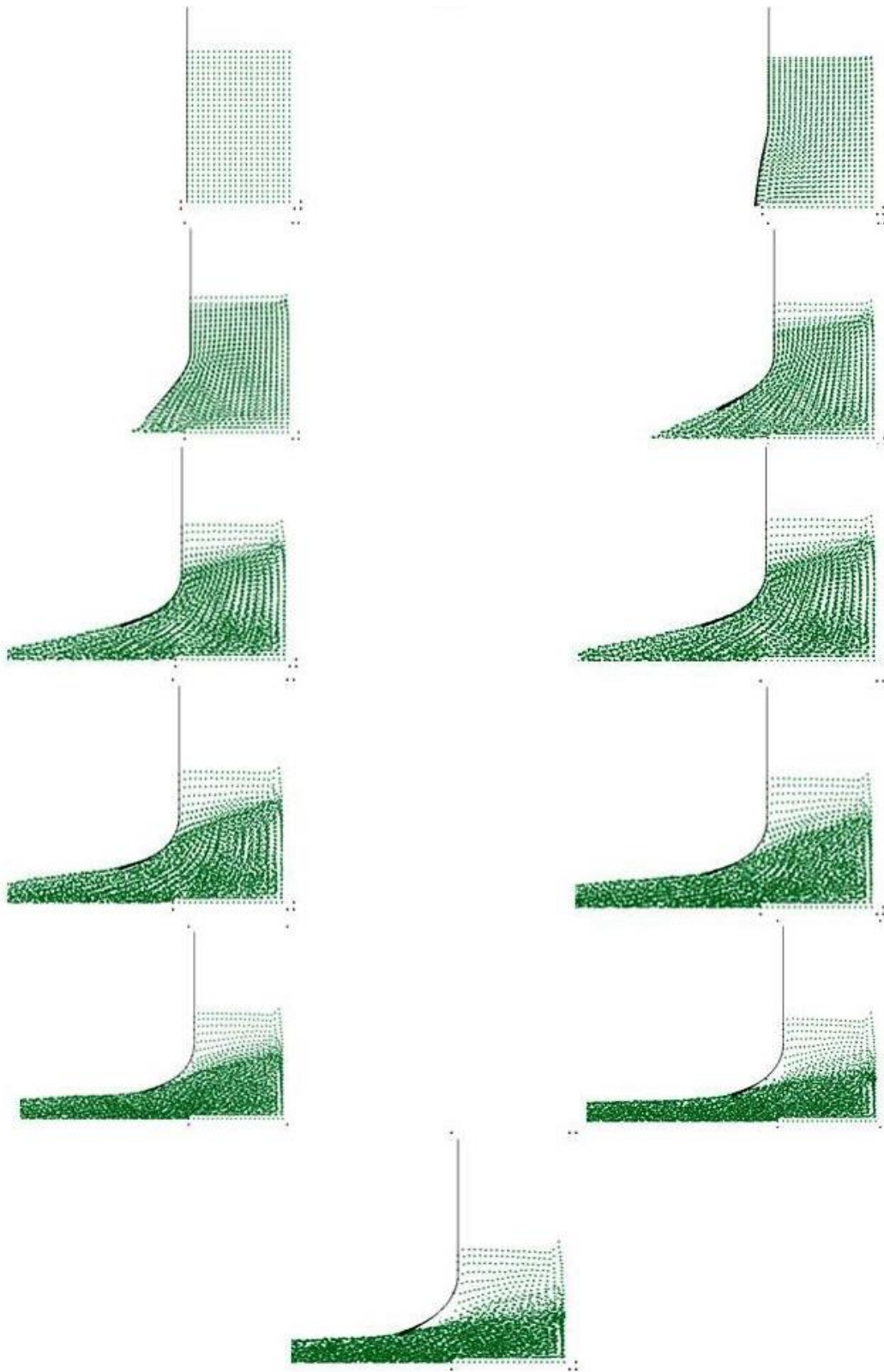


Figure 5.6: Frames and images from SPH/FE simulation (Every 0.04 s from $t = 0s$ to $t = 0.4s$)

By varying the number of processors (1, 2, 4, 6, 8, 10 and 12 CPUs), the average ALE/FE to SPH/FE clock-time ratios are found to be in the order of 4.0-4.2.

Elastic gate free end displacements – Horizontal and vertical displacements computed for the free end of the gate (from the ALE/FE formulation) are compared with those measured in the digitalized images acquired during the experiments (Figure 5.7), which shows that the displacements of the gate compare well with the experimental test data. It can also be observed that the time evolution of the phenomenon is well described by the ALE-FE/FE simulation.

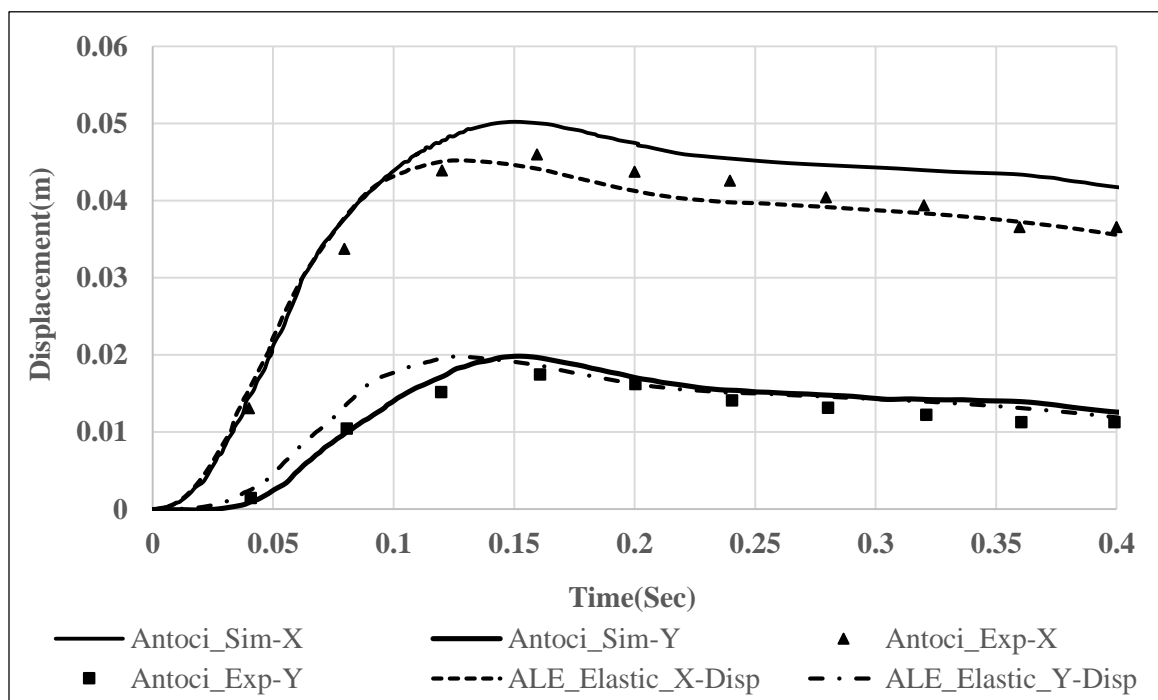


Figure 5.7: Horizontal and vertical displacements of the free end of the gate (ALE/FE)

Numerical simulation results obtained by Antoci *et al.*, (2007) demonstrate an over-prediction of the displacement. They attribute this to the water leakage at the side of the gate (observed experimentally) resulting in a pressure drop in the fluid domain (as seen in

Figure 5.7 at times larger than 0.124s). This aspect is not captured by either of the numerical methods. This difference leads to a 4% underprediction of the maximum horizontal displacement of the elastic gate.

Horizontal and vertical displacements of the free end of the gate for the SPH/FE simulation are shown in Figure 5.8. It can be observed that the displacements of the gate in the SPH/FE simulations are larger than those obtained in the experiment.

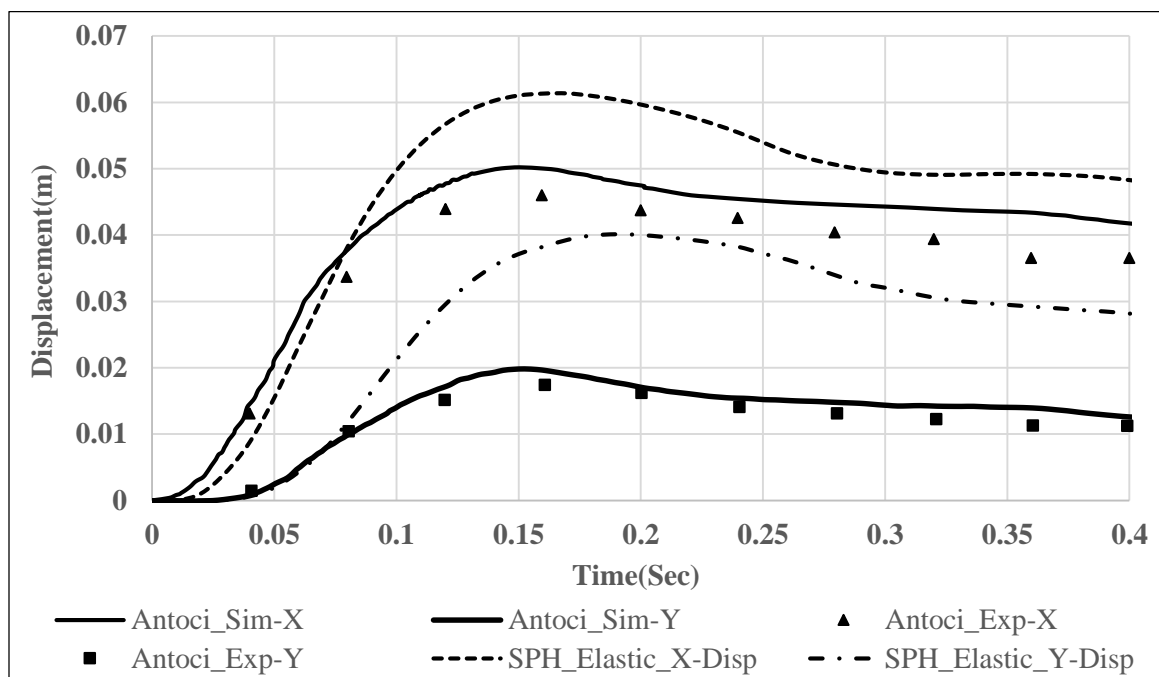


Figure 5.8: Horizontal and vertical displacements of the free end of the gate (SPH/FE)

Results of the SPH/FE simulation for the time evolution display an overprediction of the maximum horizontal and vertical displacements (37% and 71%, respectively). This can also be attributed to the fact that the contact stiffness force between the SPH water particles and the elastic gate is lower than the real one, hence resulting in a decrease in pressure and an exaggerated displacement of the free end of the gate.

Water free-surface profiles – The evolution of the water free-surface is also well reproduced by ALE-FE/FE simulation. Figures 5.9 and 5.10 shows the water level immediately behind the gate and in the middle of the tank. The computed flow rate is slightly higher than the experimental observation ($t < 0.2s$) leading to a faster decrease in the water level in the initial part of the transient phase (due to a large vertical displacement of the gate resulting in a larger gate opening). For $t > 0.2s$, the computed and measured values of the water level evolve in the same way.

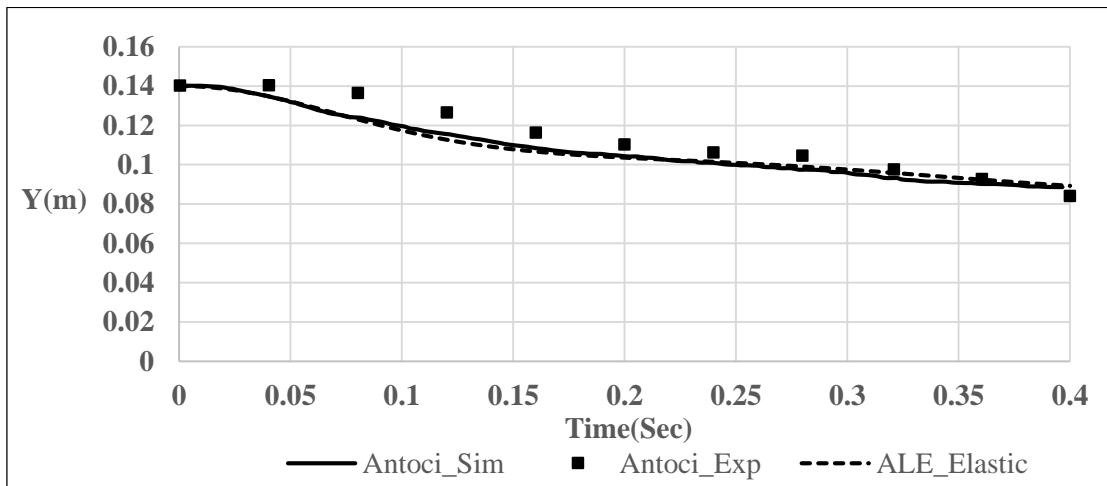


Figure 5.9: Water level (m) just behind the gate (ALE/FE)

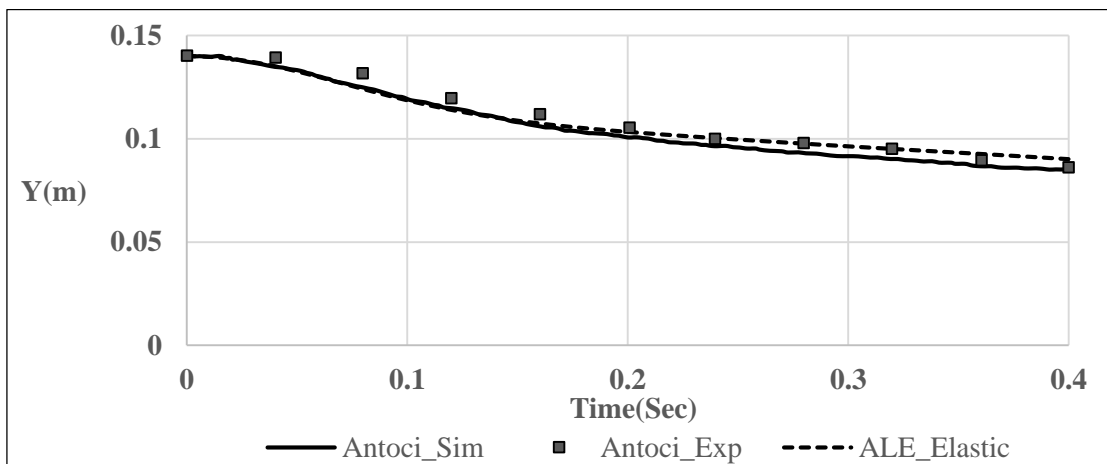


Figure 5.10: Water level (m) 5cm from gate (ALE/FE)

The evolution of the water free-surface for the SPH/FE simulations is shown in Figures 5.11 and 5.12. Though the profile of the fluid free-surface is well reproduced, the particle simulation results show a lack of agreement with the experimental test results (due to the higher flow rate resulting from the rapid opening of the gate as explained below).

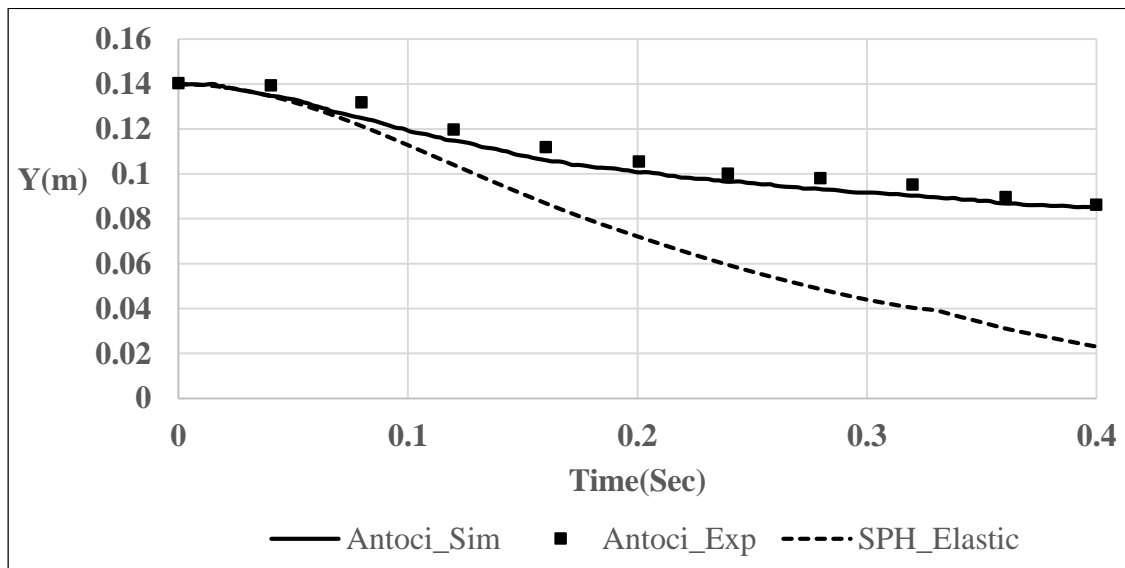


Figure 5.11: Water level (m) just behind the gate (SPH/FE)

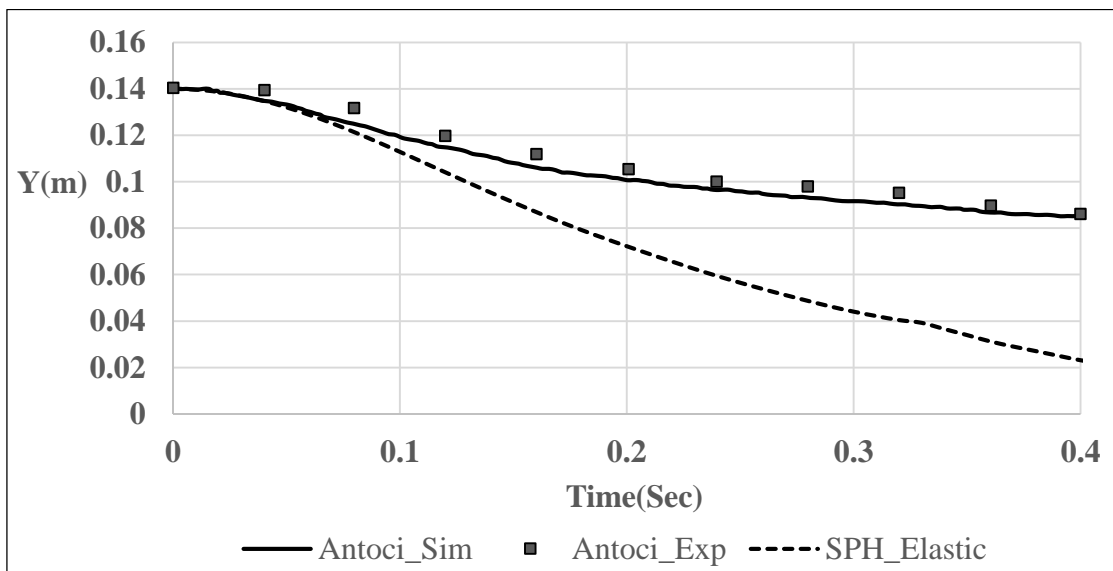


Figure 5.12: Water level (m) 5cm from gate (ALE/FE)

Figures 5.11 and 5.12 show that, for the large gate opening case, there is a large difference between the experiments and the SPH predictions for the fluid flow. Although the total force exerted by the fluid on the structure can be calculated accurately with relatively low resolution, higher resolution is needed to evaluate the pressure at a specific point in the fluid domain (Souto-Iglesias et al. 2008). The SPH simulation results show that though the general dynamics of the flow is captured systematically (Figure 5.6), the global forces exerted by the fluid on the elastic gate are not predicted accurately. This can be attributed to the less accurate pressure prediction in the SPH-FE model as delineated in Delorme et al. (2009) and Antoci et al. (2007), which pointed out that the SPH pressure field gave artificial large oscillations that needed to be suppressed by techniques such as introducing artificial viscosity to stabilize the velocity field and applying correction to the density-pressure estimates. In addition, the SPH interpolation lacks sufficient accuracy to model constant or linear functions of spatial variables (Belytschko et al. 1998). In order to reduce this interpolation error, Colagrossi and Landrini (2003) used a density re-initialization by employing a higher order moving least square (MLS) kernel which assures exact reproduction of any linear function of the spatial variables and hence accurate pressure estimates.

In the SPH model used in this study, there are different ways to calculate pressure. The kernel approximation is used in this study is based on the formulation given by eqns. (11-13) (Monaghan 1992). For this approximation, few particles enter in support of the kernel since it is evaluated near the boundary of the fluid domain leading to lower pressure estimates resulting in an artificially more rapid opening of the gate (see Figure 5.8) and a faster fluid flow, hence a lower free surface level (see Figures 5.11 and 5.12).

A key parameter that also influences the pressure estimations in the SPH model is the smoothing length (h). A mechanism in which more particles can be incorporated in the support domain is by simply varying the smoothing length. Further numerical tests were carried out to study its response on calculating the free end displacements of the elastic gate for different values of the smoothing lengths (h).

Effect of Smoothing Length – Smoothing length (h) is an important parameter in the SPH method. It is defined as the influence area that the smoothing function $W(x, h)$ has on the neighboring particles (Liu et al. 2003). In many SPH codes this parameter is given utmost importance since it not only determines the pattern for the function approximation which defines the dimension of the support domain of particles, but also determines the consistency and hence the accuracy of both the kernel and particle approximations. In a way, this criterion defines a constant that is applied to smoothing of the particles and can be thought of as the representation of the “sphere of influence” of each particle. If h is too small, there may not be enough particles in the support domain to exert forces on a given particle, which results in low accuracy. On the other hand, if the smoothing length is too large, most of the details of the particle or local properties may be smoothed out, and the accuracy suffers significantly. The particle approximations used by the SPH method depend heavily on the number of particles within the support domain. The SPH results shown in the previous sections was for a default value 1.2. Numerical test cases were carried out for the lower and upper bounds for the smoothing lengths of $h = 1.03$ and $h = 1.3$.

Figure 5.13 shows the correlation between the horizontal and vertical displacement of the gate for three different smoothing lengths. Values higher than $h = 1.3$ increases the

computational time significantly and values lower than $h = 1.03$ can lead to instability thus affecting the accuracy.

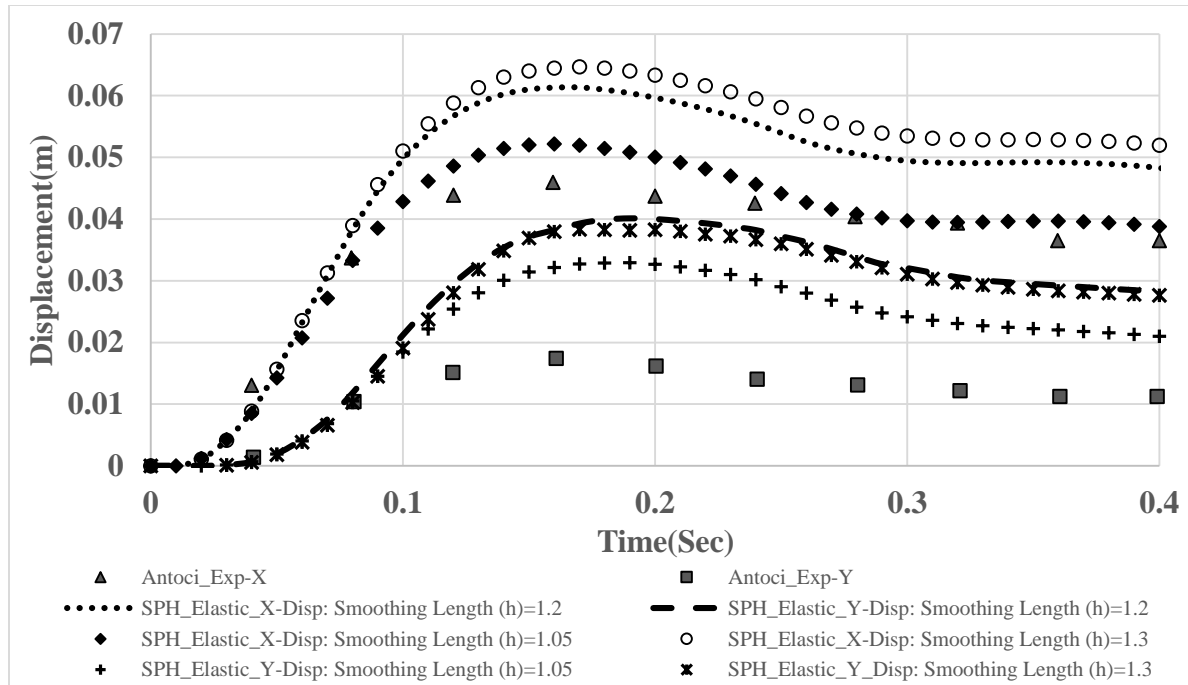


Figure 5.13: X and Y displacement time histories (of the free end of the elastic gate) for different smoothing lengths (SPH/FE)

Interestingly, deductions from Figure 5.13 gave unexpected findings in that for a high particle density, cases with $h > 1.05$ (i.e. the minimum stability value) are less accurate in predicting the displacement response. For the case with $h = 1.05$, even though there is slight improvement in the estimation of the x and y displacements of the free end of the gate, the predictions are similarly inaccurate compared to experimental observations (off by a factor $>50\%$). This finding can be explained by the boundary conditions used for the boundary SPH particles. In this study the ghost particle technique is used (see section 4.2). Observations from the simulation results (Figure 5.13) reveal that, for a higher smoothing

lengths, especially at the boundary of the tank and at the interface between the SPH fluid particles and the elastic gate, there is high particle disorder leading to high repulsive forces that lead to reduction in pressure (pressure-velocity correlation states that when the pressure decreases the flow increases). This leads to an artificially faster flow of the fluid resulting in the rapid opening of the gate. Delorme et al. (2009) mention in their study that for the local measurements of the pressure field, particularly in the zones where the particle disorder is high, it leads to large oscillations in the fluid domain. This is because when the particles are moving, the initial compatibility between mass, volume and density of the fluid particles are lost and Colagrossi and Landrini (2003) stated that this disorder could be restored by the re-initialization of the density field periodically using a higher-order kernel approximation (as mentioned above). Adding artificial bulk viscosity³ is one more way to improve the accuracy (Selhammar 1997). For different coefficients of bulk viscosity (eqn. 21) considered here, we found that there was practically no effect on the maximum displacement of the gate and the water level evolution.

Stress distribution in the elastic gate – The stresses σ_{xx} , σ_{xy} and σ_{yy} in the elastic gate are plotted at $\sim t = 0.124s$, when the displacements are maximum (Figures 5.14-5.15; 5.16-5.17 and 5.18-5.19) for both the ALE-FE/FE and SPH/FE numerical simulations. The ALE-FE/FE simulation results show that the stress distribution seems to be qualitatively correct, showing the internal part of the gate in tension (red), whereas the external part is compressed (blue). This can be attributed to an accurate stress transmission between the

³ In SPH models artificial bulk viscosity is needed to prevent interparticle penetration, to allow shocks to form and to damp post shock oscillations. However, it may lead to unwanted heating and unphysical solutions (Selhammar 1997).

water and the elastic gate ascertained by a good comparison with the experimental test data for both the horizontal/vertical displacements of the gate and accurate capturing of the free-surface profile. A maximum stress value of 0.75MPa is found for the σ_{yy} component near the clamp, while the other components show lower maximum values.

On the other hand, the SPH/FE simulation results for the stress distribution show an under-prediction of the stress values on the gate. This can be attributed to the inaccurate estimation of the contact pressure between the water particles and the elastic gate. This is largely due to the overprediction of both the horizontal and vertical displacements of the gate and a higher flow rate of the water compared to the observed experiment results. A maximum stress value of 7,400Pa is found for σ_{xx} component near the clamp, while the minor components show a much lower maximum values.

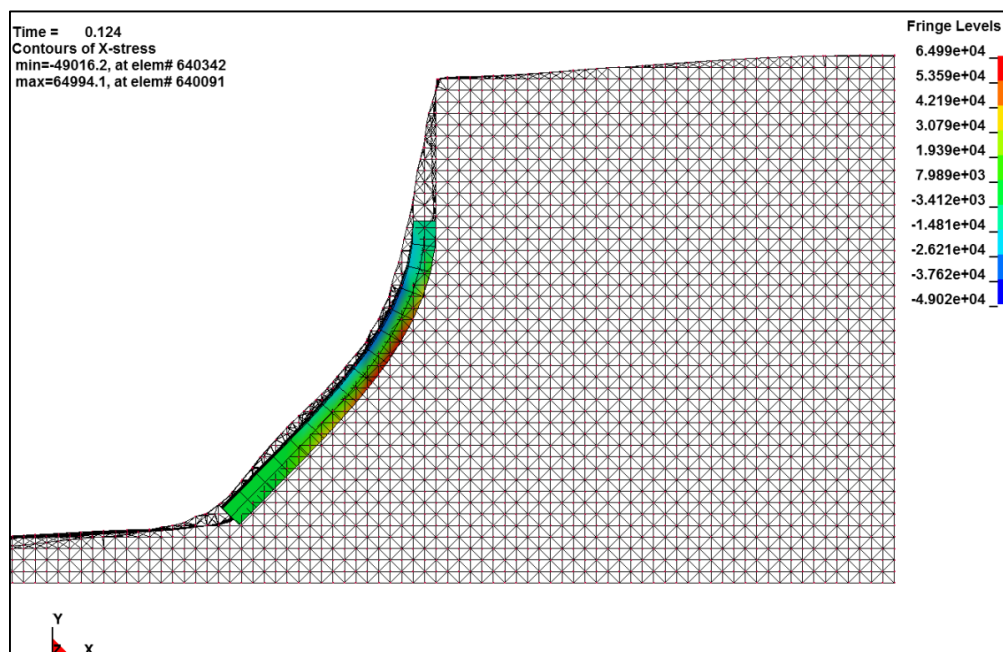


Figure 5.14: σ_{xx} distribution at $t = 0.124s$: color scale ranging from $\sigma_{xx} = -49020N / m^2$ (blue) to $\sigma_{xx} = 65000N / m^2$ (red)-ALE/FE.

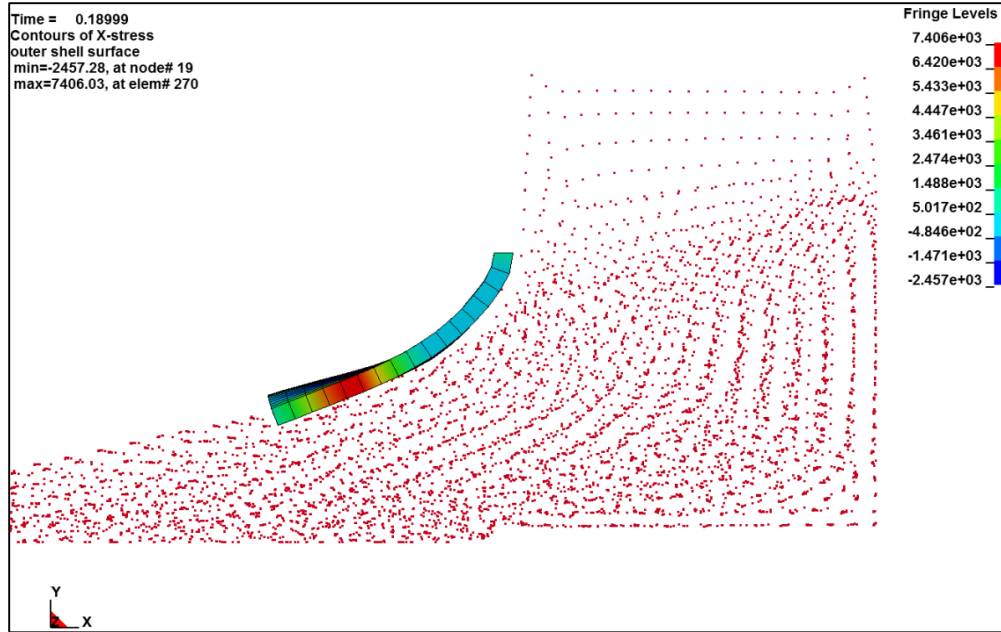


Figure 5.15: σ_{xx} distribution at $t = 0.19s$: color scale ranging from $\sigma_{xx} = -2457N/m^2$ (blue) to $\sigma_{xx} = 7406N/m^2$ (red)-SPH/FE.

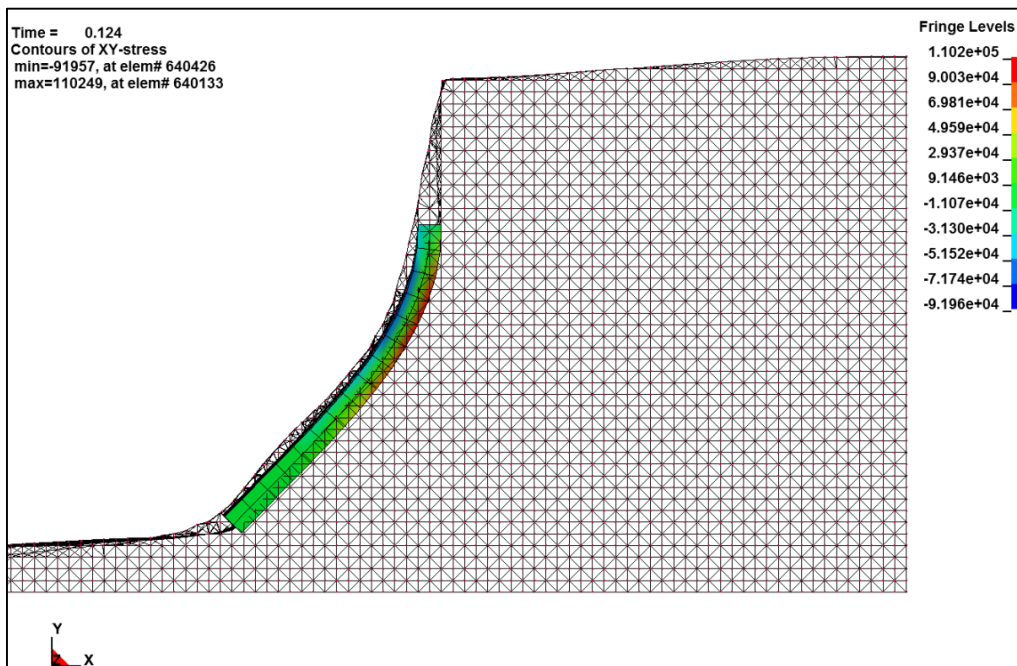


Figure 5.16: σ_{xy} distribution at $t = 0.124s$: color scale ranging from $\sigma_{xy} = -91960N/m^2$ (blue) to $\sigma_{xy} = 110200N/m^2$ (red)-ALE/FE.

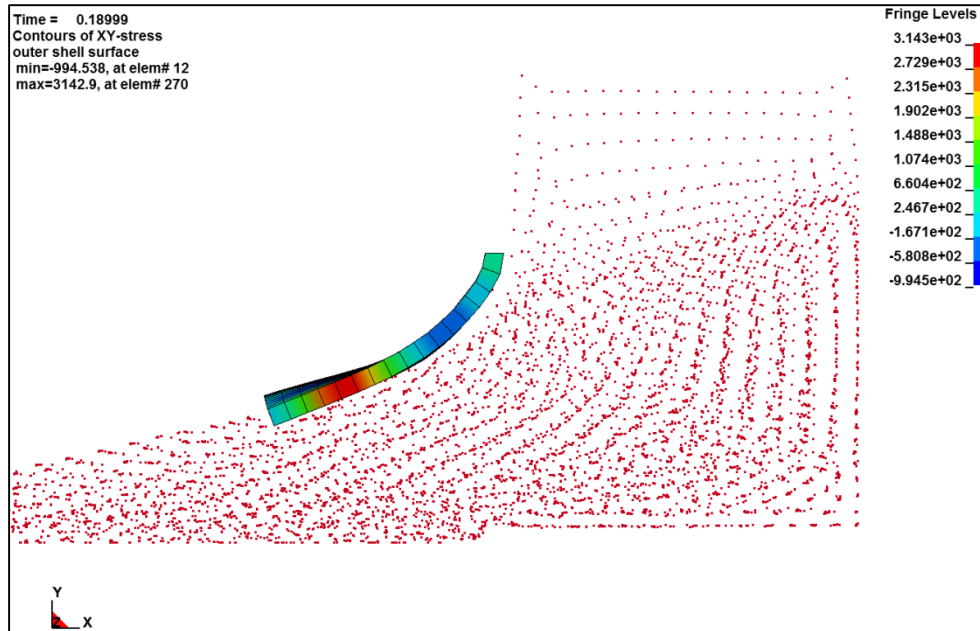


Figure 5.17: σ_{xy} distribution at $t = 0.19s$: color scale ranging from

$\sigma_{xy} = -994.5N/m^2$ (blue) to $\sigma_{xy} = 3143N/m^2$ (red)-SPH/FE.

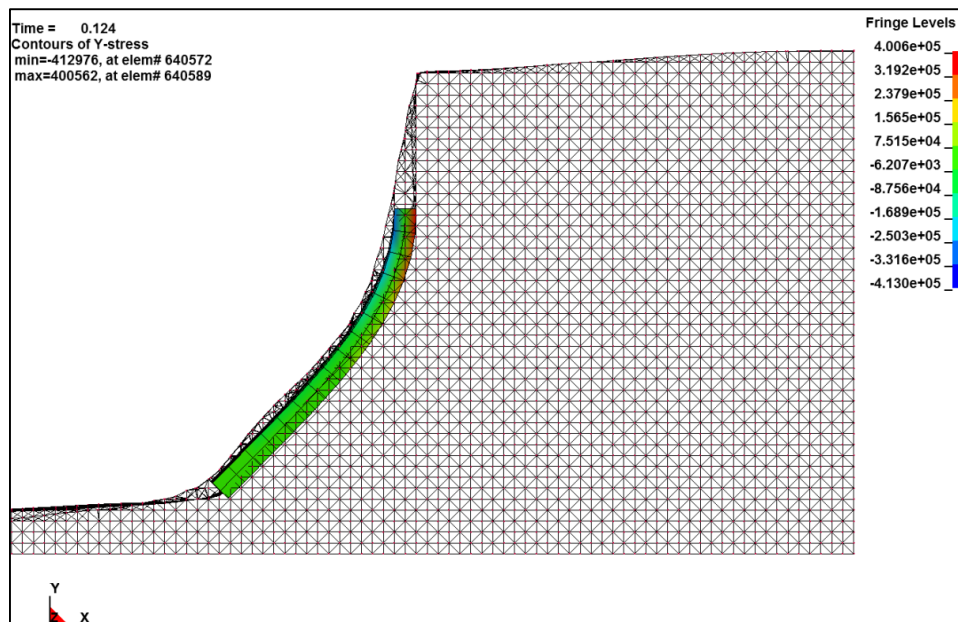


Figure 5.18: σ_{yy} distribution at $t = 0.124s$: color scale ranging from

$\sigma_{yy} = -413000N/m^2$ (blue) to $\sigma_{yy} = 400600N/m^2$ (red)-ALE/FE.

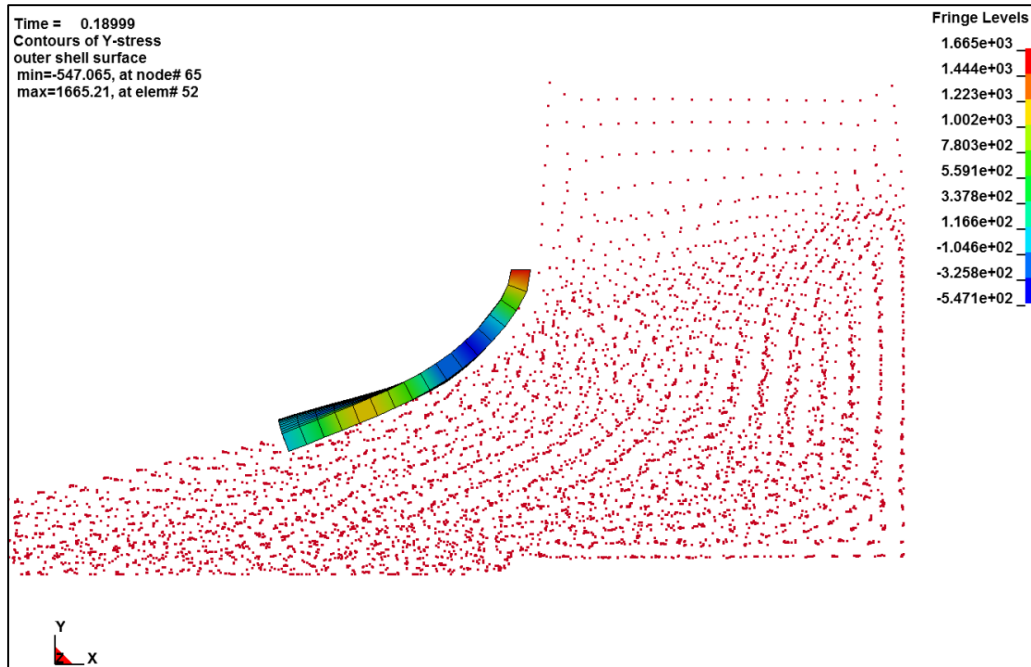


Figure 5.19: σ_{yy} distribution at $t = 0.19s$: color scale ranging from

$$\sigma_{yy} = -547 N / m^2 \text{ (blue) to } \sigma_{yy} = 1665 N / m^2 \text{ (red)-SPH/FE.}$$

5.7 Sensitivity and convergence Study

A convergence study is conducted to examine how the simulation results vary with the change of the ALE-FE/FE mesh discretization. The analysis presented below is based on the case of the deformation of an elastic gate subjected to time-dependent water pressure. Note that the convergence study was performed only for the ALE-FE/FE model only owing to its excellent predictive capability in capturing the physics (compared to the experimental test data) of not only the deformation of the free-end portion of the gate but also the accurate estimation of the water-free surface profile. (A convergence study was not conducted for the SPH because the method is deemed not sufficiently accurate for the analysis of this particular experiment set up and model.) The results shown in the previous

section for the ALE-FE/FE model are with $ds = 0.0025m$ (1:1 ALE to FE mesh ratio). A convergence study was performed for different ALE and FE mesh sizes ($ds = 0.01m, 0.0025m, 0.00125m$). All the simulation runs were performed using MPP (12 nodes).

Figures 5.20 and 5.21 show the horizontal and vertical displacement of the free end of the gate for different ALE mesh sizes, respectively. The figures show that, with the refinement of the mesh size, the results seem to converge for both the x and y displacements of the free end of the gate. Mesh size somewhat greater than $ds = 0.01m$ seem to produce the physics reasonably well, but the displacements of the free end of the gate are less than what it was in the experiments as the contact and impact force between the structure and the fluid mesh is sensitive to the number of coupling points between them. Refinement of the ALE and FE mesh between the fluid and the elastic gate also indicates a smooth transition of the fluid-structure interaction pressure. Estimation of computation time spent on the fluid and structural portions of the numerical simulations for different mesh sizes are also studied. Table 5.2 shows that the explicit ALE-FE/FE solver takes much more time for finer mesh sizes. As expected, the ALE technique consumes large amount of computational resources with increasingly finer spatial discretization.

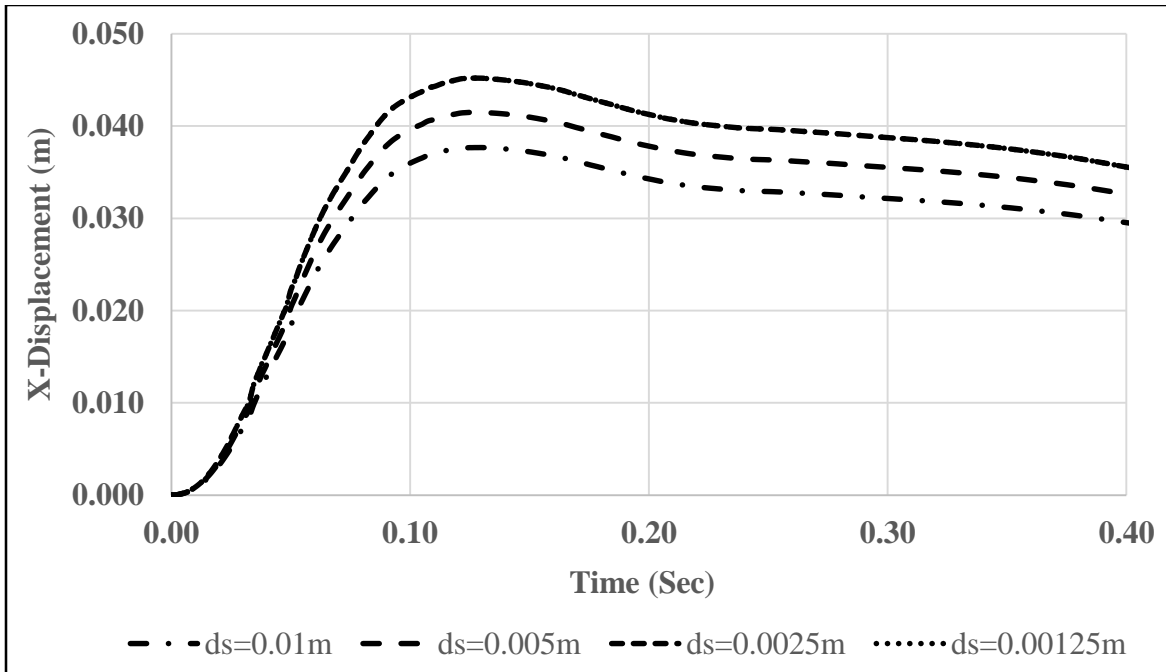


Figure 5.20: Horizontal displacement free end of the gate – ALE mesh size variations (“ds” represents the ALE/FE mesh size = all dimensions are in m)

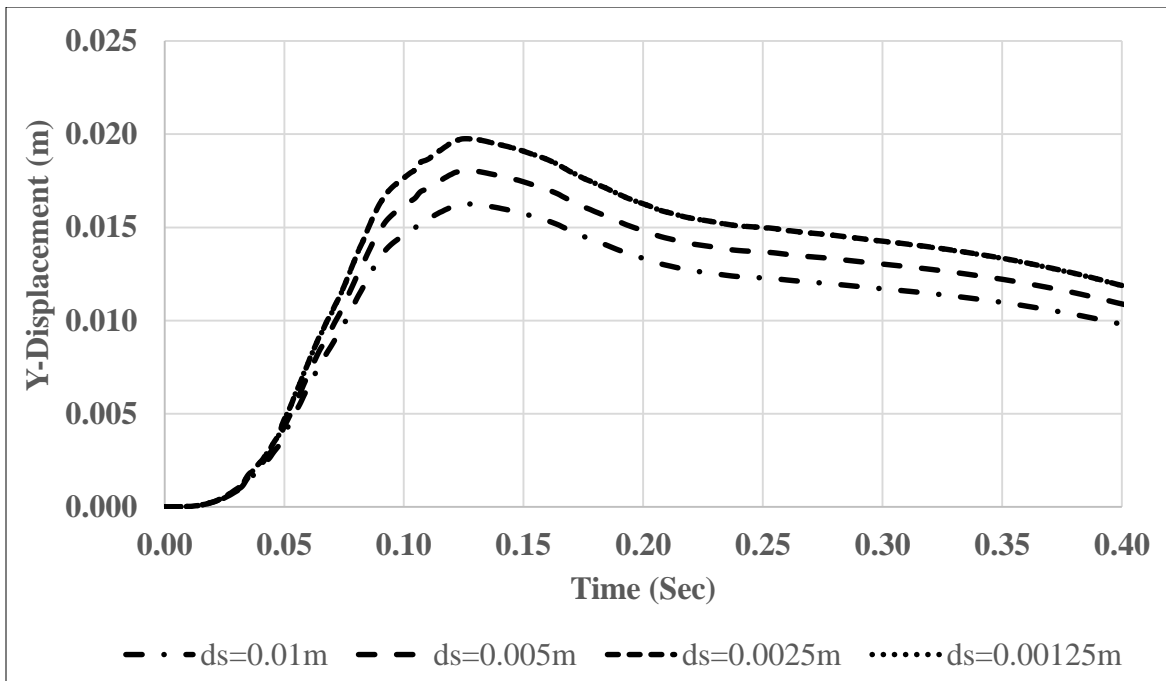


Figure 5.21: Vertical displacements of the free end of the gate – ALE mesh size variations (“ds” represents the ALE/FE mesh size – all dimensions are in m)

Table 5.2. Comparison of computation time for ALE/FE solver

FE-ALE Geometric Spacing (m)	Time Step (s)	Total Number of Time Steps	Total Time (s)
ds=0.01	1.25E-05	11480	13608
ds=0.005	2.65E-05	25250	35450
ds=0.0025	6.76E-06	68219	67895
ds=0.00125	1.72E-07	181023	156880

5.8 Conclusions

The predictive capability of an arbitrary Lagrangian-Eulerian based finite element (FE) formulation and a discrete particle method (SPH) for the numerical simulation of a benchmark fluid-structure interaction problem under a consistent computational platform is presented in this study. The interaction force between the fluid and the structure are computed through a penalty based coupling procedure. In particular, the coupling forces are calculated based on the penetration distance between the ALE materials across the Lagrangian surface. On the other hand, for the SPH particles, as there is no mesh connectivity, the interaction or coupling between the SPH fluid and the structural elements is defined using a single tied or penalty based contact definitions. Even in the presence of large displacements of the structure, no definitive treatment to capture the free-surface of the fluid is needed. The contact between the particles is initiated when they are closer than twice the smoothing length.

The performance of both the numerical models was evaluated by comparing the numerical simulation results to experimental test data of the fluid discharge in a tank interacting with

an elastic gate. Numerical simulation results show that the displacement of the elastic gate subjected to a time-dependent fluid pressure and the evolution of the fluid free-surface profiles can be predicted accurately (within 4%) by the ALE/FE formulation.

A (pure Lagrangian) smoothed-particle hydrodynamic (SPH) method predicted a significantly larger motion of the free end of the gate and a faster decrease in the fluid level leading to an over prediction of horizontal and vertical gate displacements (by 37% and 71%, respectively). This can be attributed to the well-documented less accurate pressure prediction in the SPH method which gives large oscillations in the pressure field that needs to be smoothed using techniques such as adding artificial bulk viscosity to stabilize the velocity field and by also applying correction to the density-pressure estimates using higher order kernel approximations. During the initialization of the pressure in the SPH simulations only a few particles enter in the support of the kernel, which leads to lower pressure estimates and faster opening of the gate.

Results obtained by varying the smoothing length between the lower bound (bounded by stability, $h = 1.03$ for the problem in this study) and upper bound (bounded by computational efficiency, $h = 1.30$) indicates that a larger smoothing length did not yield the most accurate results. The best prediction of the elastic gate displacement was obtained using the lower bound value (which is off by >50%). This finding can be explained by the high particle disorder (particularly at the tank wall boundaries and at the elastic gate and fluid interface) resulting in very high repulsive forces that lead to a reduction of the pressure. As delineated in the literature, this disorder can be restored by the re-initialization of the density field periodically using higher-order kernel approximations. On the other

hand, adding artificial bulk viscosity had practically no effect on the predictions of the maximum displacement of the gate and the water level evolution.

An evaluation of the computational efficiency of the two numerical methods show that the average clock ratios of the FE method is about four times faster than that of the SPH. Using more SPH particles per FE element at the fluid-structure interface often leads to higher computational costs without noticeable improvements in accuracy.

An advantage of using the SPH method is the relatively short pre-processing time and a good capture of the overall physics of the fluid motion. However, the ALE model is shown to capture the fluid-structure interaction and the fluid free-surface dynamics accurately.

5.9 Acknowledgements

Financial support from the US Office of Naval Research Grants N00014-13-1-0849 is gratefully acknowledged.

5.10 References

- Antoci, C., Gallati, M., and Sibilla, S. (2007). "Numerical simulation of fluid-structure interaction by SPH. *Journal of Computers and Structures*." 85, 879-890.
- Bathe, K.J., and Zhang, H. (2004). "Finite element developments for general fluid flows with structural interactions." *International Journal of Numerical Methods in Engineering*, 60, 213–32.
- Belytschko, T., Flanagan, D.F., and Kennedy, J. M. (1982). "Finite element method with user-controlled meshes for fluid-structure interactions." *Computer Methods in*

Applied Mechanics and Engineering, 33, 689–723.

Belytscho, T., Krogauz, Y., Dolbow, J., and Gerlach, J. (1998). “On the completeness of meshfree particle methods.” *International Journal of Numerical Methods in Engineering*, 43(5), 785-819.

Colagrossi, A., and Landrini, M. (2003). “Numerical simulation of interfacial flows by Smoothed Particle Hydrodynamics.” *Journal of Computational Physics*, 191, 448–475.

Dalrymple, R.A., and Rogers, B.D. (2006). “Numerical modeling of water waves with the SPH method.” *Coastal Engineering Journal*, 53(2), 141-147.

Delorme, L., Colagrossi, A., Souto-Iglesias, A., Zamora Rodriguez, R., and Botia-Vera, E. (2009). “A set of canonical problems in sloshing, Part I: Pressure field in forced roll—comparison between experimental results and SPH.” *Ocean Engineering*, 36, 168–178.

Donea, J., Huerta, A., Ponhot, J.P., and Rodriguez-Ferran, A. (2004). “Arbitrary Lagrangian-Eulerain Methods. Encyclopedia of Computational Mechanics.” John Wiley Sons. NY.

Dilts, G. (1999). “Moving-least-squares-particle hydrodynamics – i. consistency and stability.” *International Journal of Numerical Methods in Engineering*, 44(8), 1115-1155.

Gingold, R.A., and Monaghan, J.J. (1977). “Smoothed particle hydrodynamics: Theory and application to non-spherical stars.” *Monthly Notices of the Royal Astronomical Society*, 181, 375–389.

Hallquist, J. O. (2006). “LS-DYNA Theoretical Manual,” Livermore Software Technology

- Corporation, California, USA.
- Lacome, J. L. (2009). "Smoothed Particle Hydrodynamics (SPH): A new feature in LS-DYNA," 7th European LS-DYNA Conference, May 14th and 15th, Salzburg, Austria.
- Leer, B. V. (1977). "Towards the ultimate conservative difference scheme. IV. A new approach to numerical convection." *Journal of Computational Physics*, 167, 276-299.
- Le Tallec, P., and Mouro, J. (2000). "Fluid structure interaction with large structural displacements." *Computational Methods in Applied Mechanics Engineering*, 1–29.
- Liu, G.R., and Liu, M.B. (2003). "Smoothed Particle Hydrodynamics: a meshfree particle method," World Scientific, Singapore.
- Lucy, L. B. (1997). "A numerical approach to the testing of the fission hypothesis," *Astronomical Journal*, 82, 1013–24.
- Monaghan, J. J. (1992). "Smoothed Particle Hydrodynamics." *Annual Review of Astronomy and Astrophysics*, 30, 543-574.
- Monaghan, J. J., and Gingold, R. A. (1983). "Shock simulation by the particle method SPH." *Journal of Computational Physics*, 52, 374-389.
- Monaghan, J.J. (1994). Simulating free surface flows with SPH. *Journal of Computational Physics*, 110, 399–406.
- Monaghan, J. J. (2005). Smoothed particle hydrodynamics." *Rep Progr Phys*, 68, 1703-1759.
- Monaghan, J. J., and Kos, A. (1999). Solitary waves on a cretan beach. *Journal of the Waterway, Port, Coastal, and Ocean Engineering*, 125 (3), 145.

- Randles, P.W., and Libersky, L.D. (1996). "Smoothed particle hydrodynamics: some recent improvements and applications." *Computational Methods in Applied Mechanics Engineering*, 139, 375–408.
- Rugonyi, S., Bathe, K. J. (2001). "On finite element analysis of fluid flows fully coupled with structural interactions." *Computational Models for Engineering Science*, 2, 195–212.
- Schwer, L. (2009). "Aluminium plate perforation: A comparative case study using Lagrange with erosion, multi-material ALE, and Smooth Particle Hydrodynamics." 7th European LS-DYNA conference, Stuttgart, Germany.
- Selhammar, M. (1997). "Modified artificial viscosity in smooth particle hydrodynamics." *Journal of Astronomy and Astrophysics*, 325, 857-865.
- Souli, M., and Benson, D.J. (2010). "Arbitrary Lagrangian-Eulerian and fluid-structure interaction Numerical Simulation." Wiley, New York.
- Souto-Iglesias, A., Idelsohn, S., Marti, J., Zamora-Rodriguez, R., and Onate, E. (2008). "Modeling of free surface flows with elastic bodies interactions," 27th Symposium on Naval Hydrodynamics, Korea.

Arbitrary Lagrangian-Eulerian Finite Element Modeling and Analysis of Surface Effect
Ship Bow Seal Motions

Ravi Challa, David Newborn and Solomon C. Yim, F.ASME

To be submitted

6 NUMERICAL SIMULATION OF SURFACE EFFECT SHIP BOW FINGER SEAL FLUID-STRUCTURE INTERACTION

6.1 Abstract

This study examines the bow finger seal motions of a scale-model of a free-running surface effect ship (SES) with a fully pressurized air cushion using numerical modeling and simulations. A systematic approach in modeling the interactions of the various components of the SES, such as forward speed, air cushion pressure, and bow and stern seal interactions with the pressurized air cushion and water domains, resulted in an accurate numerical reconstruction of the experimental test conditions. Numerical simulation results are compared to experimental data from a free-running SES scale model to measure the response of flexible, hydroelastic bow finger deflections. A two pronged numerical modeling approach was developed to systematically study the behavior of a fully-pressurized SES under a steady current. First the fluid-structure interaction (FSI) behavior of a full SES model with multiple rigid bow seals is studied. Simulation results show that the fluid flow in the cushion chamber away from the hull boundaries is practically identical from seal to seal. Subsequently, the dynamics of a fully-coupled FSI behavior of a single flexible bow finger with partial submergence in a uniform current is examined in detail. Numerical results show that the predictions of the bow finger seal deflections compare well with experimental data. The fully-coupled FSI modeling and analysis methodology developed can be readily employed to perform parametric studies on a wide range of parameters including free stream water speed, air cushion pressure and depth of immersion.

Keywords: Fluid-Complex structure-Interaction, Surface Effect Ship, Cushion Pressure, Bow Finger Seal Dynamics, Finite-Element, Arbitrary Lagrangian-Eulerian Formulations

6.2 Introduction

A free-running surface effect ship (SES) is an innovative concept designed to advance the speed and logistics of naval operations. An SES is a fan-activated air cushion vessel with two side hulls which operates in modes of full displacement, partial air-cushion support and a full air-cushion support. Predicting the SES bow seal motions is of paramount importance in the design phase, as the ship motion is affected by the interaction between the pressurized air cushion, bow and aft seals, and the sea waves in different propagating water depth regimes.

Extensive background and historical perspective of SES development was documented in Lavis (2011) and Yun and Bliault (2000). Previous model and full scale SES seal dynamics studies were conducted as far back as the 1970s. A detailed quantification of SES seal motions, in particular fluttering and wear-inducing folding was conducted by Besch (1976), wherein accelerations of seals were collected by surface-mounted accelerometers. Also, Besch (1976 & 1979) included qualitative photographic monitoring of seal motions. A similar methodology to Besch (1976 & 1979) was employed by Ryken (1978), which aimed to quantify the bow finger motions and seal drag of the SES-100B ship design. The investigations included lift and drag of bow and stern seals, maneuvering performance, air cushion pressure distribution and fan rates, and time- and frequency-domain simulations based on trial data.

Doctors and McKesson (2006) developed an analytical approach to predict the deflection of two dimensional bow and stern seals. An experiment was conducted at the University of Michigan for evaluating the bow seal drag characteristics (Wiggins *et al.*, 2011). The experiment focused on two dimensional planing bow seal deflection under steady forward speed (Zalek *et al.* 2011) and position of deflected bow seals. Donnelly *et al.* (2010) used computational fluid dynamics simulations (STAR-CCM+) to study the drag and the effect of cushion pressure on rigid seals. They carried out simulations for a range of Froude numbers and in two headsea regular wave conditions. Espinosa *et al.* (2013) used a time-domain finite element model to evaluate the SES skirt dynamics using a potential flow approach with a stream-line integration of the free surface. They developed a fluid-structure algorithm to study the dynamic behavior of the seals in the interface between the air cushion and water. Kramet *et al.* (2013) studied the calm-water resistance of an SES including bow and stern seal interaction effects in steady-state operations. They developed a simple and effective 2-D numerical model based on a potential-flow solver with a single-degree-of-freedom seal model and a rigid body vessel motion model. Their numerical model offered accurate predictions for the low-speed resistance of SES seal drag and vessel motion. Yang *et al.* (2010) studied a complex fluid-structure (FSI) problem involving simulation of a two-dimensional free-stream flow interacting with a deformable, pressurized surface, such as an air cushion vehicle or surface effect ship (ACV/SES) bow seal using the finite element method (FEM) and the smoothed particle hydrodynamics (SPH), or FEM-SPH, coupling approach. In their study the fluid domain was based on SPH and the structural domain employed a large-deformation FEM. Imas *et al.* (2011) numerically examined the three-dimensional fluid-structure interaction between a free-

surface disturbance and a deformable membrane as a canonical problem representative of the interaction between an SES skirt advancing with forward speed in waves using an SPH method. Bloxom (2014) verified and validated a commercially available FSI numerical simulation tools to model the bow seal mechanics. The computational tools utilized were an iterative partitioned coupling scheme between STAR-CCM+ finite volume fluid solver and a finite element structural solver (Abaqus) to simulate the FSI response of a system. Preliminary verification and validation work was carried out to understand the numerical behavior of the codes individually and together as a FSI computational and analysis suite. Due to markedly limited literature in utilizing finite element analysis and fully coupled FSI modeling techniques for SES bow finger seals endeavors an opportunity to evaluate the bow seal motions of an SES.

This study examines the bow finger seal motions of a scale-model of a free-running surface effect ship (SES) with a fully pressurized air cushion using numerical modeling and simulations. A brief description of the set-up of an experiment conducted on a free-running SES at the Oregon State University Hinsdale Wave Research Laboratory to measure the bow seal deflections is presented first to give an insight into the concept of a pressurized air cushion while a free-running SES was underway. This is followed by a description of the numerical formulation and procedure to model the interaction between bow finger seals and the water-free surface. A two pronged numerical modeling approach was developed to systematically study the behavior of a fully-pressurized SES under a steady current. First the fluid-structure interaction (FSI) behavior of a full SES model with multiple rigid bow seals is studied. Subsequently, the dynamics of a fully-coupled FSI behavior of a single flexible bow finger with partial submergence in a uniform current is examined in detail.

Major findings are summarized in the conclusion section. (A brief introduction to the SES and the concept of air-cushion in the SES are presented in Appendix B.)

6.3 Free-running SES physical experiment

A free-running surface effect ship (SES) experiment was conducted in the Oregon State University Hinsdale Wave Research Laboratory 3D wave basin. The experiment was designed to provide data for the hydroelastic response of a bow finger seal near the centerline of the scale model. The experiment required a steady forward speed therefore the SES scale model was retrofitted to execute free-running maneuvers. Due to the weight margins of the SES of opportunity, only slow speeds were achievable. Also, due to the usable length of the three-dimensional (3D) wave basin at OSU, only relatively short runs were possible.

A principal hypothesis of the experimental investigation is that the strain in the bow finger seal material is small and does not exceed the linear region of the stress-strain relationship. Also, the seal material is assumed to behave as a membrane, where stress normal to the surface is neglected but nonlinear geometric deflections are important. Following those assumptions, the material used for the bow finger seals is confirmed to be thin enough to be modeled as a shell, and to contain negligible bending stress. A ripstop nylon fabric was used for the bow and stern seals, and the Young's modulus was approximately 14.9×10^7 N/m² and the Poisson Ratio was approximately 0.14 (Lamcotec 2014). The nylon material was part of the original configuration of the hull, so the author's did not have control of the material selection.

In order to obtain an accurate, robust surface effect ship model in a timely manner, an SES scaled model with a linear scale factor of approximately 1:30 was used. Figure 6.1 shows a free-running SES model.

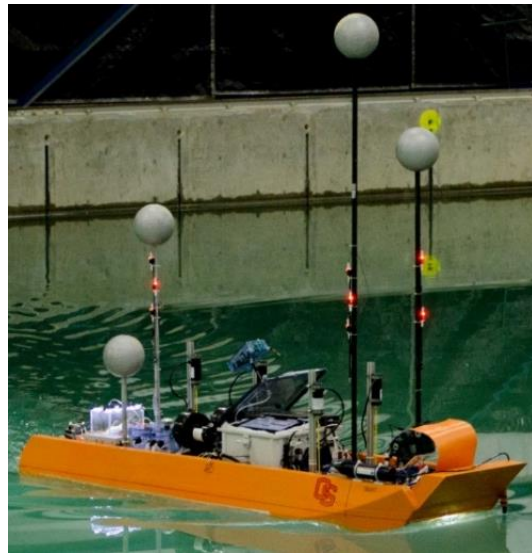


Figure 6.1: Free-running SES model

Table 6.1 shows the free-running SES experiment parameters which include the mass properties of the SES scale model and moments of inertia and the physical dimensions of the SES scale model. Two high speed cameras were mounted over an opening in the wet deck near a bow finger seal on the SES model. Figure 6.2 shows the orientation of the cameras, and an example still image from video collected during a constant speed, straight trajectory trial is shown in Figure 6.3.

Table 6.1. Free-running SES experiment parameters

SES scale model physical dimensions	Value		
Length	2.89m		
Beam width	0.76m		
Height	1.92m		
SES scale model mass Characteristics	Value		
Mass	73.3 kg		
Centre of gravity	Longitudinal	Lateral	Vertical
	1.17m	0.00m	unknown
SES scale model moments of inertia	Period of Oscillation (s)		Principal Moment of Inertia (kg-m²)
Roll	0.64		15.9 kg-m ²
Pitch	0.49		73.8 kg-m ²
Yaw	2.39		65.4 kg-m ²



Figure 6.2: As-installed orientation of bow finger seal high speed cameras mounted on acrylic window.

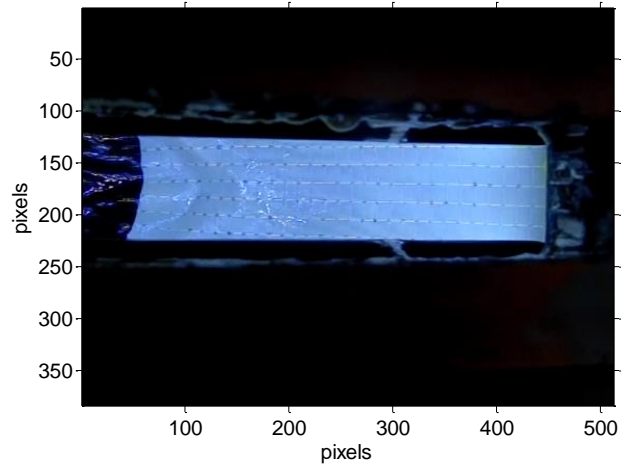


Figure 6.3: Raw color image of bow finger seal from high speed video

Experimental results for the forward motion of a model-scale SES (0.7m/s) with a fully pressurized air cushion chamber (408Pa) produced a dominant frequency of bow finger seal deflection to be approximately 12.1Hz. For the vibrating SES bow finger seal the wavelength of the predominant progressive waves were identified based on the sampling of the high-speed video in which progressive crests could be seen. The average value of the wavelength was 0.0240m.

An important quantity for the SES bow finger seal is the maximum deflection of the bow finger seal skirt nodes once a steady state is achieved. Experimental results obtained from qualitative videos for the equilibrium deflection of the skirt nodes reveal that the SES model scale has a mean x-displacement of 0.002m, y-displacement of 0.0001m and z-displacement of 0.011m, respectively.

6.4 General hydrodynamics of the flow around the SES

A high-speed vessel is defined as a craft with maximum operating speed higher than 30 knots (>15m/s) (Baird 1998). However, hydrodynamicists tend to use a Froude number $F_r = V / \sqrt{gL}$ larger than about 0.4 to characterize a fast vessel supported by the submerged hull (Faltinsen 2005), where V is the ship speed, L_s is the overall submerged length of the ship and g is the acceleration due to gravity.

The fundamental hydrodynamics present near a SES bow finger seal includes the acceleration of the quiescent fluid around the seal as the scale model travels along a free surface, the hydrostatic water pressure due to the set down of the free surface inside the air cushion cavity, and the generation of a turbulent boundary layer on the leading face of the seal.

In this study, for a flow speed of 0.7m/s, maximum submerged length of the ship of 2.46m (with the bow finger predominant length of 0.13m) and, for a water depth of 1.5m, the values of the Reynolds and Froude numbers are 9.1×10^4 (range: $3.0 \times 10^4 < Re < 1.2 \times 10^5$) and 0.18, respectively. This shows that the flow is subcritical (i.e., $F_r < 1$) and it is in the turbulent regime where the viscous effects is negligible compared to inertial effects.

Observations from the experiments reveal that the motion of the bow seal fingers can be divided mainly into three components: (i) the mean values of the bow seal deflections, which are nonlinear functions of inside pressure, outside pressure, finger material characterization, mean finger height and vessel speed, (ii) the fluctuating motions are due to turbulence, and (iii) the effect of turbulence on the bow finger motions.

6.5 Arbitrary Lagrangian-Eulerian formulation and finite-element solution procedure

The Navier Stokes equations and the ALE formulations are solved over the entire computational domain. In the ALE description, an arbitrary referential coordinate is introduced in addition to the Lagrangian and ALE coordinates (Souli and Benson 2010). The material time derivative of a variable with respect to the reference coordinate can be described as

$$\frac{dg(\bar{X}, t)}{dt} = \frac{\partial g(\bar{x}, t)}{\partial t} + (\bar{v} - \bar{w}) \cdot \overline{\text{grad}} g(\bar{x}, t) \quad (1)$$

where \bar{X} is the Lagrangian coordinate, \bar{x} is the ALE coordinate, \bar{v} is the particle velocity, and \bar{w} is the grid velocity of the numerical simulation. The ALE differential form of the conservation equations for mass, momentum, and energy are readily obtained from the corresponding Eulerian forms:

Mass:

$$\rho \frac{\partial \bar{v}}{\partial t} + \rho \text{div}(\bar{v}) + (\bar{v} - \bar{w}) \cdot \overline{\text{grad}}(\rho) = 0 \quad (2)$$

Momentum:

$$\begin{aligned} \rho \frac{\partial \bar{v}}{\partial t} + \rho (\bar{v} - \bar{w}) \cdot \overline{\text{grad}}(\bar{v}) &= \overline{\text{div}}(\bar{\sigma}) + \bar{f} \\ \rho \frac{d\bar{v}}{dt} &= \overline{\text{div}}(\bar{\sigma}) + \bar{f} \end{aligned} \quad (3)$$

Energy:

$$\begin{aligned} \rho \frac{\partial e}{\partial t} + \rho(\vec{v} - \vec{w}) \cdot \overrightarrow{\text{grad}}(e) &= \overline{\overline{\sigma}} : \overline{\overline{\text{grad}}}(\vec{v}) + \vec{f} \cdot \vec{v} \\ \rho \frac{de}{dt} &= \overline{\overline{\sigma}} : \overline{\overline{\text{grad}}}(\vec{v}) + \vec{f} \cdot \vec{v} \end{aligned} \quad (4)$$

where ρ is the mass density, \vec{f} is body force vector, and e is the total energy. $\overline{\overline{\sigma}}$ denotes the total Cauchy stress given by:

$$\overline{\overline{\sigma}} = -p\overline{\overline{I}} + \mu(\overline{\overline{\text{grad}}}(\vec{v}) + \overline{\overline{\text{grad}}}(\vec{v})^T) - 2/3\overline{\overline{\text{grad}}} \cdot \vec{v}\overline{\overline{I}} \quad (5)$$

where p is the pressure, $\overline{\overline{I}}$ is the identity tensor, μ is the dynamic viscosity, and $(\vec{v} - \vec{w})$ is the convective velocity across the grid.

6.6 Finite-Element modeling of air and water domains and SES

The fully coupled FSI problem is modeled using solid brick elements. The analysis of a SES against a steady flow in general and the bow seal deflections in particular is studied as a three-dimensional phenomenon. A numerical code for nonlinear dynamic analysis of structures in three dimensions (3D), LS-DYNA, is used in the current study (Version: mpp971d R7.0.0 and Revision: 79055) [20].

Figure 6.4 shows the initial configuration for the three dimensional ALE-FE simulation. Isometric view of the computation domain consisting of SES, water, air and air-pump is shown in Figure 6.5. Dimensions of the SES model are as per the specifications given in Table 1.

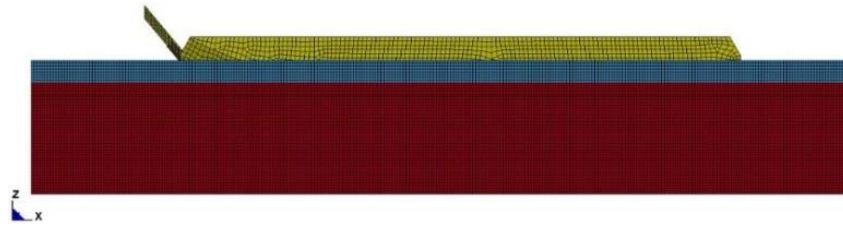


Figure 6.4: FE-ALE simulation: 3D Computational domain of SES system (Red: water domain | Blue: air domain | Yellow: SES with rigid bow finger and stern seals)

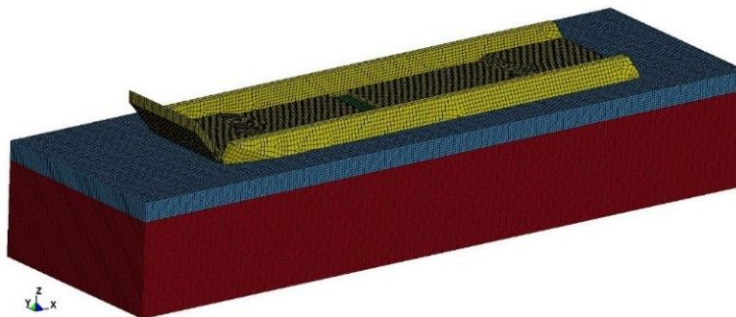


Figure 6.5: FE-ALE simulation: Isometric view of the 3D computational domain of fully coupled SES domain (SES, water, air and air-pump)

The FSI model involves three components: the water domain, the air domain and the SES (Figures 6.4 and 6.5). The air-water mesh was modeled as a rectangular mesh (mesh size of 10mm grid). The computational domain constitutes of 273,934 nodes, 237,105 solid elements with two solid parts of which there are 80,817 rigid shell elements (SES) and 156,288 deformable elements (air and water ALE solid elements). An important feature in simulating contact and impact problems is proper modeling of the two-phase flow including the presence of air. In this study we include air modeling using material properties and a governing equation of state (Challa and Yim, 2014).

Dynamic FE models for the FSI requires a detailed set-up procedure which involves modeling of the various components needed to accurately simulate the physics, material

and element characterization of the participating components followed by a proper coupling mechanism to define a contact between various materials, boundary condition and load body definitions. A fluid with very little shear strength is used to model the water and air domains with mass densities of $1,000 \text{ kg/m}^3$ and 1.29 kg/m^3 , respectively, which needs an equation of state to be defined. The bow seal is treated as a flexible body with a mass density of 0.0417 kg/m^3 , Young's modulus of $2\text{E}+07 \text{ N/m}^2$ and Poisson's ratio of 0.3.

The air-water domains have been discretized using 8-noded solid brick elements. Bow finger seals have been modeled using 4-noded Belytschko-Lin-Tsay shell element with a membrane formulation. Belytschko-Lin-Tsay shell element (Belytschko and Tsay, 1981 and 1984) is the basis for this very efficient membrane element. A triangular membrane element may be obtained by collapsing adjacent nodes of the quadrilateral. Detailed formulation of the membrane formulation is presented in Appendix C.

In the present study, a penalty based coupling is used to model the complex event between SES (bow fingers in particular) and the water-air domain. This type of interface/contact is mainly used when there is a need for the Arbitrary Lagrangian and Eulerian (ALE) transformations for the coupled contact-impact scenario.

The boundary conditions employed in the numerical model are partially the material surfaces (out-of-plane, in-plane and bending restraint). The material surfaces defined in the FE formulation are: (a) no particles can cross them and (b) stresses must be continuous across the surfaces. The elements of the water domain were given the null hydrodynamic material type which allowed a new equation of state (EOS) to be specified (Hallquist 2006). In many situations, an EOS is required to accurately simulate the material behavior. An EOS determines the hydrostatic behavior of the material by calculating pressure as a

function of density and perhaps, energy or temperature. Situations that call for an EOS (in the present case the water and air domains) are characterized by very high strain rates and material pressures. Hence EOS such as the Gruneisen is the suggested methodology to simulate fluid domains in the current FE solver. The Gruneisen equation of state with cubic shock velocity-particle velocity is applied in our numerical model and it defines pressure as:

$$p = \frac{\rho_0 C^2 \mu [1 + (1 - \frac{\gamma_0}{2})\mu - \frac{\alpha}{2}\mu^2]}{[1 - (S_1 - 1)\mu - S_2 \frac{\mu^2}{\mu + 1} - S_3 \frac{\mu^3}{(\mu + 1)^2}]} + (\gamma_0 + \alpha\mu)E \quad (6)$$

where E is the internal energy per initial volume, C is the intercept of the $u_s - u_p$ curve (speed of sound in water). S_1 , S_2 , and S_3 are the coefficients of the slope of the $u_s - u_p$ curve, γ_0 is the Gruneisen gamma, and α is the first order volume correction to γ_0 . The compression is defined in terms of the relative volume (V_r), given by $V_r = \frac{V}{V_0} = \frac{(V/M)}{(V_0/M)} = \frac{\rho_0}{\rho}$ where ρ_0 and ρ are the density at nominal/reference state (usually for a non-stress or non-deformed state) and current density, respectively. Similarly, V_0 is the reference volume and V is the current volume. A frequently used volumetric parameter (μ) is given by $\mu = \frac{1}{V_r} - 1$. Slope parameter S_1 is set to 1.979 and the volume correction factor γ_0 is set to 0.11 (also, $S_2 = S_3 = 0$). Numerical model predictions are accurate when the selected sound speed (C) is 1,484m/s. However, a value which is one-tenth of the original sound speed in water is sufficient to define the EOS for water is the pressure is not significantly influences by temperature changes.

The upstream boundary condition specifies an inlet velocity and the downstream boundary condition has a non-reflective boundary condition. The code permits automatic examination of the finite element mesh and material properties in order to determine an appropriate time step size for numerical stability. Termination time of the process and the time step increment is set by the user based on the processing time. This time step size is then automatically adjusted throughout the transient analysis based on the deformation and stress state of each structural element. Performing simulations involving fluid dynamics is computational-intensive and the complexity is magnified by the presence of the flexible structure(s) in the fluid domain. Finally, the time step in the numerical simulation is $5.45e-05$ s. A brief summary of the FE ALE simulation trials is discussed below.

6.7 Finite-element simulations

Simulations shown here are a part of a series of numerical simulation tests to confirm the modeling and simulations of SES in general and a progressive testing technique of its individual components against a steady water current in particular. A systematic approach in modeling the interactions of the various components of the SES experiment, such as forward speed, air cushion pressure, and bow and stern seal interactions with the pressurized air cushion and water domains, resulted in an accurate numerical reconstruction of the experimental test conditions.

The FE simulations were performed for two SES configurations: (1) fully-coupled FSI simulations for a full SES model with rigid seals (2) fully-coupled FSI simulations of a single flexible bow finger seal and an aft rigid seal.

Performing simulation using these two configurations require a free stream fluid velocity. While the full SES model with a rigid seal geometry was used to simulate the pressure inside the SES cushion chamber and to analyze the flow pattern around the rigid seals, a single flexible bow finger seal with an aft rigid seal geometry was used to predict the deflections of the seals. Details of both the simulations are presented below.

Fully-coupled FSI simulations: Full SES model with a flat rigid plate bow seal – In these simulations, the SES hull form is represented by shell elements for the seals. Note that the bow seal is planar, as opposed to the curved bow finger seals. At approximately amidships, a pressurized air pump is introduced via the ambient air (pressure outflow boundary condition). The cushion pressure inside the SES chamber is close to 408Pa. This air pump equalizes the air cushion pressure to the experimental conditions over the first several seconds of the simulation. The inflowing pressurized air mixes and compresses the ambient, unpressurized air that fills the air cushion at time, $t = 0s$. The result of this process is a pressurized air cushion.

The semi-transparent, isometric view of the SES FE model, emphasizing the location of the air-pump at approximately amidship is shown in Figure 6.6. An example of the air cushion air mixing and water level setdown is illustrated in Figure 6.7. Snapshots of the air pumping inside the SES chamber are shown in Figure 6.8. The pressure time history at three different locations in the SES cushion chamber are compared to the experimental cushion pressure of 408Pa. “E7113”, “E7233” and “E7353” are the elements at three strategic locations (bow, amidships and the stern) inside the SES chamber is shown in Figure 6.9. The pressure inside the cushion (from the numerical simulations) compare well with experimental data providing confidence that air pumping mechanism is accurate.

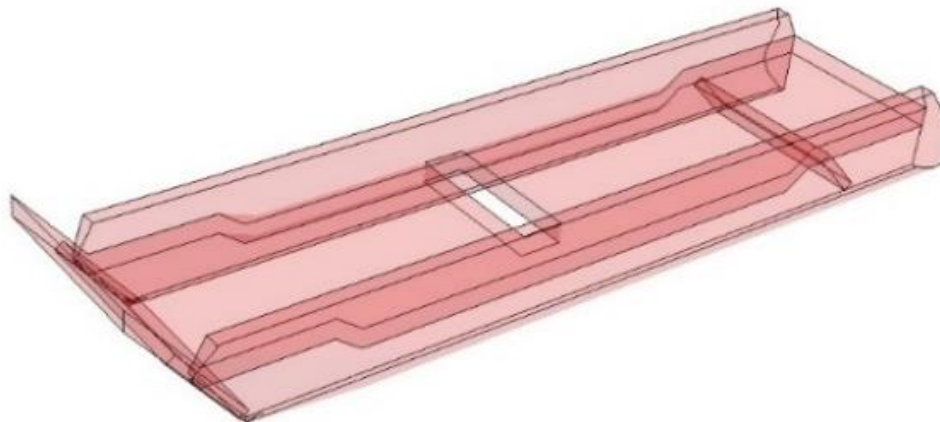


Figure 6.6: Semi-transparent, isometric view of the SES FE model, emphasizing the location of the air pump at approximately amidships

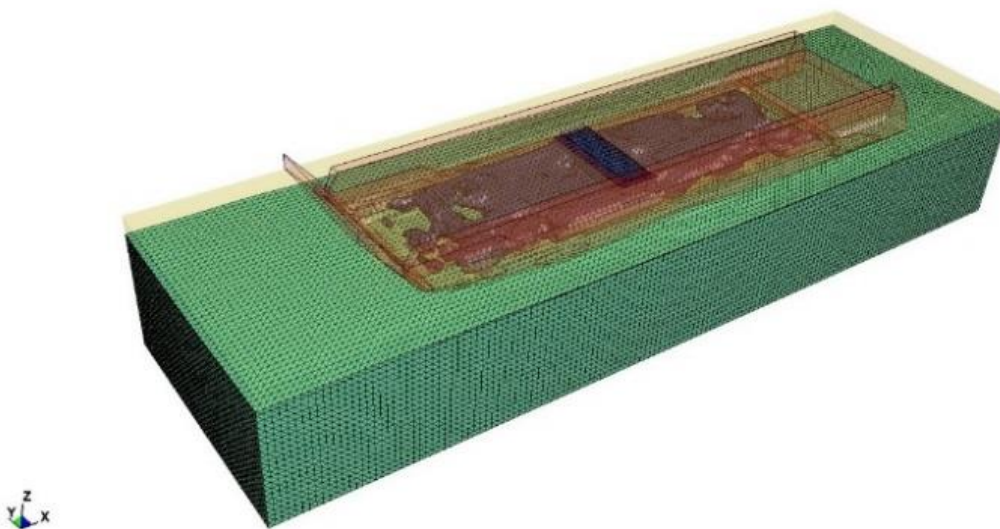


Figure 6.7: SES FE simulation near equilibrium air cushion pressure. The green domain is water, the semi-transparent red is the SES shell exterior, the purple is the pressurized air cushion, and the semi-transparent tan is ambient air

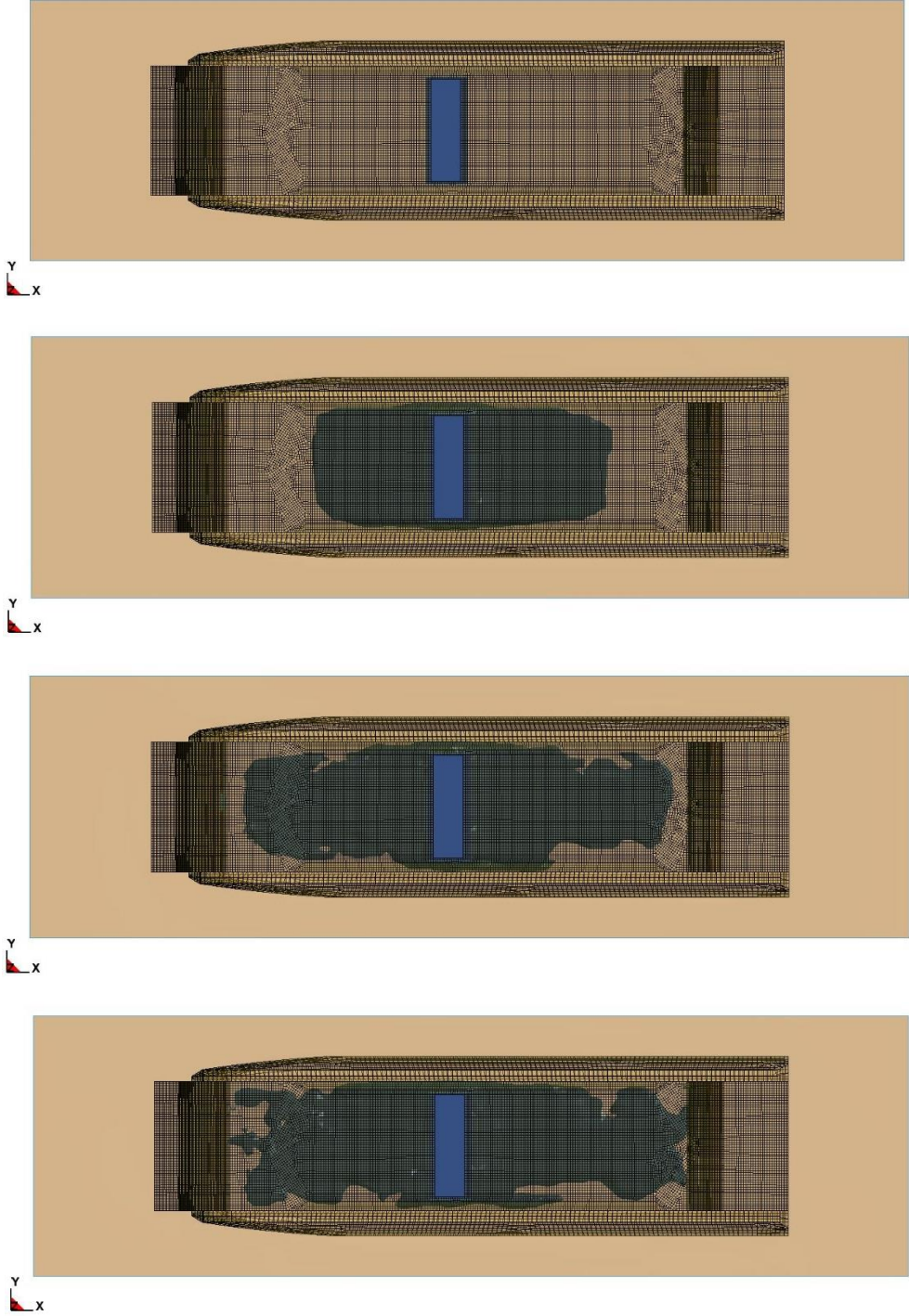


Figure 6.8: Pressurized air cushion in the SES chamber (snapshots of air pumping)

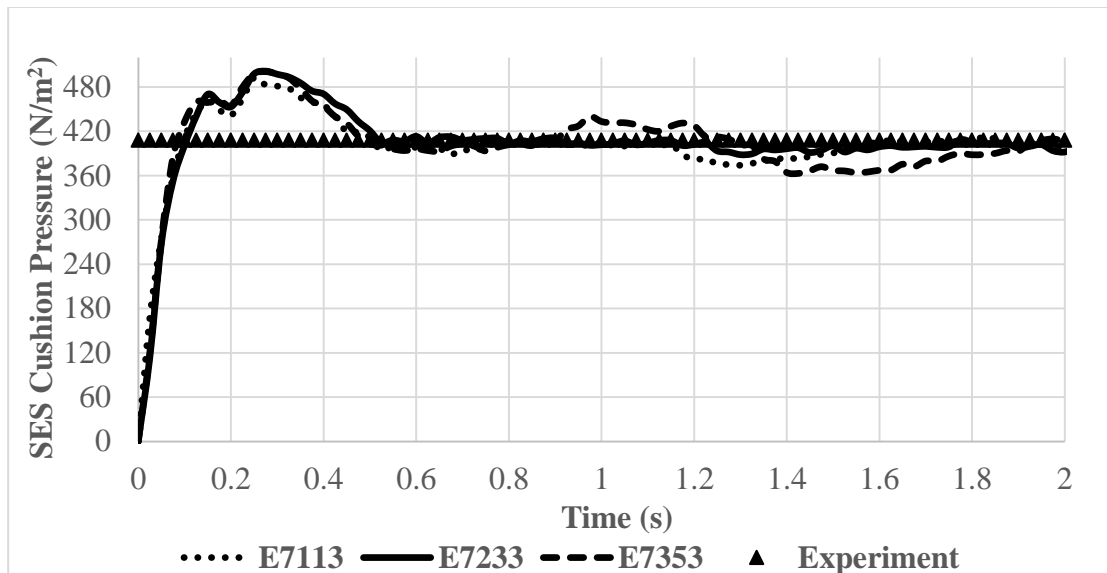


Figure 6.9: Pressure time history of three elements (bow, amidships and stern) inside the SES cushion chamber

A straight trajectory of the full SES model with rigid seals was computed for a forward speed of 0.7m/s and a cushion pressure of 408Pa. The spatially-distributed water speed for the straight trajectory case is shown in Figure 6.10. Figure 6.11 shows a truncated section of the flow around the centerline of the SES bow finger seals. Major insight into the fully-coupled FSI (for a full SES model with flat rigid plate seal) shows that the fluid flow in the cushion chamber away from the hull boundaries is approximately uniform (hence two dimensional in the x-z plane). The water accelerates very little in the y-direction. Although difficult to see due to the three dimensional nature of the flow pattern, the water flow around the planar bow seal of the SES hull form is approximately two dimensional near the centerline.

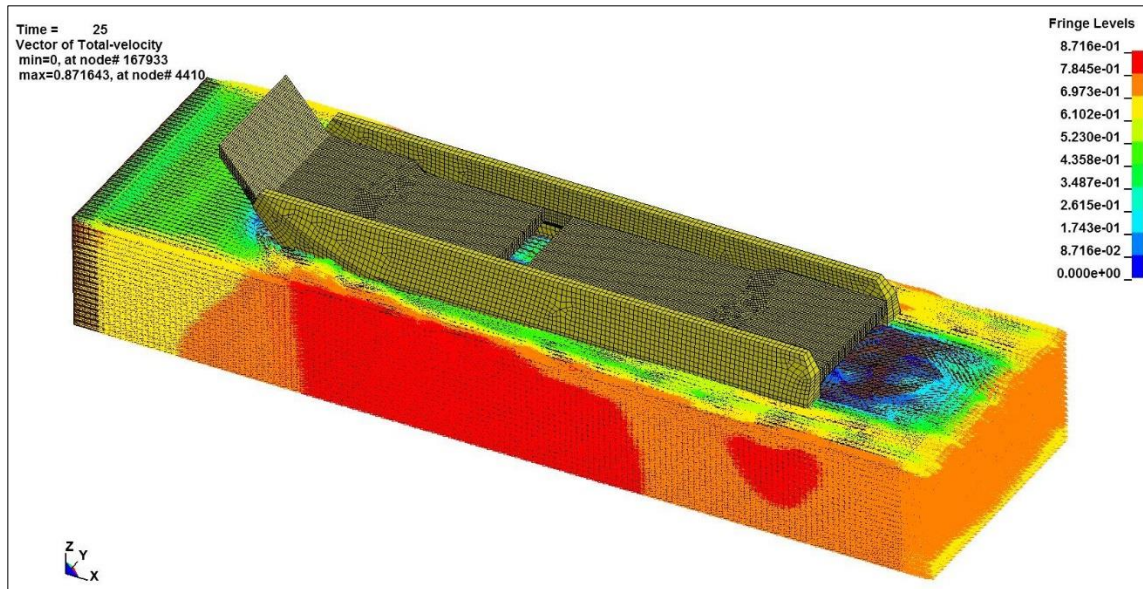


Figure 6.10: SES FEA simulation with a forward speed of 0.7m/s and velocity in the water domain given by the colorbar

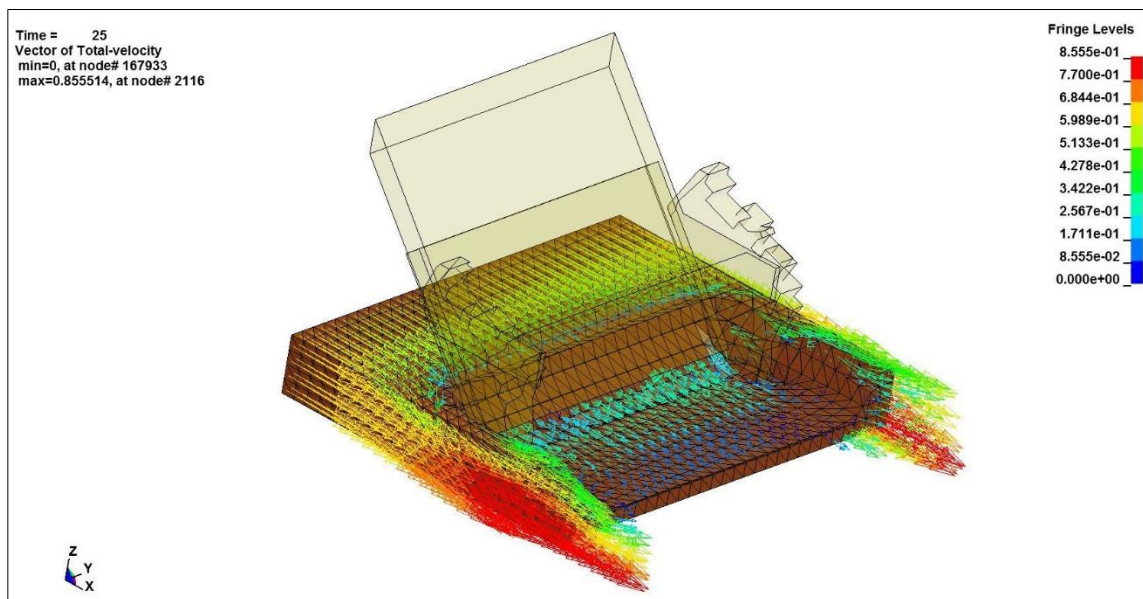


Figure 6.11: Bow section of the SES hull form with a rigid seal (yellow) and water (brown and vectors) at approximately the same forward speed as the SES experiment

Simulation results for a full SES model with the curved shape of the bow fingers also showed that the flow pattern was practically identical from finger to finger and the mean pressure distribution is similar to that of the flat plate.

Also, the qualitative analysis of the video captures in the experiment shows that the seal only vibrates in a small region with the conditions of constant forward speed and air cushion pressure. Observations from the videos of the experiments reveal that the webbing that connects the bow finger seals do not move which confirms the numerical finding that the flow behavior around the bow fingers is practically identical from finger to finger (with little or no interaction). Therefore it is sufficient to study the hydrodynamic behaviour of a representative individual bow finger alone. This is an encouraging fact that helps to identify the “region of interest” as individual bow fingers.

Fully-coupled FSI simulations: Single flexible bow finger and a rigid aft seal – Figure 6.12 shows the three dimensional isometric view of the computational domain. In order to simulate the region of interest, the top, port, and starboard edges of the single bow finger seal are held fixed in translation. A constant pressure (408Pa) was applied to the bow finger equivalent to a fully pressurized air cushion chamber of the SES (see Figure 6.9). The mean water set-down due to the air pressurization in the experiments was approximately 0.07m. A volume fraction technique (which is a volume-filling method to replace one FE material with another before the start of the simulation) is used to model this set-down (Figure 6.13). Detailed information on the volume fraction is given in Appendix D.

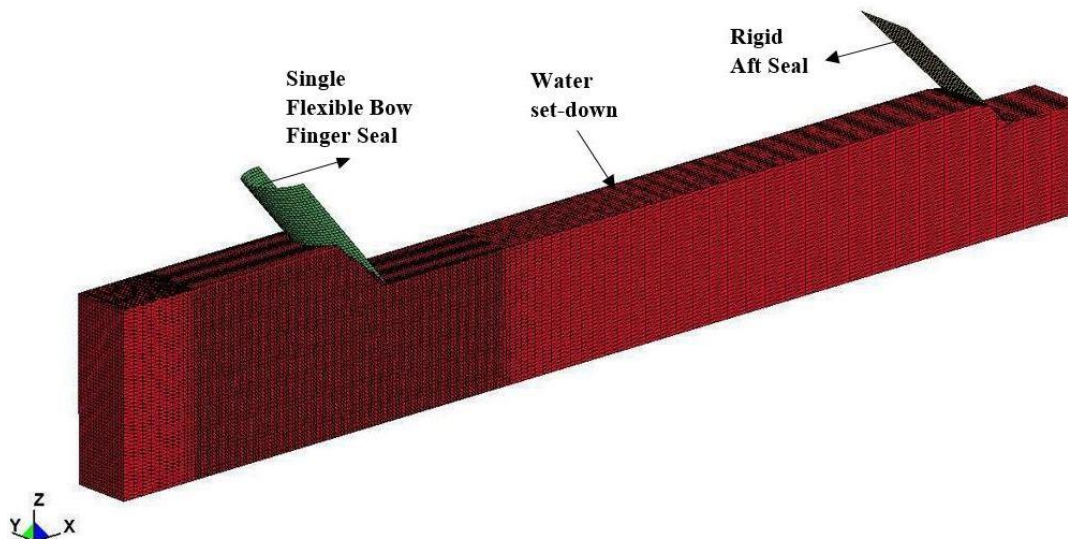


Figure 6.12: Three dimensional isometric view of the computational domain.

Before presenting the simulation results for the single flexible bow finger seal and a rigid after seal geometry the membrane formulations along with the boundary conditions applied are given below.

Membrane formulation – The membrane formulation utilizes co-rotational kinematic equations of motion and follows the fundamental membrane assumptions (Ugural 2009): (i) membrane thickness is negligible with respect to the radius of curvature, (ii) deflection of the membrane are negligible with respect to the membrane thickness, (iii) planes remain planes for the deflected midsurface of the membrane, and (iv) stress in the normal direction of the membrane is negligible. The boundary conditions of the seal are based on the qualitative interpretation and quantitative post processing of video captured from inside the air cushion with cameras attached to the wet deck. A still image example of the perspective of those cameras is shown in Figure 6.13.

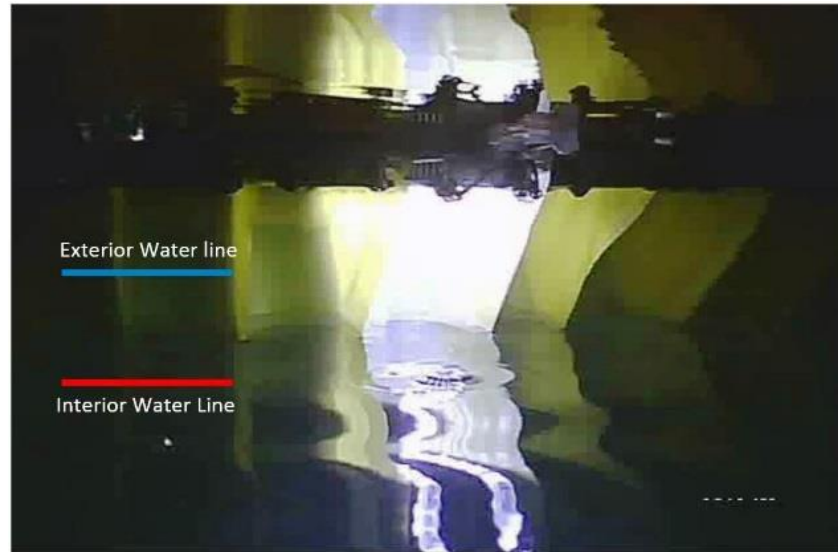


Figure 6.13: Example still image from the forward-facing wet deck camera. This image was taken while the SES scale model had zero forward speed and on full air cushion pressure (approximately 408Pa). The blue line highlights the approximate exterior water line, and the red line highlights the approximate interior water line

The intersection between the leading face of the finger seal and the web portion that attaches to the top affixed portion of the seal is called the junction, for the purpose of this work (Figure 6.13). From the video, we noticed that the junction does not vibrate during the trials. Therefore, a simplified domain of the seal geometry was used in this analysis, and a translation-fixed boundary condition was applied along the junction. Of course, a translation-fixed boundary condition is also used along the top nodes of the seal geometry. Figure 6.14 shows the nodes and elements of the SES bow finger seal simplified geometry with the translation-fixed boundary conditions identified by small triangles. The mesh used for the analysis contained 41 rows and 31 columns of nodes, forming a shell with 1,200 quadrilateral elements. The modulus of elasticity used for the material was $2.0E+07$ N/m², and the Poisson's ratio was 0.14. The material properties are based on the material evaluations provided in Cochrane *et al* (2007). The air cushion pressure is applied as point

loads to each element of the bow finger seal. The surface normals are pointed outwards to the interior face of the bow finger seal [Figure 6.14(a)]. Constant cushion pressure is applied via a follower load, which acts opposite to the surface normal [Figure 6.14(b)].

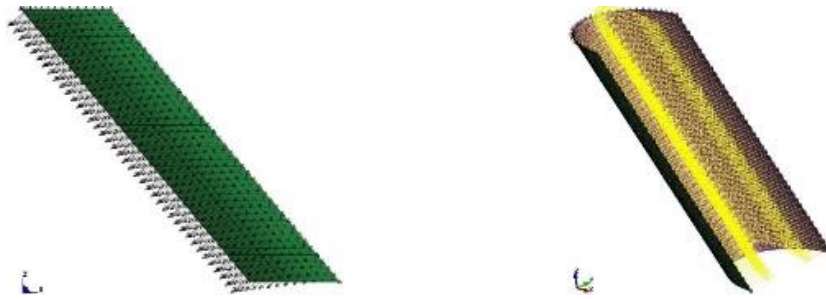


Figure 6.14: (a) SES bow finger seal simplified geometry and boundary conditions shown by small triangles [Left] (b) Membrane element normal pointed outward in direction of water current [Right]. Follower load for cushion pressure acting opposite to surface normal.

Simulation results for the fully-coupled FSI with a single flexible bow finger and a rigid aft seal geometry are shown in Figure 6.15. Snapshots of the images showing the bow seal deflection are shown in Figure 6.16.

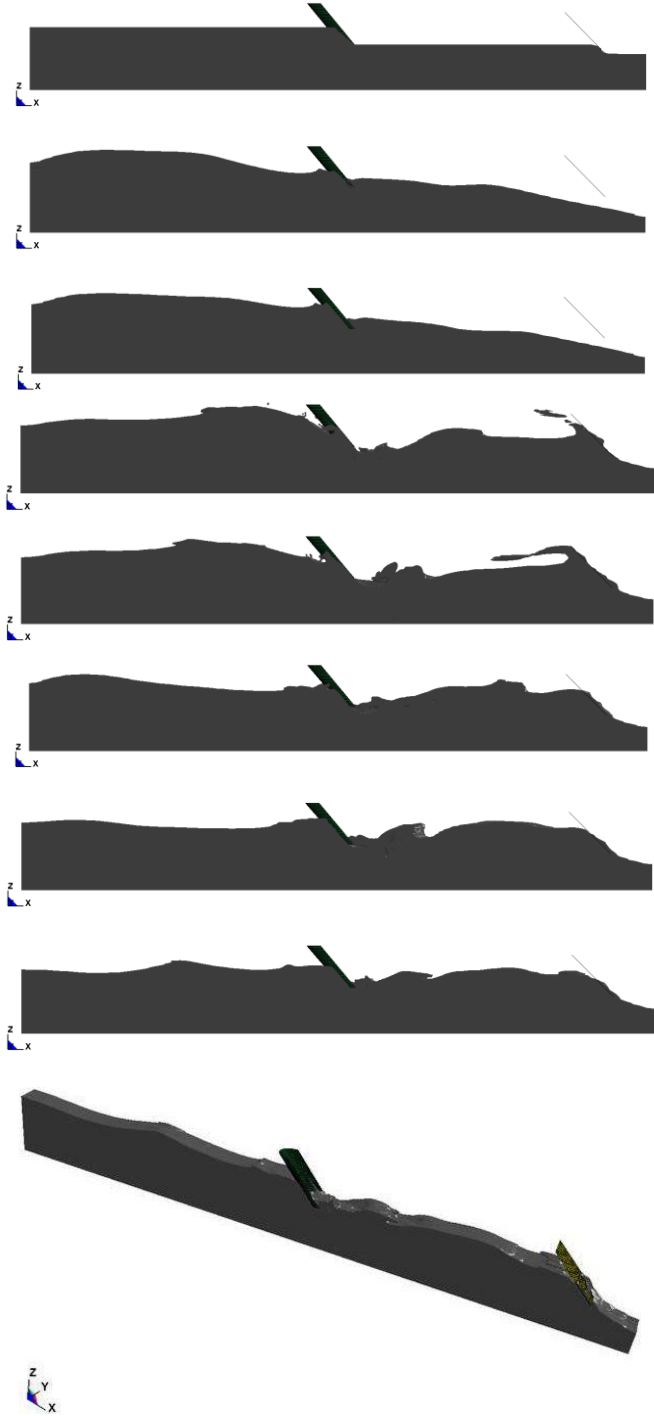


Figure 6.15: Snapshots of the simulation results for fully coupled FSI with a single flexible bow finger and a rigid aft seal geometry

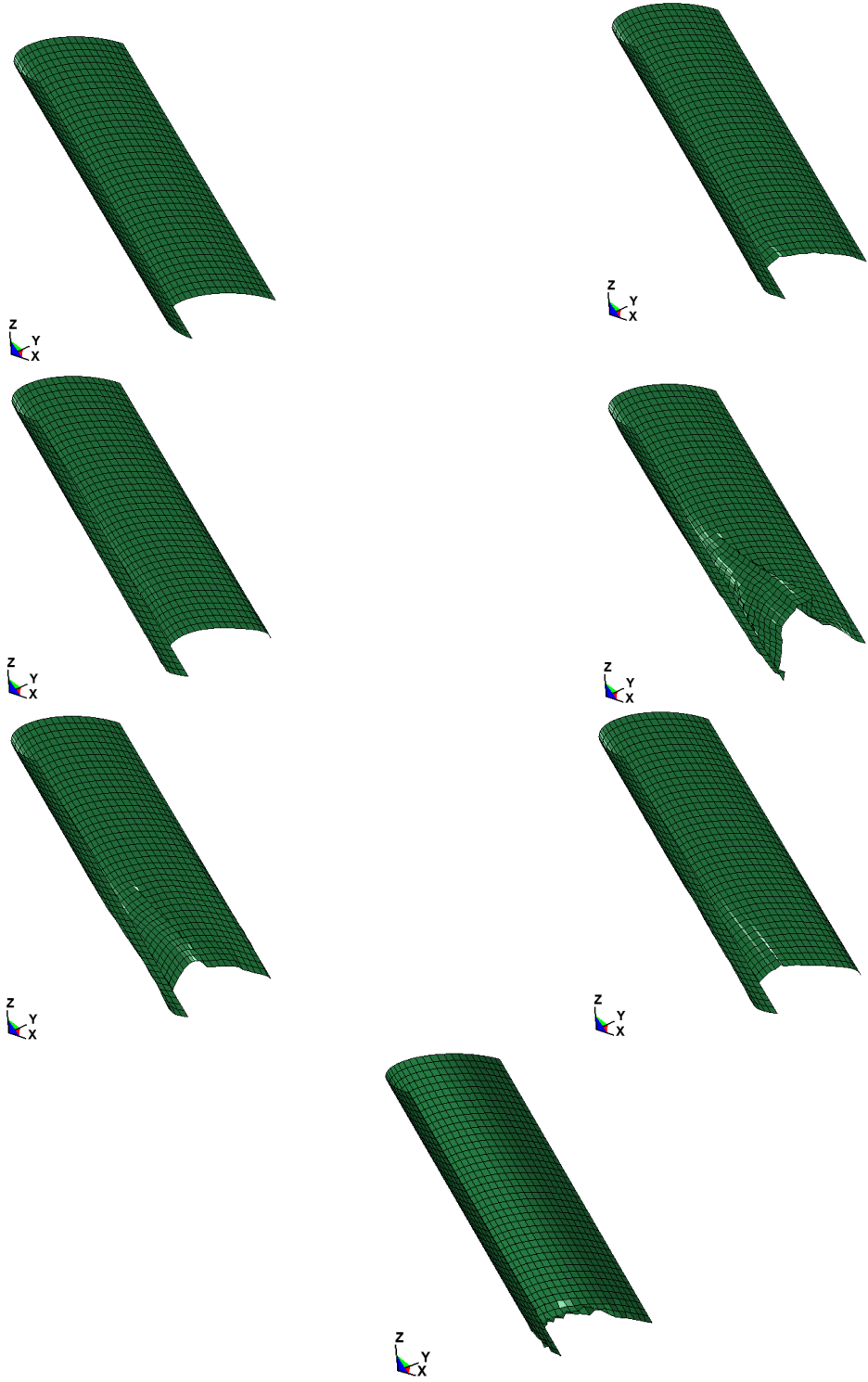


Figure 6.16: A snapshot of images depicting the bow seal deflections

6.8 FE simulation results of bow finger skirt node deflections

Numerical simulation results for the single flexible bow finger displacement time histories are shown for: (i) all the skirt nodes of the flexible bow finger, (ii) three adjacent nodes on the centerline and pressure and stress time histories for three adjacent membrane elements at the centerline (Figure 6.17). Note that the simulation test cases shown below are carried out at the prototype scale to take advantage of the bigger size of the elements and hence a larger time step size.

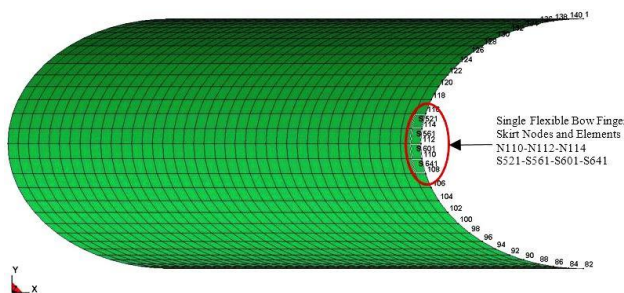


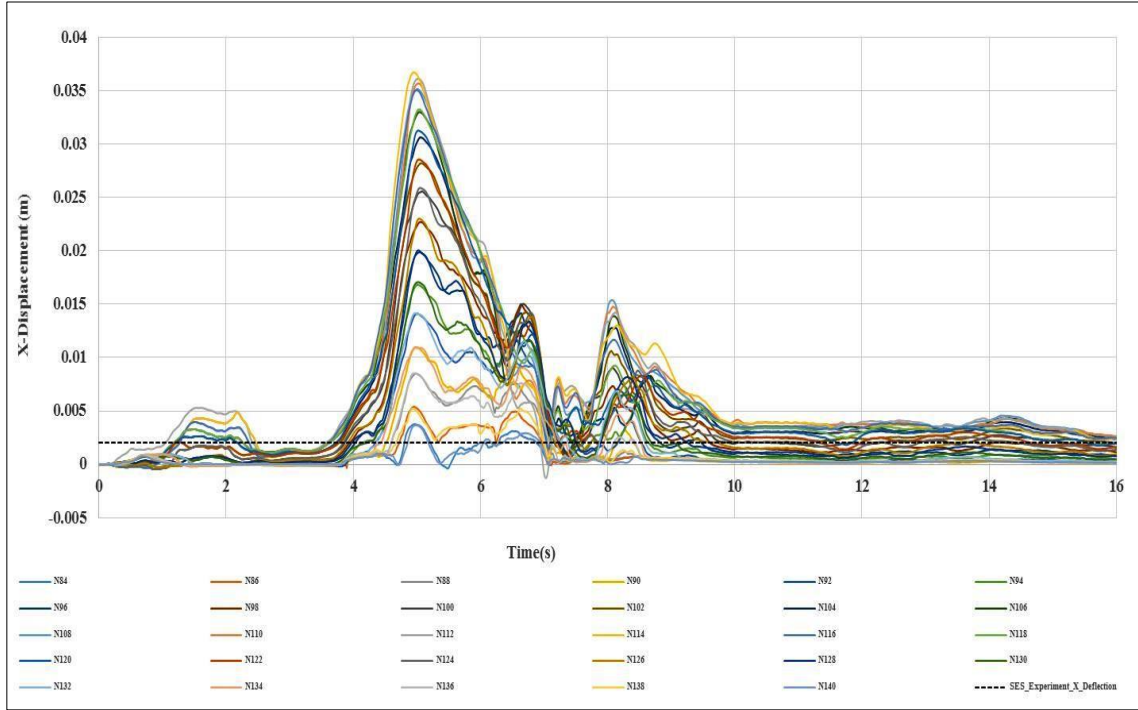
Figure 6.17: Bottom skirt nodes of the bow finger seal and the middle three nodes and membrane elements of the bow finger seal

Simulation results shown below are for the computational set-up with a single flexible bow finger seal with a rigid stern seal geometry (Figures 6.18-6.20). Note that the gravity is ramped gradually from zero to 0.2sec and the pressure on the bow finger (acting opposite to the direction of the shell segment normal) comes into full effect at 4 seconds. Also notice that the bow finger reaches its initial maximum deflection due to the incoming water current from 3.8 to 6.6 seconds and once the cushion pressure comes into full effect and the current in the numerical water tank reaches a steady state the bow seal stabilizes and reaches an equilibrium which can be observed from 10 to 16 seconds. As mentioned at the

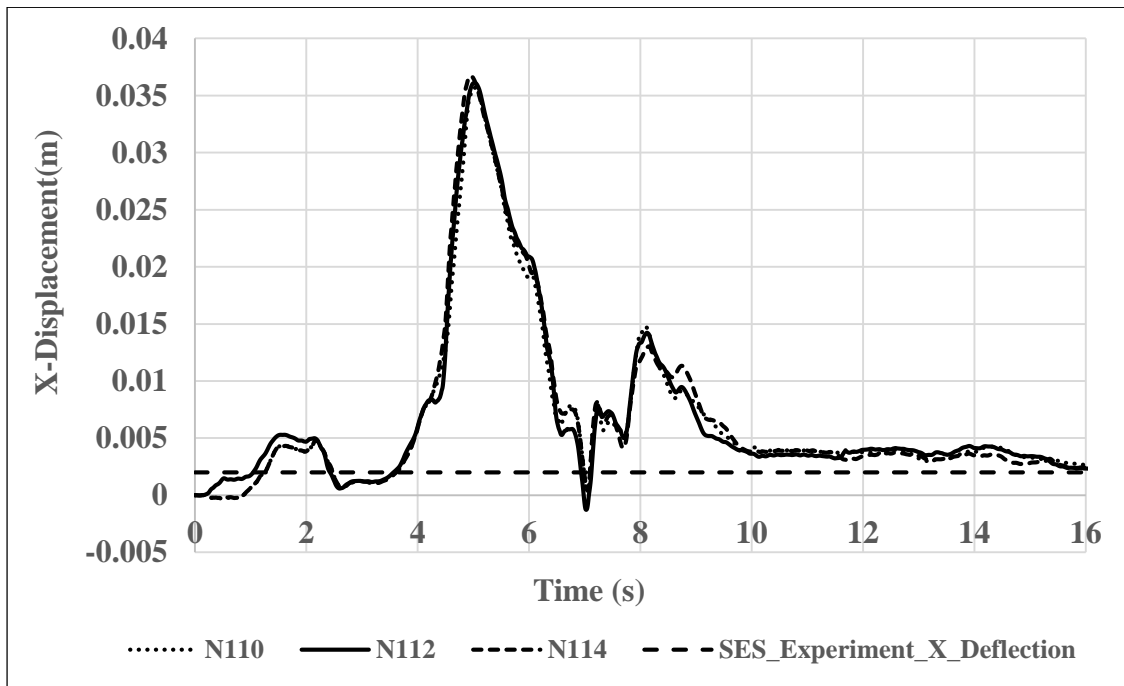
end of the experimental section, the results obtained from qualitative videos for the equilibrium deflection of the bow seal bottom skirt nodes reveal that the SES model scale has an x-displacement of 0.002m, y-displacement of 0.0001m and z-displacement of 0.011m respectively.

Figures 6.18(a) and (b) show the x-displacement time histories of bow finger skirt nodes and the centerline three middle nodes of the bow finger seal skirt nodes, respectively. Corresponding results for y-displacement time histories are shown in Figures 6.19(a) and 6.19(b) and z-displacement time histories are shown in Figures 6.20(a) and 6.20(b).

The maximum x, y and z displacements from the numerical simulations are 0.005m, 0.0001m and 0.008m, respectively. Interestingly, even though the presence of the stern stabilizes the mean water-level satisfactorily, the bow finger seal skirt region is very sensitive to the fluctuating water line aft of the bow finger seal (especially at the complex air-water-skirt interface). This can be attributed to: (i) open boundary on the downstream, and (ii) mean depression of water set-down detaches from the seal-water interface eventually. Note that the bow finger seal in general and the skirt nodes in particular are sensitive to the water level set-down. Any small fraction of change in the water level will result in a significant change in the x and y bow seal deflections.

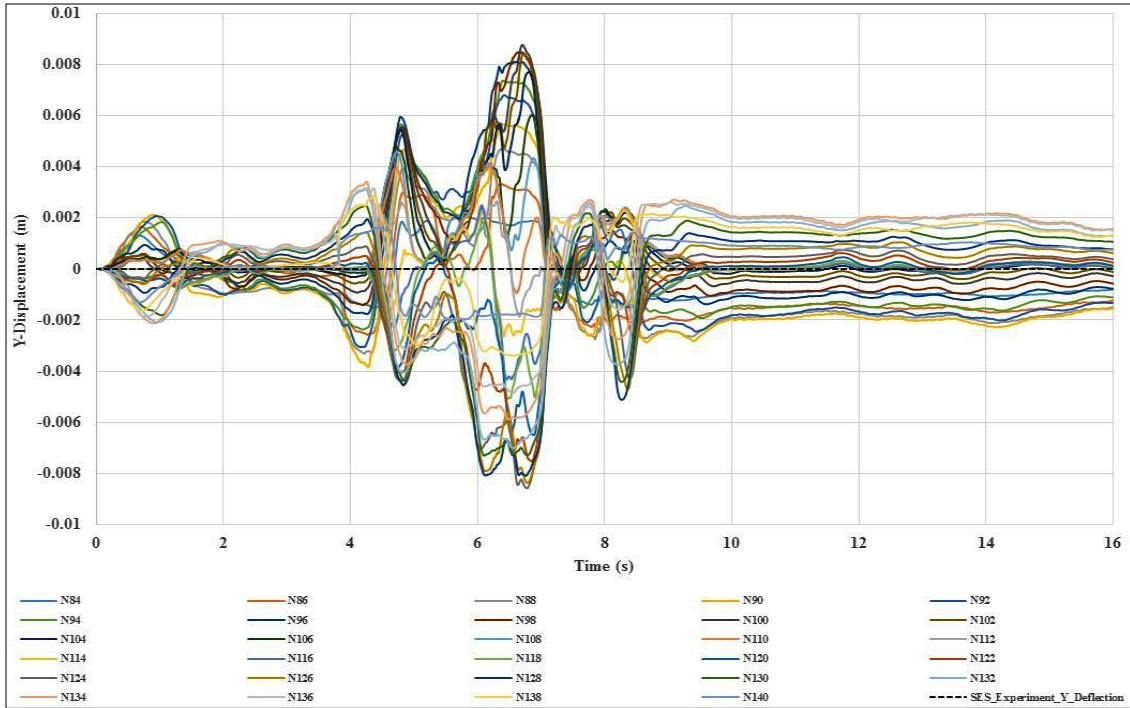


(a) Bow finger seal skirt nodes

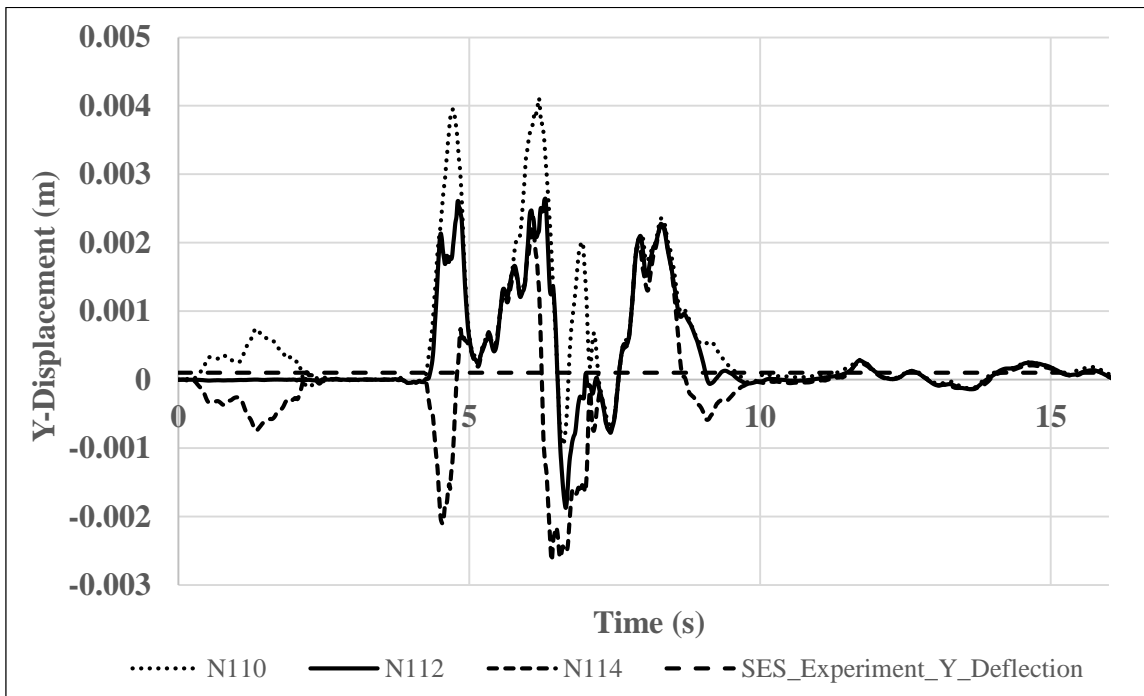


(b) Three center bow finger seal nodes (N110-N112-N114)

Figure 6.18: X-Displacement time history of bow seal skirt nodes

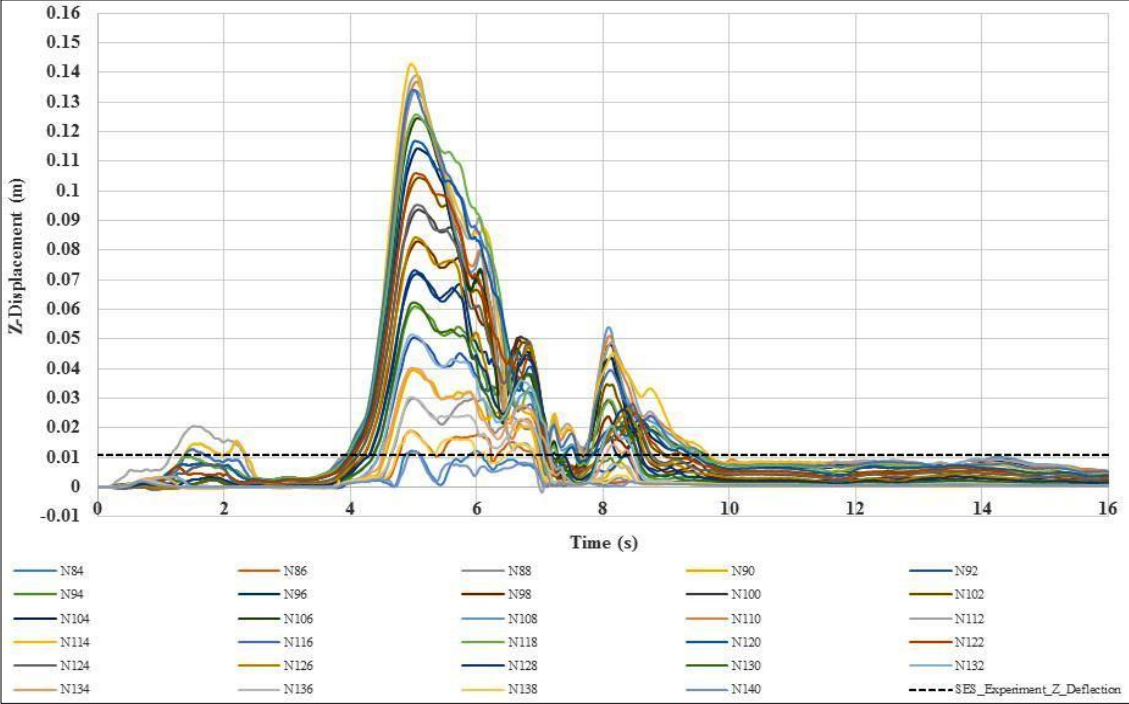


(a) Bow finger seal skirt nodes

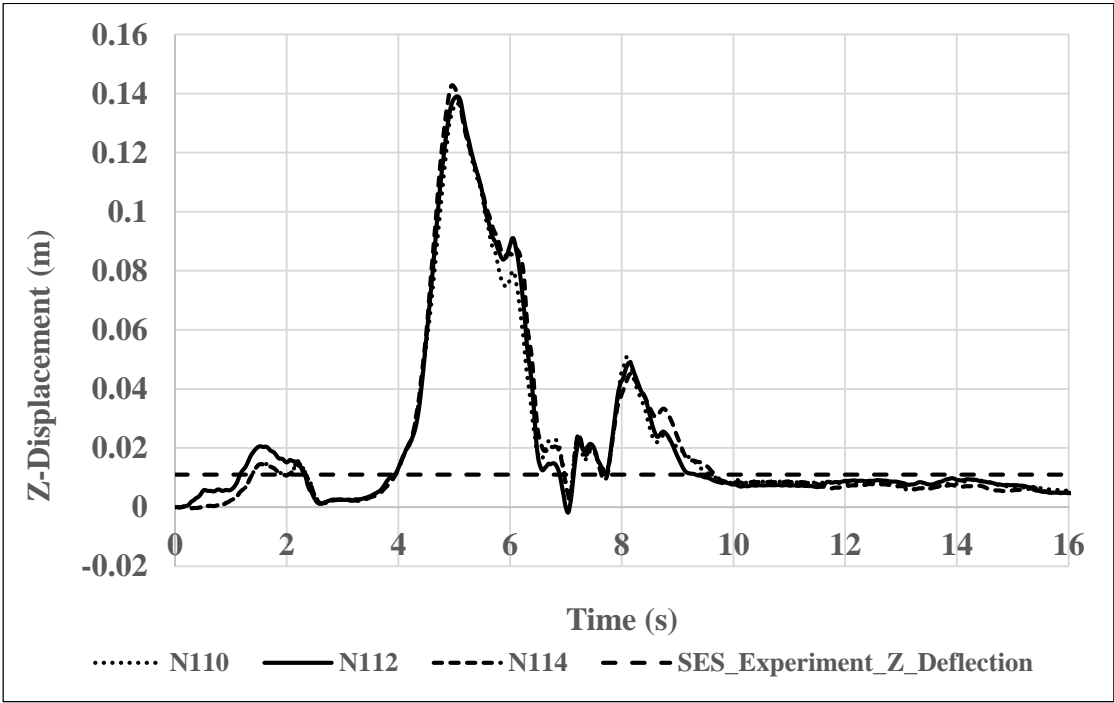


(b) Three center bow finger seal nodes (N110-N112-N114)

Figure 6.19: Y-Displacement time history of bow seal skirt nodes



(a) Bow finger seal skirt nodes



(b) Three center bow finger seal nodes (N110-N112-N114)

Figure 6.20: Z-Displacement time history of bow seal skirt nodes

A comparison of the mean equilibrium deflection for the three center nodes calculated from the numerical simulation results with those obtained by experimental tests are shown in Table 6.2. Note that the values presented in Table 6.2 are the average of three runs. The final values are the mean of displacement values obtained from 10 seconds to 16 seconds of the data plotted in Figures 6.18(b), 6.19(b) and 6.20(b).

Table 6.2: Comparison between experimental and numerical simulation results for mean equilibrium deflections of the bow finger seal

Coordinate	Experiment (Mean Equilibrium Deflection) (m)	Numerical (Mean Equilibrium Deflection) (m)
X	0.002	0.005
Y	0.0001	0.0001
Z	0.011	0.009

Figure 6.21 shows the pressure time history of the three elements of the skirt membrane elements (see Figure 6.17) for which the displacement time histories are available. Maximum pressure on the bow finger seal is approximately 1,200 Pa at the skirt node. The effective stress time histories of the three elements of the skirt membrane elements that accompany the nodes are shown in Figure 6.22. Maximum effective stress in the bow seal is 3,500 N/m².

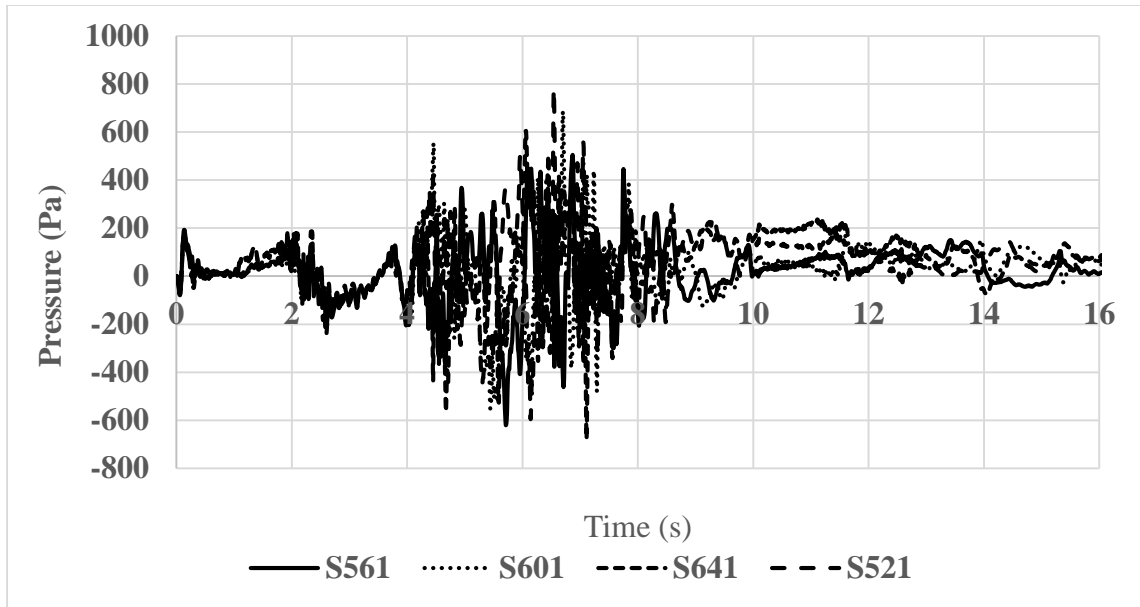


Figure 6.21: Pressure time history for the bottom skirt elements

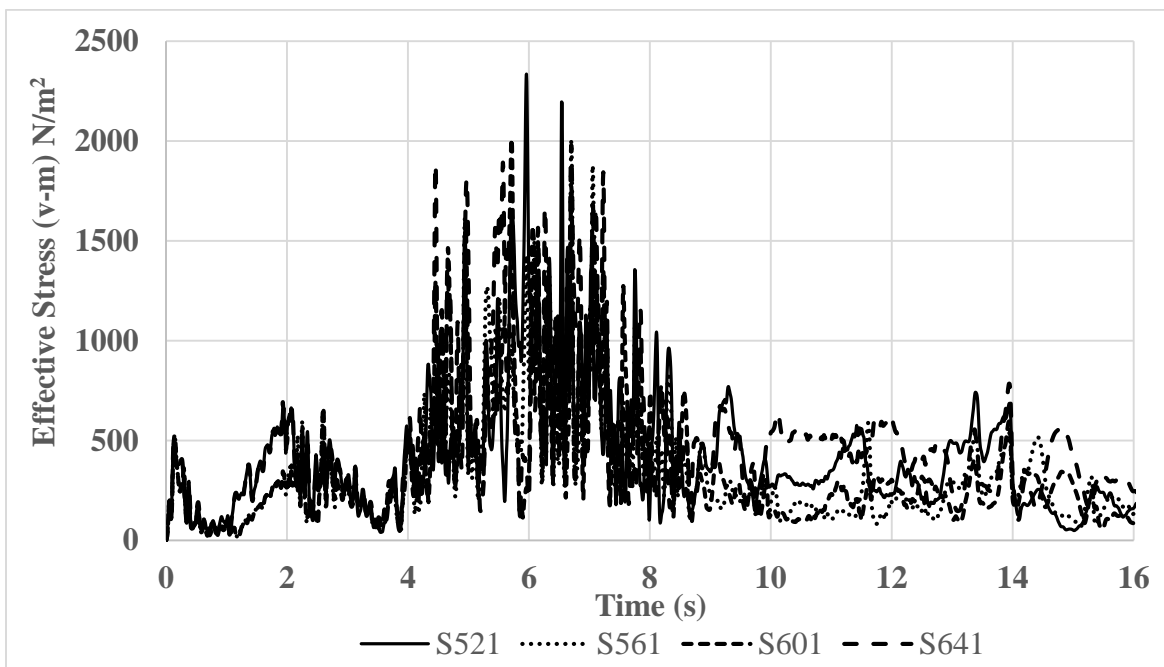


Figure 6.22: Stress time history for the bottom skirt elements

Figure 6.23 shows the computation time for different mesh configurations. Figure 6.23 also shows that for the 1200 element case takes approximately 334 hours for a termination time of 20 seconds. Figure 6.24 shows the maximum x, y and z deflections of the bow finger seal skirt nodes for different mesh sizes and the deflection values seem to converge for a higher mesh fidelity. It is important to bear in mind the 550 hour computation time for a 2400 element test case for which repeatability is difficult (given the fact that water level set down plays a significant role in determining the bow seal skirt node deflections).

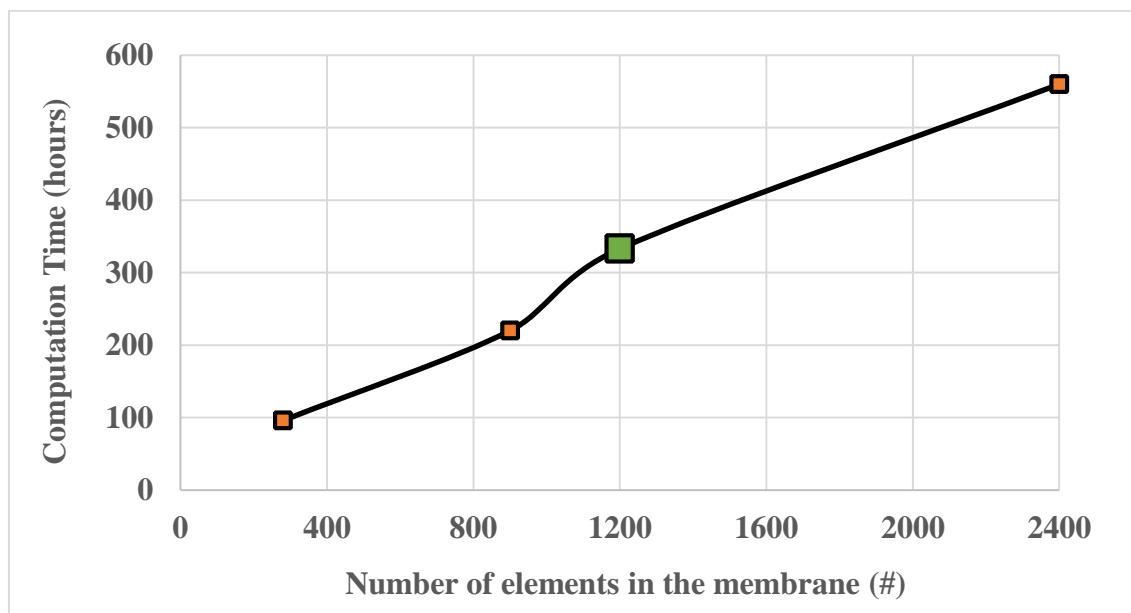


Figure 6.23: Computation time for different mesh configurations (Green: 1200 element case for which the numerical results are shown)

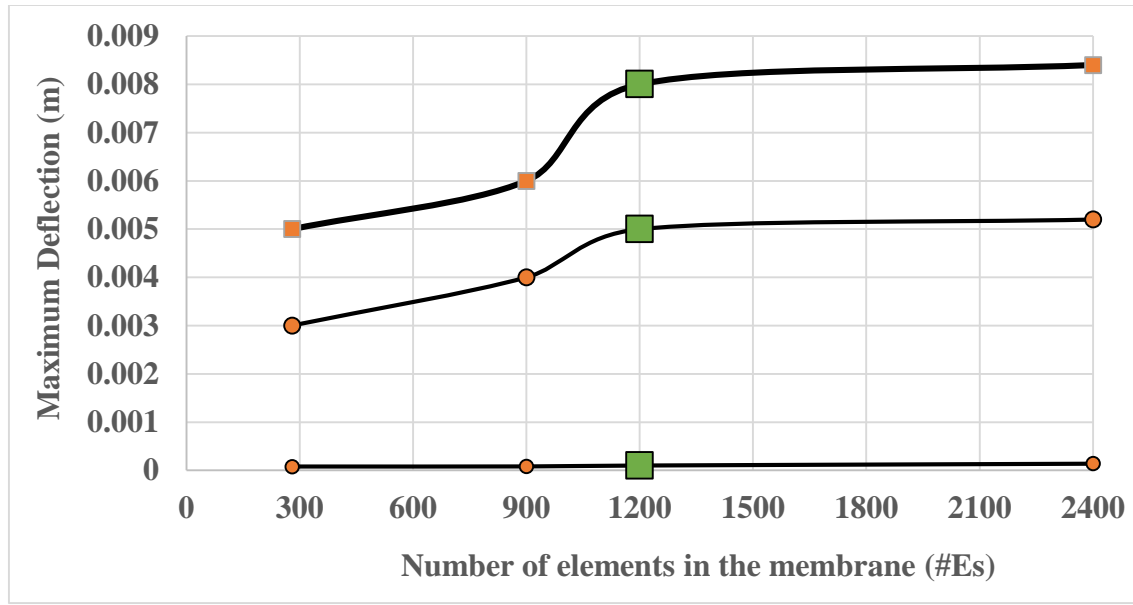


Figure 6.24: Maximum x, y and z deflections for four different mesh configurations (Green: 1200 element case for which the numerical results are shown)

6.9 Conclusions

This study examines the bow finger seal motions of a scale-model of a free-running surface effect ship (SES) with a fully pressurized air cushion using numerical simulations. The predictive capability of a finite element model with arbitrary Lagrangian-Eulerian formulation is validated for the bow seal deflections using experimental data. A fluid flexible-structure interaction model was used to model a water channel and various components of an SES to predict the maximum deflections of the bow seals. A systematic approach in modeling the interactions of the various components of the SES experiment including forward speed, air cushion pressure, and bow and stern seal interactions with the pressurized air cushion and water domains, resulted in an accurate numerical

reconstruction of the experimental test conditions. The major conclusions obtained from the numerical analysis are summarized below:

- For a fully-coupled FSI, full SES model with a flat rigid plate seal showed that the fluid flow in the cushion chamber away from the hull boundaries is approximately uniform (hence two dimensional). Numerical simulation results for the air cushion pressure inside the SES chamber also compared well with experimental data.
- For a fully-coupled FSI, full SES model with rigid seals with the actual shape of the bow fingers showed that the flow pattern was practically identical from finger to finger and the pressure distribution was similar to that of the flat plate. Therefore, it may be sufficient to study the motion behavior of a representative individual bow finger.
- A fully-coupled FSI simulation of a single flexible bow finger and a rigid aft seal geometry with partial submergence in a uniform current is shown to predict the maximum bow finger seal skirt deflections accurately with experimental data.
- Results from a mesh convergence study show that the numerical model can accurately predict the maximum displacement with a reasonable number of elements (on the order of thousands).
- In light of the good comparison with the experimental data, the fully-coupled FSI modeling and analysis can be readily employed to perform parametric studies on a wide range of free stream water speeds, air cushion pressures and depths of immersions.

6.10 Acknowledgments

Financial support from the US Office of Naval Research Grants N0014-11-1-0094 and N00014-13-1-0849 are gratefully acknowledged. Authors also wish to thank Kelly Cooper, Office of Naval Research for funding this project.

6.11 References

- Belytschko, T., Flanagan, D. F., and Kennedy, J. M., (1982). "Finite Element Method with User-Controlled Meshes for Fluid-Structure Interactions," *Computational Methods in Applied Mechanics and Engineering*, 33, pp. 689–723.
- Besch, P. K., (1976). "Motions of Bow Fingers in a Surface Effect Ship Flexible Seal." DTNSRDC, Ship Performance Department.
- Baird, N. (1998). "The World Fast Ferry Market," Melbourne, Australia, Baird publications.
- Bishop, R. C., Silver, A. L., Tahmasian, D., Lee, S. S., Snyder, L. A., Park, J. T. 2010. "T-Craft Seabase Ramp Loads Model Test Data Report," Naval Surface Warfare Center Carderock Division, NSWCCD-50-TR-2010/073, Hydromechanics Department Report.
- Bloxom, A. L. (2014). "Numerical Simulation of the Fluid-Structure Interaction of a Surface Effect Ship Bow Seal," Ph.D. dissertation submitted to the faculty of the Virginia Polytechnic Institute, Department of Aerospace Engineering, September 12, Blacksburg, VA.
- Challa, R., and Yim, S. C. (2014). "Rigid-Object Water-Entry Impact Dynamics: Finite-

Element/Smoothed Particle Hydrodynamics Modeling and Experimental Validation,”
Journal of Offshore Mechanics and Arctic Engineering. 136(3): 031102-031102-12,
doi: 10.1115/1/4027454.

Challa, R., Newborn, D., and Yim, S. C. (2013). “Finite Element Contact/Impact Modeling
Capability of Complex Surface Effect Ship Dynamics: Preliminary Assessment,” Odd
M. Faltinsen Honoring Symposium on Marine Hydrodynamics – Proceedings of
ASME 55430, 9.

Cochrane, C., Koncar, V., Lewandowski, M., and Dufour, C. (2007). “Design and
Development of a Flexible Strain Sensor for Textile Structures Based on a Conductive
Polymer Composite,” *Sensors*, 7, 473-492.

Doctors, L. J., and McKesson, C. B. (2006). “The Resistance Components of a Surface-
Effect Ship,” Proceedings of the Twenty-Sixth Symposium on Naval Hydrodynamics,
Rome, Italy, 17-22.

Doctors, L. L., (2009). “A Study of Resistance Characteristics of Surface-Effect-Ship
Seals,” Proceedings of the High-Performance Marine-Vehicle Symposium, November
9-10, pp. 1-11.

Donnelly, D. J. (2010). “Numerical simulation of surface effect ship air cushion and free
surface interaction,” PhD dissertation submitted to Virginia Polytechnic Institute,
Blacksburg, VA.

Espinosa, J. G., Camas, B. S., Capua, D., Fuentes, P. U., and Onate, E. I. (2013). “Advances
in the development of a FEM model for evaluation of a surface-effect ship including
skirt dynamics,” *Naval Engineering Journal*, 920, 86-91.

Faltinsen, O. M. (2005). “Hydrodynamics of High-Speed Marine Vehicles,” Cambridge

University Press, New York, USA.

Hallquist, J.O. (2006). LS-DYNA Theory Manual. Livermore Software Technology Corporation, Livermore, California.

Hodges, C., Silver, R., Wieser, J., and Adelsen, A. (2009). "SES T-Craft Model Testing," Naval Surface Warfare Center Carderock Division NSWCCD-CISD-2009/007, Technical Report.

Imas, L., and Pardes, Ruben. (2011). "Application of SPH for fluid-structure interaction problems involving free-surface hydrodynamics," 11th International Conference on Fast Sea Transportation (FAST), Honolulu, Hawaii, USA.

Kramer, M. R. (2013). "Numerical investigation of the steady state interaction between surface effect ship seals, air cushion, free-surface waves, and vessel motion," PhD Dissertation submitted to University of Michigan, Ann Arbor, USA.

Lamcotec, "70 Denier Nylon Ripstop." Website:

http://www.lamcotec.com/pr_70_denier_nylon_ripstop.php, accessed 11 March 2014.

ISO 9001:2008.

Lavis, D. (2011). "Forty-Plus Years of Hovercraft Development," Severna Park, Maryland, USA.

Newland, D. E. (1993). "An Introduction to Random Vibrations, Spectral and Wavelet Analysis," John Wiley & Sons, 3rd edition.

Ryken, John. (1978). "Test Data Analysis and Correlation Report: SES100B Finger Motions and Finger Drag." Textron, Bell Aerospace. Report 7593-925003.

Souli, M., and Benson, D.J. (2010). "Arbitrary Lagrangian-Eulerian and fluid-structure interaction numerical." Wiley publications, USA.

- Ugural, Ansel C. (2009). "Stresses in Beams, Plates, and Shells." 3rd ed., CRC Press.
- Wiggins A. D., Zalek, S. F., Perlin, M., Ceccio, S. L., Doctors, L. J and Etter, R. J. (2011). "Development of a Large Scale Surface Effect Ship Bow Seal Testing Program," 11th International conference on Fast Sea Transportation (FAST), Honolulu, Hawaii, USA.
- Yang, Q., Jones, V., and McCue, L. (2011). "Free-surface flow interactions with deformable structures using a SPH-FEM model," *Ocean Engineering*, 55, 136-147.
- Yun, L. and Bliault, A. (2000). "Theory and Design of Air Cushion Vehicles." John Wiley and Sons, Inc.,
- Zalek, S. F., Karr, D. G., Jabbarizadeh, S., and Maki, K. J. (2011). "Modeling of air cushion vehicle's flexible seals under steady state conditions." *Ocean Systems Engineering*, Vol. 1, No. 1, pp 17-29.

7 GENERAL CONCLUSIONS

This dissertation systematically examines contact and impact fluid-structure interaction (FSI) applied to various practical multi-physics ocean engineering problems. To this end, numerical simulations were performed to study: (A) rigid body contact and impact (drop tests and fluid sloshing in a LNG tank), (B) flexible body contact and impact (elastic plate deformation), and (C) complex flexible body contact and impact (bow finger seal motions of a surface effect ship). The main findings of the work presented in this dissertation are provided below.

(A) Concluding remarks on the rigid-body contact and impact

- A conical shaped water landing object (WLO) with a spherical nose compared to the convex shape of the base used for Apollo Command Module (ACM) provided a unique opportunity to study the rigid-body/water-surface impact dynamic response using experimental and numerical investigations.
- Experimental results from a series of drop tests show that for a crew member onboard the rigid body will experience a maximum impact acceleration of $5 g$.
- For a conical bottomed rigid-body, the analytical results showed a large difference between the experimental peak impact accelerations and those obtained by classical von-Karman and Wagner closed-form solutions.
- An improved approximate solution procedure using an “equivalent” radius (r) of the rigid body was estimated (owing to the large difference between the experimental

accelerations and close-formed analytical solutions) and the results show that the von Karman approach tends to estimate a higher value of the impact radius

- von Karman predictions for maximum impact accelerations were not found to be significant in determining the maximum impact accelerations as the effect of local rise up of the water are important during water entry of a 3-D rigid body
- Results from the mean equivalent radius approach show that the analytical solutions of von Karman and Wagner can be used to obtain design maximum accelerations of the rigid body consistent with experimental results.
- For the design of a WLO, the Wagner approach provides a correct estimate of the equivalent radius and the importance of the shape of a rigid-body during water impact can be ascertained by the results obtained from the closed form solutions of von Karman and Wagner
- The reliability and accuracy in evaluating the predictive capability of a non-linear transient dynamic finite code with arbitrary Lagrangian-Eulerian (ALE) formulation and a smoothed particle hydrodynamics (SPH) for simulating the impact event showed that the simulation results for maximum impact accelerations (upon touchdown) compare well with those obtained from experimental data.
- Both the numerical methods are shown to capture the impact event, hydrodynamic force, and impact accelerations accurately, the computational effort required of the SPH method is significantly higher than that of ALE.
- A comprehensive study shows the importance of proper modeling of the two-phase flow with the actual modeling of the air and the positioning of the rigid-body. This provided important “realizations” that not only facilitates the accurate way of

capturing of the physics of the impact event accurately but also provides data sets that are comparable to experimental test cases.

- A systematic numerical study conducted to analyze the physics of fluid sloshing process in a tank subjected to a forced rolling motion (for three different excitation frequencies) showed that the fluid sloshing in the tank is practically periodic with wave breaking in the interior of the fluid domain or impacting the tank walls.
- Numerical results are shown to capture not only the global sloshing scenario in terms of the fluid free surface but also the overall dynamics of the wave breaking and impact process.
- Maximum impact pressure results for all the cases show that general impact behavior of the pressure response is well reproduced and the numerical simulations appear to slightly over predict the impact pressures which was attributed to the complex random nature of the air-water-bubble mixture at the impact zone (which tends to smooth of the impact pressures). Importantly, the maximum impact pressure was found to occur at an excitation frequency that is higher than the first sloshing frequency (case C) where the amount of air entrapped is significantly less.
- Numerical simulation results presented in terms of pressure impulse (not just the pressure maxima) showed greater consistency as the variation of the pressure impulse with the oscillation cycles is minimal.
- Numerical results for a low-fill situation show that the air compressibility has negligible effect on the non-dimensional pressure maxima for all the three excitation periods. Though the complex air-water mixture at the impact zone can locally effect the pressure, the global values of the maximum impact pressure do not vary

significantly thus validating the assumption the effect of air on sloshing impact pressures is negligible.

- A detailed sensitivity analysis for two high-filled condition shows that the pressure field is highly sensitive to the compressibility of air. Numerical simulations neglecting the presence of air consistently under-predict the maximum impact pressures by several orders of magnitude.

(B) Concluding remarks for the flexible-body contact and impact

- A consistent computational platform to study the predictive capability of an arbitrary Lagrangian-Eulerian based finite element (FE) formulation and a discrete particle method (SPH) for the numerical simulation of a benchmark fluid-structure interaction was presented.
- Numerical simulation results show that the displacement of the elastic gate subjected to a time-dependent fluid pressure and the evolution of the fluid free-surface profiles can be predicted accurately (within 4%) by the ALE/FE formulation.
- A (pure Lagrangian) SPH method predicted a significantly larger motion of the free end of the gate and a faster decrease in the fluid level leading to an over prediction of horizontal and vertical gate displacements (by 37% and 71%, respectively).
- Reasons for the higher predictions of the elastic gate displacements by the SPH method were identified and analyzed in detail. The large oscillations in the pressure field need smoothing techniques such as adding artificial bulk viscosity to stabilize the velocity field and by also applying correction to the density-pressure estimates using higher order kernel approximations.

- Results obtained by varying the smoothing length between the lower bound (bounded by stability, $h = 1.03$ for the problem in this study) and upper bound (bounded by computational efficiency, $h = 1.03$) indicates that a larger smoothing length did not yield the most accurate results. The best prediction of the elastic gate displacement was obtained using the lower bound value (which is off by $>50\%$).
- An evaluation of the computational efficiency of the two numerical methods showed that the average clock ratios of the FE method is about four times faster than that of the SPH.
- Numerical simulation results show that using more SPH particles per FE element at the fluid-structure interface leads to higher computational costs without noticeable improvements in accuracy.
- An advantage of using the SPH method is the relatively short pre-processing time and a good capture of the overall physics of the fluid motion. However, the ALE model is shown to capture the fluid-structure interaction and the fluid free-surface dynamics accurately.

(C) Concluding remarks for complex flexible body contact and impact

- A two pronged numerical modeling approach (using the finite element method) was developed to systematically study the behavior of a fully-pressurized scale-model of an SES under a steady current.
- Numerical simulation results for a full SES model with multiple rigid bow seals showed that the air cushion pressure inside the SES chamber also compared well with experimental data.

- For a fully-coupled FSI, full SES model with a flat rigid plate seal showed that the fluid flow in the cushion chamber away from the hull boundaries is approximately uniform (hence two dimensional).
- For a fully-coupled FSI, full SES model with rigid seals with the actual shape of the bow fingers showed that the flow pattern was practically identical from finger to finger and the pressure distribution was similar to that of the flat plate. Therefore, it may be sufficient to study the motion behavior of a representative individual bow finger.
- A fully-coupled FSI simulation of a single flexible bow finger and a rigid aft seal geometry with partial submergence in a uniform current is shown to predict the maximum bow finger seal skirt deflections accurately with experimental data.
- Results from a mesh convergence study show that the numerical model can accurately predict the maximum displacement with a reasonable number of elements (on the order of thousands).
- In view of the good comparison with the experimental data, the fully-coupled FSI modeling and analysis can be readily employed to perform parametric studies on a wide range of free stream water speeds, air cushion pressures and depths of immersions.

BIBLIOGRAPHY

- Antoci, C., Gallati, M., and Sibilla, S. (2007). Numerical simulation of fluid-structure interaction by SPH. *Journal of Computers and Structures*, 85, 879-890.
- Aquelet, N., Souli, M., Gabrys, J., and Olovson, L. (2003). A new ALE formulation for sloshing analysis, *Structural Engineering and Mechanics*, 16(4), 423-440.
- Bagnold, R. (1939). Interim report on wave-pressure research. *Journal of ICE*, 12, 202-226.
- Baird, N. (1998). "The World Fast Ferry Market," Melbourne, Australia, Baird publications.
- Baker, E., and Westine, S. (1967). Model tests for structural response of Apollo Command Module to water impact, *Journal of Spacecraft and Rockets*, 4(2), 201-208.
- Bass, R., Bowles, E., Trudell, R., Navickas, J., Peck, J., Endo, N., and Pots, B. (1985). Modeling criteria for scaled LNG sloshing experiments, *Transactions of the ASME*, 107, 272-280.
- Bathe, K. J., and Zhang, H. (2004). Finite element developments for general fluid flows with structural interactions, *International Journal of Numerical Methods in Engineering*, 60, 213-32.
- Berg, A. (1987). Scaling laws and statistical distributions of impact pressures in liquid sloshing, Technical Report No. 87-2008, Det Norske Veritas (DNV).
- Besch, P. K. (1976). Motions of Bow Fingers in a Surface Effect Ship Flexible Seal, DTNSRDC, Ship Performance Department.
- Belytschko, T., Flanagan, D. F., and Kennedy, J. M. (1982). Finite element method with user-controlled meshes for fluid-structure interactions. *Journal of Computer Methods in Applied Mechanics and Engineering*, 33, 689-723.

- Belytscho, T., Krogauz, Y., Dolbow, J., and Gerlach, J. (1998). On the completeness of meshfree particle methods, *International Journal of Numerical Methods in Engineering*, 43(5), 785-819.
- Bishop, R. C., Silver, A. L., Tahmasian, D., Lee, S. S., Snyder, L. A., Park, J. T. (2010). T-Craft Seabase Ramp Loads Model Test Data Report, Naval Surface Warfare Center Carderock Division, NSWCCD-50-TR-2010/073, Hydromechanics Department Report.
- Bloxom, A. L., and McCue, L.S. (2014). Numerical Simulation of the Fluid-Structure Interaction of a Surface Effect Ship Bow Seal, Ph.D. dissertation submitted to the faculty of the Virginia Polytechnic Institute, Department of Aerospace Engineering, September 12, Blacksburg, VA.
- Brooks, J. R., and Anderson, L. A. (1994). Dynamics of a space module impacting water. *Journal of Spacecraft and Rockets*. 31(3), 509-515.
- Challa, R., Newborn, D., and Yim, S. C. (2013). Finite Element Contact/Impact Modeling Capability of Complex Surface Effect Ship Dynamics: Preliminary Assessment, Odd M. Faltinsen Honoring Symposium on Marine Hydrodynamics – Proceedings of ASME 55430, 9.
- Challa, R., Yim, S. C., Idichandy, V. G., and Vendhan, C. P. (2014). Rigid-Body Water-Surface Impact Dynamics: Experiment and Semi-Analytical Approximation. *Journal of Offshore Mechanics and Arctic Engineering*, 136, 011102, 1-10: 031102-031102-12, doi: 10.1115/1/4027454.
- Cochrane, C., Koncar, V., Lewandowski, M., and Dufour, C. (2007). Design and Development of a Flexible Strain Sensor for Textile Structures Based on a Conductive Polymer Composite, *Sensors*, 7, 473-492.
- Colagrossi, A., and Landrini, M. (2003). Numerical simulation of interfacial flows by Smoothed Particle Hydrodynamics, *Journal of Computational Physics*, 191, 448–475.

- Day, J. (2010). Guidelines for ALE modeling in LS-DYNA. Livermore Software Technology Corporation (LSTC).
- Doctors, L. J., and McKesson, C. B. (2006). The Resistance Components of a Surface-Effect Ship, Proceedings of the Twenty-Sixth Symposium on Naval Hydrodynamics, Rome, Italy, 17-22.
- Doctors, L. L. (2009). A Study of Resistance Characteristics of Surface-Effect-Ship Seals, Proceedings of the High-Performance Marine-Vehicle Symposium, November 9-10, 1-11.
- Donnelly, D. J. (2010). "Numerical simulation of surface effect ship air cushion and free surface interaction," PhD dissertation submitted to Virginia Polytechnic Institute, Blacksburg, VA.
- Dalrymple, R.A., and Rogers, B. D. (2006). Numerical modeling of water waves with the SPH method. Coastal Engineering Journal, 53(2-3), 141-147.
- Delorme, L., Colagrossi, A., Souto-Iglesias, A., Zamora-Rodriguez, R., and Botia-Vera, E. (2009). A set of canonical problems in sloshing, Part I: Pressure field in forced roll-comparison between experimental results and SPH, Ocean Engineering, 36, 168-178.
- Donea, J., Huerta, A., Ponthot, J. P., and Rodr'iguez-Ferran, A. (2004). Arbitrary Lagrangian-Eulerian methods. Encyclopedia of Computational Mechanics. John Wiley & Sons, Ltd.
- Dilts, G. (1999). Moving-least-squares-particle hydrodynamics-i. consistency and stability, International Journal of Numerical Methods in Engineering, 44(8), 1115-1155.
- Espinosa, J. G., Camas, B. S., Capua, D., Fuentes, P. U., and Onate, E. I. (2013). "Advances in the development of a FEM model for evaluation of a surface-effect ship including skirt dynamics," Naval Engineering Journal, 920, 86-91.

- Faltinsen, O. M. (1990). *Sea loads on ships and offshore structures*. Cambridge University Press, Cambridge.
- Faltinsen, O. M. (1997). The effect of hydroelasticity on slamming. *Phil. Trans. R. Soc. Lond. A*, 355, 575–91.
- Faltinsen, O. M. (1999). Water entry of a wedge by hydroelastic orthotropic plate theory. *Journal of Ship Research*, 43(3), 180–193. DOI 0022-4502/99/4303-0180\$00.53/0
- Faltinsen, O.M., Rognebakke, O.F., Lukovsky, I.A., and Timokha, A.N. (2000). Multidimensional modal analysis of nonlinear sloshing in a rectangular tank with finite water depth. *Journal of Fluid Mechanics*, 407, 201-234.
- Faltinsen, O. M. (2005). *Hydrodynamics of high-speed marine vehicles*. Cambridge University Press.
- Faltinsen, O. M., and Timokha, A. N. (2009). *Sloshing*, Cambridge University Press, NY.
- Gingold, R. A., and Monaghan, J. J. (1977). Smoothed particle hydrodynamics: Theory and application to nonspherical stars. *Monthly Notices of the Royal Astronomical Society*, 181, 375–389.
- Hallquist, J. O. (1998). *LS-DYNA Theoretical Manual*, Livermore Software Technology Corporation.
- Hallquist, J. O. (2006). *LS-DYNA Theoretical Manual*, Livermore Software Technology Corporation, California, USA.
- Hattori, M., Arami, A., and Yui, T. (1994). Wave impact pressure on vertical walls under breaking waves of various types, *Coastal Engineering*, 22, 79-114.
- Herault, A., Vicari, A., Negro, C., and Dalrymple, R. A. (2009). Modeling water waves in the surf zone with GPU-SPHysics. 4th International SPHERIC Workshop, Nantes France, May 27-29.
- Hirano, Y., and Miura, K. (1970). Water impact accelerations of axially symmetric bodies.

Journal of Spacecraft and Rockets, 7(6), 762-764.

Hodges, C., Silver, R., Wieser, J., and Adelsen, A. (2009). SES T-Craft Model Testing, Naval Surface Warfare Center Carderock Division NSWCCD-CISD-2009/007, Technical Report.

Imas, L., and Pardes, Ruben. (2011). Application of SPH for fluid-structure interaction problems involving free-surface hydrodynamics, 11th International Conference on Fast Sea Transportation (FAST), Honolulu, Hawaii, USA.

Jackson, K. E., and Fuchs, Y. T. (2008). Comparison of ALE and SPH simulations of vertical drop tests of a composite fuselage section into water. Proceedings of the 10th International LS-DYNA Users Conference, Dearborn, MI, June 8-10.

Kaplan, A. (1968). Simplified dynamic analysis of Apollo water impact, including effects of the flexible heat shield. 11176-11176-6004-R0-00, TRW, Redondo Beach, California, USA.

Karman, T. von. (1929). The impact on seaplane floats during landing. NACA, Tech. Note No. 321, Washington, D.C.

Korobkin, A.A. (2005). Three-dimensional nonlinear theory of water impact. Proceedings of the 18th International Congress of Mechanical Engineering (COBEM). Ouro Preto, Minas Gerais, Brazil.

Korobkin, A. A., and Scolan, Y. M. (2006). Three-dimensional theory of water impact. Part 2. Linearized Wagner problem. Journal of Fluid Mechanics, 549, pp. 343-373.

Kramer, M. R. (2013). "Numerical investigation of the steady state interaction between surface effect ship seals, air cushion, free-surface waves, and vessel motion," PhD Dissertation submitted to University of Michigan, Ann Arbor, USA.

Lacome, J. L. (2009). Smoothed Particle Hydrodynamics (SPH): A new feature in LS-DYNA, 7th European LS-DYNA Conference, May 14th and 15th, Salzburg, Austria.

Lamcotec (2008). 70 Denier Nylon Ripstop, Website:

http://www.lamcotec.com/pr_70_denier_nylon_ripstop.php, accessed 11 March 2014.
ISO 9001:2008.

Lavis, D. (2011). Forty-Plus Years of Hovercraft Development, Severna Park, Maryland, USA.

Lee, D., Kim, M., Kwon, S., and Lee, Y. (2007). A parametric sensitivity study on LNG tank sloshing loads by numerical simulations, *Ocean Engineering*, 34, 3-9.

Lee, S. G, Baek, Y., Lee, I. H., Yang, K. K., and Kim, Y. (2010). Numerical simulation of 2D sloshing by using ALE2D technique of LS-DYNA and CCUP methods, *Proceedings of the Twentieth International Offshore and Polar Engineering Conference*, Beijing, China, June 20-25, 192-199.

Leer, B. V. (1977). Towards the ultimate conservative difference scheme. IV. A new approach to numerical convection, *Journal of Computational Physics*, 167, 276-299.

Schwer, L. (2009). Aluminium plate perforation: A comparative case study using Lagrange with erosion, multi-material ALE, and Smooth Particle Hydrodynamics, 7th European LS-DYNA conference, Stuttgart, Germany.

Le Tallec, P., and Mouro, J. (2000). Fluid structure interaction with large structural displacements, *Computational Methods in Applied Mechanics Engineering*, 1-29.

Liu, G. R., and Liu, M. B. (2003). *Smoothed Particle Hydrodynamics: a meshfree particle method*, World Scientific, Singapore.

Lucy, L. (1977). A numerical approach to testing of the fusion process. *The Astronomical Journal*, 88, 1013-1024.

Melis, E. M., and Bui, K. (2002). Characterization of water impact splashdown event of space shuttle solid rocket booster using LS-DYNA. 7th International LS-DYNA Users Conference, May 19-21, Dearborn, Michigan, USA.

- Miloh, T. (1991). On the initial-stage slamming of a rigid sphere in a vertical water entry. *Applied Ocean Research*, 13(1), 43-48.
- Monaghan, J. J. (1992). Smoothed Particle Hydrodynamics, *Annual Review of Astronomy and Astrophysics*, 30, 543-574.
- Monaghan, J. J., and Gingold, R. A. (1983). Shock simulation by the particle method SPH, *Journal of Computational Physics*, 52, 374-389.
- Monaghan, J. J. (1994). Simulating free surface flows with SPH. *Journal of Computational Physics*, 110, 399-406.
- Monaghan, J. J. (2005). Smoothed particle hydrodynamics, *Rep Progr Phys*, 68, 1703-1759.
- Monaghan, J. J., and Kos, A. (1999). Solitary waves on a Cretan beach. *Journal of the Waterway, Port, Coastal, and Ocean Engineering*, 125 (3), 145.
- Newland, D. E. (1993). *An Introduction to Random Vibrations, Spectral and Wavelet Analysis*, John Wiley & Sons, 3rd edition.
- Pastoor, W., Klungseth-Ostvold, T., Byklum, E., Valsgard, S. (2005). Sloshing load and response in LNG carriers for new designs, new operations and new trades, Technical report, Det Norske Veritas (DNV) Technical Paper.
- Peregrine, D. (2003). Water-wave impact on walls. *Annual Review of Fluid Mechanics*, 35, 23-43.
- Randles, P. W., and Libersky, L. D. (1996). Smoothed particle hydrodynamics: some recent improvements and applications, *Computational Methods in Applied Mechanics Engineering*, 139, 375-408.
- Rugonyi, S., Bathe, K. J. (2001). On finite element analysis of fluid flows fully coupled with structural interactions, *Computational Models for Engineering Science*, 2, 195-212.

- Ryken, J. (1978). Test Data Analysis and Correlation Report: SES100B Finger Motions and Finger Drag, Textron, Bell Aerospace. Report 7593-925003.
- Scolan, Y. M., and Korobkin, A. A. (2001). Three-dimensional theory of water impact. Part 1. Inverse Wagner problem. *Journal of Fluid Mechanics*, 440, 293-326.
- Scolan, Y.M., and Korobkin, A.A. (2012). Hydrodynamic impact (Wagner) problem and Galin's theorem. Proceedings of the 27th International Workshop on Water Waves and Floating Bodies, Copenhagen, Denmark.
- Seddon, C. M., and Moatamedi, M. (2006). Review of water entry with applications to aerospace structures. *International Journal of Impact Engineering*, 32, 1045-1067.
- Selhammar, M. (1997). Modified artificial viscosity in smooth particle hydrodynamics, *Journal of Astronomy and Astrophysics*, 325, 857-865.
- Souli, M., Olovsson, L., and Do, I. (2002). ALE and Fluid-Structure Interaction Capabilities in LS-DYNA. 7th International LS-DYNA Users Conference.
- Souli, M., and Benson, D.J. (2010). Arbitrary Lagrangian-Eulerian and fluid-structure interaction – Numerical Simulation. Wiley publications, USA.
- Souto-Iglesias, A., Idelsohn, S., Marti, J., Zamora-Rodriguez, R., and Onate, E. (2008). Modeling of free surface flows with elastic body interactions, 27th Symposium on Naval Hydrodynamics, Korea.
- Tutt, B. A., and Taylor, A. P. (2004). The use of LS-DYNA to simulate the water landing characteristics of space vehicles. 8th International LS-DYNA Users Conference, May 2-4, Dearborn, Michigan, USA.
- Ugural, A. C. (2009). *Stresses in Beams, Plates, and Shells*, 3rd edition, CRC Press.
- Vandamme, J., Zou, Q., and Reeve, D. E. (2011). Modeling floating object entry and exit using Smoothed Particle Hydrodynamics. *Journal of Waterway, Port, Coastal, and Ocean Engineering*, 137(5), 213-224.

- Von Karman, T. (1929). The impact of seaplane floats during landing. NACA TN 321, National Advisory Committee for Aeronautics, Washington, USA.
- Yang, Q., Jones, V., and McCue, L. (2011). Free-surface flow interactions with deformable structures using a SPH-FEM model, *Ocean Engineering*, 55, 136-147.
- Yun, L. and Bliault, A. (2000). *Theory and Design of Air Cushion Vehicles*, John Wiley and Sons, Inc.,
- Yung, T. W., Sandstrom, R. E., He, H., and Minta, M. K. (2010). On the physics of vapor/liquid interaction during impact on solids. *Journal of Ship Research*, 54, 174-183.
- Wagner, H. (1932). Trans. Phenomena associated with impacts and sliding on liquid surfaces. *Journal of Mathematics and Mechanics*, 12(4), 193-215.
- Wang, J. T., and Lyle, K. H. (2007). Simulating space capsule water landing with explicit finite element method. 48th AIAA/ASME Conference, April 23-26, Waikiki, HI, USA.
- Wiggins A. D., Zalek, S. F., Perlin, M., Ceccio, S. L., Doctors, L. J and Etter, R. J. (2011). Development of a Large Scale Surface Effect Ship Bow Seal Testing Program, 11th International conference on Fast Sea Transportation (FAST), Honolulu, Hawaii, USA.
- Zalek, S. F., Karr, D. G., Jabbarizadeh, S., and Maki, K. J. (2011). Modeling of air cushion vehicle's flexible seals under steady state conditions, *Ocean Systems Engineering*, 1(1), 17-29.
- Zhao, R., Faltinsen, O. M., Aarsnes, J. V. (1996). Water entry of arbitrary two-dimensional sections with and without flow separation. *Proceedings of the 21st Symposium on Naval Hydrodynamics*, 408–23, Washington, D.C.: National Academy Press.

APPENDICES

Appendix–A: Inertial properties of the WLO model

The inertial properties of WLO model include the following calculations:

Center of Gravity Calculations (V_{CG}):

$$\text{Distance, } Z_1 = 0.06 \text{ m}$$

$$\text{Distance, } Z_2 = 0.20 \text{ m}$$

$$\text{Tension in Rope 1, } T_1 = 0.750 \text{ kg}$$

$$\text{Tension in Rope 1, } T_2 = 1.271 \text{ kg}$$

$$\text{Mass of the Model, } W = 2.030 \text{ kg}$$

$$V_{CG} = Z_1 + T_2 (Z_2 - Z_1)/W \quad \text{or}$$

$$V_{CG} = Z_2 - T_1 (Z_2 - Z_1)/W \text{ from top of the body}$$

$$= \underline{147.8 \text{ mm}} \text{ from nose of the model}$$

Details of Moment of Inertia Calculations (I_{xx}):

$$\text{Mass of the model + Pendulum, } m_1 = 12.43 \text{ kg}$$

$$\text{Mass of the Pendulum } m_2 = 10.40 \text{ kg}$$

$$\text{Mass of the model } m = 2.03 \text{ kg}$$

$$\text{Length of the Pendulum for } m_1, L_1 = 1.627 \text{ m}$$

$$\text{Length of the Pendulum for } m_2, L_2 = 0.725 \text{ m}$$

$$\text{Vertical Centre of Gravity, } V_{CG} = 147.8 \text{ mm}$$

$$\text{Dist. from Bearing to Model CG, } L = 0.848 \text{ m}$$

$$\text{Time Period for } m_1, t_1 = 2.3835 \text{ sec}$$

$$\text{Time Period for } m_2, t_2 = 1.9480 \text{ sec}$$

$$I_o = \frac{t_1^2 m_1 g L_1}{4\pi^2} - \frac{t_2^2 m_2 g L_2}{4\pi^2}$$

$$I_{xx} = I_o - mL^2 = \underline{0.02173 \text{ kg m}^2}$$

Moment of Inertia Calculations (I_{yy}):

Mass of the Body + Pendulum, m ₁	=	12.43kg
Mass of the Pendulum, m ₂	=	10.40kg
Mass of the Body, m	=	2.030kg
Length of the Pendulum for m ₁ , L ₁	=	1.627m
Length of the Pendulum for m ₂ , L ₂	=	0.725m
Vertical Centre of Gravity, V _{CG}	=	147.8mm
Dist. From Bearing to Model CG, L	=	0.848mm
Time Period for m ₁ , t ₁	=	2.398sec
Time Period for m ₂ , t ₂	=	1.992sec

$$I_o = \frac{t_1^2 m_1 g L_1}{4\pi^2} - \frac{t_2^2 m_2 g L_2}{4\pi^2}$$

$$I_{yy} = I_o - mL^2 = \underline{0.021892} \text{ kg m}^2$$

Moment of Inertia Calculations (I_{zz}):

Mass of the Body + Pendulum, m ₁	=	10.13kg
Mass of the Pendulum, m ₂	=	8.10kg
Mass of the Body, m	=	2.03kg
Length of the Pendulum for m ₁ , L	=	1.692m
Vertical Centre of Gravity, V _{CG}	=	147.8mm
Distance between Suspenders, b	=	340mm
Time Period for m ₁ , t ₁	=	2.180sec
Time Period for m ₂ , t ₂	=	2.240sec

$$I_{zz} = \frac{(T_1 b)^2 m_1 g}{4(2\pi)^2 L} = \underline{0.1852} \text{ kgm}^2$$

$$\text{Mass moment inertia of attachments } I_{zz}^2 = \underline{0.17113} \text{ kgm}^2$$

$$\text{Yaw moment of inertia} = I_{zz}^1 - I_{zz}^2 = \underline{0.01402} \text{ kg m}^2$$

Center of Gravity

Vertical center of gravity of fabricated WLSC model (measured from nose) =147.8mm

Moments of Inertia

Moment of inertia of the model with respect to major (X) axis (I_{xx}) =0.02173 kg m²

Moment of inertia of the model with respect to minor (Y) axis (I_{yy}) =0.02189 kg m²

Moment of inertia of the model with respect to vertical (Z) axis (I_{zz}) =0.01402 kg m²

Appendix-B: Surface Effect Ships

Surface effect ships (SES) or air-cushion catamarans of lengths less than 40m were frequently built for commercial use until the mid-1990s. The vessel is supported by an air cushion that is bounded by flexible seal systems at the bow and stern and by two side hulls. The aft seal is usually a flexible air bag consisting of a loop of flexible material open against the side hulls, with one or two internal webs restraining the aft face of the loop into a two or three-loop configuration (Faltinsen 2005). Figure 1 shows an example of a surface effect ship (SES). The bow seal (skirt) is usually a finger seal consisting of a row of vertical loops of flexible material.



Figure B-1. Sweden's SES test vessel – HMS "Smyge"
(Source: http://www.islandengineering.com/ses_museum.html)

A schematic of the concept of the air cushion and the water level inside the SES at zero forward speed is shown in Figure 2. An air fan system provides the excess pressure in the air cushion which lifts the SES up, thereby reducing the water resistance. The excess pressure in the air cushion causes a mean depression of the water level inside the cushion which is lower than the water level outside. The buoyancy of the side hulls carries the rest

of the weight at zero speed. Evidently, when the vessel speed increases, the vertical side hull forces due to the water are caused by both hydrostatic (buoyancy) and hydrodynamic pressures. The fluid mechanics equations that govern the SES is presented below. Figure 2 also shows the concept of air cushion and the water level inside the SES at zero forward speed.

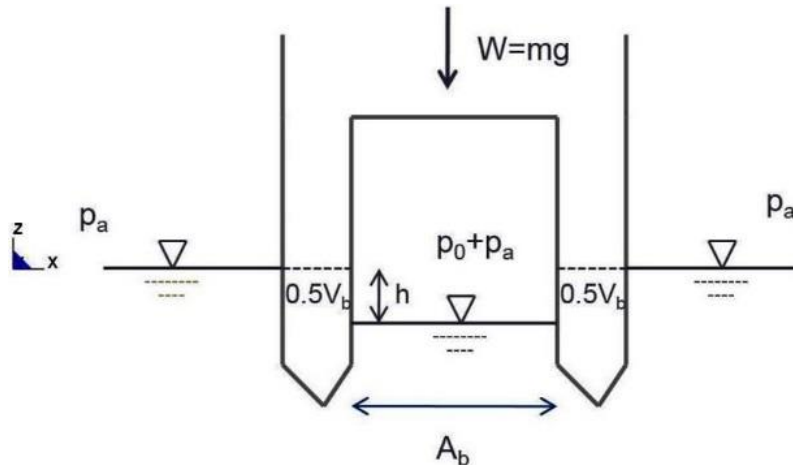


Figure B-2. Concept of air cushion of SES at zero forward speed

The pressure in the water is simply

$$p = p_a - \rho g z \quad (1)$$

where p_a is the atmospheric pressure. The coordinate system is defined in Figure 3, with the Z -axis pointing vertically upward and $z=0$ corresponding to the mean free-surface level outside the cushion. By applying eq. (1) on the water surface inside the cushion, we find

$$p_0 + p_a = p_a + \rho g h \quad (2)$$

$$\text{that is, } h = \frac{p_0}{\rho g} \quad (3)$$

We can find the buoyant volume of the side hulls of the SES (Figure 2) by balancing the weight, cushion pressure forces, and buoyancy forces, that is

$$p_0 A_b + \rho g V_b = Mg \quad (4)$$

where A_b is the cushion area, V_b is the hull volume below $z=0$, and M is the mass of the SES.

Therefore, by rearranging terms in equation 4 gives

$$A_b h = \frac{mg}{\gamma} - V_b \quad (5)$$

which shows that the depressed volume equals to the displacement minus the submerged hull volume.

Appendix–C: Membrane Element Formulation

Membrane element

The Belytschko-Lin-Tsay shell element (Belytschko and Tsay, 1981 and 1984) is the basis for this very efficient membrane element. In this section we briefly outline the theory employed which, like the shell on which it is based, uses a combined co-rotational and velocity-strain formulation. The efficiency of the element is obtained from the mathematical simplifications that result from these two kinematical assumptions. The co-rotational portion of the formulation avoids the complexities of nonlinear mechanics by embedding a coordinate system in the element. The choice of velocity strain or rate of deformation in the formulation facilitates the constitutive evaluation, since the conjugate stress is the more familiar Cauchy stress. In the membrane elements the rotational degrees of freedom at the nodal points may be constrained, so that only the translational degree-of-freedom contribute to the straining of the membrane. A triangular membrane element may be obtained by collapsing adjacent nodes of the quadrilateral (Hallquist 2006).

Co-rotational coordinates

The mid-surface of the quadrilateral membrane element is defined by the location of the element's four corner nodes (Hallquist 2006). An embedded element coordinate system that deforms with the element is defined in terms of these nodal coordinates (Figure 1). The procedure for constructing the co-rotational coordinate system begins by calculating a unit vector normal to the main diagonal of the element:

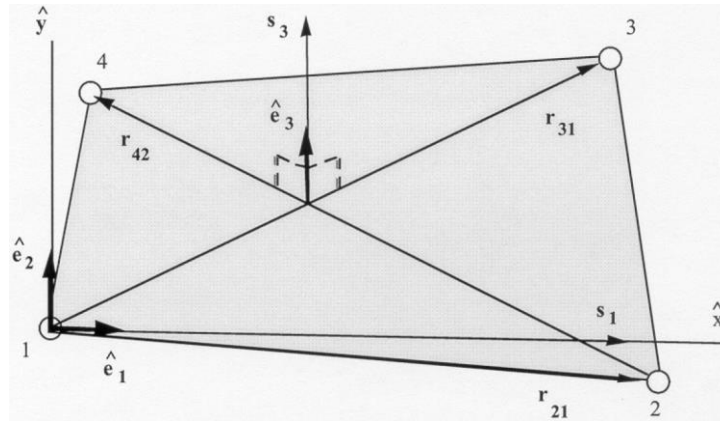


Figure C-1. Construction of membrane element coordinate system (Hallquist, 2006)

$$\hat{e}_3 = \frac{s_3}{\|s_3\|} \quad (1)$$

$$\|s_3\| = \sqrt{S_{31}^2 + S_{32}^2 + S_{33}^2} \quad (2)$$

$$s_3 = r_{31} \times r_{42} \quad (3)$$

It is desired to establish the local x axis \hat{x} approximately along the element edge between nodes 1 and 2. This definition is convenient for interpreting the element stresses, which are defined in the local \hat{x} - \hat{y} coordinate system. The procedure for constructing this unit vector is to define a vector s_1 that is nearly parallel to the vector r_{21} , viz

$$s_1 = r_{21} - (r_{21} \cdot \hat{e}_3) \hat{e}_3 \quad (4)$$

$$\hat{e}_1 = \frac{s_1}{\|s_1\|} \quad (5)$$

The remaining unit vector is obtained from the vector cross product

$$\hat{e}_2 = \hat{e}_3 \times \hat{e}_1 \quad (6)$$

The global components of this co-rotational triad define a transformation matrix between

the global and local element coordinate system. This transformation operates on vectors with global components $A = (A_x, A_y, A_z)$ and element coordinate components

$\hat{A} = (\hat{A}_x, \hat{A}_y, \hat{A}_z)$, and is defined as:

$$\{A\} = [\mu] \{\hat{A}\} \quad (7)$$

where $[\mu]$ contains the global components of the element coordinate unit vectors.

Velocity-strain displacement relations

The co-rotational components of the velocity strain (rate of deformation) are given by (Hallquist 2006):

$$\hat{d}_{ij} = \frac{1}{2} \left(\frac{\partial \hat{v}_i}{\partial \hat{x}_j} + \frac{\partial \hat{v}_j}{\partial \hat{x}_i} \right) \quad (8)$$

The above velocity-strain relations are evaluated only at the center of the shell. Standard bilinear nodal interpolation is used to define the mid-surface velocity, angular velocity, and the element's coordinates (isoparametric representation). These interpolation relations are given by

$$v^m = N_1(\xi, \eta) v_I \quad (9)$$

$$x^m = N_1(\xi, \eta) x_I \quad (10)$$

Where the subscript I is summed over all the element's nodes and the nodal velocities are obtained by differentiating the nodal coordinates with respect to time, i.e. $v_I = \dot{x}_I$. The bilinear shape functions are defined by:

$$\begin{aligned}
N_1 &= \frac{1}{4}(1-\xi)(1-\eta) \\
N_2 &= \frac{1}{4}(1+\xi)(1-\eta) \\
N_3 &= \frac{1}{4}(1+\xi)(1+\eta) \\
N_4 &= \frac{1}{4}(1-\xi)(1+\eta)
\end{aligned} \tag{11}$$

The velocity strains at the center of the element, i.e. at $\xi = 0$, and $\eta = 0$, are obtained as

$$\begin{aligned}
\hat{d}_x &= B_{1I} \hat{v}_{xI} \\
\hat{d}_y &= B_{2I} \hat{v}_{yI} \\
2\hat{d}_{xy} &= B_{2I} \hat{v}_{xI} + B_{1I} \hat{v}_{yI}
\end{aligned} \tag{12}$$

where

$$\begin{aligned}
B_{1I} &= \frac{\partial N_I}{\partial \hat{x}} \\
B_{2I} &= \frac{\partial N_I}{\partial \hat{y}}
\end{aligned} \tag{13}$$

Stress resultants and nodal forces

After suitable constitutive evaluations using the above velocity strains, the resulting stresses are multiplied by the thickness of the membrane, h , to obtain local resultant forces (Hallquist 2006).

Therefore,

$$\hat{f}_{\alpha\beta}^R = h \hat{\sigma}_{\alpha\beta} \tag{14}$$

where the superscript R indicates a resultant force and the Greek subscripts emphasize the limited range of the indices for plane stress plasticity.

The above element centered force resultants are related to the local nodal forces by

$$\begin{aligned} \hat{f}_{xI} &= A(B_{1I} \hat{f}_{xx}^R + B_{2I} \hat{f}_{xy}^R) \\ \hat{f}_{yI} &= A(B_{2I} \hat{f}_{yy}^R + B_{1I} \hat{f}_{xy}^R) \end{aligned} \quad (15)$$

where A is the area of the element.

The above local nodal forces are then transformed to the global coordinate system using the transformation relation given by (1).

Appendix–D: ALE Modeling Guidelines for Fluid-Structure Interaction

Situations involving the fluid modeling (wherein the deformation of the finite element mesh exactly follows the deformation of the material), a pure Lagrangian approach is often not suitable owing to the very large deformation of the material. Severe mesh distortion can lead to a smaller explicit time step and eventual instability. In the Lagrangian approach the nodes move directly along with the material and therefore the elements and materials translate, rotate and deform together. Material does not cross the element boundaries and thus the mass of the material within each Lagrangian element never changes

In an Eulerian solution method, the materials flows (or advects) through the Eulerian mesh which is fixed in space. This material can move and deform within the fixed mesh. As the simulation progresses, at each time step some small amount of material may advect out of one cell and into an adjacent cell. At any given point in time, each Eulerian element may contain a mixture of multiple materials, hence referred to as “multi-material”.

In contrast, in an arbitrary Lagrangian-Eulerian (ALE) formulation, the material flows (or advects) through the ALE mesh which is directed to move in some prescribed fashion as the simulation progresses, and is much better suited to modeling of fluid behavior. Note that though the material advection across the element boundaries is still required, a small amount of material advected each time step is generally less as compared to the Eulerian approach since the mesh is also moving. Eulerian method is a special case of ALE wherein the prescribed reference mesh velocity is zero.

In many fluid-structure interaction (FSI) models these two methods can be combined using a coupling algorithm. Thus structural components that deform a moderate amount, such as

structural components of elastic members, composite fibers, or membranes, can be modeled with Lagrangian elements whereas fluids, such as air and water, and gas can be modeled with ALE elements. Presented below are some of the brief guidelines for ALE modeling in LS-DYNA provided by LSTC (2010).

Applications to Fluid-Structure Interaction modeling

ALE element formulation

Generally when two or more fluids or fluid-like materials are to be modeled using the ALE approach in LS-DYNA, the recommended element formulation for those materials is the multi-material ALE formulation (ELFORM = 11 in *SECTION_SOLID). As the ALE materials flow through the ALE mesh, the material boundaries or interfaces in general do not coincide with the mesh lines. These material interfaces are internally reconstructed each time step based on the volume fractions of the materials within the elements. Each material is tracked independently using a unique ALE multi-material group (AMMG) ID using the command *ALE_MULTI-MATERIAL_GROUP.

In some situations where the ALE mesh is initially devoid of material (called void) provides space into which other, higher density materials can be transported. Such materials are modeled with *MAT_VACUUM. If the space is occupied by air or an ideal gas with nonzero density *Mat_Null with an equation-of-state (EOS) such as *Gruneisen or *Linear polynomial is used. Situations where the motion of the ALE mesh in a specific predetermined fashion is essential (e.g., fluid sloshing in a tank) *ALE_Reference_System_Node/Group should be used.

Element distortion (called Hourglassing) is an essential feature while dealing with

modeling large deformation problems. For materials modeled as gases or liquids using ALE, hourglass formulation 1 and a much reduced hourglass coefficient, e.g., 1.0E-6 or less, are recommended to prevent application of inappropriate hourglass forces. The default hourglass coefficient for ELFORM=11 is generally set to 1.E-06.

ALE meshing

Hexahedral elements with good aspect ratios are used for the ALE mesh. Initial mesh of the ALE domain is constructed to conform to the shape of the initial configuration. Degenerate element shapes, such as tetrahedrons and pentahedrons, should be avoided as they lead to reduced accuracy and perhaps numerical instability during the advection process.

Fluid and structure coupling

Most often, in modeling FSI problems, the fluids are modeled with ALE hexahedron elements and the structure is modeled with Lagrangian shell or solid elements. In such models, the Lagrangian mesh usually does not share nodes with the ALE mesh. Rather, the interaction between the two meshes is performed using a coupling algorithm defined with the command `*CONSTRAINED_LAGRANGE_IN_SOLID`. This coupling mechanism serves to generate forces (by adding springs between elements) that resist penetration of the ALE material through the Lagrangian components. Coupling is a complex and important aspect of ALE modeling. Changing just a single parameter will change how the system behaves. Recommendations for using this feature for a proper coupling are provided below for certain important parameters.

Constrained Lagrange in Solid

1	COUPID	TITLE							
0		Bow Seal with Air and Water							
2	SLAVE	MASTER	SSTYP	MSTYP	NQUAD	CTYPE	DIREC	MCOUP	
3	1	1	0	4	4	1	0		
3	START	END	PFAC	FRIC	FRCMIN	NORM	NORMTYP	DAMP	
0.0	1.000e+010	0.1000000	0.0	0.5000000	0	0	0.0		
4	CQ	HMIN	HMAX	ILEAK	PLEAK	LCIDPOR	NVENT	BLOCKAGE	
0.0	0.0	0.0	0	0.1000000	0	0	0		
5	IBOXID	IPENCHK	INTFORC	JALESOFF	LAGMUL	PFACMM	THKE		
0	0	0	0	0.0	0	0.0			

Total Card: 2 Smallest ID: 1 Largest ID: 2 Total deleted card: 0

Figure D-1. Constrained Lagrange in Solid Keyword

In this coupling mechanism the master is always the ALE elements and the slave is always the Lagrange elements. The opposite is valid for the SPH model. The amount of coupling between these two elements is dictated by NQUAD. It determines the number of coupling points distributed over each Lagrangian slave segment. For example, if NQUAD=2, then there are $2 \times 2 = 4$ coupling points on each Lagrangian slave segment. If the Lagrangian slave segments are approximately the same size as or smaller than the Eulerian/ALE element faces, NQUAD=2 will generally suffice. On the other hand, if the Lagrangian slave segments are coarser/larger than the ALE element faces, NQUAD may need to be raised to 3 or higher to provide proper coupling. Note that a larger value of NQUAD can make the computation very expensive. An insufficient value of NQUAD may lead to leakage of the ALE material through the Lagrangian elements. Therefore, an optimum value based on a trial and error procedure is needed to model the correct physics of the problem without the leakage.

The parameter CTYPE identifies the coupling algorithm employed. The most common

parameter, the one that is used extensively in this research, is the penalty based coupling.

In most FSI applications, penalty based coupling is more robust and is set to 4.

Direction of coupling (compression or tension) is determined by the DIREC parameter.

There are three options: compression and tension in the normal direction, compression only in the normal direction, and compression and tension in all directions. When simulating a fluid flow, coupling in compression is needed.

The parameter MCOUP defines the AMMG(s) to which the Lagrangian slave side is coupled. Comparatively if one AMMG dominates the forces imparted to the Lagrangian structure compared to the other, MCOUP should be set to 1. This is typical in situations where the density of one AMMG is far greater than the density of the other. Importantly, in cases where the effects of two or more groups take part in active coupling, MCOUP can be set to a negative number.

Initial Volume Fraction Geometry

Keyword Input Form

NewID Draw Pick Add Accept Delete Default Done

Use *Parameter (Subsys: 1) Setting

*INITIAL_VOLUME_FRACTION_GEOMETRY (1)

FMSID	FMIDTYP	BAMMG	NTTRACE
1	0	1	3

Repeated Data by Button and List

CONTYP	FILLOPT	FAMMG	VX	XY	XZ	RADVEL	UNUSED
3	0	2	0.000	0.000	0.000	0	0

X0	Y0	Z0	XCOS	YCOS	ZCOS	UNUSED	UNUSED
0.000	0.000	0.000	0.000	0.000	1.000000	0.000	0.000

1	3	0	2.00000e+000	0.00000e+000	0.00000e+000	0	0 / 0.0000e+000 0.0000e+000 0.0000e+000 0.0000
2	3	0	2.00000e+000	0.00000e+000	0.00000e+000	0	0 / 3.1819e+001 0.0000e+000 -1.6826e+000 6.4152
3	3	1	1.00000e+000	0.00000e+000	0.00000e+000	0	0 / 0.0000e+000 0.0000e+000 -1.6826e+000 0.0000
4	3	0	2.00000e+000	0.00000e+000	0.00000e+000	0	0 / 5.6399e+001 0.0000e+000 -2.5678e+000 7.0700
5	3	1	1.00000e+000	0.00000e+000	0.00000e+000	0	0 / 0.0000e+000 0.0000e+000 -2.5678e+000 0.0000

COMMENT:

Total Card:1 Smallest ID:1 Largest ID:1 Total deleted card: 0

Figure D-2. Initial Volume Fraction Geometry Keyword

Initial Volume Fraction Geometry (IVFVG) is volume-filling command for defining the volume fractions of various AMMGs that initially occupy various spatial regions in an ALE mesh (Hallquist, 2006). In many situations, where both the ALE and Lagrangian elements much have overlapping meshes, the interior portions of the Lagrangian materials contain the material from ALE. This card works well with shell elements only.

This can be achieved by a two-step process. First step is to define all the AMMGs that need to be adjusted. A background ALE multi-material group (BAMMG) is to be removed and a new filling ALE multi-material group (FAMMG) is added (first level of the card). The second step is the type of filling/evacuation of the materials. This can be done by a container type procedure where a “container” defines a Lagrangian surface boundary of a specific region, inside (or outside) of which, an AMMG would fill up (second and third levels of the card).

Note that if the Lagrange element is made of shell elements, it is defined as a part or part set. If the Lagrange is a solid element, a segment set has to be defined. Once this is achieved, the FAMMG needs to be defined as the ALE material that is going to fill the container. A normal direction can also be specified to either fill the outside or inside to the container. Note that the IVFG card initializes the ALE elements before any calculation are performed.

Modeling tips and leakage control

The relative mesh resolution between Lagrangian to ALE meshes should be close to 1:1 as possible. What constitutes an appropriate degree of refinement for the ALE mesh is at least partially dictated by the geometric characteristics of the Lagrangian parts. A reasonable

goal is to have the ALE elements be nearly the same size as the Lagrangian elements where coupling is to take place. The meshes should be smooth and regular with good aspect ratios.

In many occasions leakage occurs due to bad meshes.

To use penalty coupling, there should be at least three or four element layers of ALE domain beyond the Lagrangian shell part/surface. For example, to model a tank sloshing, the ALE domain should extend outside the Lagrangian shell tank. This is to provide the ALE space for the AMMGs to flow into and the fluid penetration amount across the shell be computed.

When coupling with a shell surface, having distinct AMMG IDs on either side is a good practice. This is a necessary condition when there are two physically different materials on either side. When coupling to a solid structure, providing an AMMG in front of the solid Lagrangian part is needed so that the impacting surface will be different from the one behind the surface.

Leakage is an undesirable condition whereby coupling does not prevent unreasonable penetration of ALE material through Lagrangian surfaces. A small amount of leakage is to be expected and can be tolerated for penalty-based coupling, analogous to the case of small penetrations that are observed for penalty-based contact.

NQUAD should be set to at least two coupling points per ALE element. As the NQUAD is distributed over each Lagrangian element surface, the relative Lagrangian to ALE mesh resolution is important. Increasing the value of NQUAD if there are too few coupling points on the Lagrangian segments is a good practice. Note that increasing NQUAD drives up the CPU time and it can provide a very stiff response and can lead to numerical instability.

An appropriate coupling stiffness is key to good coupling behavior with CTYPE=4. In most cases, the default penalty stiffness (PFAC=0.1) is sufficient and works as a good starting point. If the default coupling stiffness is inadequate, increasing PFAC can resolve the leakage problem. A more logical approach is to set PFAC to a negative integer, which tells the code that the coupling stiffness comes from curve |PFAC| wherein the abscissa is penetration distance and the ordinate is coupling pressure (see manual for details).